THE HONG KONG
POLYTECHNIC UNIVERSITY
香港理工大學
Pao Yue-kong Library
包玉剛圖書館

Copyright Undertaking

This thesis is protected by copyright, with all rights reserved.

By reading and using the thesis, the reader understands and agrees to the following terms:

1. The reader will abide by the rules and legal ordinances governing copyright regarding the use of the thesis.
2. The reader will use the thesis for the purpose of research or private study only and not for distribution or further reproduction or any other purpose.
3. The reader agrees to indemnify and hold the University harmless from and against any loss, damage, cost, liability or expenses arising from copyright infringement or unauthorized usage.

IMPORTANT

If you have reasons to believe that any materials in this thesis are deemed not suitable to be distributed in this form, or a copyright owner having difficulty with the material being included in our database, please contact lbsys@polyu.edu.hk providing details. The Library will look into your claim and consider taking remedial action upon receipt of the written requests.

Pao Yue-kong Library, The Hong Kong Polytechnic University, Hung Hom, Kowloon, Hong Kong

http://www.lib.polyu.edu.hk

BEHAVIOUR OF WAVY-SHAPED FRP-UHPC HYBRID REBARS

LI XINYUN

PhD

The Hong Kong Polytechnic University

2026

The Hong Kong Polytechnic University

Department of Civil and Environmental Engineering

Behaviour Of Wavy-Shaped Frp-Uhpc Hybrid Rebars

LI XINYUN

A Thesis Submitted in Partial Fulfilment of the Requirements for the

Degree of Doctor of Philosophy

May 2025

CERTIFICATE OF ORIGINALITY

I hereby declare that this thesis is my own work and that, to the best of my knowledge and belief, it reproduces no material previously published or written, nor material that has been accepted for the award of any other degree or diploma, except where due acknowledgement has been made in the text.

_____________ (Signed)

LI Xinyun (Name of Student)

DECLARATION OF USE OF GENERATIVE AI

I declare that a Generative AI tool has been used to assist in the preparation of this thesis. The tool was used exclusively for revising and providing feedback on my drafts. The specific tool and its uses are as follows:

OpenAI ChatGPT

- English grammar verification
- Recommendations for alternative vocabulary
- British English conventions and usage checking

To My Family

ABSTRACT

Fibre-reinforced polymer (FRP) rebars have seen increasing adoption in concrete structures to replace steel rebars due to their advantages of high strength-to-weight ratio and excellent corrosion resistance. However, FRP rebars have much weaker compressive performance than their tensile performance due to fibre micro-buckling under compression. A novel hybrid rebar, featuring an outer FRP tube, a central FRP rebar, and an annular layer of ultra-high performance concrete (UHPC), has been proposed by J.G. Teng and his associates at The Hong Kong Polytechnic University (PolyU) to address this issue. The central FRP rebar is well supported by the UHPC and the latter is well confined by the outer FRP tube when the hybrid rebar is under compression. Therefore, global buckling of the rebar and fibre micro-buckling in the central FRP rebar can be suppressed or delayed. In the initial proposal by Teng and associates, the outer FRP tube had a uniform cross-section in the longitudinal direction (referred to as a uniform FRP tube hereafter), and as a result, the bond between such hybrid rebars (referred to as uniform hybrid rebars hereafter) and the surrounding concrete, as well as that between the FRP tube and the inner UHPC, is less than satisfactory. Against this background, this Ph.D. research project was concerned with a new form of hybrid rebars with a wavy shape for the FRP tube in the longitudinal direction. The wavy-shaped surface introduces mechanical interlocking between the hybrid rebar and the surrounding concrete, which is expected to substantially enhance the bond performance.

The initial phase of this Ph.D. research programme explored the manufacturing method of wavy-shaped FRP tubes with the filament winding technology. The resin burn-off test and the digital image processing method were employed to determine the fibre volume fractions of the fabricated wavy-shaped FRP tubes at different locations. Split disk tests and internal air pressure tests were conducted to examine the hoop elastic moduli of wavy-shaped FRP tubes.

The second part of this Ph.D. research programme focused on the compressive performance of FRP-confined UHPC/ultra-high performance fibre reinforced concrete (UHPFRC) with a compressive strength of over 180 MPa. The experimental investigations on FRP-confined UHPC/UHPFRC under axial compression were first conducted. The existing predictive models which had been proposed for FRP-confined normal strength concrete (NSC) and UHPC/UHPFRC were then evaluated and developed.

The third part of this Ph.D. research programme included experimental studies on the compressive performance of wavy-shaped hybrid rebars under monotonic axial compression and cyclic axial compression. The test results indicated that the proposed wavy-shaped hybrid rebars exhibited compressive strengths and ductility levels comparable to uniform hybrid rebars under either monotonic or cyclic axial compression. An improved stress-strain model for FRP-confined UHPC under cyclic axial compression was developed, which was used subsequently to accurately predict the cyclic axial compressive behaviour of wavy-shaped hybrid rebars.

In the final part of this Ph.D. research programme, pull-out tests were conducted to investigate the bond performance of wavy-shaped hybrid rebars. The test variables included the FRP confinement level, the bond length, and the type of FRP rebars. The test results indicated that the adoption of wavy-shaped FRP tubes significantly enhances the bond performance between wavy-shaped hybrid rebars and surrounding concrete.

ACKNOWLEDGEMENTS

First and foremost, I wish to convey my sincere gratitude to my chief supervisor, Professor Jin-Guang Teng, and my co-supervisor, Dr. Guan Lin, for granting me the opportunity to pursue my Ph.D. degree at The Hong Kong Polytechnic University. Over the past several years, Professor Teng and Dr. Lin have provided me with tremendous encouragement, generous support, and invaluable guidance on my research project. It has been a great privilege to explore this topic under their supervision. Their meticulous attitude, humility, diligence, and passion for academic research will have a lasting impact on me throughout my life.

I would also like to thank my colleagues and friends who have provided me with substantial assistance in my research work. I wish to thank Dr. Shuai Li, Dr. Yu Xiang, Dr. Cheng Jiang, Dr. Bo-Tong Zheng, Dr. Pan Zhang, Dr. Kai-Cheng Liu, Dr. Meng-Han Zhao, Dr. Yi-Wen Zhang, Dr. Wei Xiong, Dr. Meng Xiao, Mr. Rui-Long Li, Ms. Chu-Ying Cui, Mr. Jia-Ming Zhu, and Ms. Xi Li for their help and meaningful discussions.

Additionally, I would like to thank the technical staff of the Structural Engineering Laboratory, Concrete Technology Laboratory, Geology Laboratory, Rock Mechanics Laboratory and Mechanics Laboratory at The Hong Kong Polytechnic University. They are Mr. David H.Y. Leung, Mr. Harry Lai, Mr. Kwok-Lung Cheung, Ms. Fion Cheng, Mr. Raymond Leung and Mr. Ka-Chung Cheung. I am grateful for their assistance during the preparation and execution of my experiments.

Sincere gratitude is also extended to Professor Jin-Guang Teng for granting me the opportunity to work as a research assistant in his research group from September 2018 to August 2019, prior to the commencement of my Ph.D. studies. The experiments constituting Batch 1 in Chapter 4 were carried out during the afore-mentioned research assistantship period, while the remaining experiments, analyses, and discussions presented in this chapter were undertaken during my Ph.D. study period.

I gratefully acknowledge the financial support received from The Hong Kong Polytechnic University, the Hong Kong Research Grants Council (Project Nos.: T22-502/18-R and BQ54K) and Southern University of Science and Technology.

Lastly, I am profoundly grateful to my parents for their everlasting love and selfless support. Without their support, I would not have been able to complete my Ph.D. research. This work is dedicated to them.

CONTENTS

LIST OF TABLES

LIST OF FIGURES

LIST OF ACRONYMS

CFFT	concrete-filled FRP tube
CFRP	carbon fibre-reinforced polymer
CFST	concrete-filled steel tube
CoV	coefficient of variation
DFOS	distributed fibre optic sensing
DIP	digital image processing
FA	fly ash
FRP	fibre-reinforced polymer
FWM	filament winding method
GFRP	glass fibre-reinforced polymer
GBFS	granulated blast furnace slag
HSC	high-strength concrete
LP	limestone powder
LVDT	linear variable differential transformer
MRI	magnetic resonance imaging
NSC	normal-strength concrete
OM	optical microscopy
OPC	ordinary Portland cement
PVC	polyvinyl chloride
RC	reinforced concrete
SD	standard deviation
SEM	scanning electron microscopy
SF	silica fume
SS	steel slag
SSC	seawater sea-sand concrete
UHPC	ultra-high performance concrete
UHPFRC	ultra-high performance fibre-reinforced concrete
UHPSSC	ultra-high performance seawater sea-sand concrete

NOTATION

A_a	cross-sectional area of concrete annulus filled between the central FRP rebar and the outer FRP tube
A_b	cross-sectional area of FRP rebar
A_t	cross-sectional area of FRP tube
A_u	cross-sectional area of FRP-confined solid UHPC column
b	width of an FRP ring in Chapter 3
b_w	width of a tow
D	diameter of concrete core
D_M	diameter of a mandrel
D_{avg}	average inner diameter of a wavy-shaped tube
D_f	density of glass fibres
D_{max}	maximum inner diameter of a wavy-shaped tube
D_{min}	minimum inner diameter of a wavy-shaped tube
D_s	density of original FRP sample
d	effective diameter of an FRP rebar
d_w	distance between two adjacent parallel tows along the longitudinal direction of the mandrel
E_1	slope of the linear first portion of a stress-strain curve in Chapter 5
E_2	slope of the linear second portion of a stress-strain curve
E_3	slope of the linear third portion of a stress-strain curve in Chapter 5
E_C	elastic modulus of concrete
E_b	compressive elastic modulus of FRP rebar in Chapter 5
E_{frp}	elastic modulus of FRP
E_i	experimental value for i^{th} data point
E_{re}	slope of linear portion of a reloading curve
F	pullout load

F_a	load resisted by FRP-confined UHPC annulus in a hybrid rebar
F_b	load resisted by FRP rebar in a hybrid rebar
F_h	summed load resistance of FRP-confined UHPC annulus and FRP rebar
F_t	applied tensile force
F_u	load resisted by FRP-confined solid UHPC column
f_1, f_2, f_3, f_4	axial stresses at the first, second, third and fourth characteristic points of a hybrid rebar in Chapter 5
f'_{c1}, f'_{c2}, f'_{c3}	axial stresses at the first, second, third and fourth characteristic points in Chapter 4
f'^{*}_{cc}	peak axial stress of concrete at a given lateral confining pressure
f'_{co}	unconfined concrete strength
f'_{cu}	axial stress at ultimate axial strain
f_d	stress drop after first peak stress in Chapter 6
f_l	lateral confining pressure
h	vertical distance between peak and trough of a wave
k_ε	strain efficiency factor
l	embedment length of an FRP rebar
L_u	unbraced length of an FRP rebar
M_f	fibre weight content
P	air pressure in internal air pressure tests
P_i	predicted value for i^{th} data point
R	internal radius of a tube at measured cross-section in Chapter 3
S_{mf}	free end slip at peak bond stress of an FRP rebar
S_{ml}	loaded end slip at peak bond stress of an FRP rebar
t	thickness of an FRP jacket or tube
V_f	fibre volumetric fraction
W_1	weight of original FRP sample

W_2	weight of residue after burning
α	hoop-winding angle
ε_1, ε_2, ε_3, ε_4	axial strains corresponding to f_1, f_2, f_3, f_4 in Chapter 5
$\varepsilon_{h,rup}$	hoop rupture strain of an FRP jacket or tube
ε_h	hoop strain of an FRP jacket/tube
ε_c	axial strain of concrete
ε_{c1}, ε_{c2}, ε_{c3}	axial strains corresponding to f'_{c1}, f'_{c2}, f'_{c3} in Chapter 4
ε_{cc}^*	axial strain corresponding to $f_{cc}^{\prime *}$
ε_{co}	axial strain at peak stress of unconfined concrete
ε_{cu}	ultimate axial strain
ε_f	FRP rupture strain determined from tensile tests of flat coupons
ε_m	membrane strain of an FRP tube
ε_{fu}	FRP hoop strain at failure observed in test cylinders
$\varepsilon_{pl,stage\ 3}$	plastic strain of a hybrid rebar before failure of the central FRP rebar
$\varepsilon_{pl,stage\ 4}$	plastic strain of a hybrid rebar after the failure of the central FRP rebar
$\varepsilon_{pl,co}$	plastic strain of UHPC in a hybrid rebar
ε_{pl}	plastic strain
ε_{ref}	reference strain of an unloading path
$\varepsilon_{ret,env}$	unloading strain from an envelope curve
ε_t	axial strain at intersection of two portions
ε_{un}	unloading strain of an unloading path
$\overline{\varepsilon_c}$	average hoop strain from two strain gauges on the initially compressive side
$\overline{\varepsilon_t}$	average hoop strain from two strain gauges on the initially tensile side
η	parameter controlling rate of change in the degree of non-linearity of an unloading path

θ	helical-winding angle
ρ_k	confinement stiffness ratio
ρ_ε	strain ratio
σ_c	axial stress of concrete
σ_f	membrane stress
σ_l	confining pressure from an FRP jacket
σ_{new}	new stress on a reloading path
σ_{re}	reloading stress of a reloading path
$\sigma_{ret,env}$	envelope returning stress
σ_{un}	unloading stress of an unloading path
τ	average bond stress of an FRP rebar
τ_m	peak bond stress of an FRP rebar
φ	stress deterioration ratio

CHAPTER 1
INTRODUCTION

1.1 RESEARCH BACKGROUND

Fibre-reinforced polymer (FRP) composites represent an advanced class of materials with fibres (typically made from carbon, glass, or aramid) embedded within a polymer matrix. The fibres provide most of the strength and stiffness of the composites, while the polymer matrix binds and protects the fibres. Over the past several decades, FRP composites have been extensively utilised in construction due to their high strength-to-weight ratios and excellent corrosion resistance. In structural engineering, FRP materials have emerged as a viable alternative to steel, particularly in structures prone to environmental attacks, such as offshore and coastal structures. Traditional steel-reinforced concrete (RC) structures are susceptible to corrosion, prompting the development of FRP-concrete structures as a solution. The excellent corrosion resistance of FRP composites allows the direct incorporation of seawater and sea-sand in concrete. The resulting structures, composed of FRP and seawater sea-sand concrete (SSC), are referred to as FRP-SSC structures, which not only reduce the demand for freshwater and river sand but also offer a sustainable solution for construction in coastal areas (Teng et al., 2016a). The use of seawater and sea-sand in concrete production has been explored in various studies, highlighting its feasibility and benefits (Yang et al., 2020; Zhang et al., 2022; Xu et al., 2023).

In FRP-concrete structures, FRP composites can be used as either external confinement or internal reinforcement. FRP confinement has been found to effectively and significantly enhance both the strength and ductility of concrete. Wrapping fibre sheets impregnated with polymer matrix around an existing column to form an FRP wrap or FRP jacket is a common method of providing confinement to the column for enhanced performance. FRP tubes are commonly fabricated using the filament winding process or the pultrusion process. Filament-wound FRP tubes have been widely used for constructing concrete columns or beams in which the concrete is confined by the FRP tube. Particularly, columns constructed with such FRP tubes, such as concrete-filled FRP tubular (CFFT) columns, have gained more and more acceptance as structural elements in practice (Mirmiran et al., 2001; Fam et al., 2003; Zhu et al., 2006; Zeng et al., 2018; Chen et al., 2022; Chen, 2024). In addition to the utilisation of FRP jackets and tubes as external confinement materials, FRP tubes have also been employed as internal reinforcement within concrete structures. Examples include concrete-filled steel tubular (CFST) columns with inner FRP tubes and GFRP rebar-reinforced concrete beam-column joints with an embedded FRP tube (Long et al., 2018; Lin et al., 2022). The existence of an internal FRP tube in CFST columns could offer continuous and supplementary confinement to the core concrete and restrict its lateral expansion, resulting in delayed local buckling in the steel tube and excellent performance of the column in terms of ductility (Long et al., 2018). In GFRP rebar-reinforced concrete beam-column joints, the incorporation of an FRP tube could serve as a substitute for stirrups within the joint zone. This substitution alleviates the strain-softening behaviour of the concrete in the joint due to the confinement provided by the FRP, thus enhancing the joint's capacity to resist compressive and shear forces (Lin et al., 2022).

In addition to FRP tubes, FRP rebars are more commonly employed as longitudinal or transverse reinforcements in concrete structures for internal reinforcement. Substituting FRP rebars for traditional steel rebars in concrete structures offers several distinct advantages. Notably, FRP rebars exhibit excellent corrosion resistance, ensuring good durability of the structure in harsh environments. Additionally, their lower density compared to steel rebars facilitates easier construction and transportation. Furthermore, FRP rebars are non-magnetic and non-conductive, making them an ideal choice for applications sensitive to electromagnetic fields, such as magnetic resonance imaging (MRI) units.

Despite the benefits of FRP rebars, their use as longitudinal reinforcement in concrete columns has been limited due to their significantly less favourable performance under compression. Fibre micro-buckling is likely to occur in FRP rebars when exposed to compressive forces, resulting in a compressive strength that is significantly lower than their tensile strength. Moreover, due to their high strength-to-modulus ratio, FRP rebars are prone to buckling unless sufficiently supported by a confining material (Kobayashi and Fujisaki, 1995; Deitz et al., 2003). Due to the inferior performance of FRP rebars under compression and the scarcity of experimental data, the ACI 440.1R-15 (2015) design guide does not recommend the use of FRP rebars as longitudinal reinforcement in compression members, while in CSA S806-12 (R2017), the compressive contribution of FRP rebars is considered to be negligible. Consequently, FRP rebars are primarily used as tensile reinforcement in concrete structures.

1.2 FRP-UHPC HYBRID REBARS

To tackle the problem presented in the previous section, an innovative form of rebars, referred to as hybrid rebars, was proposed by Professor Jin-Guang Teng and his associates at The Hong Kong Polytechnic University (Teng et al., 2018). As shown in Figure 1.1, a hybrid rebar consists of an outer FRP confining tube (e.g., with a diameter of 50 mm) filled with a high-strength cementitious material such as ultra-high performance concrete (UHPC) as well as a central FRP rebar (e.g., with a diameter of 25 mm) as internal reinforcement. Hybrid rebars can resist both tension and compression effectively, with tension being mainly resisted by the central FRP rebar and compression being resisted by both the FRP rebar and the FRP-confined UHPC. A preliminary experimental study on the compressive behaviour of such hybrid rebars was carried out by Teng et al. (2018). The test results showed that the FRP rebar at the centre of the hybrid rebar was well supported by the surrounding cementitious material and the failure modes of global buckling and fibre micro-buckling of the FRP rebar were both effectively prevented. Hybrid rebars can be used to replace all or part of FRP rebars in FRP rebar-reinforced concrete columns, resulting in the so-called hybrid rebar-reinforced concrete columns, which are expected to perform better than concrete columns reinforced with conventional FRP rebars only.

UHPC is an ideal material to be used as the filling material in hybrid rebars. UHPC is characterised by its exceptionally high compressive strength, typically exceeding 150 MPa, as well as its low permeability, and outstanding durability (Richard and Cheyrezy, 1995; Graybeal and Tanesi, 2007). The composition of UHPC includes a carefully proportioned blend of high-quality cementitious materials such as Portland cement, silica fume (SF), granulated blast furnace slag (GBFS), fly ash (FA), metakaolin, limestone powder (LP), steel slag powder (SS), and various nanoparticles (Shi et al., 2015). These components are selected to optimise the microstructure of the concrete, thereby enhancing its performance characteristics. Additionally, UHPC incorporates fine aggregates such as quartz powder and quartz sand, along with superplasticizers to improve workability and reduce water content.

Fibres, such as steel fibres or carbon fibres, are commonly added to UHPC to improve its ductility and toughness in tension (Wille et al., 2014). To distinguish between UHPC with and without fibres, the subsequent text in this Ph.D. thesis refers to UHPC with fibres as ultra-high performance fibre-reinforced concrete (UHPFRC) (Shi et al., 2015), while UHPC without fibres is simply referred to as UHPC. Historically, the production of UHPC/UHPFRC required specialised treatments, such as vacuum mixing, pressure setting, and thermal curing at elevated temperatures (De Larrard and Sedran, 1994). However, recent advancements have demonstrated that UHPC/UHPFRC can achieve its high performance characteristics with more conventional curing conditions, such as atmospheric pressure and ambient temperatures (Zhang et al., 2008; Wille et al., 2011). Professor Jin-Guang Teng's research group has also succeeded in achieving compressive strengths of up to 180 MPa for UHPC without coarse aggregate using locally available UHPC raw materials and standard ambient curing conditions (Teng et al., 2019). Despite these advancements, studies focusing on FRP-confined UHPC/UHPFRC remain limited, particularly for UHPC without steel fibres with compressive strengths greater than 150 MPa. Therefore, further research on FRP-confined UHPC/UHPFRC is essential to facilitate the subsequent utilisation of UHPC in hybrid rebars.

1.3 WAVY-SHAPED HYBRID REBARS

As hybrid rebars are used as internal reinforcement in concrete structures, a strong bond between the hybrid rebar and its surrounding concrete is of great importance to reliable performance of structures with hybrid rebars under various loading conditions. This bond ensures that effective transfer of stresses between hybrid rebars and concrete, thus maintaining the reliability and safety of the structures. The original form of hybrid rebars proposed by Professor Jin-Guang Teng and associates, as shown in Figure 1.2, possess an FRP tube with a uniform cross-section in the longitudinal direction (referred to as a uniform FRP tube hereafter), resulting in a relatively weak bond between the hybrid rebar (referred to as a uniform hybrid rebar hereafter) and the surrounding concrete, as well as that between the FRP tube and the UHPC.

This Ph.D. research project was undertaken to explore new techniques to enhance the bond behaviour of hybrid rebars with the surrounding concrete. As shown in Figure 1.3, filament-wound FRP tubes with a wavy shape were proposed and used to fabricate wavy-shaped hybrid rebars. For steel rebars, the bond mechanism is understood to rely on three primary components: (1) friction resistance; (2) chemical adhesion; and (3) mechanical interlocking (Pillai and Kirk, 1983). The mechanical interlock, which is more significant in magnitude than the preceding two components, is a vital element contributing to the bond between a steel rebar and the surrounding concrete. In the case of uniform hybrid rebars, the absence of surface features results in negligible mechanical interlocking with the surrounding concrete. In contrast, a wavy-shaped hybrid rebar facilitates mechanical interlocking with the surrounding concrete through physical engagement, thereby significantly enhancing the bond performance. The diameter of the wavy-shaped hybrid rebars must be large enough to accommodate both the central FRP rebar and the high-strength cementitious filling material. Generally, casting high-strength cementitious material requires a gap of at least about 10 mm. Therefore, assuming a central FRP bar of 6 mm as the minimum FRP bar size, the minimum diameter of the hybrid rebar should be 26 mm. These wavy-shaped hybrid rebars hold considerable promise for use in FRP-SSC structures as reinforcement

(Figure 1.4). They offer advantages over both conventional FRP rebars and uniform hybrid rebars, in terms of both bond performance and structural performance. This advancement could lead to more reliable FRP-concrete structures, expanding the applications of hybrid rebars in practice.

1.4 RESEARCH OBJECTIVES

This Ph.D. research project aimed at the development of a fabrication method for wavy-shaped hybrid rebars and the investigation into the mechanical behaviour of such hybrid rebars and their bond performance with concrete. The objectives of this Ph.D. research project are as follows:

1) To fabricate wavy-shaped FRP tubes and experimentally investigate their material properties (Chapter 3);
2) To investigate the compressive behaviour of FRP-confined UHPC/UHPFRC specimens under monotonic axial compression (Chapter 4);
3) To investigate the compressive behaviour of wavy-shaped hybrid rebars under monotonic axial compression (Chapter 5);
4) To investigate the compressive behaviour of wavy-shaped hybrid rebars under cyclic axial compression (Chapter 6); and
5) To investigate the bond behaviour of wavy-shaped hybrid rebars embedded in concrete with pull-out tests (Chater 7).

1.5 LAYOUT OF THE THESIS

This Ph.D. thesis comprises eight chapters, beginning with an introduction to the research background. The detailed layout of the Ph.D. thesis is as follows:

Chapter 1 provides a brief introduction to the background and the objectives of this Ph.D. research programme.

Chapter 2 presents a comprehensive literature review relevant to the topics of the Ph.D. research project. The literature review starts with existing research on GFRP rebars and uniform hybrid rebars, followed by a review of the filament winding technology, including winding machines, winding procedures and winding configurations. The existing UHPC mixtures and experimental studies on FRP-confined UHPC/UHPFRC are also reviewed. Chapter 2 ends with a literature review on bond tests of GFRP rebars.

Chapter 3 details the fabrication process of wavy-shaped FRP tubes with the filament winding technology. The physical properties and mechanical properties of wavy-shaped FRP tubes, including the thicknesses, fibre content and elastic modulus in the hoop direction, were studied in detail. Resin burn-out (BO) tests and the digital image processing (DIP) method were deployed to measure the fibre content. The elastic modulus of FRP tubes in the hoop direction was measured through split disk tests and internal air pressure tests.

Chapter 4 presents an experimental investigation into the compressive behaviour of FRP-confined UHPC/UHPFRC specimens. The failure mode, axial stress-axial strain behaviour, axial strain-lateral strain behaviour, FRP confinement efficiency, and FRP hoop rupture strain were investigated. The minimum levels of FRP confinement necessary for both FRP-confined UHPC and FRP-confined UHPFRC to achieve sufficient confinement with hardening stress-strain behaviour were identified, respectively. The experimental results were used to evaluate the performance of existing stress-strain models of FRP-confined UHPC/UHPFRC. New equations for predicting the compressive strengths and the ultimate axial strains of FRP-confined UHPC and UHPFRC were proposed.

Chapters 5 presents an experimental study on wavy-shaped FRP tube-confined UHPC specimens and wavy-shaped hybrid rebar specimens under monotonic axial compression. The effects of wave height and thickness of wavy-shaped GFRP tube on the compressive behaviour were investigated in detail. The failure modes, axial load-axial strain curves, and the axial strain-lateral strain curves of the test hybrid rebars were studied. The presence of a wavy shape in the GFRP tube did not significantly influence the failure modes of hybrid rebars. A prediction model based on Jiang and Teng's model (Jiang and Teng, 2007) was developed to predict the test results.

Chapters 6 presents an experimental study on the behaviour of wavy-shaped FRP tube - confined UHPC specimens and wavy-shaped hybrid rebars under cyclic axial compression. The predictions from existing stress-strain models were compared with the test data. New equations were proposed to predict the plastic strains and stress deteriorations for both wavy-shaped FRP tube-confined UHPC specimens and wavy-shaped hybrid rebar specimens.

Chapter 7 presents an experimental investigation into the bond behaviour of hybrid rebars, including the bond between FRP rebar and UHPC in hybrid rebars, as well as the bond between hybrid rebar and surrounding concrete by carrying out pull-out tests on 30 specimens. The experimental results demonstrated that wavy-shaped hybrid rebars exhibited enhanced bond performance, characterised by higher peak bond stresses and reduced slips at equivalent bond stresses, compared to uniform hybrid rebars. The effects of the level of FRP confinement, the bond length and the type of FRP rebar on the bond behaviour of hybrid rebars were discussed.

Chapter 8 summarises the key conclusions derived from this Ph.D. research project and highlights the need for future work.

1.6 REFERENCES

Chen, G.M. (2024). "Case study: The world's first open-spandrel deck arch bridges with the main arches constructed using FRP-concrete-steel (FCS) double-skin tubular members (DSTMs)", *FRP International*, 21, No. 2, pp. 19-21.

Chen, G.M., Lu, Y.C., Xie, P., Teng, J.G., Yu, T., Xiang, Y., Cheng, T., Li, Z.B., Hu, F.N. and Liu, W.N. (2022). "Analysis and design methods for FRP-concrete-steel double-skin tubular bridge piers", *China Journal of Highway and Transport*, 35(2), 12-38 (in Chinese).

De Larrard, F. and Sedran, T. (1994). "Optimization of ultra-high-performance concrete by the use of a packing model", *Cement and Concrete Research*, 24(6), 997-1009.

Deitz, D., Harik, I.E. and Gesund, H. (2003). "Physical properties of glass fiber reinforced polymer rebars in compression", *Journal of Composites for Construction*, ASCE, 7(4), 363-366.

Fam, A., Flisak, B. and Rizkalla, S. (2003). "Experimental and analytical modeling of concrete-filled FRP tubes subjected to combined bending and axial loads", *ACI Structural Journal*, 100(4), 499-509.

Graybeal, B. and Tanesi, J. (2007). "Durability of an ultrahigh-performance concrete", *Journal of Materials in Civil Engineering*, ASCE, 19(10), 848-854.

Jiang, T. and Teng, J.G. (2007). "Analysis-oriented stress–strain models for FRP–confined concrete", *Engineering Structures*, 29(11), 2968-2986.

Kobayashi, K. and Fujisaki, T. (1995). Compressive behavior of FRP reinforcement in non-prestressed concrete members. In *Non-metallic (FRP) Reinforcement for Concrete*

Structures: Proceedings of the Second International RILEM Symposium, Ghent, Belgium.

Lin, G., Zeng, J.J., Liang, S.D., Liao, J.J. and Zhuge, Y. (2022). "Seismic behavior of novel GFRP bar reinforced concrete beam-column joints internally reinforced with an FRP tube", *Engineering Structures*, 273, 115100.

Long, Y.L., Li, W.T., Dai, J.G. and Gardner, L. (2018). "Experimental study of concrete-filled CHS stub columns with inner FRP tubes", *Thin-Walled Structures*, 122, 606-621.

Mirmiran, A., Shahawy, M. and Beitleman, T. (2001). "Slenderness limit for hybrid FRP-concrete columns", *Journal of Composites for Construction*, ASCE, 5(1), 26-34.

Pillai, S.U. and Kirk, D.W. (1983). *Reinforced concrete design in Canada*. McGraw-Hill Ryerson.

Richard, P. and Cheyrezy, M. (1995). "Composition of reactive powder concretes", *Cement and Concrete Research*, 25(7), 1501-1511.

Shi, C.J., Wu, Z.M., Xiao, J.F., Wang, D.H., Huang, Z.Y. and Fang, Z. (2015). "A review on ultra high performance concrete: Part I. Raw materials and mixture design", *Construction and Building Materials*, 101, 741-751.

Teng, J.G., Dai, J.G. and Chen, G.M. (2016a). Proceedings of the International Workshop on Seawater Sea-sand Concrete (SSC) Structures Reinforced with FRP Composites. In *International Workshop on Seawater Sea-Sand Concrete (SSC) Structures Reinforced with FRP Composites*,

Teng, J.G., Xiang, Y., Yu, T. and Fang, Z. (2019). "Development and mechanical behaviour of ultra-high-performance seawater sea-sand concrete", *Advances in Structural Engineering*, 22(14), 3100-3120.

Teng, J.G., Zhang, B., Zhang, S.S. and Fu, B. (2018). "Steel-free hybrid reinforcing bars for concrete structures", *Advances in Structural Engineering*, 21(16), 2617-2622.

Wille, K., El-Tawil, S. and Naaman, A.E. (2014). "Properties of strain hardening ultra high performance fiber reinforced concrete (UHP-FRC) under direct tensile loading", *Cement and Concrete Composites*, 48, 53-66.

Wille, K., Naaman, A.E. and Parra-Montesinos, G.J. (2011). "Ultra-high performance concrete with compressive strength exceeding 150 MPa (22 ksi): A simpler way", *ACI Materials Journal*, 108(1).

Xu, J.J., Wu, Z.M., Jia, H.B. and Cao, Q. (2023). "Flexural behavior and serviceability performance of SSC beams reinforced with hybrid GFRP-stainless steel bars", *Structures*, 54, 1350-1359.

Yang, J., Wang, J. and Wang, Z. (2020). "Axial compressive behavior of partially CFRP confined seawater sea-sand concrete in circular columns–Part I: Experimental study", *Composite Structures*, 246, 112373.

Zeng, J.J., Lv, J.F., Lin, G., Guo, Y.C. and Li, L.J. (2018). "Compressive behavior of double-tube concrete columns with an outer square FRP tube and an inner circular high-strength steel tube", *Construction and Building Materials*, 184, 668-680.

Zhang, K.J., Zhang, Q.T. and Xiao, J.Z. (2022). "Durability of FRP bars and FRP bar reinforced seawater sea sand concrete structures in marine environments", *Construction and Building Materials*, 350, 128898.

Zhang, Y.S., Sun, W., Liu, S.f., Jiao, C.J. and Lai, J.Z. (2008). “Preparation of C200 green reactive powder concrete and its static–dynamic behaviors”, *Cement and Concrete Composites*, 30(9), 831-838.

Zhu, Z.Y., Ahmad, I. and Mirmiran, A. (2006). “Seismic performance of concrete-filled FRP tube columns for bridge substructure”, *Journal of Bridge Engineering*, ASCE, 11(3), 359-370.

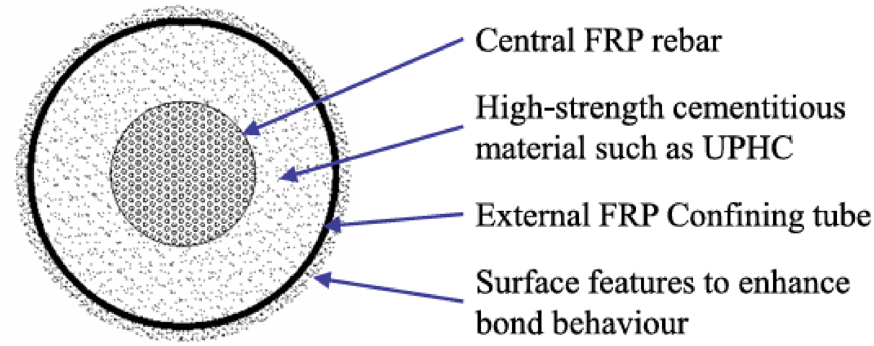

Figure 1.1 Cross section of a hybrid rebar [extracted from Teng et al. (2018)]

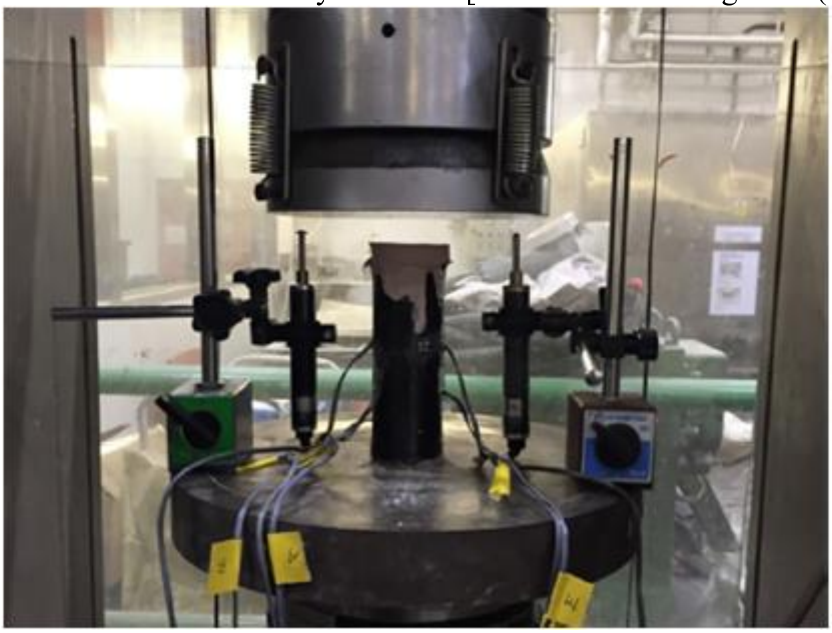

Figure 1.2 Axial compression test on uniform hybrid rebars [extracted from Teng et al. (2018)]

Figure 1.3 Hybrid rebar with a wavy shape

Figure 1.4 Concrete column reinforced with wavy-shaped hybrid rebars

CHAPTER 2
LITERATURE REVIEW

2.1 INTRODUCTION

This chapter provides a comprehensive literature review on previous studies related to the topics of the present Ph.D. research project. As mentioned in Chapter 1, due to the inferior performance of fibre-reinforced polymer (FRP) rebars under compression, an improved form of steel-free hybrid rebars, comprising a central FRP rebar, a wavy-shaped FRP tube and an annulus of high-strength cementitious material (such as ultra-high performance concrete, UHPC) sandwiched between the two tubes, is proposed in this Ph.D. research project. With the wavy-shaped FRP tube, the improved form of hybrid rebars retains the advantages of the original version of hybrid rebars with a uniform cross section along the tube but possesses much enhanced bond performance between the hybrid rebar and the surrounding concrete.

This chapter starts with a review on the material properties and bond behaviour of GFRP rebars, followed by a review on FRP-UHPC hybrid rebars. In the present research, the wavy-shaped GFRP tubes are fabricated with the filament winding method (FWM). Thus, a review on the FWM is also presented. The chapter then proceeds with a review of FRP-confined concrete, focusing on (1) experimental investigations; (2) existing predictive models for monotonic axial compression behaviour; and (3) existing predictive models for cyclic compression behaviour. Subsequently, a comprehensive review is conducted on previous studies concerning FRP-confined UHPC/UHPFRC, including the mix proportions of UHPC/UHPFRC, experimental investigations, and stress-strain models for FRP-confined UHPC/UHPFRC.

2.2 GFRP REBARS

2.2.1 Material Properties

Over the past 30 years, GFRP reinforcing rebars (Figure 2.1) have been extensively utilised and studied as a viable alternative to traditional steel rebars in concrete structures, primarily to address the serious issue of steel corrosion (Cosenza et al., 1997; Benmokrane et al., 2006; Ahmed et al., 2017). Despite the advantages of GFRP rebars, such as excellent durability and cost-effectiveness in harsh environments (e.g., marine environments), the utilisation of GFRP rebars as longitudinal reinforcement in compression members has been limited due to their poor compressive performance (Kobayashi and Fujisaki, 1995; Deitz et al., 2003; Zhang and Ou, 2006; Zhou et al., 2008; Sun and Wang, 2011; Bruun, 2014; AlAjarmeh et al., 2019). Consequently, the Canadian Code CSA S806-12 (R2017) specifies that the contribution of GFRP rebars is ignored in evaluating the compressive performance of columns. The inferior compressive performance of GFRP rebars is mainly attributable to the fact that GFRP rebars are prone to fibre micro-buckling and global buckling under compression. In addition, the low interlaminar shear strength of GFRP composites makes them prone to shear failure (Bai and Keller, 2009).

Existing experimental studies have revealed that the compressive strengths of short GFRP rebars are approximately 50% of their corresponding tensile strengths, while the compressive elastic moduli are generally close to the tensile elastic moduli (Deitz et al., 2003). Deitz et al. (2003) experimentally studied the compressive behaviour of 15-mm-diameter GFRP rebars through testing of short rebar specimens with unbraced length-to-rebar diameter ratios (i.e., L_u/d_b) ranging from 3.3 to 25.3 with both ends embedded in hollow steel caps. For rebar specimens with L_u/d_b ratios less than 7.3, the failure mode was identified as crushing failure, characterized by internal fibre buckling under compression. For rebar specimens with L_u/d_b ratios exceeding 7.3, the compressive strength was deteriorated due to the global buckling of the rebar. Kobayashi and Fujisaki (1995) reported similar findings, with the compressive strengths of GFRP rebars being approximately 30-50% of their tensile strengths.

Recently, AlAjarmeh et al. (2019) tested a series of high-modulus GFRP rebars with diameters ranging from 9.5 mm to 19.1 mm and found that the rebars with smaller diameters exhibited higher compressive strengths. Specially, the GFRP rebars with a diameter of 9.5 mm demonstrated a compressive strength comparable to their tensile strength. However, the GFRP rebars with larger diameters of 15.9 mm and 19.1 mm failed with compressive stresses of approximately 75% and 65% of their tensile strengths, respectively. This failure was mainly attributed to uneven micro-fibre buckling within the larger-dimension rebar, partially caused by significant shear lag failure. Due to variations in testing methods and test specimens, different experimental studies have yielded varying strength deterioration levels of FRP rebars under compression compared to those under tension. Despite these variations, a consistent conclusion has been drawn: the compressive strength of GFRP rebars could not be fully developed in their current applications.

2.2.2 Bond Behaviour

Commercial FRP rebars exhibit diversity due to various surface enhancement treatments, such as sand coating, helical wrapping, and ribs, which are designed to improve bond performance with concrete (Emparanza et al., 2017). A strong bond is essential in reinforced concrete structures to prevent debonding failure. Several experimental methods are available to assess the bond strength of FRP rebars, including pullout tests, overlap splice tests, cantilever beam tests, and hinged beam-end tests (ACI 440.3R-12 2012).

As illustrated in Figure 2.2(a), pullout tests are the most commonly used method for experimentally determining the bond strength of FRP rebars used as reinforcing rebars or prestressing tendons. Figure 2.2 (b) shows the detailed information on the specimens for the bond tests suggested in ACI 440.3R-12 (2012). The FRP rebar is embedded parallel to the direction of concrete casting in a 200-mm concrete cube. The recommended bonded length for the FRP rebar should be five times its diameter. To prevent bonding outside the designated bonded region, the embedded rebar outside the bonded region should be encased in a polyvinyl chloride (PVC) tube or a tube made from other suitable materials. The average bond stress should be calculated using the following equation:

$$\tau = \frac{F}{\pi d l} \tag{2.1}$$

where τ represents the average bond stress; d is the effective diameter of the FRP rebar; l is the embedment length of the FRP rebar; and F is the pullout load. According to ASTM D7957/7957-17, FRP rebars should have a minimum bond strength of 7.6 MPa. ACI 440.6M-08 (2008) and CSA S807-19 (2019) require a minimum bond strength of 9.6 MPa and 10 MPa, respectively. In addition, CSA S807-19 (2019) specifies a 0.5 mm slip limit at the loaded end at 10 MPa.

Compared to steel rebars, the bond behaviour of FRP rebars is remarkably different due to their different surface characteristics, as well as lower elastic moduli and shear stiffnesses (fib.CEB-FIP, 2000). The bond behaviour of FRP rebars is influenced by various factors, including rebar diameter, surface treatment, concrete compressive strength, and utilisation of confining spirals or stirrups (Nanni et al., 1995; Aiello et al., 2002). Pullout tests from numerous studies have revealed that the bond strength of FRP rebars generally decreases as the rebar diameter increases (Benmokrane and Tighiouart, 1996; Cosenza et al., 1997; Tighiouart et al., 1998; Baena et al., 2009; Kotynia et al., 2017). A 21% bond strength reduction was reported by Kotynia et al. (2017) with the increase of ribbed FRP rebar diameter from 12 mm to 16 mm. In addition to rebar diameter, Antonietta et al. (2007) has concluded that the bonding performance of FRP rebars largely depends on their surface treatment. In comparison to sand-coated FRP rebars, FRP rebars with surface deformations exhibited a bond strength that was 3 to 4 times higher, owing to the effective contribution of mechanical interlocking (Antonietta et al., 2007). The strength of concrete affects the bond failure mode of FRP rebars during pullout tests. Baena et al. (2009) observed that as the concrete compressive strength increased from 28.6 MPa to 52.2 MPa, there was an increase in bond strength and a change in the failure mode from pull-out failure to splitting failure for sand-coated rebars with diameters ranging from 16 mm to 19 mm. For larger diameter FRP rebars, the specimens exhibited a higher risk of splitting failure in the surrounding concrete. Ichinose et al. (2004) and Plizzari and Metelli (2009) conducted experimental studies on FRP rebars from 17 mm to 52 mm in diameter. It was found that all specimens without sufficient confinement failed by concrete splitting. Stirrups or spiral reinforcements provided confinement to the concrete, which delayed the splitting cracking and changed the failure modes, thus enhancing the bond performance of the FRP rebars

(Yan et al., 2016).

2.3 FRP-UHPC HYBRID REBARS

The original form of steel-free FRP-UHPC hybrid rebars was proposed by Teng et al. (2018) to address the aforementioned limitations of FRP rebars. As illustrated in Figure 2.3, these hybrid rebars consist of an outer FRP confining tube, a central FRP rebar, and an annular layer of high-strength cementitious material. UHPC and filament-wound GFRP tubes are the ideal materials for confining the central GFRP rebar. These steel-free hybrid rebars possess significant potential for applications in seawater sea-sand concrete structures as well as special structures such as hospital buildings housing magnetic resonance imaging (MRI) equipment.

Teng et al. (2018) conducted a preliminary experimental study involving six hybrid rebar specimens with high-strength mortar and carbon fibre-reinforced polymer (CFRP) tubes as the confining materials. The test results revealed that the high-strength mortar and the CFRP tube could effectively support the rebar against global buckling and fibre micro-buckling. The axial load-axial strain curves of the hybrid rebars exhibited an elastic-plastic response with a post-yielding strain-hardening behaviour (see Figure 2.4). The predictions based on an existing stress-strain model for FRP-confined concrete matched closely the test data, suggesting that the axial load-axial strain responses of hybrid rebars could be designed to meet specific requirements.

Zeng et al. (2022) subsequently investigated the compressive and transverse shear behaviour of FRP-UHPC hybrid rebars. They found that, in addition to improved compressive performance, the transverse shear performance of the hybrid rebars was significantly superior to that of traditional FRP rebars. This enhancement is mainly attributed to the presence of the FRP-confined UHPC section.

2.4 FILAMENT WINDING TECHNOLOGY

The filament winding technology (FWT) has been recognised as one of the most effective methods for manufacturing tube- and pipe-shaped composites (Shen, 1995). As shown in Figure 2.5, the production system for this technology comprises several key components: a mandrel, a carriage, a payout eye, a tensioner, a sensor stand, and a computer controller (Hahn et al., 1994). The mandrel serves as a mould, determining the geometry of the filament-wound FRP tube. The carriage and the payout eye are responsible for winding the raw material onto the mandrel in specific patterns. These winding patterns are pre-programmed and stored in the computer controller. The sensor stand and the tensioner are used to control the tension forces of the fibres.

Two winding patterns are most predominately employed in the FWT: the hoop winding pattern and the helical winding pattern (as shown in Figure 2.6) (Hahn et al., 1994). For the sake of clarity, the outer surface of the cylindrical mandrel is conceptually “cut” along its length and then unfolded into a rectangle; thus, the width of this rectangle would correspond to the circumference of the mandrel. The winding angle of the hoop winding pattern can be calculated in the following equation:

$$\tan(\alpha) = \frac{\pi D_M}{b_w} \tag{2.2}$$

where α is the hoop-winding angle; D_M represents the diameter of the mandrel; and b_w is the width of the tow [Figure 2.6(a)]. The helical winding pattern [Figure 2.6(b)] implies that the tows are wound onto the mandrel at a constant angle relative to the longitudinal axis. The winding angle of the helical winding pattern can be calculated in the following equation:

$$\tan(\theta) = \frac{\pi D_M}{d_w} \tag{2.3}$$

where θ is the helical-winding angle; and d_w represents the distance between two adjacent parallel tows along the longitudinal direction of the mandrel.

The transverse motion of the payout eye begins at the left end and stops upon reaching the right end. This motion from one end to the other is termed one stroke. Upon completing the first stroke, as shown in Figure 2.7(a), the payout eye halts at the end while the mandrel continues to rotate for a dwell angle, allowing the tow to change direction. Subsequently, the second stroke commences from the right end to the left end of the mandrel with the same angle. As shown in Figure 2.7(b), the two strokes intersect at several points on the mandrel. The entire process of the two strokes constitutes one circuit. This process is repeated until the mandrel's surface is uniformly covered with fibres [Figure 2.7(c)].

2.5 FRP-CONFINED CONCRETE

2.5.1 FRP-Confined Concrete under Monotonic Axial Compression

2.5.1.1 Experimental investigations

Extensive experimental research has been carried out on FRP-confined concrete columns subjected to monotonic compression (Mirmiran and Shahawy, 1997; Mirmiran et al., 1998; Xiao and Wu, 2000; Fam and Rizkalla, 2001a; Teng and Lam, 2004; Li, 2006; Ozbakkaloglu, 2013). In the test specimens, fibres were typically oriented in the hoop direction around the circumference of the concrete column to restrain the dilation of core concrete. The test results have demonstrated that the confinement provided by FRP could significantly enhance both the compressive strength and ductility of the concrete core. FRP-confined specimens generally failed with the rupture of the external FRP jacket or tube. As illustrated in Figure 2.8, the lateral confining pressure continues to increase until the FRP jacket or tube ruptures. For the concrete core in circular columns, FRP provides uniform lateral confining pressure with its maximum value f_l calculated in the following equation:

$$f_l = \frac{2E_{frp}\varepsilon_{h,rup}t}{D} \tag{2.4}$$

where E_{frp} = elastic modulus of FRP; D = diameter of the concrete core; $\varepsilon_{h,rup}$ = hoop rupture strain of the FRP jacket or tube; t = thickness of the FRP jacket or tube.

2.5.1.2 Design-oriented stress-strain models

Over the past three decades, numerous researchers have devoted significant efforts to establishing and refining stress-strain models for FRP-confined concrete (Lam and Teng, 2003; Teng et al., 2009; Rousakis et al., 2012; Kwan et al., 2015). Existing stress-strain models can be categorised into design-oriented models and analysis-oriented models. Among the design-oriented models, the model proposed by Teng et al. (2009), which is an improvement version of Lam and Teng (2003) model, is considered one of the most accurate models in predicting the compressive strength (f'_{cc}) and the ultimate axial strain

(ε_{cu}) of FRP-confined concrete (Campione et al., 2015; Zhang et al., 2020; Liao et al., 2021). In this model, the compressive strain and ultimate axial strain are calculated in the following equations:

$$\frac{f'_{cc}}{f'_{co}} = 1 + 3.5(\rho_k - 0.01)\rho_\varepsilon, \text{if } \rho_\varepsilon \geq 0.01 \tag{2.5a}$$

$$\frac{f'_{cc}}{f'_{co}} = 1, \text{if } \rho_k \leq 0.01 \tag{2.5b}$$

$$\frac{\varepsilon_{cu}}{\varepsilon_{co}} = 1.75 + 6.5\rho_k^{0.8}\rho_\varepsilon^{1.45} \tag{2.6}$$

where ρ_k = confinement stiffness ratio; ρ_ε = strain ratio; f'_{co} = unconfined concrete strength; ε_{co}= axial strain at peak stress of unconfined concrete. The expressions of the two ratios are as follows:

$$\rho_k = \frac{2E_{frp}t}{(f'_{co}/\varepsilon_{co})D} \tag{2.7}$$

$$\rho_\varepsilon = \frac{\varepsilon_{h,rup}}{\varepsilon_{co}} \tag{2.8}$$

where E_{frp} = elastic modulus of FRP; $\varepsilon_{h,rup}$ = FRP hoop rupture strain.

As shown in Figure. 2.9, the stress-strain curve of FRP-confined concrete in Teng et al. (2009) is represented by a parabolic first portion and a linear second portion, which are depicted by the following equation:

$$\sigma_c = \begin{cases} E_c\varepsilon_c - \dfrac{(E_c - E_2)^2}{4f'_{co}}\ \varepsilon_c^2 & (0 \le \varepsilon_c \le \varepsilon_t) \\ \begin{cases} f'_{co} + E_2\varepsilon_c & if\ \rho_k < 0.01 \\ f'_{co} - \dfrac{f'_{co} - f'_{cu}}{\varepsilon_{cu} - \varepsilon_{co}}(\varepsilon_c - \varepsilon_{co}) & if\ \rho_k < 0.01 \end{cases} & (\varepsilon_t < \varepsilon_c \le \varepsilon_{cu}) \end{cases} \tag{2.9}$$

where ε_t = axial strain at the intersection of the two portions; E_2 = slope of the linear second portion. The two parameters ε_t and E_2 are calculated in the following two equations, respectively:

$$\varepsilon_t = \frac{2f'_{co}}{E_C - E_2} \tag{2.10}$$

$$E_2 = \frac{f'_{cc} - f'_{co}}{\varepsilon_{cu}} \tag{2.11}$$

where E_C = elastic modulus of concrete which may be evaluated using $4730\sqrt{f'_{co}}$ (in MPa) (ACI 318 2005).

2.5.1.3 Analysis-oriented stress-strain models

Teng et al. (2007) proposed an analysis-oriented stress-strain model of FRP-confined concrete, in which the stress-strain curves are generated through an incremental numerical process. The model was subsequently refined by Jiang and Teng (2007). In contrast to design-oriented models, analysis-oriented models involve more complex calculations but allow the interactions between FRP and concrete to be explicitly considered and they are also more suited for advanced analysis, e.g., nonlinear finite element analysis (Teng et al., 2007). Figure 2.10 illustrates the generation of an axial stress-strain curve for FRP-confined concrete in Teng et al.'s (2007) model. In this model, the axial stress and axial strain of concrete confined with an FRP jacket are assumed to be the same as those of the same concrete actively confined with a constant confining pressure equal to that provided by the FRP. In other words, it is assumed that the stress-strain behaviour of FRP-confined concrete is not influenced by its stress path.

In Teng et al.'s (2007) model, the stress-strain relationship originally proposed by Popovics (1973) and later adopted by Mander et al. (1988) for actively confined concrete is utilised as the active confinement model. The stress-strain curve of actively confined concrete is described using Eq. 2.12 and Eq. 2.13.

$$\frac{\sigma_c}{f'^*_{cc}} = \frac{(\varepsilon_c/\varepsilon^*_{cc})r}{r - 1 + (\varepsilon_c/\varepsilon^*_{cc})^r} \tag{2.12}$$

$$\mathrm{r} = \frac{E_c}{E_c - f'^*_{cc}/\varepsilon^*_{cc}} \tag{2.13}$$

where σ_c and ε_c are the axial stress and the axial strain of concrete, respectively; and f'^*_{cc} and ε^*_{cc} represent the peak axial stress and its corresponding axial strain at a given lateral confining pressure, which are calculated by the following equations:

$$\frac{f_{cc}'^{*}}{f_{co}'} = 1 + 3.5\frac{\sigma_l}{f_{co}'} \tag{2.14}$$

$$\frac{\varepsilon_{cc}^{*}}{\varepsilon_{co}} = 1 + 17.5\,\frac{\sigma_l}{f_{co}'} \tag{2.15}$$

where σ_l is the confining pressure from the FRP jacket, which is calculated by:

$$\sigma_l = \frac{2E_{frp}\varepsilon_h t}{D} \tag{2.16}$$

In this equation, ε_h is the hoop strain of the FRP jacket/tube.

The axial strain-hoop strain relationship is depicted by the following equation:

$$\frac{\varepsilon_c}{\varepsilon_{co}} = 0.85\left(1 + 8\frac{f_l}{f_{co}'}\right) \times \left\{\left[1 + 0.75\left(\frac{\varepsilon_h}{\varepsilon_{c0}}\right)\right]^{0.7} - exp\left[-7\left(\frac{\varepsilon_h}{\varepsilon_{co}}\right)\right]\right\} \tag{2.17}$$

Previous studies have demonstrated that Teng et al.'s (2007) analysis-oriented model provides accurate predictions for both the axial stress-strain curves and the axial strain-hoop strain curves of FRP-confined concrete in circular specimens (Jiang and Teng, 2007; Teng et al., 2007). However, Jiang and Teng (2007) identified that the model proposed by Teng et al. (2007) tends to overestimate the ultimate axial stress of concrete that is weakly or moderately confined. Consequently, Jiang and Teng (2007) proposed a refined equation for the ultimate strain:

$$\frac{\varepsilon_{cc}^{*}}{\varepsilon_{co}} = 1 + 17.5\left(\frac{\sigma_l}{f_{co}'}\right)^{1.2} \tag{2.18}$$

This refinement improved the accuracy of Teng et al.'s (2007) model for both weakly and moderately-confined concrete. The performance of Jiang and Teng's (2007) model has been validated in numerous studies in the literature (Zohrevand and Mirmiran, 2011; Chen et al., 2016; Zeng et al., 2020).

2.5.2 FRP-Confined Concrete under Cyclic Axial Compression

2.5.2.1 Experimental Investigations

A considerable amount of research has been undertaken to explore the stress-strain response of FRP-confined concrete subjected to cyclic axial compression. (Lam et al., 2006; Rousakis et al., 2007; Lam and Teng, 2009; Abbasnia and Ziaadiny, 2010; Ozbakkaloglu and Akin, 2012; Li and Wu, 2016). It was found that unloading/reloading cycles had little effect on the envelope curve of the stress-strain response of FRP-confined concrete (Figure 2.11), while repeated unloading/reloading cycles exhibited an accumulated effect on plastic strains and stress deteriorations.

Ozbakkaloglu and Akin (2012) performed a series of experiments on the cyclic compressive behaviour of FRP-confined normal-strength concrete (NSC) and FRP-confined high-strength concrete (HSC). The strength enhancement ratios (f'_{cc}/f'_{co}) and strain enhancement ratios ($\varepsilon_{cu}/\varepsilon_{co}$) at ultimate conditions were found to be lower for FRP-confined HSC specimens than for FRP-confined NSC specimens under cyclic loading conditions. A sudden drop in axial stress at the transition region was observed in the stress-strain response of FRP-confined HSC under cyclic axial compression, which is similar to the case under monotonic axial compression. Zhang et al. (2015) further explored the behaviour of concrete-filled FRP tubes (CFFTs) with NSC or HSC under cyclic axial compression through a systematic experimental programme. The test results indicated that the compressive behaviour of CFFTs is similar to that of the corresponding concrete confined with an FRP wrap. However, the fibre rupture in FRP tubes occurred gradually, starting from the outermost layer, which differed from the failure mode of concrete confined with FRP wraps. The test results of Zhang et al. (2015) were compared with the predictions from cyclic stress-strain model proposed by Lam and Teng (2009). Lam and Teng's (2009) models were found to be suitable for NSC in CFFTs, but the predictions were not so accurate for HSC in CFFTs.

2.5.2.2 Cyclic stress-strain models

Numerous cyclic stress-strain models have been proposed to predict the stress-strain hysteresis loops of FRP-confined concrete under cyclic axial compression (Shao et al., 2006; Lam and Teng, 2009; Yu et al., 2015; Tian et al., 2020; Huang et al., 2021). The model of Shao et al. (2006) is among the earliest cyclic stress-strain models for FRP-confined concrete, which was developed based primarily on their own test database. This model was later found to be inaccurate due to the limited test data used for the development of the model (Lam et al., 2006).

Lam and Teng (2009) subsequently proposed a more accurate stress-strain model for FRP-confined concrete under cyclic axial compression based on the test results from Lam et al. (2006) and other studies. Figure 2.12 presents comparisons between test stress-strain curves and predicted stress-strain curves based on Lam and Teng's (2009) model. This model includes a monotonic stress-strain model for the envelope curve, algebraic expressions for unloading/reloading paths, and equations for predicting plastic strains and stress deteriorations. Yu et al. (2015) further improved Lam and Teng's (2009) model for specimens with HSC, based on an enlarged database containing more FRP-confined HSC specimens. Comparisons between the revised model and the original model indicated that Yu et al.'s (2015) model provides more accurate predictions for the cyclic stress-strain behaviour of FRP-confined HSC.

2.6 FRP-CONFINED UHPC

2.6.1 UHPC Mix Proportions

UHPC is commonly defined as a cementitious material with a compressive strength exceeding 150 MPa and exhibiting excellent durability (Richard and Cheyrezy, 1995; Graybeal and Tanesi, 2007; Wille et al., 2011; Wille et al., 2014). The raw materials for UHPC typically include water, cement, silica fume (SF), supplemental fine materials [e.g., granulated blast furnace slag (GBFS), fly ash (FA), limestone powder (LP), silica powder, quartz powder (QP), steel slag (SS) powder], aggregates, superplasticizers (SPs), and fibres (Shi et al., 2015). The ultra-high strength of UHPC is achieved by optimising particle packing density and enhancing its homogeneity. The water-to-binder ratio of UHPC is typically around 0.2, which is significantly lower than that of NSC (Shi et al., 2015). Steel fibres are frequently incorporated into UHPC to enhance its tensile strength and fracture toughness, leading to the so-called ultra-high-performance fibre-reinforced concrete (UHPFRC) (Shi et al., 2015). It should be noted that steel fibres are costly and significantly contribute to the high expense of UHPFRC.

Professor Jin-Guang Teng's research group has successfully developed UHPC without steel fibres, achieving a compressive strength of over 180 MPa using tab water, ordinary Portland cement (OPC), SF, FA, QP, river sand, and SP with room temperature curing (Teng et al. 2019). The absence of steel fibres significantly reduces the cost of UHPC, and the potential drawbacks associated with the elimination of steel fibres could be largely mitigated by the combined use of UHPC with FRP confinement. The ductility of UHPC in compression can be greatly enhanced by FRP confinement.

By replacing steel with FRP, it becomes possible to directly utilise seawater and sea-sand in concrete mixing, thereby conserving fresh water and river sand resources. Teng et al. (2019) conducted the first experimental study on the development of ultra-high performance seawater sea-sand concrete (UHPSSC). In this study, 15 mixes consisting of six constituents [i.e., cement, SF, QP, FA, fine aggregate, water, and SP) were designed and tested. As depicted in Figure 2.13, it was revealed that the use of seawater and sea sand led to a slight improvement in the early compressive strength but a slight decrease in strength at 7 days and beyond. Furthermore, increased salinity resulted in a minor reduction in the workability and density of the UHPC. The research demonstrated that the utilisation of seawater and sea-sand did not cause significant detrimental effects on the short-term performance of UHPC.

The costs of white cement and QP are higher compared to OPC and FA. Therefore, the most economical mix proportion of UHPC was achieved using OPC and FA. The mix proportion design attained a cubic compressive strength of 174 MPa (Teng et al. 2019). The proportions of the various constituents, as detailed in Table 2.1, serve as the principal reference for the design of the UHPC mix proportions in this Ph.D. research programme throughout Chapters 4 to 7.

2.6.2 Experimental Investigations on FRP-Confined UHPC

While UHPFRC or UHPC possesses high performance in terms of compressive strength and tensile toughness, it exhibits significantly brittle failure under compression. As a result, FRP confinement is proposed to enhance its ductility in compression. The elevated fluidity of UHPFRC and UHPC has enabled the construction of complex hybrid FRP-UHPFRC or FRP-UHPC structures. Although numerous studies have investigated the material properties of UHPFRC and UHPC over the past two decades, research focusing on both UHPFRC and UHPC confinement, particularly with FRP, remains limited. Table 2.2 summarises the details of all existing studies on FRP-confined UHPFRC/UHPC to the best of the author's knowledge. Most existing studies have focused on FRP-confined UHPFRC with a steel fibre volume ratio of 1% to 2%, while the UHPC specimens without steel fibres were tested for reference. The addition of steel fibres has been found to significantly enhance the compressive strength of UHPC (Wang et al. 2018; Tian et al. 2019; Liao et al. 2021, Wang et al. 2023). Partially due to this reason, the compressive strengths of UHPC without steel fibres in some of the above studies were relatively low. For example, the compressive strengths of UHPC in Wang et al.'s (2018) and Tian et al.'s (2019) studies were only 88 MPa and 83.6 MPa, respectively, which did not meet the strength requirement for UHPC. Only the specimens tested by Berthet et al. (2005) and Oliveira et al. (2019) had an unconfined UHPC compressive strength larger than 150 MPa. Among the 24 specimens tested by Oliveira et al. (2019), 12 UHPC specimens subjected to thermal curing achieved a compressive strength of 204 MPa while the remaining 12 UHPC specimens without thermal curing had a compressive strength of 161 MPa. Another research gap is that most FRP-confined UHPFRC/UHPC specimens in the existing studies had relatively high FRP confinement stiffness ratios to ensure sufficiently strong FRP confinement. Thus, the FRP confinement efficiency (i.e., the minimum FRP confinement required to ensure an ascending second branch of the axial stress-strain curve of UHPFRC/UHPC) has not been clearly identified.

An experimental study on FRP-confined UHPFRC by Zohrevand and Mirmiran (2011) demonstrated that sufficient FRP confinement significantly enhances both the ductility and compressive strength of UHPFRC. However, the FRP confinement efficiency for UHPFRC is inferior to NSC. Wang et al. (2018) carried out a study comparing the compressive behaviour of FRP-confined UHPFRC/UHPC, HSC and NSC. Compared to FRP-confined HSC and NSC, FRP-confined UHPC has been found to exhibit more brittle behaviour, i.e., the enhancement ratios of compressive strength and strain decreased with an increase in concrete strength.

As shown in Figure 2.14, a sudden stress drop or stress fluctuation could be observed at the transition region for both FRP-confined UHPFRC and FRP-confined UHPC specimens. It was observed that the axial stress in the transition region exceeded the strength of unconfined concrete. Following the stress drop, the axial stress will increase if the confinement is sufficient or continuously decrease if the confinement is inadequate. Similar to FRP-confined NSC and HSC, FRP-confined UHPFRC/UHPC failed with the rupture of the FRP jacket or tube (Figure 2.15). However, FRP-confined UHPFRC/UHPC is characterised by the development of localised macrocracks and exhibits more severe failure. The inclusion of steel fibres also impacts the failure modes of FRP-confined UHPC. Compared to FRP-confined UHPFRC, the absence of steel fibres resulted in smaller remaining concrete segments for FRP-confined UHPC after explosive failure (Wang et al., 2018).

To study the impact of unconfined concrete strength on FRP confinement, de Oliveira et al. (2019) carried out a comprehensive experiment on 102 concrete cylinders, including NSC, HSC, UHPC cylinders. Figure 2.16 presents typical stress-strain curves for FRP-confined NSC, HSC, and UHPC (de Oliveira et al., 2019). To describe the features of FRP-confined UHPC, it is essential to first define the stress efficiency factor (k_ε). As shown in Eq. 2.19, the strain efficiency factor (k_ε) is the ratio between the FRP hoop strain at failure observed in the test cylinders (ε_{fu}) and the FRP rupture strain determined from the tensile tests of flat coupons (ε_f):

$$k_\varepsilon = \frac{\varepsilon_{fu}}{\varepsilon_f} \tag{2.19}$$

The unconfined concrete strength f'_{co} was found to negatively affect the strain efficiency factor (k_ε). Conversely, the confinement stiffness (ρ_k) positively influenced k_ε. The average value of the strain efficiency factor (k_ε) for CFRP-confined UHSC in this research was 0.37. Specifically, the factor for UHSC confined with 4 layers of FRP jacket was 0.435 on average, lower than the value of 0.586 for CFRP-confined specimens reported by Lam and Teng (2003). Wang et al. (2018) reached similar conclusions regarding the variation tendency of the strain efficiency factor against f'_{co} and ρ_k, but reported higher strain efficiency factors for FRP-confined UHPC specimens than those reported by de Oliveira et al. (2019). In Wang et al. (2018), the strain efficiency factor exceeded 0.586 for the specimens confined with an FRP jacket with more than 3 layers of fibres. The different observations between the two studies of de Oliveira et al. (2019) and Wang et al. (2018) may be attributed to the different calculation methods for FRP hoop rupture strain. More test results are thus required to further examine the FRP strain efficiency factors of FRP-confined UHPFRC/UHPC.

In addition to studying FRP-confined UHPC under monotonic compression, Huang et al. (2021) carried out an experimental study on the compressive behaviour of confined UHPC under cyclic axial compression. They found that the unloading path for confined UHPC is more linear than those of confined NSC and confined HSC. Consequently, a modified cyclic axial stress-strain model for FRP-confined UHPC was established based on regression analysis of test results. The detailed equations of the aforementioned Lam and Teng (2009), Yu et al. (2015), and Huang et al. (2021) are presented in Chapter 7.

2.6.3 Design-Oriented Stress-Strain Models

Compared to FRP-confined HSC and NSC, the stress-strain models for FRP-confined UHPFRC/UHPC are limited. Several studies have been conducted on the assessment of existing stress-strain models in predicting the behaviour of FRP-confined UHPFRC/UHPC. Guler (2014) found that the conventional stress-strain models, which were originally proposed for NSC, generally overestimated the compressive strengths of FRP-confined UHPFRC/UHPC. Similarly, Zohrevand and Mirmiran (2011) found that their selected models, namely, the models of Mander et al. (1988), Samaan et al. (1999), Toutanji (1999), and Lam and Teng (2003), underestimated the compressive strengths of FRP-confined UHPFRC/UHPC with relatively high confinement ratios. Consequently, Guler (2014) and Zohrevand and Mirmiran (2013) proposed new stress-strain models based on their experimental results. The most recent models are those proposed by Liao et al. (2022) and Lam et al. (2021), which were developed based on Lam and Teng (2003) model for FRP-confined NSC. Wang et al. (2023) carried out compression tests on 40 FRP-confined UHPFRC/UHPC concrete cylinders and evaluated the aforementioned models using their test results. Among these models, those by Zohrevand and Mirmiran (2013), Liao et al. (2022) , and Lam et al. (2021) were found to predict the compressive strengths reasonably well. However, the accuracies of all the models in predicting the ultimate axial strains were relatively low.

One of the reasons for the low accuracy of existing stress-strain model stems from the discrepancy in methods of measuring axial strains of FRP-confined UHPFRC/UHPC specimens in different studies (Zohrevand and Mirmiran, 2011; Guler, 2014; Wang et al., 2018; Wang et al., 2023). For instance, as shown in Figure 2.17(a), Zohrevand and Mirmiran (2011) adopted only one Linear Variable Differential Transformer (LVDT) to capture the shortenings between the two loading plates. However, during the loading process, the axial deformations of a specimen may not be uniform over the cross section. Additionally, the so-obtained deformations included those of the levelling plasters at both ends into tight contact with the loading plates. Wang et al. (2023), however, employed four LVDTs, including two (LVDTs-M1/M2) measuring the axial shortening of the mid-height region and another two (LVDTs-F1/F2) measuring the full-height axial shortenings of the specimens [Figure 2.17(b)]. Each pair of LVDTs was placed at 180° apart from each other. This arrangement scheme of LVDTs is obviously more reasonable than that of Zohrevand and Mirmiran (2011).

2.7 CONCLUSIONS

In this chapter, existing studies relevant to research on FRP-UHPC hybrid rebars have been reviewed. FRP-UHPC hybrid rebars have great potential of application in seawater sea-sand concrete structures. However, the bonding between hybrid rebars and the surrounding concrete remains an issue to be addressed before they could be confidently adopted in practice. The present Ph.D. research project was thus proposed to address the above major problem of hybrid rebars. Specifically, based on the literature review presented in this chapter, the following issues need to be addressed:

(1) Experimental investigations of FRP-confined UHPC, particularly UHPC with compressive strengths exceeding 150 MPa, remain limited. More experimental studies are thus urgently needed to enrich the test database. Additionally, existing design models for FRP-confined UHFRC/UHPC require thorough evaluation to assess their accuracy and applicability.

(2) FRP-UHPC hybrid rebars with enhanced bond performance should be developed. An improved form of hybrid rebars with a wavy shape was proposed in the present Ph.D. research project. To this end, wavy-shaped FRP tubes should first be fabricated using the filament winding technology. The mechanical properties of the wavy-shaped FRP tubes should also be measured before they are used in fabricating wavy-shape hybrid rebars.

(3) The compressive behaviour of the proposed wavy-shaped hybrid rebars under both monotonic and cyclic axial compression needs to be investigated through experimental studies. A detailed and systematic experimental programme needs to be designed and

conducted as part of this Ph.D. research work.

(4) The bond stress-slip relationships between different components of a wavy-shaped hybrid rebar, and between the hybrid rebar and the surrounding concrete need to be clarified to understand the bond behaviour of the hybrid rebar.

By addressing the above issues, this Ph.D. thesis contributes to the development and optimisation of FRP-UHPC hybrid rebars for practical applications in concrete structures in marine environments.

2.8 REFERENCES

Abbasnia, R. and Ziaadiny, H. (2010). "Behavior of concrete prisms confined with FRP composites under axial cyclic compression", *Engineering Structures*, 32(3), 648-655.

ACI 318-05 (2005). *Building Code Requirements for Structural Concrete and Commentary*, American Concrete Institute, Farmington Hills, Michigan, USA.

ACI 440.3-12 (2012). *Guide Test Methods for Fibre-Reinforced Polymers (FRPs) for Reinforcing or Strengthening Concrete Structures*, American Concrete Institute, Farmington Hills, Michigan, USA.

ACI 440.6-08 (R2017). *Specification for Carbon and Glass Fiber-Reinforced Polymer Bar Materials for Concrete Reindorcement*, American Concrete Institute, Farmington Hills, Michigan, USA.

Ahmed, E.A., Benmokrane, B. and Sansfaçon, M. (2017). "Case study: Design, construction, and performance of the La Chancelière parking garage's concrete flat slabs reinforced with GFRP bars", *Journal of Composites for Construction*, ASCE, 21(1), 05016001.

Aiello, M.A., Leone, M. and Pecce, M. (2002). Influence of surface treatments on bond between FRP rebars and concrete. In *International Conference "Bond in Concrete-from Research to Standards"*, Budapest University of Technology and Economics, Budapest, Hungary.

AlAjarmeh, O., Manalo, A., Benmokrane, B., Vijay, P., Ferdous, W. and Mendis, P. (2019). "Novel testing and characterization of GFRP bars in compression", *Construction* *and Building Materials*, 225, 1112-1126.

Antonietta, A.M., Leone, M. and Pecce, M. (2007). "Bond performances of FRP rebars-reinforced concrete", *Journal of Materials in Civil Engineering*, ASCE, 19, 205-213.

Baena, M., Torres, L., Turon, A. and Barris, C. (2009). "Experimental study of bond behaviour between concrete and FRP bars using a pull-out test", *Composites Part B: Engineering*, 40(8), 784-797.

Bai, Y. and Keller, T. (2009). "Shear failure of pultruded fiber-reinforced polymer composites under axial compression", *Journal of Composites for Construction*, ASCE, 13(3), 234-242.

Benmokrane, B., El-Salakawy, E., El-Ragaby, A. and Lackey, T. (2006). "Designing and testing of concrete bridge decks reinforced with glass FRP bars", *Journal of Bridge Engineering*, ASCE, 11(2), 217-229.

Benmokrane, B. and Tighiouart, B. (1996). "Bond strength and load distribution of composite GFRP reinforcing bars in concrete", *Materials Journal*, 93(3), 254-259.

Bruun, E. (2014). "GFRP bars in structural design: Determining the compressive strength versus unbraced length interaction curve", *Journal of Student Science and Technology*, 7(1).

Campione, G., La Mendola, L., Monaco, A., Valenza, A. and Fiore, V. (2015). "Behavior in compression of concrete cylinders externally wrapped with basalt fibers", *Composites Part B: Engineering*, 69, 576-586.

Chen, G., He, Y., Jiang, T. and Lin, C. (2016). "Behavior of CFRP-confined recycled aggregate concrete under axial compression", *Construction and Building Materials*, 111, 85-97.

Cosenza, E., Manfredi, G. and Realfonzo, R. (1997). "Behavior and modeling of bond of FRP rebars to concrete", *Journal of Composites for Construction*, ASCE, 1(2), 40-51.

CSA S807-19 (2019). *Specification for Fibre-Reinforced Polymers*, Canadian Standards Association, Rexdale, ON, Canada.

de Oliveira, D.S., Raiz, V. and Carrazedo, R. (2019). "Experimental study on normal-strength, high-strength and ultrahigh-strength concrete confined by carbon and glass FRP laminates", *Journal of Composites for Construction*, ASCE, 23(1), 04018072.

Deitz, D., Harik, I.E. and Gesund, H. (2003). "Physical properties of glass fiber reinforced polymer rebars in compression", *Journal of Composites for Construction*, ASCE, 7(4), 363-366.

Emparanza, A.R., Kampmann, R. and De Caso y Basalo, F. (2017). "State-of-the-practice of global manufacturing of FRP rebar and specifications", *ACI Fall Convention*, 327, 45.41-45.14.

Fam, A.Z. and Rizkalla, S.H. (2001a). "Behavior of axially loaded concrete-filled circular fiber-reinforced polymer tubes", *ACI Structural Journal*, 98(3), 280-289.

fib.CEB-FIP. (2000). *Bond of Reinforcement in Concrete*. Bulletin 10. International Federation for Structural Concrete (fib) ed. Vol. State-of-art report prepared by Task Group Bond Models (former CEB Task Group 2.5).

Graybeal, B. and Tanesi, J. (2007). “Durability of an ultrahigh-performance concrete”, *Journal of Materials in Civil Engineering*, ASCE, 19(10), 848-854.

Guler, S. (2014). “Axial behavior of FRP-wrapped circular ultra-high performance concrete specimens”, *Structural Engineering Mechanics*, 50(6), 709-722.

Hahn, H.T., Jensen, D.W., Claus, S.J., Pai, S.P. and Hipp, P.A. (1994). *Structural Design Criteria for Filament-Wound Composite Shells*, Report No. NASA-CR-195125.

Huang, L., Xie, J.H., Li, L.M., Xu, B.Q., Huang, P.Y. and Lu, Z.Y. (2021). “Compressive behaviour and modelling of CFRP-confined ultra-high performance concrete under cyclic loads”, *Construction and Building Materials*, 310, 124949.

Ichinose, T., Kanayama, Y., Inoue, Y. and Bolander Jr, J. (2004). “Size effect on bond strength of deformed bars”, *Construction and Building Materials*, 18(7), 549-558.

Jiang, T. and Teng, J.G. (2007). “Analysis-oriented stress–strain models for FRP–confined concrete”, *Engineering Structures*, 29(11), 2968-2986.

Kobayashi, K. and Fujisaki, T. (1995). Compressive behavior of FRP reinforcement in non-prestressed concrete members. In *Non-metallic (FRP) Reinforcement for Concrete Structures: Proceedings of the Second International RILEM Symposium*, Ghent, Belgium.

Kotynia, R., Szczech, D. and Kaszubska, M. (2017). “Bond behavior of GRFP bars to concrete in beam test”, *Procedia Engineering*, 193, 401-408.

Kwan, A.K.H., Dong, C.X. and Ho, J.C.M. (2015). “Axial and lateral stress–strain model for FRP confined concrete”, *Engineering Structures*, 99, 285-295.

Lam, L., Huang, L., Xie, J.H. and Chen, J.F. (2021). “Compressive behavior of ultra-high performance concrete confined with FRP", *Composite Structures*, 274, 114321.

Lam, L. and Teng, J. (2009). "Stress–strain model for FRP-confined concrete under cyclic axial compression", *Engineering Structures*, 31(2), 308-321.

Lam, L. and Teng, J.G. (2003). "Design-oriented stress–strain model for FRP-confined concrete", *Construction and Building Materials*, 17(6-7), 471-489.

Lam, L., Teng, J.G., Cheung, C.H. and Xiao, Y. (2006). "FRP-confined concrete under axial cyclic compression", *Cement and Concrete Composites*, 28(10), 949-958.

Li, G.Q. (2006). "Experimental study of FRP confined concrete cylinders", *Engineering Structures*, 28(7), 1001-1008.

Li, P.D. and Wu, Y.F. (2016). "Stress–strain behavior of actively and passively confined concrete under cyclic axial load", *Composite Structures*, 149, 369-384.

Liao, J., Yang, K.Y., Zeng, J.J., Quach, W.M., Ye, Y.Y. and Zhang, L.H. (2021). "Compressive behavior of FRP-confined ultra-high performance concrete (UHPC) in circular columns", *Engineering Structures*, 249, 113246.

Liao, J.J., Zeng, J.J., Gong, Q.M., Quach, W.M., Gao, W.Y. and Zhang, L.H. (2022). "Design-oriented stress-strain model for FRP-confined ultra-high performance concrete (UHPC)", *Construction and Building Materials*, 318, 126200.

Mander, J.B., Priestley, M.J. and Park, R. (1988). "Theoretical stress-strain model for confined concrete", *Journal of Structual Engineering*, ASCE, 114(8), 1804-1826.

Mirmiran, A. and Shahawy, M. (1997). "Behavior of concrete columns confined by fiber composites", *Journal of Structual Engineering*, ASCE, 123(5), 583-590.

Mirmiran, A., Shahawy, M., Samaan, M., Echary, H.E., Mastrapa, J.C. and Pico, O. (1998).

"Effect of column parameters on FRP-confined concrete", *Journal of Composites for Construction*, ASCE, 2(4), 175-185.

Nanni, A., Al-Zaharani, M., Al-Dulaijan, S., Bakis, C. and Boothby, I. (1995). 17 bond of FRP reinforcement to concrete-experimental results. In *Non-metallic (FRP) Reinforcement for Concrete Structures: Proceedings of the Second International RILEM Symposium*, Ghent, Belgium.

Ozbakkaloglu, T. (2013). "Compressive behavior of concrete-filled FRP tube columns: Assessment of critical column parameters", *Engineering Structures*, 51, 188-199.

Ozbakkaloglu, T. and Akin, E. (2012). "Behavior of FRP-confined normal-and high-strength concrete under cyclic axial compression", *Journal of Composites for Construction*, ASCE, 16(4), 451-463.

Plizzari, G. and Metelli, G. (2009). "Experimental study on the bond behavior of large bars", *Technical Report*.

Popovics, S. (1973). "A numerical approach to the complete stress-strain curve of concrete", *Cement and Concrete Research*, 3(5), 583-599.

Richard, P. and Cheyrezy, M. (1995). "Composition of reactive powder concretes", *Cement and Concrete Research*, 25(7), 1501-1511.

Rousakis, T.C., Karabinis, A.I. and Kiousis, P.D. (2007). "FRP-confined concrete members: Axial compression experiments and plasticity modelling", *Engineering Structures*, 29(7), 1343-1353.

Rousakis, T.C., Rakitzis, T.D. and Karabinis, A.I. (2012). "Design-oriented strength model for FRP-confined concrete members", *Journal of Composites for Construction*, ASCE, 16(6), 615-625.

Shao, Y., Zhu, Z. and Mirmiran, A. (2006). “Cyclic modeling of FRP-confined concrete with improved ductility”, *Cement and Concrete Composites*, 28(10), 959-968.

Shen, F.C. (1995). “A filament-wound structure technology overview”, *Materials Chemistry and Physics*, 42(2), 96-100.

Shi, C.J., Wu, Z.M., Xiao, J.F., Wang, D.H., Huang, Z.Y. and Fang, Z. (2015). “A review on ultra high performance concrete: Part I. Raw materials and mixture design”, *Construction and Building Materials*, 101, 741-751.

Sun, L. and Wang, H. (2011). “Study of GFRP bar's mechanical properties in compression”, *Journal of Shenyang Jianzhu University(Natural Science)*, 27(6), 1037-1042.

Teng, J.G., Huang, Y.L., Lam, L. and Ye, L.P. (2007). “Theoretical model for fibre-reinforced polymer-confined concrete”, *Journal of Composites for Construction*, ASCE, 11(2), 201-210.

Teng, J.G., Jiang, T., Lam, L. and Luo, Y.Z. (2009). “Refinement of a design-oriented stress–strain model for FRP-confined concrete”, *Journal of Composites for Construction*, ASCE, 13(4), 269-278.

Teng, J.G. and Lam, L. (2004). “Behavior and modeling of fiber reinforced polymer-confined concrete”, *Journal of Structural Engineering*, 130(11), 1713-1723.

Teng, J.G., Xiang, Y., Yu, T. and Fang, Z. (2019). “Development and mechanical behaviour of ultra-high-performance seawater sea-sand concrete”, *Advances in Structural Engineering*, 22(14), 3100-3120.

Teng, J.G., Zhang, B., Zhang, S.S. and Fu, B. (2018). “Steel-free hybrid reinforcing bars for concrete structures", *Advances in Structural Engineering*, 21(16), 2617-2622.

Tepfers, R., Görlin, J. and Samuelsson, T. (1973). "Concrete Subjected to pulsating load and pulsating deformation of different pulse waveform", *Nordisk Betong*, 17(4).

Tian, H.W., Zhou, Z., Wei, Y. and Lu, J. (2020). "Behavior and modeling of ultra-high performance concrete-filled FRP tubes under cyclic axial compression", *Journal of Composites for Construction*, ASCE, 24(5), 04020045.

Tighiouart, B., Benmokrane, B. and Gao, D. (1998). "Investigation of bond in concrete member with fibre reinforced polymer (FRP) bars", *Construction and Building Materials*, 12(8), 453-462.

Toutanji, H. (1999). "Stress-strain characteristics of concrete columns externally confined with advanced fiber composite sheets", *Materials Journal*, 96(3), 397-404.

Wang, J.J., Zhang, S.S., Nie, X.F. and Yu, T. (2023). "Compressive behavior of FRP-confined ultra-high performance concrete (UHPC) and ultra-high performance fiber reinforced concrete (UHPFRC)", *Composite Structures*, 312, 116879.

Wang, W.Q., Wu, C.Q., Liu, Z.X. and Si, H.L. (2018). "Compressive behavior of ultra-high performance fiber-reinforced concrete (UHPFRC) confined with FRP", *Composite Structures*, 204, 419-437.

Wille, K., El-Tawil, S. and Naaman, A.E. (2014). "Properties of strain hardening ultra high performance fiber reinforced concrete (UHP-FRC) under direct tensile loading", *Cement and Concrete Composites*, 48, 53-66.

Wille, K., Naaman, A.E. and Parra-Montesinos, G.J. (2011). "Ultra-high performance concrete with compressive strength exceeding 150 MPa (22 ksi): A simpler way", *ACI Materials Journal*, 108(1).

Xiao, Y. and Wu, H. (2000). “Compressive behavior of concrete confined by carbon fiber composite jackets”, *Journal of materials in civil engineering*, ASCE, 12(2), 139-146.

Yan, F., Lin, Z. and Yang, M. (2016). “Bond mechanism and bond strength of GFRP bars to concrete: A review”, *Composites Part B: Engineering*, 98, 56-69.

Yu, T., Zhang, B. and Teng, J.G. (2015). “Unified cyclic stress–strain model for normal and high strength concrete confined with FRP”, *Engineering Structures*, 102, 189-201.

Zeng, J.J., Gao, W.Y., Duan, Z.J., Bai, Y.L., Guo, Y.C. and Ouyang, L.J. (2020). “Axial compressive behavior of polyethylene terephthalate/carbon FRP-confined seawater sea-sand concrete in circular columns”, *Construction and Building Materials*, 234, 117383.

Zeng, J.J., Ye, Y.Y., Quach, W.M., Lin, G., Zhuge, Y. and Zhou, J.K. (2022). “Compressive and transverse shear behaviour of novel FRP-UHPC hybrid bars”, *Composite Structures*, 281, 115001.

Zhang, B., Hu, X.M., Zhao, Q., Huang, T., Zhang, N.Y. and Zhang, Q.B. (2020). “Effect of fiber angles on normal-and high-strength concrete-filled fiber-reinforced polymer tubes under monotonic axial compression”, *Advances in Structural Engineering*, 23(5), 924-940.

Zhang, B., Yu, T. and Teng, J.G. (2015). “Behavior of concrete-filled FRP tubes under cyclic axial compression”, *Journal of Composites for Construction*, ASCE, 19(3), 04014060.

Zhang, X.Y. and Ou, J.P. (2006). “Experimental research on compressive properties of concrete stub square column reinforced with FRP bars”, *Journal of Xi’an University of Architecture and Technology*, 38(4), 467-485(in Chinese).

Zhou, J., Du, Q., Yuan, M. and Li, G. (2008). “Experimental study on compressive mechanical properties of GFRP rebars”, *Journal of Hohai University (Natural Sciences)*, 36(4), 542-545.

Zohrevand, P. and Mirmiran, A. (2011). “Behavior of ultrahigh-performance concrete confined by fiber-reinforced polymers”, *Journal of Materials in Civil Engineering*, ASCE, 23(12), 1727-1734.

Zohrevand, P. and Mirmiran, A. (2013). “Stress-strain model of ultrahigh performance concrete confined by fiber-reinforced polymers”, *Journal of Materials in Civil Engineering*, ASCE, 25(12), 1822-1829.

Table 2.1 UHPSSC mix proportions (Teng et al., 2019)

	Mix proportion (kg) for 1 m^3 concrete
Ordinary Portland cement (OPC)	830
Seawater	164
Sea-sand	913
Silica fume (SF)	207
Fly ash	207
HRWR	27
Total	2348

Table 2.2 Existing tests on FRP-confined UHPFRC and UHPC

Reference	Number of specimens	Specimen size (cylinder) Diameter (mm)	Height (mm)	Unconfined concrete strength (MPa)	FRP types[1]	Steel fibre volume fraction (%)	Confinement stiffness ratio ρ_K[2]	Number of specimens with f'_{co}>150 MPa and without steel fibres
Berthet et al. (2005)	2	70	140	169.7	CFRP wrap	0	0.04~0.11	2
Zohrevand and Mirmiran (2011)	16	108	191	188.2	CFRP/GFRP tube	2	0.02~0.11	0
Guler (2014)	36	100	200	159	GFRP/CFRP/AFRP wrap	6	0.08~0.24	0
Wang et al. (2018)	14	150	300	88, 136	CFRP/GFRP wrap	0, 2	0.02~0.11	0
Oliveira et al. (2019)	24	50	100	161, 204	CFRP/GFRP wrap	0	0.01~0.17	24
Tian et al. (2019)	42	100	200	83.6~131.2	GFRP tube	0, 2	0.03~0.14	0
Liao et al. (2021)	52	50, 100	100, 200	127~156	CFRP wrap/GFRP tube	0, 1, 2	0.02~0.1	0
Lam et al. (2021)	12	100	200	128~155	CFRP wrap	1, 2	0.05~0.15	0
Wang et al. (2023)	40	100, 150	200, 300	119.0~158.1	CFRP wrap/GFRP wrap	0, 1, 2	0.03~0.11	0

Note:
1. CFRP: carbon FRP; GFRP: glass FRP; AFRP: aramid FRP; the FRP wrap or jacket was formed by wrapping a resin impregnated fibre sheet around the specimen via the wet lay-up method; the FRP tube was prefabricated and used as the formwork for casting concrete.
2. Confinement stiffness ratio $\rho_K = 2E_f t_f/(f'_{co}/\varepsilon_{co})/D$, where E_f = elastic modulus of FRP jacket/tube in the hoop direction; t_f = thickness

of FRP jacket/tube; f'_{co} = unconfined concrete strength; ε_{co} = axial strain at peak axial stress of unconfined concrete; D = diameter of confined concrete cylinder

Figure 2.1 GFRP rebars

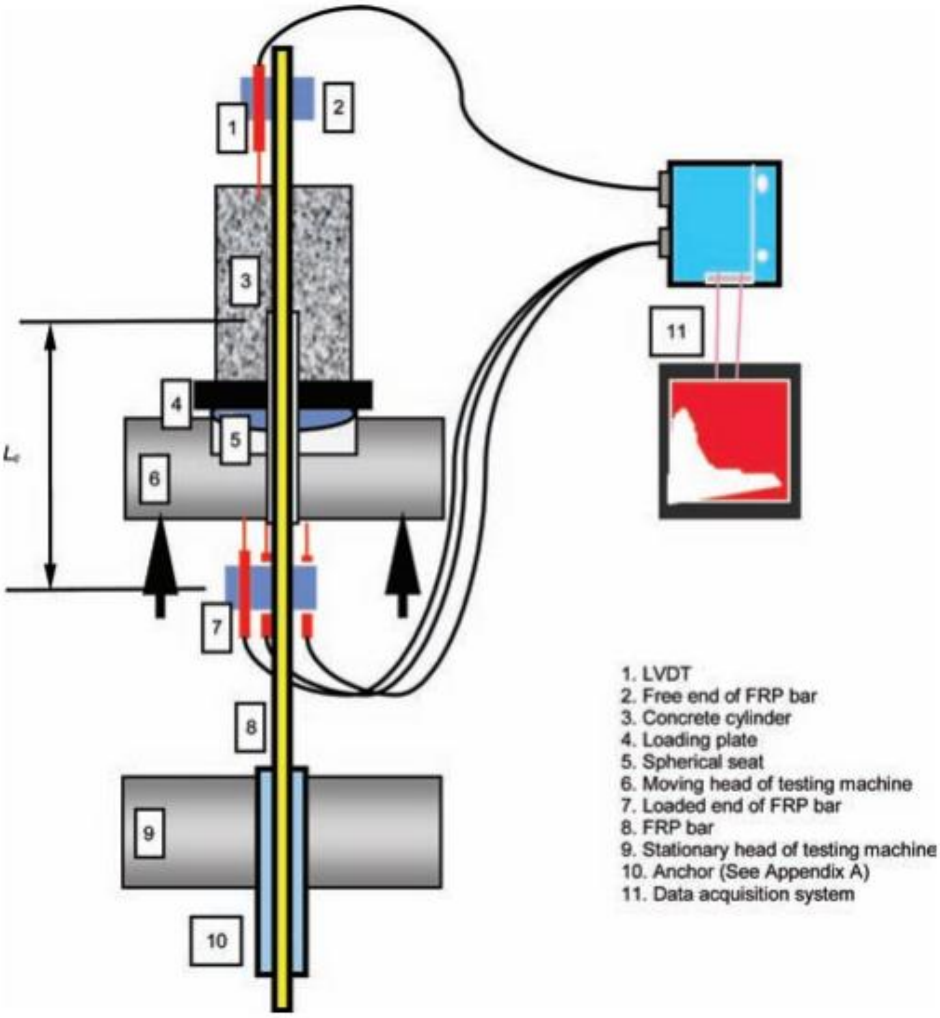

(a) Schematic details of test set-up for pullout tests

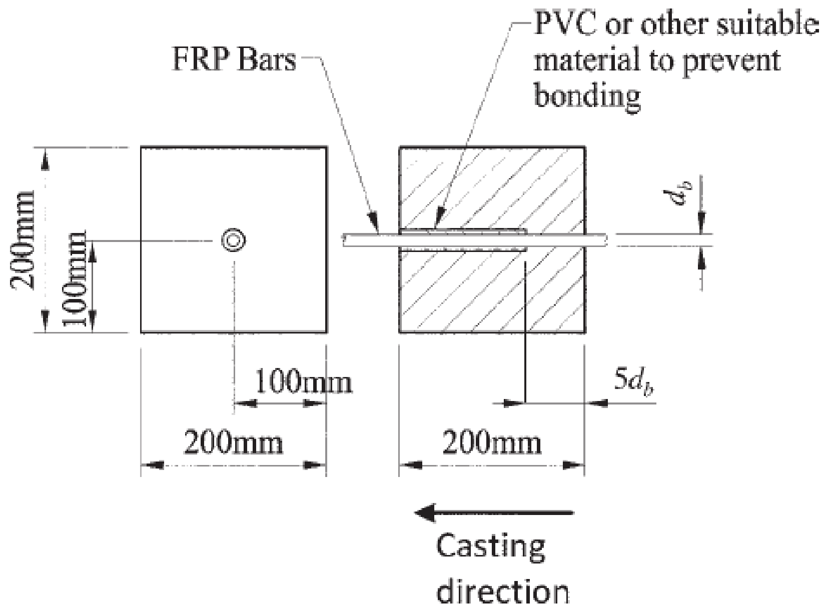

(b) Standard specimens for the pullout test

Figure 2.2 Pullout test [extracted from ACI440.3R-12 (2012)]

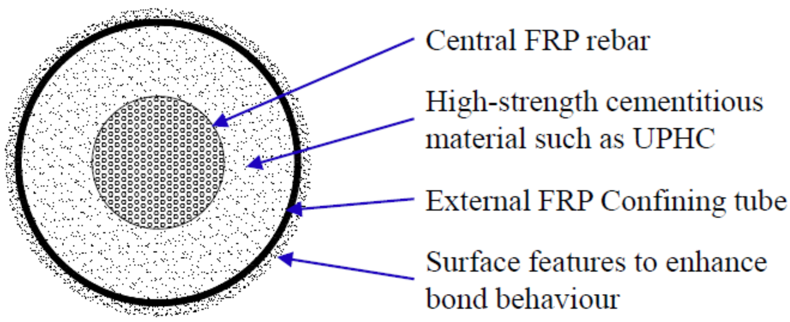

Figure 2.3 Typical cross section of a hybrid rebar [extracted from Teng et al. (2018)]

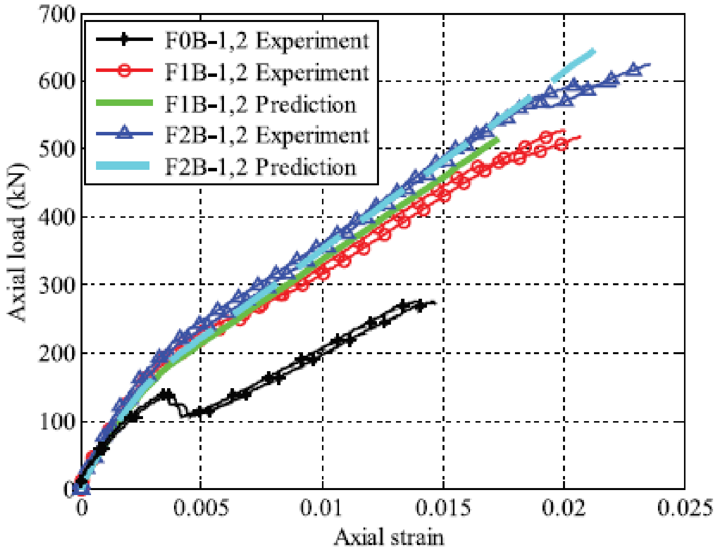

Figure 2.4 Axial load-axial strain curves of hybrid rebars [extracted from Teng et al. (2018)]

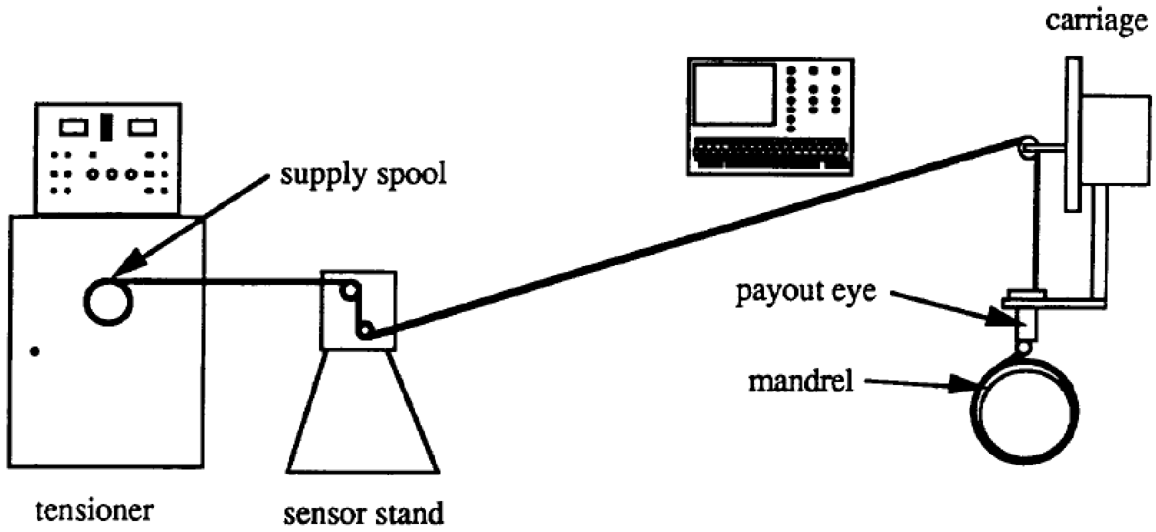

Figure 2.5 Typical equipment layout of the filament winding technology [extracted from Hahn et al. (1994)]

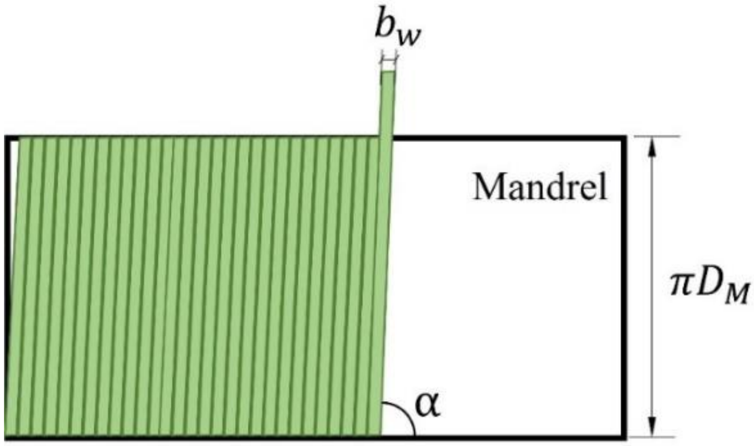

(a) Hoop filament-winding pattern

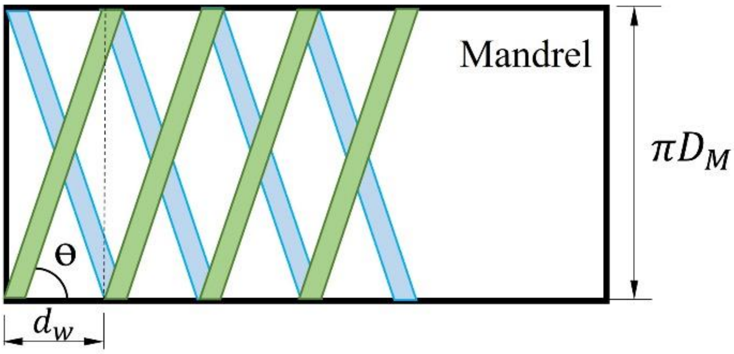

(b) Helical-winding pattern

Figure 2.6 Two common filament-winding patterns

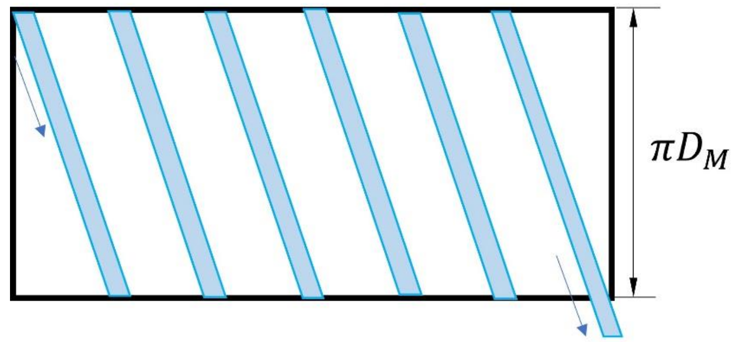

(a) The first stroke of a helical winding pattern

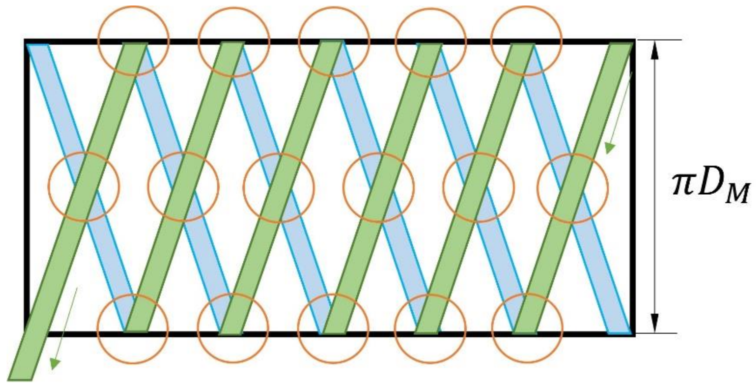

(b) The first and second strokes of a helical winding pattern with fibre crossovers circled

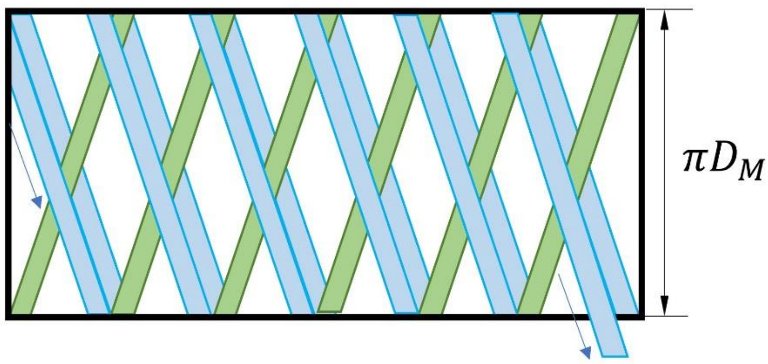

(c) Fibre arrangement during the second winding circuit

Figure 2.7 Winding process of the helical-winding pattern

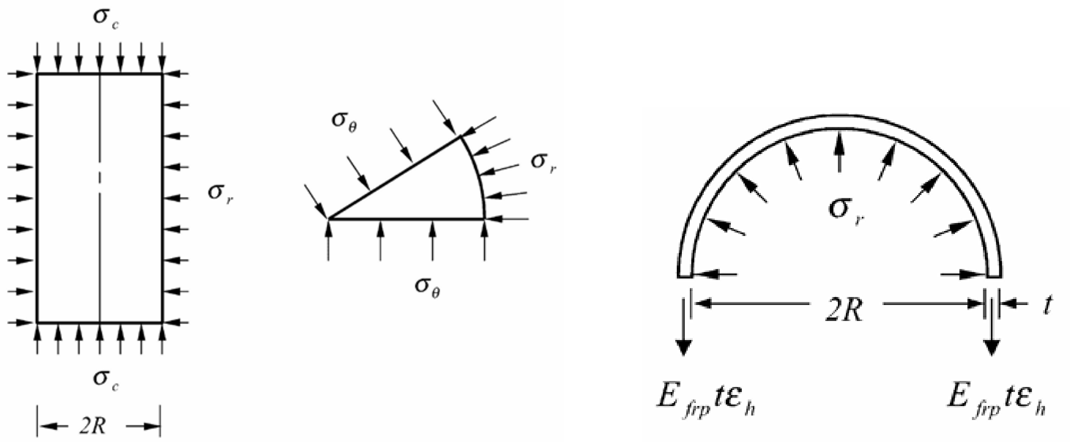

(a) Concrete (b) FRP jacket

Figure 2.8 Confining mechanism of FRP-confined concrete in a circular column [extracted from Lam and Teng (2003)]

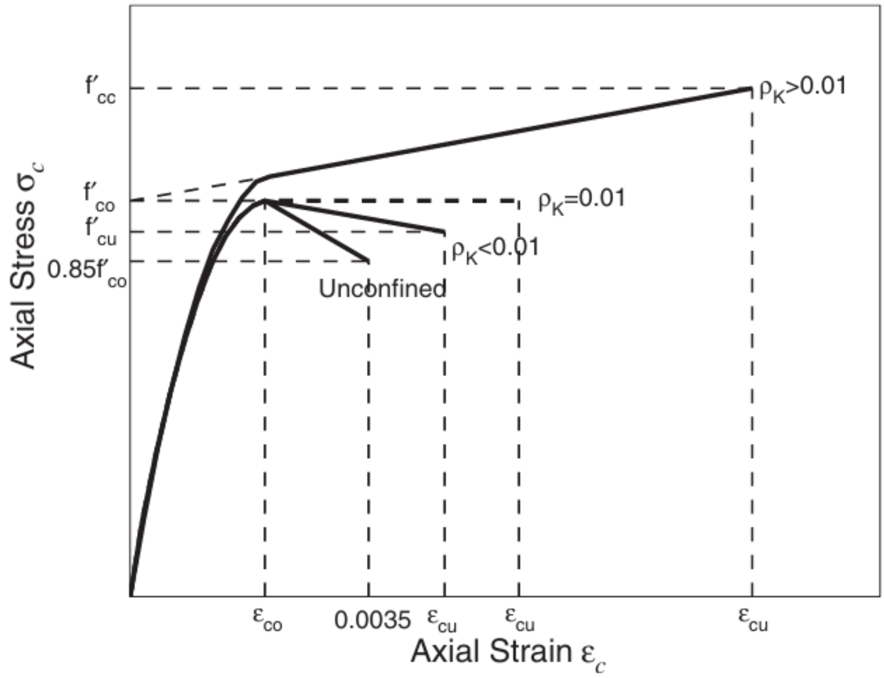

Figure 2.9 Teng et al.'s (2009) stress-strain model for FRP-confined concrete [extracted from Teng et al. (2009)]

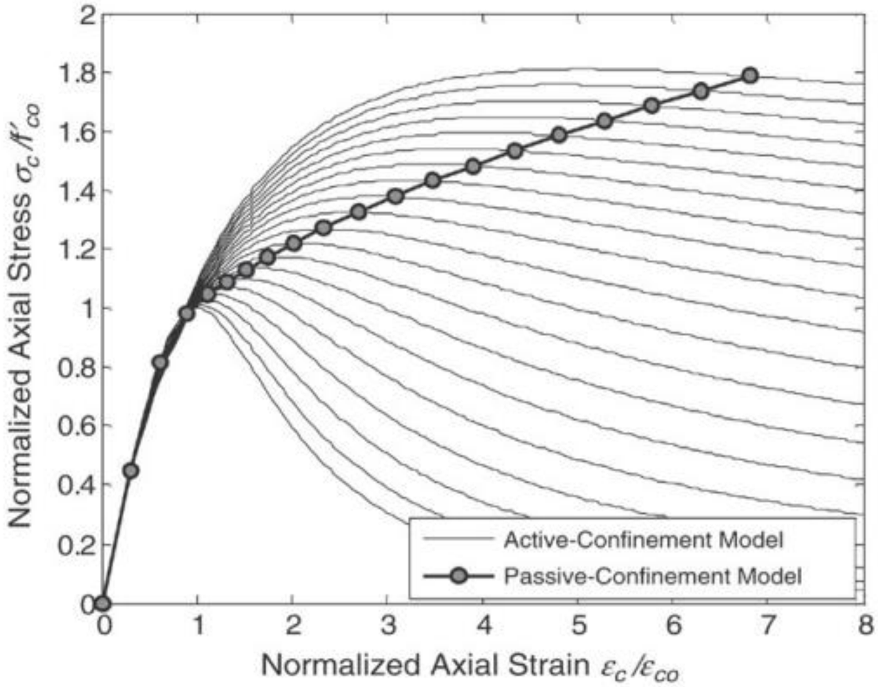

Figure 2.10 Generation of a stress-strain curve for FRP-confined concrete [extracted from Jiang and Teng (2007)]

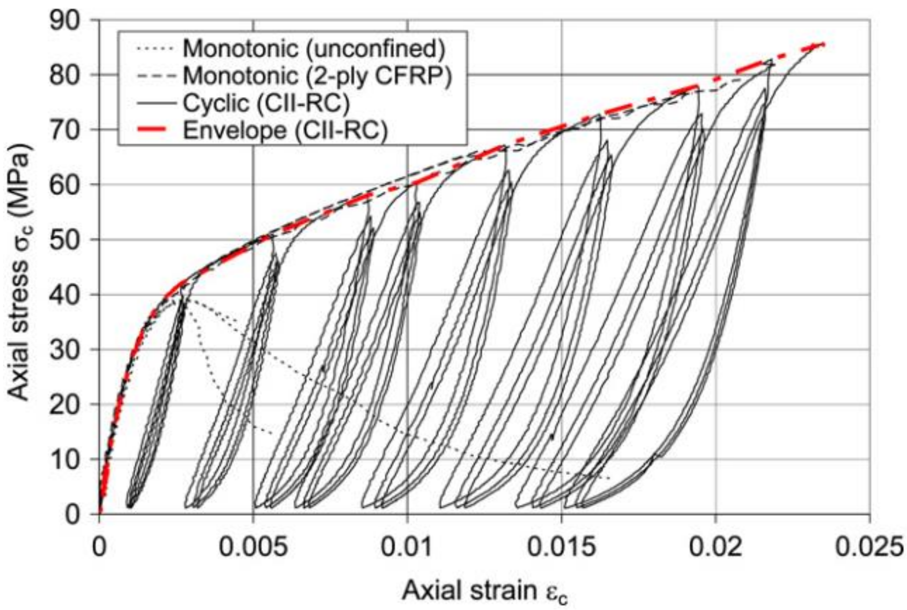

Figure 2.11 Monotonic and cyclic stress-strain curves of FRP-confined normal-strength concrete [extracted from Lam and Teng (2009)]

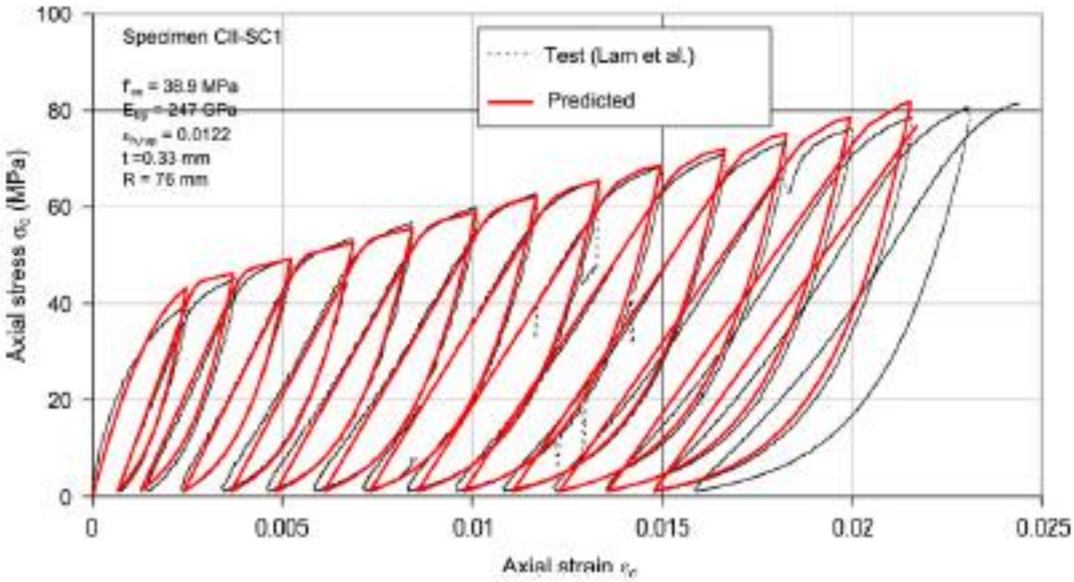

(a) Specimen CII-SC1

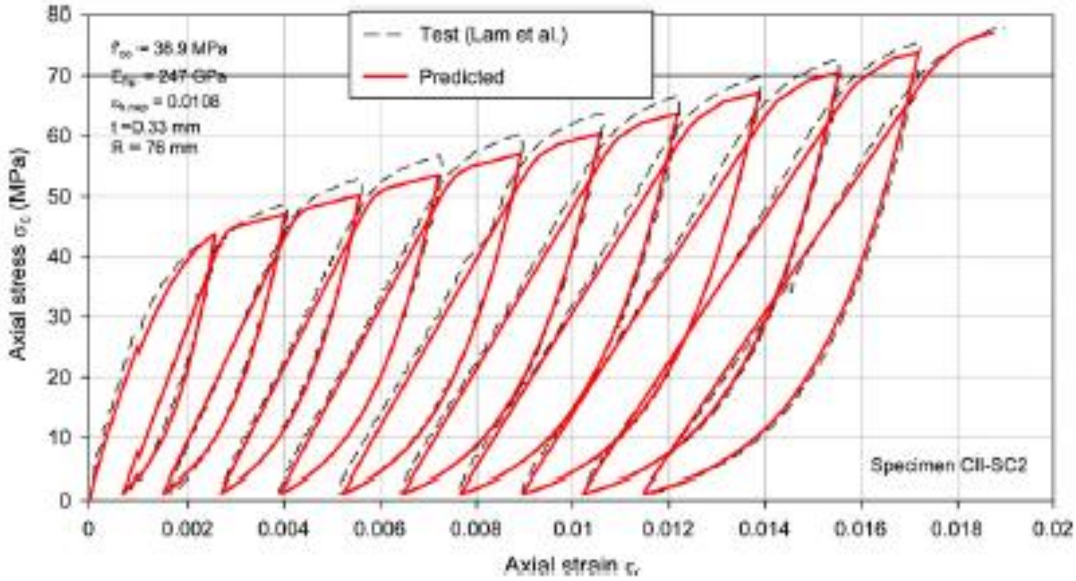

(b) Specimen CII-SC2

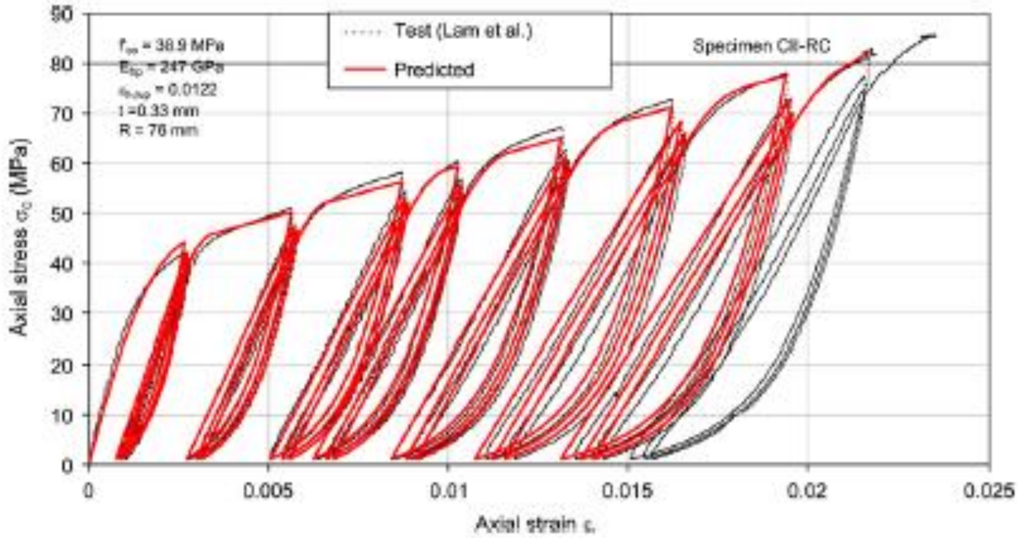

(c) Specimen CII-RC

Figure 2.12 Comparisons between test stress-strain curves and predicted stress-strain curves [extracted from Lam and Teng (2009)]

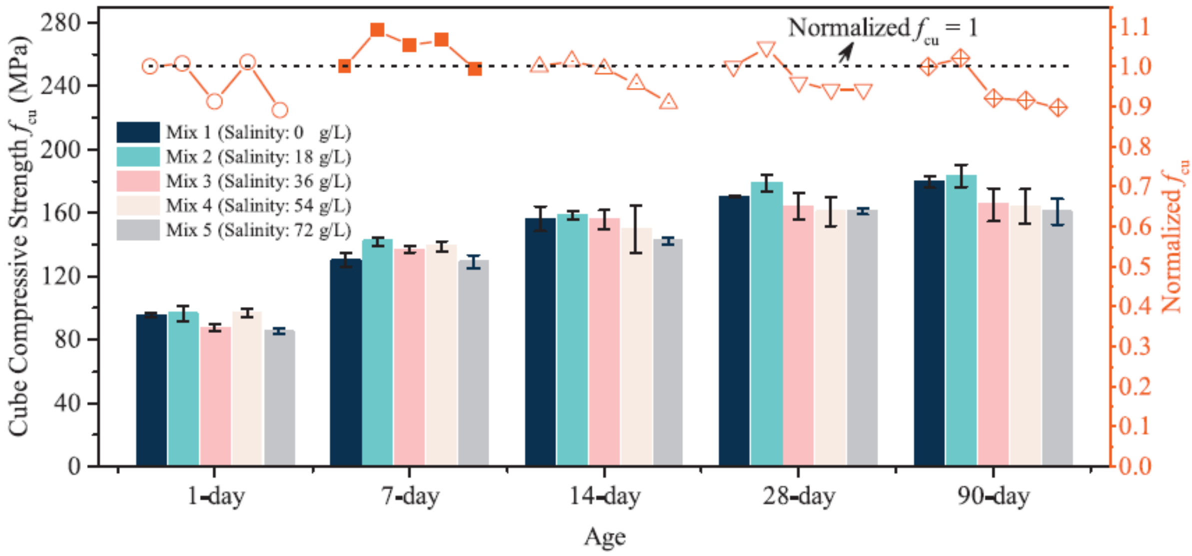

Figure 2.13 Effect of salinity on compressive strength of UHPC [extracted from Teng et al. (2019)]

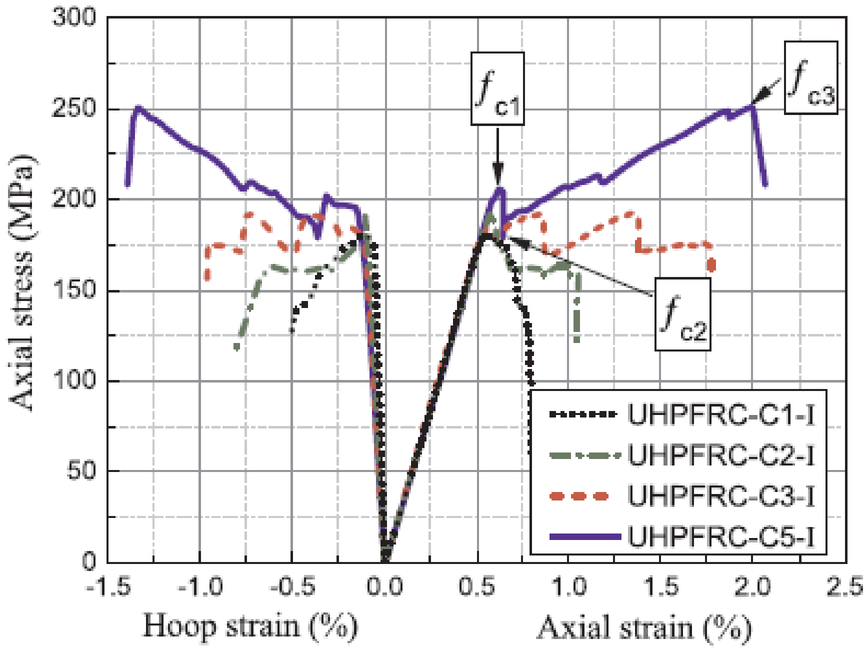

(a) UHPFRC

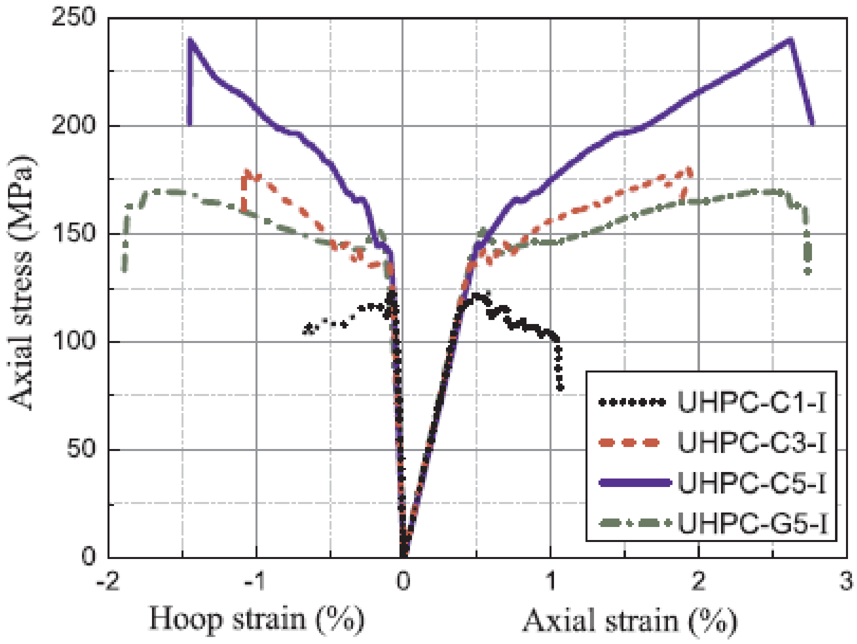

(b) UHPC

Figure 2.14 Axial stress-strain curves of FRP-confined UHPFRC and UHPC specimens [extracted from Wang et al. (2018)]

Figure 2.15 Typical failure modes of FRP-confined UHPFRC/UHPC [extracted from Wang et al. (2018)]

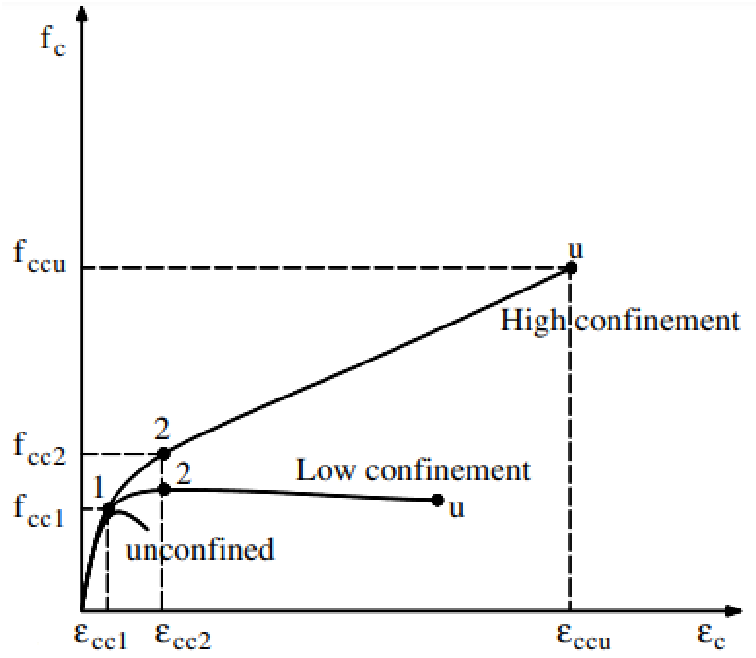

(a) FRP-confined NSC

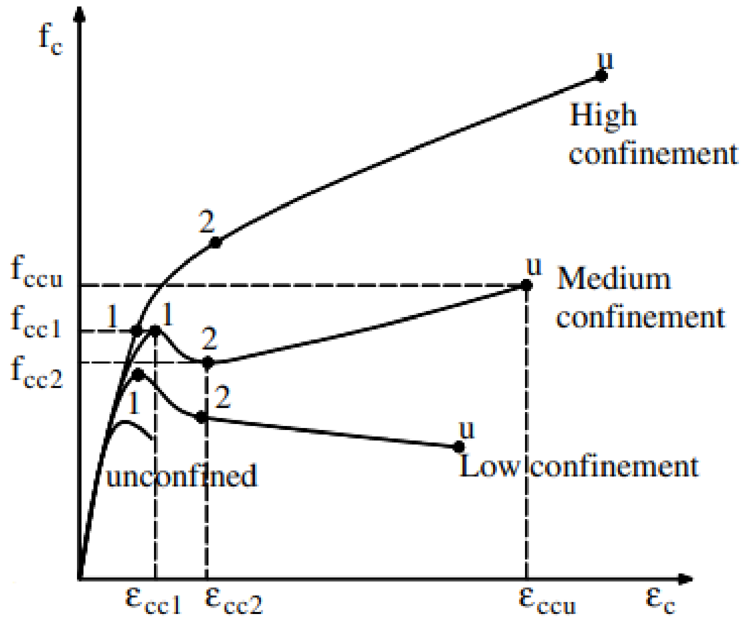

(b) FRP-confined HSC

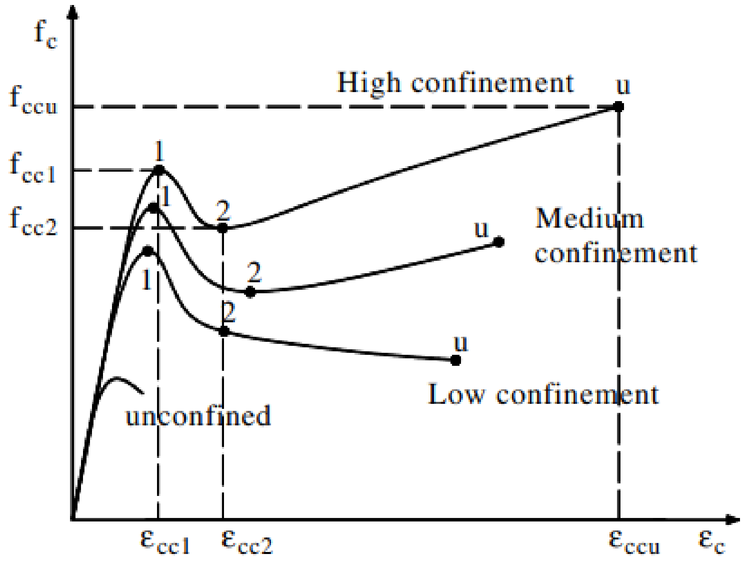

(c) FRP-confined UHSC

Figure 2.16 Typical stress-strain curves for FRP-confined NSC, HSC, and UHSC [extracted from de Oliveira et al. (2019)]

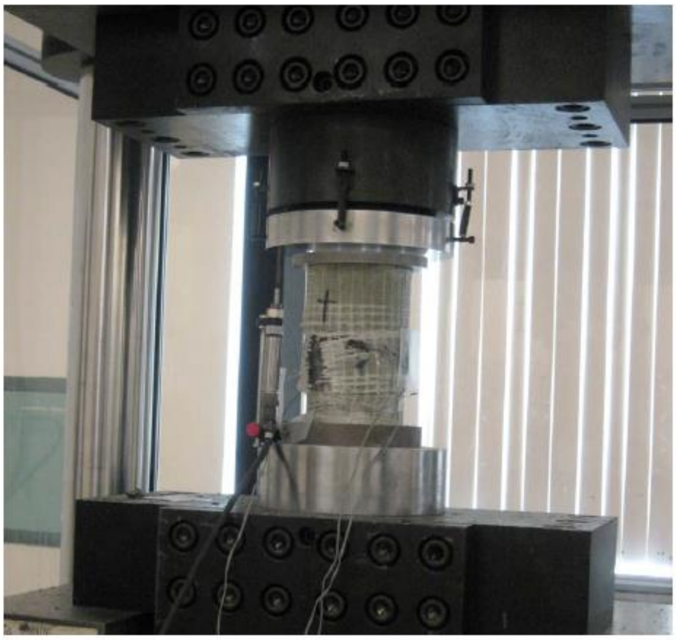

(a) Test set-up of Zohrevand and Mirmiran (2011) [extracted from Zohrevand and Mirmiran (2011)]

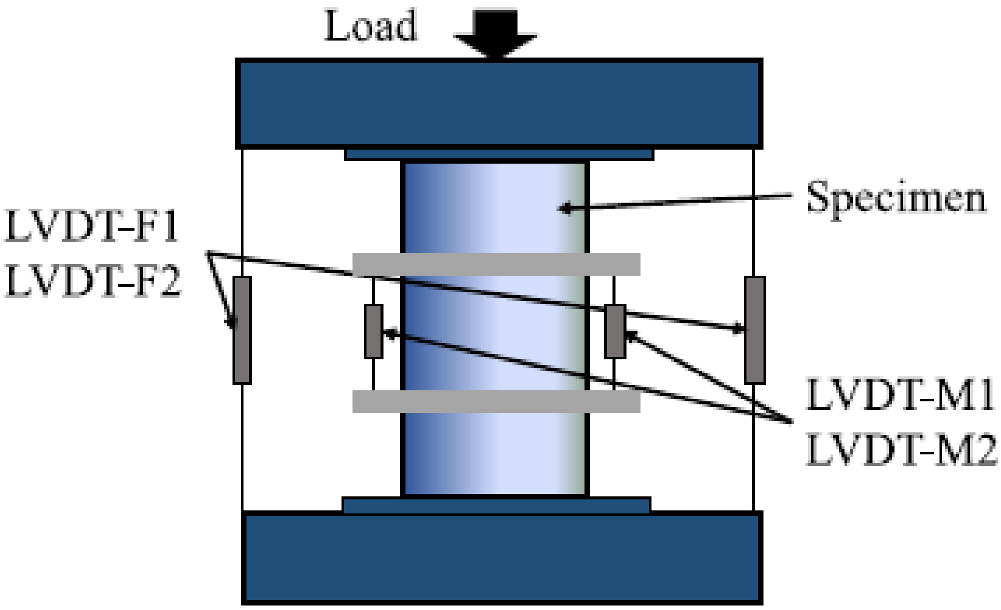

(b) Test set-up of Wang et al. (2023) [extracted from Wang et al. (2023)]

Figure 2.17 Different arrangements of test set-up

CHAPTER 3
MANUFACTURING AND MECHANICAL PROPERTIES OF WAVY-SHAPED GFRP TUBES

3.1 INTRODUCTION

Filament-wound glass fibre-reinforced polymer (GFRP) tubes have been extensively used as pressure vessels in the piping industry due to their distinct features of high strength-to-weight ratio and corrosion resistance (Xia et al., 2001; Rafiee and Amini, 2015; Prabhakar et al., 2019). In the past two decades, GFRP tubes have also been introduced to structural engineering, serving mainly as an outer confining device and/or permanent formwork for structural components, such as beams and columns (Mirmiran and Shahawy, 1997; Fam and Rizkalla, 2001b; Mohamed and Masmoudi, 2010). Concrete-filled FRP tubes (CFFTs) are a common form of structural components utilizing FRP tubes. FRP confinement has been found to be effective in enhancing both the compressive strength and ductility of concrete (Ozbakkaloglu and Oehlers, 2008; Park et al., 2011; Zhang et al., 2015; Teng et al., 2016b). FRP tubes are usually fabricated by the filament winding method (FWM) or the manual wet lay-up method. The cross sections of filament-wound GFRP tubes are generally uniform along the axis of the tube (referred to as uniform GFRP tubes hereafter). If such tubes are used in CFFTs or as reinforcing tubes inside concrete, the bond between the tube and the inner concrete core or the surrounding concrete is relatively weak due to the uniform cross section of the tubes. However, the bond behaviour between FRP tubes and concrete is of great importance to the flexural strength and stiffness of the structural member especially when the tubes possess a significantly large axial stiffness. Indeed, some researchers have explored enhancing the bond performance between FRP tubes and concrete through the use of shear connectors such as resin ribs or sand-coating on the surfaces of the FRP tubes (Helmi, 2007; Ali et al., 2020). However, the above treatments led to limited enhancement to the tube-to-concrete bond strength (ranged from 0.63 MPa to 0.9 MPa) due to the small stiffness and strength of the resin for generating ribs or bonding sands.

To better enhance the bond performance between hybrid rebars and concrete, a novel form of wavy-shaped GFRP tubes is proposed and used in fabricating hybrid rebars in this Ph.D. research programme. As shown in Figure 3.1, the cross-sections of the GFRP tubes are non-uniform along the axis of the tube to form a wavy-shaped surface for enhanced bond behaviour. The wavy-shaped GFRP tubes can be used in replacing conventional uniform GFRP tubes in fabricating hybrid rebars originally proposed by Teng et al. (2018), resulting in a novel form of wavy-shaped hybrid rebars. Compared with the original hybrid rebars with a uniform cross-section, the employment of wavy-shaped GFRP tubes is expected to lead to much better bond behaviour of hybrid rebars due to the mechanical interlocking of the waves with the surrounding concrete. To this end, the design and fabrication of wavy-shaped GFRP tubes of high quality need to be well-addressed. The mechanical properties, such as the elastic moduli, the ratio and distribution of fibres, of the wavy-shaped FRP tubes need to be examined in detail. In addition, the microstructure of the novel tubes needs to be examined both qualitatively and quantitatively.

Against this background, this chapter presents a fabrication method for filament wound wavy-shaped GFRP tubes and a comprehensive experimental study on determining the mechanical properties and fibre content of these tubes. The detailed fabrication method of wavy-shaped FRP tubes is explained in Section 3.2. A new testing method was proposed, which could provide a more accurate way to assess the hoop elastic modulus of wavy-shaped tubes than the commonly used split disk tests.

3.2 FABRICATION METHOD

To produce wavy-shaped FRP-UHPC hybrid rebars, wavy-shaped GFRP tubes should be fabricated first. The filament winding technology was used to fabricate such wavy-shaped GFRP tubes. A mandrel was required to serve as an internal mould in the filament winding process (Hahn et al., 1994). Due to the non-uniform cross-section of the GFRP tube, the mould was separated into several parts to facilitate demoulding of the mould internally from the GFRP tube (Figure 3.3). To ensure a smooth removal process of the internal mould, the maximum width of the separate part should be less than the minimum internal diameter of the wavy-shaped GFRP tubes. In the present study, the internal mould was 3D-printed with ABS plastic using a stereolithographic 3D printer.

The mandrel was degreased with acetone to prevent chemical bonding between the matrix and the surface of the mandrel. In addition, a light layer of release agent LOCTITE 770-NC was coated to the surface of the mandrel with a clean lint-free cloth to facilitate the demoulding process after curing. After coating, the solvents in the release agent were evaporated for 10 minutes. Next, the mandrel was coated again with the release agent until this process was repeated at least three times in accordance with the technical data sheet of LOCTITE 70-NC. With the help of the release agent, the GFRP tube could be easily demoulded from the mandrel.

As shown in Figure 3.4, the filament winding process was carried out on an X-Winder winding machine (4X-23). The winding machine consists of an aluminium frame, a carriage, a payout eye, a mandrel, a resin bath and a computer controller (Figure 3.4). JN-CM epoxy with a tensile elongation of 1.9% (as provided by the manufacturer) was used to pre-impregnate the glass fibres before winding. The glass fibres. 2400-386T glass fibres from CHINA JUSHI CO., LTD were adopted to produce the filament winding tubes.

According to GB 1499.2-24, a recommended rib height of 3.2 mm is given for a 50-mm-diameter steel rebar. Therefore, three types of wave height (i.e., 5 mm, 3 mm, and 1 mm) were included to fabricate the 50-mm diameter wavy-shaped GFRP tube. Since it is very difficult to wind on concave shapes of large curvature at a trough, the wavelength was designed as 80 mm in order to limit the longitudinal curvature in a concave zone. The specific shape of a wave is calculated based on the sine function:

$$y = 0.5h\sin(2\pi x/\lambda) \tag{3.1}$$

where h is the vertical distance between peak and trough of a wave and λ is the wavelength.

The fibre winding process has specific requirements for the design of the mandrel, which necessitates a convex shape. Concave winding is challenging because the tensioned fibres tend to bridge across the concave surface instead of achieving the desired shape. Therefore, a hoop-winding technique was employed to shape the fibres into a wavy pattern in the present study. Each tow was wound around the mandrel in a shallow helix, forming an angle of approximately 89 degrees with the axis of rotation. Therefore, the mandrel was covered with one layer of fibre after the motion of the carriage from one end to the other. In the present study, three layers or five layers of glass fibres were wound to the mandrel in the fabrication of three-layer or five-layer GFRP tubes, respectively. Before the winding process, the critical winding parameters such as the winding angle, the number of fibre layers, the mandrel diameter, and the winding length needed to be input in the winding machine. Due to the wavy shape of the mandrel, the fibres near the peak tend to slide to the adjacent concave location, leading to significantly lower fibre content near the peak. To tackle this problem, varied carriage speeds along the axis of the mould were adopted during the winding process. Three carriage speeds were adopted for three different regions, i.e., the peak region, the trough region, and the middle region (i.e., the region between a peak and an adjacent trough), respectively, as shown in Figure 3.5. In this Ph.D. research programme, the widths of the three regions were equal and set to one quarter of the wavelength. For the specimen IDs, “H0”, “H1”, “H3”, and “H5” refer to the tube with a wave height of 0, 1, 3, and 5 mm, respectively; “L” and a digital number refer to the number of fibre layers; “P”, “M”, and “T” refer to the peak, middle, and trough locations of the wavy tube. Table 3.1 lists the carriage speeds in the different regions, which were obtained through trial-and-error processes. With the above winding pattern, the wavy-shaped FRP tubes at different locations possess similar thicknesses. Table 3.1 lists the average measured thicknesses at different locations of the wavy-shaped FRP tubes fabricated in the present study.

After the winding process, the mandrel was kept rotating for 24 hours at room temperature for the curing of resin. After curing, the internal mould of different parts was peeled from the wavy-shaped GFRP tube. Figure 3.1 shows the final products of the wavy-shaped GFRP tubes fabricated in the present study. Wavy-shaped hybrid rebar fabricated with such wavy-shaped GFRP tubes are presented in Figure 3.6.

3.3 MATERIAL PROPERTIES

3.3.1 General

The elastic modulus of an FRP tube was obtained from split disk tests according to ASTM D2290-19a (2019). Figure 3.2(a) shows the typical test fixture of the split disk tests. However, this method is more suitable for FRP tubes with a relatively large diameter. For a large FRP tube (with a diameter equal to or larger than 200 mm), the readings of the strain gauges installed on the outer surface of the tube ring at the gaps between the two semi-circular disks were observed to be lower than the membrane strains due to the bending effect. Consequently, strain gauges were typically installed on the outer surface of the FRP ring, positioned around 15 mm from the gap between the two semi-circular disks, to reduce the impact of bending (Zhang, 2014). Since the FRP tubes in FRP-UHPC hybrid rebars proposed by Teng et al. (2018) are relatively small (with a diameter of only around 50 mm), the split disk tests may lead to more pronounced bending deformation of the ring specimen during the initial loading stage and are thus not reliable for FRP tubes of such a small diameter. To tackle this problem, improved split disks as shown in Figure 3.2(b) were used to provide cavities for the placement of strain gauges on both the inner and outer sides of the FRP rings. Moreover, it is not easy to obtain the elastic moduli of wavy-shaped FRP tubes using the split disk tests. To maintain the accuracy of test results, the split disk must match the shape of a wavy-shaped FRP tube. This requirement means that considerable time and effort will be expended in designing a specifically shaped split disk and in aligning it with the wavy-shaped FRP tube. Therefore, a new testing method (i.e., the internal air pressure test) should be proposed for wavy-shaped tubes.

Another concern of using wavy-shaped FRP tubes is to evaluate their fibre fractions (i.e., the ratio of fibres to the composite) at different locations. In current research on FRP-confined concrete, the fibre volume fractions of FRP jackets or tubes were frequently neither quantified nor specified. This is due to the relatively uniform distribution of fibres within the FRP jackets or tubes utilised in these specimens. Consequently, the material properties at different locations on the resin-impregnated FRP sheets or prefabricated FRP tubes were comparatively consistent. However, this does not apply to wavy-shaped FRP tubes, owing to their distinctive wavy shape. Ensuring uniform fibre content across all locations is challenging when employing FWM for their production. Therefore, assessing the fibre content at different locations of the wavy-shaped FRP tubes is of significant importance for their quality control.

The standardized methods for the determination of fibre content in FRP composites include resin burn-off tests (ASTM 2584-18, 2018) and chemical tests (ASTM D3171-15, 2015). In these two methods, the fibres are separated from the matrix and the weight change is recorded. In addition to these two methods, the digital image processing (DIP) method (Morales et al., 2020; Chatzinas et al., 2021; Srivastava et al., 2022), which utilizes photos obtained from optical microscopy (OM) or scanning electron microscopy (SEM), has also been commonly used for calculating the fibre volume ratio of an FRP composite. By assuming that the fibre content is uniform across the entire composite material, the fibre volume ratio can be determined from the ratio of the fibre area to the total area of the cross-section.

Coupon specimens were cut from the fabricated tubes and tested for obtaining the fibre contents and mechanical properties of the wavy-shaped FRP tubes. Table 3.2 summarises all the specimens for four different tests (i.e., resin burn-off tests, DIP tests, split disk tests, and internal air pressure tests). The details of the specimens, including their nomenclatures, are described in the following sections.

3.3.2 Fibre Content

3.3.2.1 Resin burn-off tests

Since the fibre content is of great importance to the mechanical properties of FRP composites, resin burn-off tests were conducted to assess the fibre contents at different locations of the wavy-shaped FRP tubes according to ASTM D2584 (2011). Ring samples with a width of 10 mm were cut from the wavy-shaped FRP tubes at three representative locations (i.e., peak, middle, and trough). Three samples were prepared for each location of the FRP tube of each wave height. In total, 30 samples were prepared for the resin burn-off tests (Table 3.2). In the resin burn-off tests, "R" refers to resin burn-off tests; three nominally identical specimens were prepared, which were marked by "1", "2", and "3" at the end of the specimen names. For example, "R-H1L3-P1" represents one of the three nominally identical specimens at the peak location of a wavy-shaped FRP tube with a wave height of 1 mm and 3 layers of fibres.

Before burning, the samples were conditioned in 23 ± 2℃ and 50 ± 10% relative humidity for not less than 40 hours. The resin of the samples was burned off in an Electric Muffle Furnace (as shown in Figure 3.7) at a temperature of 565 ± 28 ℃ for more than two hours. An analytical balance was used to measure the weights of the samples before and after burning. The fibre weight content M_f can be calculated in the following equation:

$$M_f = 1 - [(W_1 - W_2)/W_1] \tag{3.2}$$

where W_1 represents the weight of each original sample; W_2 represents the weight of the residue after burning.

The fibre volumetric fraction V_f can be calculated in the following equation:

$$V_f = \frac{M_f D_s}{D_f} \tag{3.3}$$

where D_f is the density of the glass fibres; D_s is the density of the original sample.

3.3.2.2 DIP method

The DIP method was also conducted to evaluate the fibre content of the fabricated wavy-shaped GFRP tubes. Two samples with a width of 10 mm and a height of 5 mm were cut from each type of tubes at three different locations (i.e., peak, middle, and trough) for wavy-shaped GFRP tubes and sealed in an epoxy "puck" as shown in Figure 3.8(a). The length direction of the cut samples should be aligned with the axial direction of the wavy-shaped tubes, the width direction should be aligned with the circumferential direction of the wavy-shaped tubes. Besides, two samples were also taken from a uniform GFRP tube as control groups. The fibres in the cross-section surface of the samples were to be observed; therefore, during sealing, the cross-section of the sample to be observed should be facing upwards. After curing, the epoxy pucks with GFRP tube samples embedded were grinded and polished with a Buehler AutoMet 300 grinder-polisher. Prior to imaging, all specimens were coated with a thin layer of gold-palladium through a vapour deposition process to enhance their electrical conductivity, thereby improving the quality of the images. For each sample, three locations of each sample were selected as representative areas for fibre calculation [Figure 3.8(b)].

In total, 20 specimens as listed in Table 3.2 were prepared for the observation. The ID of each sample starts with "D" referring to the DIP method and "H" referring to the wave height ("H0", "H1", "H3", and "H5" refer to the FRP tube with a wave height of 0, 1, 3, and 5 mm, respectively); "L" and a digital number refer to the number of fibre layer; "P", "M", and "T" followed refer to the peak, middle, and trough locations of the wavy tube, respectively. Two nominally identical specimens were prepared for each configuration, as indicated by "1", and "2" at the end of the sample ID. For example, "D-H1L3-P1" represents one of the two nominally identical samples cut from the peak of a wavy-shaped GFRP tube with a wave height of 1 mm and 3 layers of fibres.

SEM images were obtained on VEGA3 TESCAN (Scanning Electron Microscopy) at an accelerating voltage of 20 kV (Figure 3.9). For the convenience of image processing, a magnification level of 200 × was found to produce the most suitable images. A public domain open-source image processing software *ImageJ* was used to analyse the SEM images. The original images were first converted into 8-bit binary images (grayscale) for distinguishing the fibres and the resin [Figure 3.10(a)]. In the grayscale images, the fibres were shown as light grey while the resin matrix was shown as dark grey. As illustrated in the 3D view [Figure 3.10(b)], the DIP method presumes that the same cross-sectional profile extends throughout the length of the sample. Consequently, the area fraction of the fibres in this cross-section is considered equivalent to the volume fraction of the fibres in the entire sample. With a proper range of intensity, as shown in Figures 3.10(c) and (d), the total area of the resin matrix (i.e., low range threshold) and the fibre (i.e., high range threshold), each highlighted in red, could be distinguished in the entire analysed area. Then, the corresponding percentage of the two components based on the entire analysed area could be determined by measuring the pixels of a certain area (i.e., the red-coloured area) using an algorithm incorporated in the *ImageJ* software.

3.3.3 Hoop Elastic Modulus

3.3.3.1 Split disk tests

Ring split-disk tests were first conducted on conventional GFRP tubes with a uniform cross-section for reference. As shown in Table 3.2, five-ring samples with a width of 20 mm were cut from a GFRP tube. "S" in the sample ID refers to the split-disk test, and "H0L3" refers to a uniform FRP tube (wave height = 0) with 3 layers of fibres. The last number in the sample ID is used to distinguish five nominally identical specimens. Four strain gauges with a gauge length of 5 mm were installed on the tube at the disk gap level on both the compression (outer) and tension (inner) surface of the tube to measure the hoop membrane strains as shown in Figure 3.11(a). The tests were conducted on a universal tensile testing machine with a capacity of 100 kN [Figure 3.11(b)]. A displacement-control mode with a rate of 1.0 mm/min was adopted through a self-aligning splitting disk testing fixture which exerted tensile loads to the ring samples. A data logger and a load cell were used to record the data of strains and loads, respectively. The loading process of the tensile tests consisted of two stages. During the initial stage of loading, the deformation of the specimen was primarily characterized by bending deformations at the locations of the disk gaps. The hoop strains on the outer surface of the FRP tube were negatively small because of compressive strains due to bending. With the increase of the tensile load, the magnitude of compressive strains reduced and tensile strains gradually developed. The membrane strain (ε_m) and membrane stress (σ_f) in the FRP tube can be calculated by:

$$\varepsilon_m = \frac{1}{2}(\overline{\varepsilon_c} + \overline{\varepsilon_t}) \tag{3.4}$$

$$\sigma_f = \frac{F_t}{2bt} \tag{3.5}$$

where $\overline{\varepsilon_c}$ and $\overline{\varepsilon_t}$ are the average hoop strains from two strain gauges at the initially compression sides [i.e., SG-1, SG-4 in Figure 3.11(a)] and initially tension sides [i.e., SG-2, SG-3 in Figure 3.11(a)], respectively; F_t is the applied tensile force; b and t are the width and thickness of the FRP ring, respectively.

3.3.3.2 Internal air pressure tests

The internal air pressure tests were adapted from the hydraulic pressure tests of the filament-wound tubes in the open literature (Hull et al., 1978; Rosenow, 1984; Soden et al., 1993; Xie et al., 2020). In the present study, hydraulic pressure tests were originally adopted for obtaining the elastic moduli of the produced tubes. However, due to limitations in the experimental conditions, the poor sealing at both ends of the GFRP tubes resulted in water leakage even at very low internal pressures. Therefore, a gasbag was installed inside the GFRP tube. When the air was pumped into the gasbag inside the GFRP tube, the gasbag swelled into contact with the GFRP tube; therefore, the internal air pressure was transferred from the gasbag to the GFRP tube. Figure 3.12 shows the test set-up for the internal air pressure test, which included high-pressure gas pump with a pressure capacity of 40 MPa, a gas pressure meter, a fixture, neoprene gaskets, and a gasbag. The neoprene gaskets were placed between each end of the FRP tube and the fixture to eliminate the influence of unevenness at both ends. To conduct the internal air pressure tests, the GFRP tubes, including both wavy-shaped GFRP tubes and uniform GFRP tubes, were divided into segments measuring 100 mm in length. Totally, 18 specimens were prepared and tested. The details of the specimens are summarized in Table 3.2. Each specimen was given an ID starting with "I" referring to the internal air pressure test, followed by "H" plus a digital number denoting the wave height in mm and "L" plus a digital number denoting the number of fibre layer. The ID ends with "1", "2", and "3" indicating three nominally identical specimens. The hoop moduli of each FRP tube specimen at different locations of the tube (i.e., peak, middle, and trough) can be measured simultaneously. The pressure was measured by a gas pressure pump. The interval for data acquisition was around 0.1 MPa. The relationship between the internal air pressure and the hoop stress is as follows:

$$\sigma_f = \frac{PR}{t} \tag{3.6}$$

where P is the air pressure; R is the internal radius of the tube at the measured cross-section; t represents the thickness of the FRP tube.

For each FRP tube with a uniform cross section (wave height = 0), four strain gauges with a gauge length of 5 mm were evenly installed at the mid-height section for measuring the hoop strains. For each wavy-shaped FRP tube, a total of 12 strain gauges with a gauge length of 5 mm were installed at the peak, middle, and trough regions of the tube.

3.4 TEST RESULTS AND DISCUSSIONS

3.4.1 Fibre Content

The average fibre volume fractions of GFRP samples cut from each type of GFRP tubes were determined through the BO tests and the DIP method. The average value and standard deviation of the fibre volume fractions obtained from both methods and the difference between these two methods are shown in Table 3.3. The "H0L3" specimens exhibited the highest average fibre volume fractions, with values of 42.23% and 44.48% obtained from the BO tests and DIP method, respectively. The "H5L3-M" specimens demonstrated the lowest average volume fractions, measuring 29.29% and 30.4% through the BO tests and the DIP method. The standard deviations (S.D.s) obtained from the BO tests for a given location are generally smaller than those obtained from the DIP method. The greater variability in the data from the DIP method could be attributed to the presence of voids in the GFRP tubes.

Figure 3.13 plots the fibre and resin contents of the samples obtained from the two methods. It is clear that the values of fibre content of wavy-shaped FRP tubes are generally smaller than those of the uniform FRP tubes. This figure distinctly illustrates the variation in fibre volume fraction at various locations along a wavy FRP tube with different wave heights. For the GFRP tubes labelled "H5L3" and "H3L3", the fibre content measured using both the BO tests and DIP method revealed the lowest values in the middle region (i.e., 29.28% and 35.06% based on the BO tests; 30.4% and 34.01% based on the DIP method). Among the three regions of the wavy tubes with a wave height of 5 mm, the peak region possessed the highest fibre volume fraction with values of 36.73% and 40.94% based on the BO tests and DIP method, respectively. For the wavy tubes with a wave height of 3 mm, the BO tests indicated that the fibre volume fraction was the highest at the peak region, with a value of 38.28%, while the DIP method suggested that the fibre volume fraction was highest at the trough region, measuring 41.10%. The tubes with a wave height of 1 mm ("H1L3") possessed relatively uniform fibre distributions at different locations.

The difference in fibre volume fraction at different locations of a wavy FRP tube could be attributed to the effect of wavy shape in the fabrication of the wavy tubes. The fibre distributions of wavy shaped tubes were not perfectly uniform, with the fibre content being slightly lower in the middle region between the peaks and troughs, although the variable-speed winding scheme was employed during the winding process as discussed in the preceding sections. The fibres intended to be placed between the peak and trough regions of a wavy FRP tube tended to slide to the trough region, leading to lower fibre content in the middle region. However, the difference in fibre content at different locations of GFRP tube samples "H1L3" was relatively small as shown in Figure 3.12, implying that fibre sliding was less likely to occur for GFRP tubes with a wave height of 1 mm.

The difference in fibre volume fraction between the BO tests and the DIP method ranges from 1.05 to 4.21%. This result indicates that the fibre volume fractions obtained from both test methods are comparable. Additionally, the differences between the two methods are in line with the values reported in the literature. Up until now, there is limited literature comparing the use of DIP method to quantify fibre content with conventional methods. The differences between the results obtained from DIP method and conventional methods are generally within 5%. In the study conducted by Morales et al. (2020), both the BO tests and the DIP method were employed to determine the fibre volume fractions of GFRP bars. The reported differences between the two methods ranged from 0.2% to 5%. Similarly, the acid digestion method and the DIP method were carried out on graphite composite specimens and an agreement ranging from 1.6% to 5% between the two methods was reported (Cilley et al., 1974; Waterbury and Drzal, 1989; Viens, 1990).

In addition to the fibre volume fraction, the total cross-section area of fibres captured in SEM images can also serve as an indicator to describe the overall fibre quantity at different locations. Figure 3.14 displays a comparison of the total cross-sectional area of fibres for samples with varying wave heights and from different regions. In Figure 3.14, the areas of fibres were represented by the number of pixels in the SEM images. It is clear that the wavy-shaped tubes and the conventional uniform FRP tubes have a comparable fibre amount at the peak and middle regions (i.e., 4.3×10^5 pixels to 5.4×10^5 pixels and 4.6×10^5 pixels). The wavy-shaped tubes exhibit slightly higher fibre amount at the trough region (i.e., 4.9×10^5 pixels to 7.4×10^5 pixels). However, as previously noted, the fibre volume fractions of conventional uniform GFRP tubes were higher than those of the wavy-shaped GFRP tubes. Besides, the GFRP tube at the trough region did not possess the highest fibre volume fraction for the "H5L3" tubes. The discrepancy was due to the varying thicknesses across different regions. For example, as shown in Table 3.1, the trough region of the "H5L3" tubes had a thickness of 1.92 mm, while the GFRP tube in the peak region had a thickness of 1.67 mm. Therefore, despite the volume fraction not being the highest, the total fibre content at the trough region was larger.

3.4.2 Elastic Modulus

Figure 3.15 presents the failure modes of the FRP rings in the ring split disk tests. The specimens failed with FRP rupture at one of the corners of the disks in the gaps due to stress concentration. The stress-strain curves of the GFRP tubes are plotted in Figure 3.16. The stresses and strains are calculated in Eqs. 3.4 and 3.5, respectively. The elastic modulus of the tube was taken as the secant stiffness between the original point and the ultimate point in the stress-strain curves. The test result shows that the average elastic modulus of the conventional uniform tubes fabricated with 3 and 5 layers of fibres were 42.6 GPa and 43.9 GPa, respectively (Table 3.4). In comparison to the data reported in the literature, the scatter in this study's data is relatively large, ranging from 36.7 GPa to 49.4 GPa. The discrepancies between the data from the two sources may be attributed to the adverse effects of bending during tensile testing.

As for the internal air pressure tests, typical stress-strain curves are plotted in Figure 3.17. The hoop stresses were calculated in Eq. 3.6. The hoop strains were taken from the average value of four strain gauges around the peak, middle or trough level of the tube. The jitters of the stress-strain curves at the beginning were excluded from the calculation of the elastic moduli. The test results of all the 18 specimens are summarized in Table 3.5 and plotted in Figure 3.17.

Figure 3.18 shows that for both the 5-ply and 3-ply filament-wound GFRP tubes with a wavy shape, the GFRP tube at the middle region had the smallest elastic modulus in the hoop direction for all wave heights. The average elastic moduli of the wavy tubes ranged from 25.4 GPa to 50.2 GPa for 3-ply tubes and from 26.0 GPa to 40.7 GPa for 5-ply tubes for all three regions. The elastic moduli of the 3-ply and the 5-ply GFRP uniform tube were 38.4 GPa and 36.1 GPa, respectively. Compared with wavy-shaped GFRP tubes, the elastic moduli of both the 3-ply and the 5-ply uniform tubes were slightly lower than those of the FRP tubes at the peak region for I-H5L3, I-H5L5, and I-H3L3 specimens, but higher than those at the middle and trough regions. Elastic moduli of 42.6 GPa and 43.9 GPa for the 3-ply and 5-ply uniform GFRP tubes were obtained from the internal air pressure tests, which were slightly higher than the values of 38.4 GPa and 36.1 GPa obtained from the split disk tests. This may be attributed to the influence of bending in the split disk test. Similar results have been reported by Xie (2018). Furthermore, the I-H0L3 samples exhibited a standard deviation of 2.0 MPa, while the S-H0L3 samples had a standard deviation of 8.6 MPa. This indicates that the variance in the internal pressure test results for uniform tubes was lower than that observed in the split disk tests. Concerning the fibre layers, the 5-ply tubes demonstrated lower scatters in the test results for both wavy-shaped tubes and uniform tubes. Visual observations revealed that both the uniform tubes and the wavy tubes with 5-ply fibres possessed a smooth outer surface. The possible reason is that with an increase in the number of fibre layers, the distribution of fibres becomes more uniform.

3.4.3 Comparison and Discussion

The elastic moduli of the filament wound GFRP tubes are mainly determined by the fibre content and the winding angle. For the GFRP tubes with a winding angle of 89° in the present study, the elastic moduli were primarily determined by the fibre content. The fibre contents at the three regions shared a similar trend to the elastic moduli, with the middle region consistently displaying the lowest values. In the fibre content tests, the uniform tube had the largest fibre content among all tubes. However, the average elastic moduli of the uniform tubes are smaller than the elastic moduli of specimens H5P, H3P, H5T, H3T, H1P, H1M, and H1T for the 3-ply tubes. The difference may come from the biaxial stress status of the GFRP tubes in the internal pressure tests. The friction between the gasbag and the GFRP tube may lead to the underestimation of the hoop strain and the overestimation of the elastic modulus at the peak and trough locations.

3.5 CONCLUSIONS

This chapter has presented a fabrication method of wavy-shaped GFRP tubes with the filament winding technology. The properties of the fabricated wavy-shaped FRP tubes were evaluated and compared with those of the conventional uniform tubes. Burn-off (BO) tests and the digital image processing (DIP) method were deployed to obtain the properties of the tube samples. The elastic modulus of the FRP tube in the hoop direction was measured using two different methods, i.e., the split disk test and the internal air pressure test. Based on the test results and discussions, the following conclusions could be made:

(1) The BO tests and the DIP method were successfully used to obtain the volume fraction of fibre content of the fabricated GFRP tubes. A difference of only 4.21% was found for the results between BO tests and the DIP method.

(2) The conventional uniform tubes had a higher fibre volume fraction than that of wavy-shaped tubes. The fibre volume fraction at the middle region was the smallest for the wavy tubes with wave heights of 5 mm and 3 mm. The distribution of fibre content in the “H1L3” tubes was more uniform than in the “H5L3” tubes and “H3L3” tubes.

(3) The internal air pressure tests showed that the proposed testing device of the internal

pressure tests could provide results of elastic modulus comparable to those of split disk tests for conventional uniform GFRP tubes. However, the obtained results for wavy-shaped tubes may not be sufficiently accurate due to the effect of friction between the gasbag and the GFRP tube.

(4) The total cross-sectional areas of fibres (i.e., 4.3×10^5 pixels to 5.4×10^5 pixels) of wavy-shaped tubes at the peak and the middle regions were found to be similar to those of conventional uniform tubes (i.e., 4.6×10^5 pixels), implying the success of fabricating wavy-shape GFRP tubes in the present Ph.D. research programme. The confining and bonding performances of the fabricated wavy-shaped FRP tubes in FRP-confined UHPC specimens and hybrid rebars will be verified in the subsequent chapters.

3.6 REFERENCES

Ali, A., Dieng, L. and Masmoudi, R. (2020). “Experimental, analytical and numerical assessment of the bond-slip behaviour in concrete-filled-FRP tubes.”, *Engineering Structures*, 225, 111254.

Chatzinas, P.S., Tsiourva, D.E., Bilalis, E.P. and Tsouvalis, N.G. (2021). Comparison of fiber content measuring methods of filament wound CFRPs. In *Developments in the Analysis and Design of Marine Structures: Proceedings of the 8th International Conference on Marine Structures*, Trondheim, Norway.

Cilley, E., Roylance, D. and Schneider, N. (1974). Methods of fiber and void measurement in graphite/epoxy composites. In *Composite Materials: Testing and Design (Third Conference)*, ASTM STP 546, American Society for Testing and Materials, pp. 237-249.

Fam, A.Z. and Rizkalla, S.H. (2001b). “Confinement model for axially loaded concrete confined by circular fiber-reinforced polymer tubes”, *Structural Journal*, 98(4), 451-461.

Hahn, H.T., Jensen, D.W., Claus, S.J., Pai, S.P. and Hipp, P.A. (1994). *Structural Design Criteria for Filament-Wound Composite Shells*, Report No. NASA-CR-195125.

Helmi, K. (2007). *The Effects of Driving Forces and Reversed Bending Fatigue of Concrete-Filled FRP Circular Tubes for Piles and Other Applications*, Ph.D. thesis, The University of Manitoba, Winnipeg, Manitoba.

Hull, D., Legg, M. and Spencer, B. (1978). “Failure of glass/polyester filament wound pipe”, *Composites*, 9(1), 17-24.

Mirmiran, A. and Shahawy, M. (1997). "Behavior of concrete columns confined by fiber composites", *Journal of Structual Engineering*, ASCE, 123(5), 583-590.

Mohamed, H.M. and Masmoudi, R. (2010). "Axial load capacity of concrete-filled FRP tube columns: Experimental versus theoretical predictions", *Journal of Composites for Construction*, ASCE, 14(2), 231-243.

Morales, C.N., Claure, G., Álvarez, J. and Nanni, A. (2020). "Evaluation of fiber content in GFRP bars using digital image processing", *Composites Part B: Engineering*, 200, 108307.

Ozbakkaloglu, T. and Oehlers, D.J. (2008). "Concrete-filled square and rectangular FRP tubes under axial compression", *Journal of Composites for Construction*, ASCE, 12(4), 469-477.

Park, J.H., Jo, B.W., Yoon, S.J. and Park, S.K. (2011). "Experimental investigation on the structural behavior of concrete filled FRP tubes with/without steel rebar", *KSCE Journal of Civil Engineering*, 15, 337-345.

Prabhakar, M.M., Rajini, N., Ayrilmis, N., Mayandi, K., Siengchin, S., Senthilkumar, K., Karthikeyan, S. and Ismail, S.O. (2019). "An overview of burst, buckling, durability and corrosion analysis of lightweight FRP composite pipes and their applicability", *Composite Structures*, 230, 111419.

Rafiee, R. and Amini, A. (2015). "Modeling and experimental evaluation of functional failure pressures in glass fiber reinforced polyester pipes", *Computational Materials Science*, 96, 579-588.

Rosenow, M. (1984). "Wind angle effects in glass fibre-reinforced polyester filament wound pipes”, *Composites*, 15(2), 144-152.

Soden, P., Kitching, R., Tse, P., Tsavalas, Y. and Hinton, M. (1993). “Influence of winding angle on the strength and deformation of filament-wound composite tubes subjected to uniaxial and biaxial loads”, *Composites Science and Technology*, 46(4), 363-378.

Srivastava, H., Pearce, H., Mac, G. and Gupta, N. (2022). “Determination of fiber content in 3-D printed composite parts using image analysis”, *IEEE Embedded Systems Letters*, 14(3), 115-118.

Teng, J.G., Zhang, B., Zhang, S.S. and Fu, B. (2018). “Steel-free hybrid reinforcing bars for concrete structures”, *Advances in Structural Engineering*, 21(16), 2617-2622.

Teng, J.G., Zhao, J., Yu, T., Li, L.-J. and Guo, Y. (2016b). “Behavior of FRP-confined compound concrete containing recycled concrete lumps”, *Journal of Composites for Construction*, ASCE, 20(1), 04015038.

Viens, M.J. (1990). *Determination of Fiber Volume in Graphite/Epoxy Materials using Computer Image Analysis*, Report No. NAS 1.15: 100770, NASA Goddard Space Flight Center Greenbelt, MD, United States.

Waterbury, M.C. and Drzal, L.T. (1989). “Determination of fiber volume fractions by optical numeric volume fraction analysis”, *Journal of Reinforced Plastics and Composites*, 8(6), 627-636.

Xia, M., Takayanagi, H. and Kemmochi, K. (2001). “Analysis of multi-layered filament-wound composite pipes under internal pressure”, *Composite Structures*, 53(4), 483-491.

Xie, P. (2018). *Behavior of Large-Scale Hybrid FRP Concrete-Steel Double-Skin Tubular*

Columns subjected to Concentric and Eccentric Compression, Ph.D. thesis, Department of Civil and Environmental Engineering, The Hong Kong Polytechnic University, Hong Kong, China.

Xie, P., Lin, G., Teng, J. and Jiang, T. (2020). "Modelling of concrete-filled filament-wound FRP confining tubes considering nonlinear biaxial tube behavior", *Engineering Structures*, 218, 110762.

Zhang, B. (2014). *Hybrid FRP-Concrete-Steel Double-Skin Tubular Columns under Static and Cyclic Loading*, Ph.D. thesis, Department of Civil and Environmental Engineering, The Hong Kong Polytechnic University, Hong Kong, China.

Zhang, B., Yu, T. and Teng, J.G. (2015). "Behavior of concrete-filled FRP tubes under cyclic axial compression", *Journal of Composites for Construction*, ASCE, 19(3), 04014060.

Table 3.1 Carriage speed and thickness of GFRP tube

Specimen	Carriage speed (mm/s)	Average thickness of GFRP tube (mm)
H0L3	3.76	1.42
H0L5	3.76	2.20
H1L3_P	3.38	1.19
H1L3_M	3.76	1.44
H1L3_T	4.14	1.52
H3L3_P	2.63	1.44
H3L3_M	3.76	1.86
H3L3_T	4.89	1.82
H5L3_P	2.37	1.67
H5L3_M	4.18	2.00
H5L3_T	7.23	1.92
H5L5_P	2.37	2.59
H5L5_M	4.18	2.77
H5L5_T	7.23	3.52

Note: P-Peak region; M-Middle region; T-Trough region

Table 3.2 Specimens details

Samples	Wave height (mm)	No. of fibre layers	Test method
R-H0L3-1,2,3	0	3	Resin burn-off (BO) test
R-H1L3-P1,2,3	1		
R-H1L3-M1,2,3			
R-H1L3-T1,2,3			
R-H3L3-P1,2,3	3		
R-H3L3-M1,2,3			
R-H3L3-T1,2,3			
R-H5L3-P1,2,3	5		
R-H5L3-M1,2,3			
R-H5L3-T1,2,3			
D-H0L3-1,2	0	3	Digital image processing (DIP) method
D-H1L3-P1,2	1		
D-H1L3-M1,2			
D-H1L3-T1,2			
D-H3L3-P1,2	3		
D-H3L3-M1,2			
D-H3L3-T1,2			
D-H5L3-P1,2	5		
D-H5L3-M1,2			
D-H3L3-T1,2			
S-H0L3-1,2,3,4,5	0	3	Split disk test
S-H0L5-1,2,3,4,5		5	
I-H0L3-1,2,3	0	3	Internal air pressure test
I-H1L3-1,2,3	1		
I-H3L3-1,2,3	3		
I-H5L3-1,2,3	5		
I-H0L5-1,2,3	0	5	
I-H5L5-1,2,3	5		

Table 3.3 Fibre volume fraction obtained from DIP and BO tests

Sample	Fibre volume fraction (%)				Absolute difference between DIP and BO (%)	SD for different wave heights	
	DIP		BO			DIP	BO
	Average	SD	Average	SD			
H0L3	44.48	4.95	42.23	1.5	2.26	/	/
H5L3-P	40.94	4.3	36.73	1.6	4.21		
H5L3-M	30.4	2.52	28.29	1.37	2.12	4.33	3.66
H5L3-T	36.71	3.32	35.12	2.16	1.58		
H3L3-P	36.34	1.78	38.28	1.55	1.94		
H3L3-M	34.01	4.77	35.06	3.05	1.05	2.95	1.44
H3L3-T	41.10	3.15	37.94	2.86	3.15		
H1L3-P	36.43	2.80	38.03	0.90	1.6		
H1L3-M	39.24	1.76	37.69	1.31	1.55	1.60	0.51
H1L3-T	35.47	1.23	36.81	4.68	1.33		

Table 3.4 Split disk test results

Specimen ID	Elastic modulus (GPa)	Average	SD
S-H0L3-1	49.4		
S-H0L3-2	49.7		
S-H0L3-3	36.7	42.6	5.7
S-H0L3-4	39.3		
S-H0L3-5	38.1		
S-H0L5-1	46.9		
S-H0L5-2	49.8		
S-H0L5-3	42.7	43.9	4.2
S-H0L5-4	37.3		
S-H0L5-5	42.7		

Table 3.5 Internal air pressure test results

Specimen ID	E_p (GPa)	E_m (GPa)	E_t (GPa)	E (GPa)
I-H0L3-1	/	/	/	38.4
I-H0L3-2	/	/	/	40.9
I-H0L3-3	/	/	/	36.0
Average	/	/	/	38.4
SD	/	/	/	2.0
I-H0L5-1	/	/	/	35.7
I-H0L5-2	/	/	/	34.8
I-H0L5-3	/	/	/	37.9
Average	/	/	/	36.1
SD	/	/	/	1.3
I-H1L3-1	47.9	40.3	37.6	/
I-H1L3-2	46.1	34.8	50.2	/
I-H1L3-3	55.2	46.3	40.7	/
Average	49.7	40.5	42.8	/
SD	3.9	4.7	5.4	/
I-H3L3-1	52.3	32.2	36.5	/
I-H3L3-2	54.9	32.7	34.1	/
I-H3L3-3	43.5	42.4	33.2	/
Average	50.2	35.8	34.6	/
SD	4.9	4.7	1.4	/
I-H5L3-1	44.4	23.7	32.5	/
I-H5L3-2	37.6	23.8	28	/
I-H5L3-3	35.4	28.8	30.4	/
Average	39.1	25.4	30.3	/
SD	3.8	2.4	1.8	/
I-H5L5-1	42.9	28.2	32.1	/
I-H5L5-2	38.2	26.5	31.6	/
I-H5L5-3	41	23.3	28.5	/
Average	40.7	26.0	30.7	/
SD	1.4	1.6	1.6	/

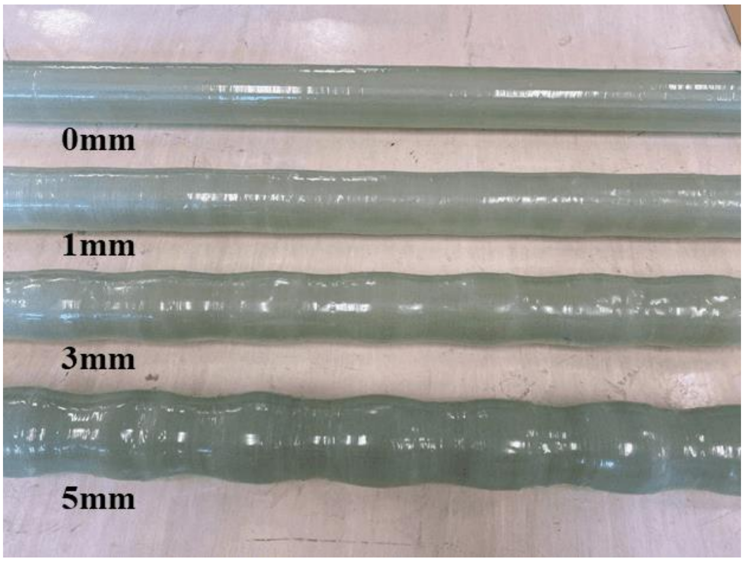

Figure 3.1 Filament-wound GFRP tubes with a uniform or wavy shape

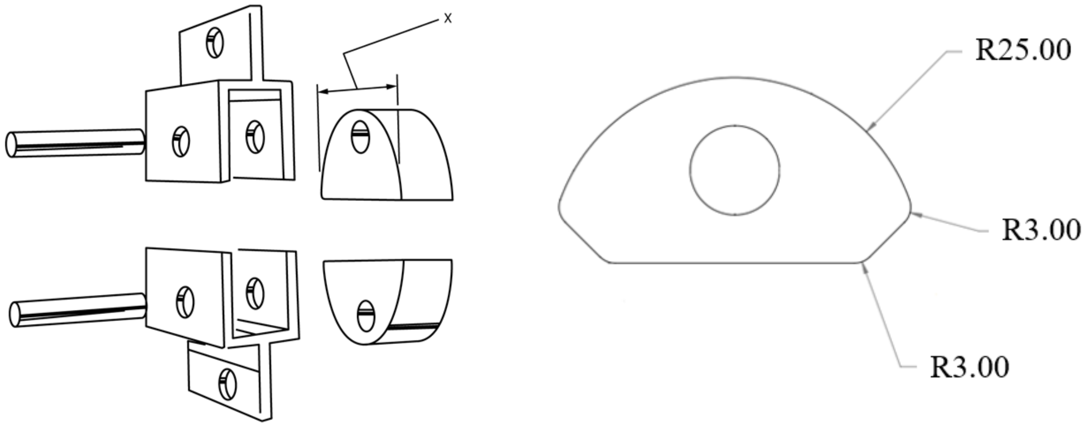

(a) Typical test fixture [extracted from ASTM D2290-19a (2019)]

(b) Improved split disk

Figure 3.2 Split disk test

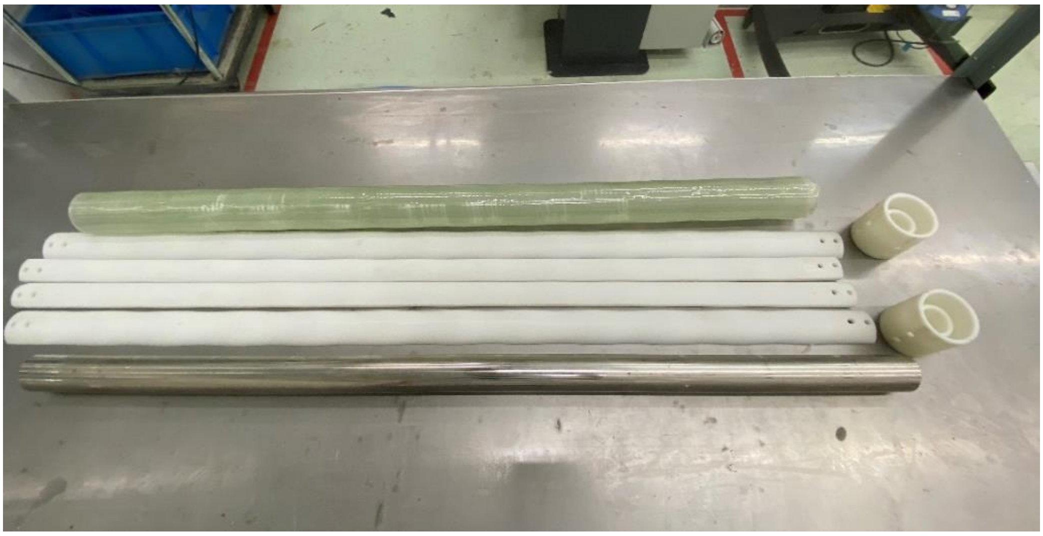

Figure 3.3 3D printed internal mould for filament winding

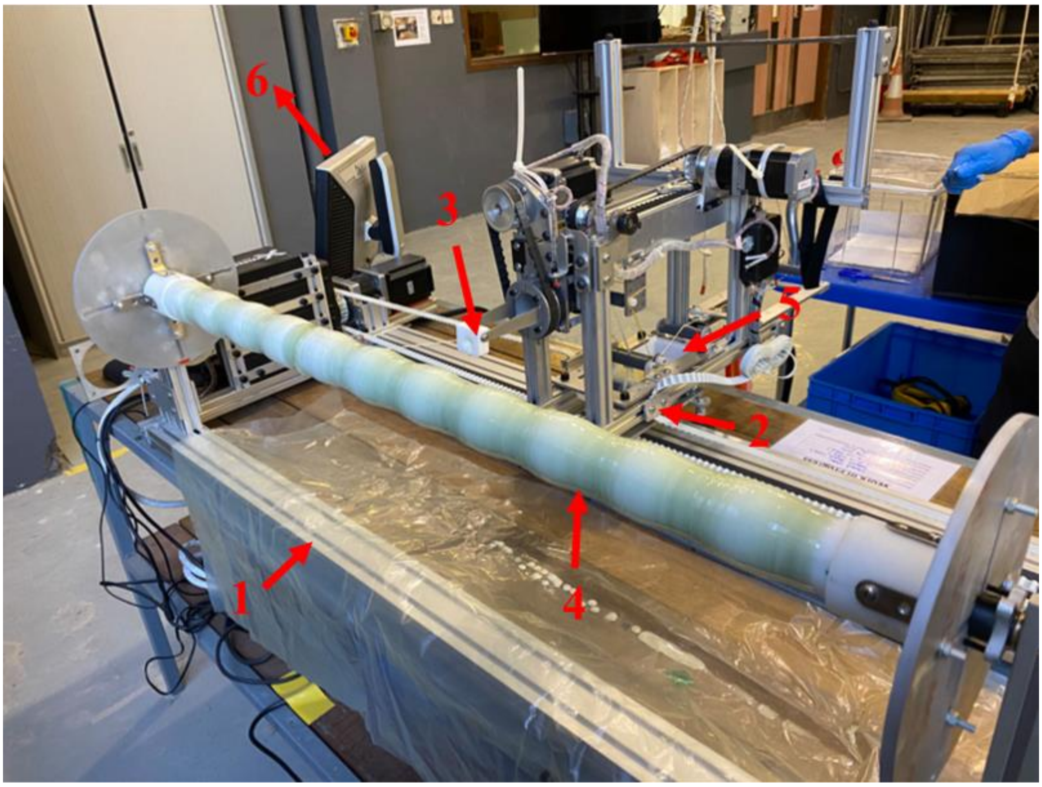

Figure 3.4 X-winder winding machine 4X-23: (1) aluminium frame; (2) carriage: (3) payout eye; (4) mandrel; (5) resin bath; (6) computer controller

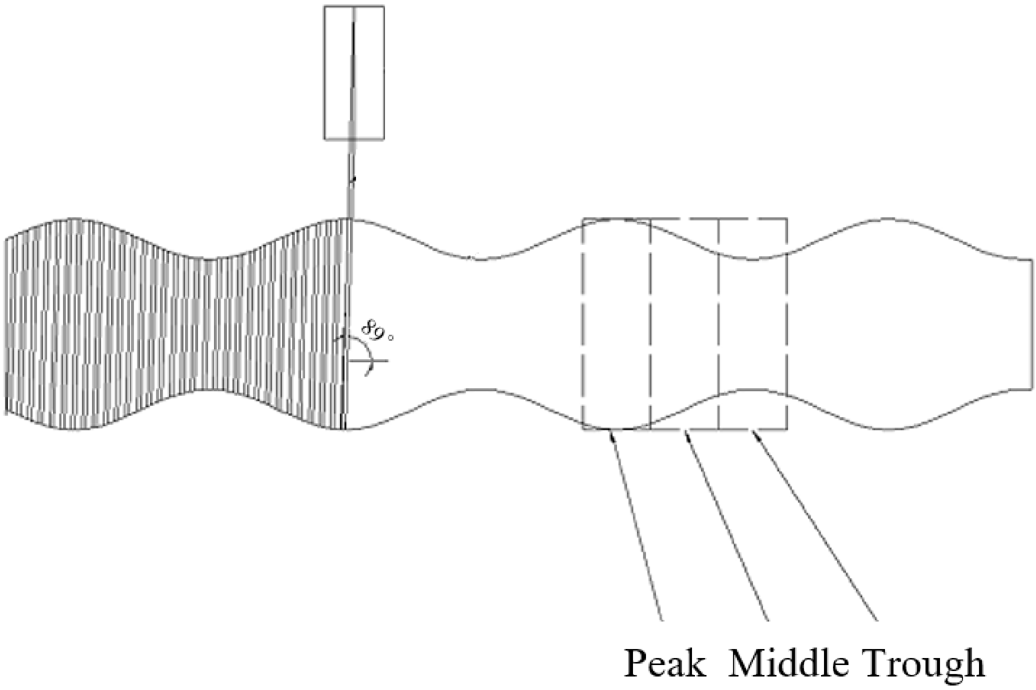

Figure 3.5 Different regions on a wavy-shaped tube.

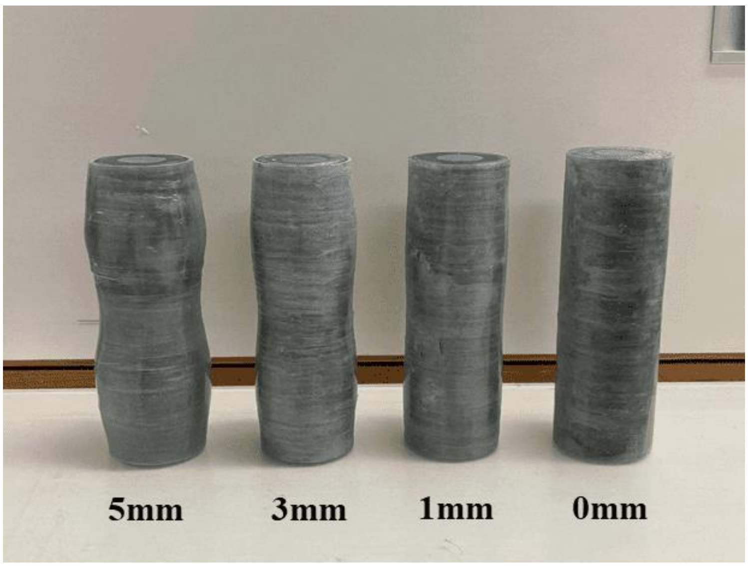

Figure 3.6 Wavy-shaped hybrid rebars and a uniform hybrid rebar

(a) Electric Muffle Furnace

(b) samples before burning

Figure 3.7 Burn-off test

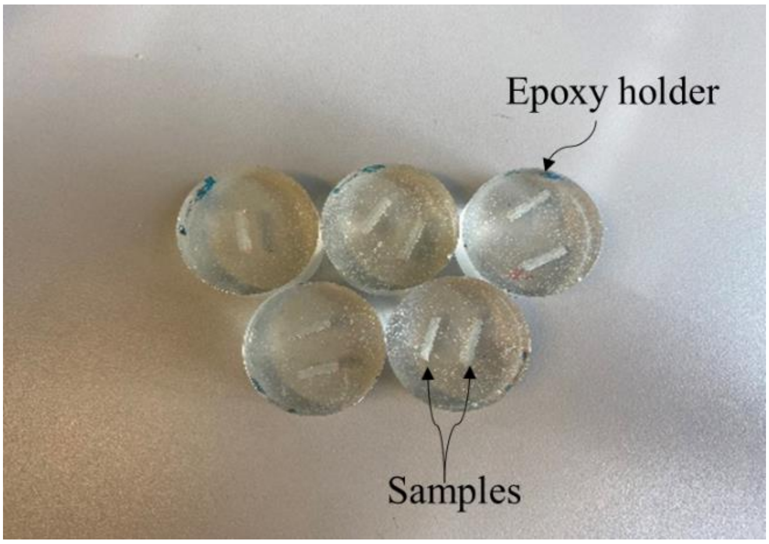

(a) FRP samples encased in epoxy resin pucks

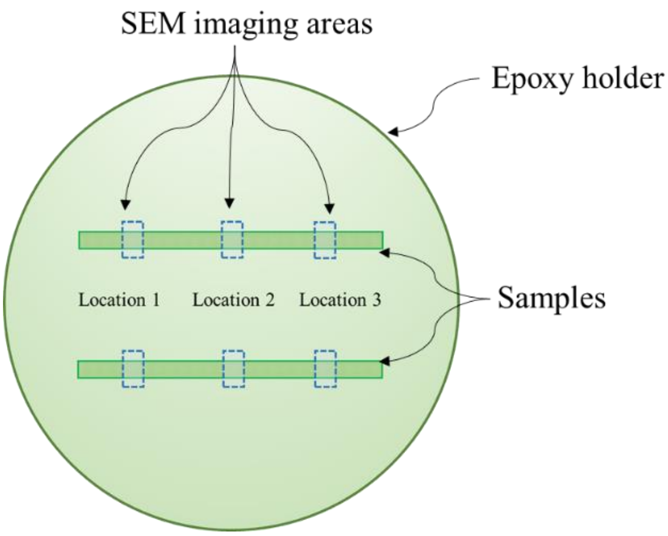

(b) Imaging areas

Figure 3.8 Encased specimens and imaging areas of the DIP method

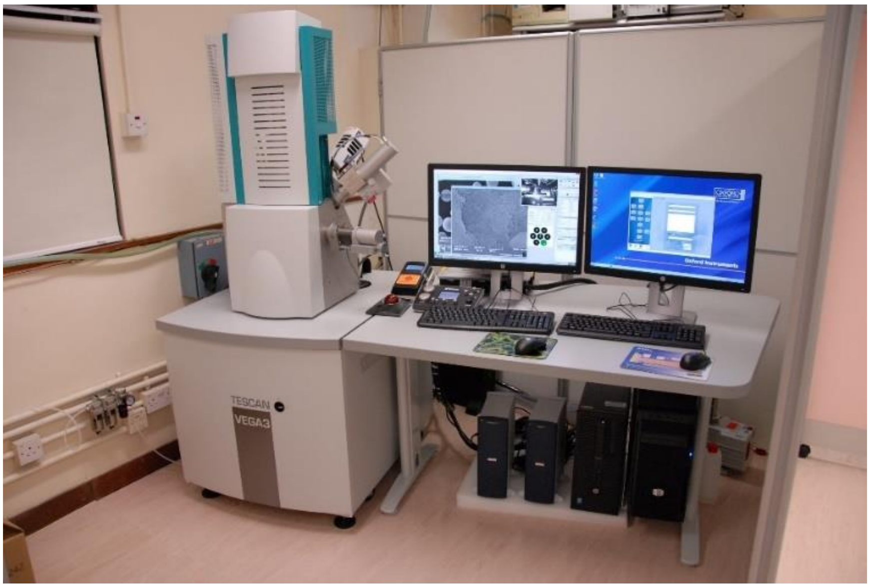

Figure 3.9 SEM machine of the DIP method (extracted from https://www.polyu.edu.hk/umf/facility/materials-research-centre/sem-tescan-vega3/)

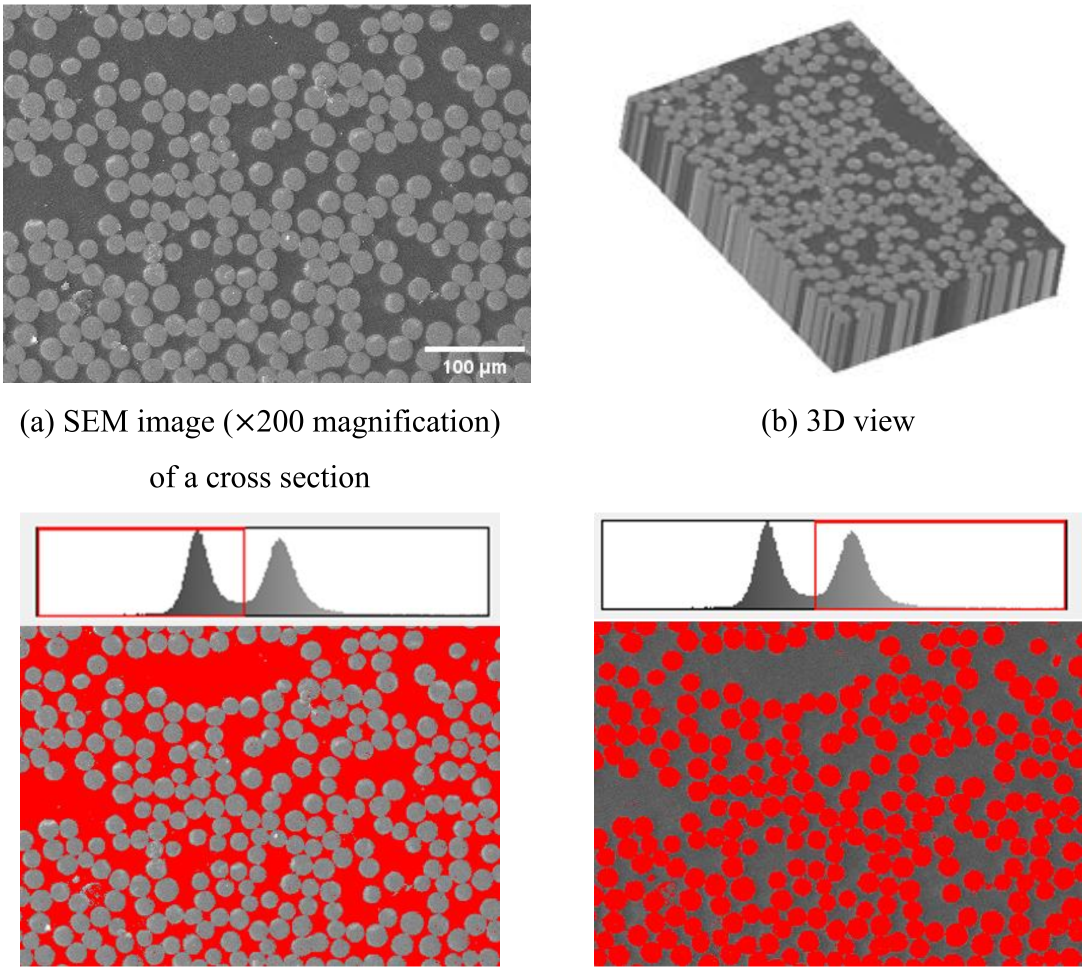

(a) SEM image (×200 magnification) of a cross section

(b) 3D view

(c) Resin matrix, i.e., low range threshold

(d) Glass fibres, i.e., high range threshold

Figure 3.10 Typical results from the DIP method

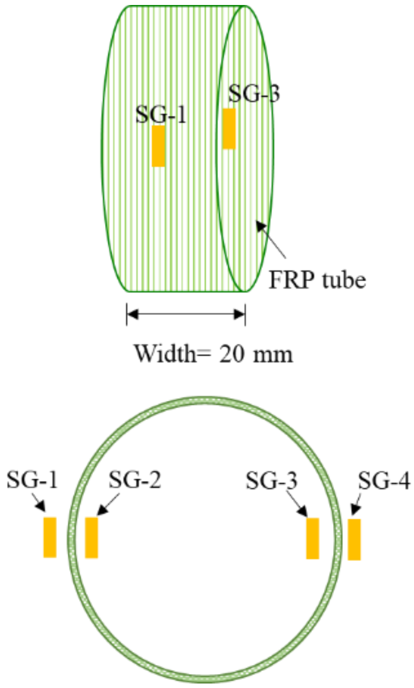

(a) Layout of strain gauges

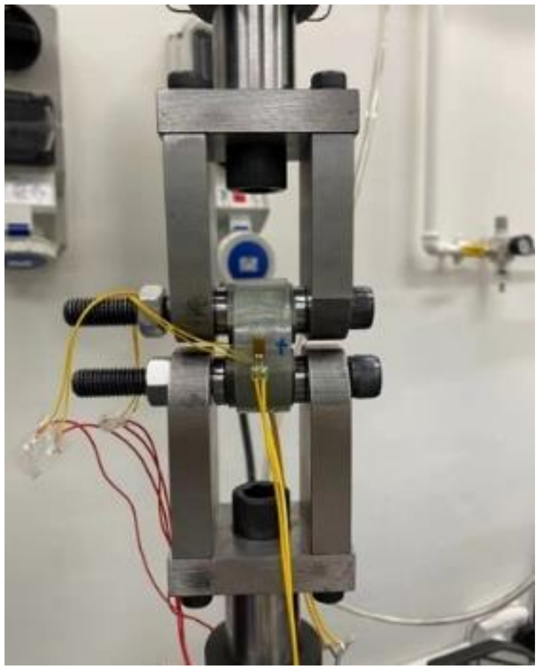

(b) Test set-up

Figure 3.11 Split disk tests

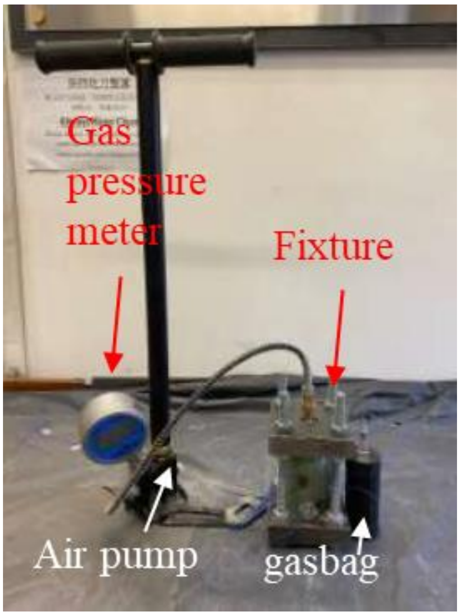

(a) Test set-up

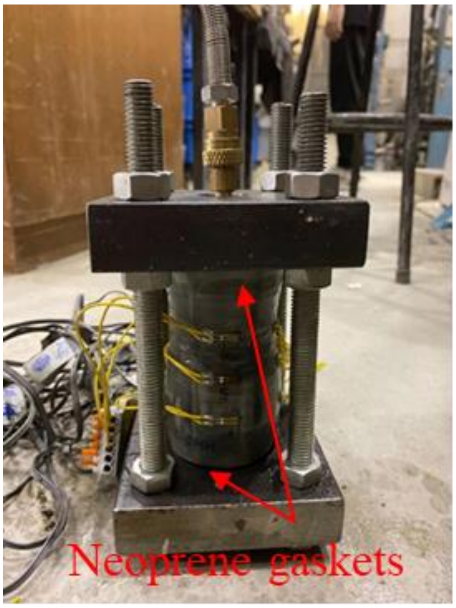

(b) Specimen fixure

(c) GFRP tubes

Figure 3.12 Interal air pressure test

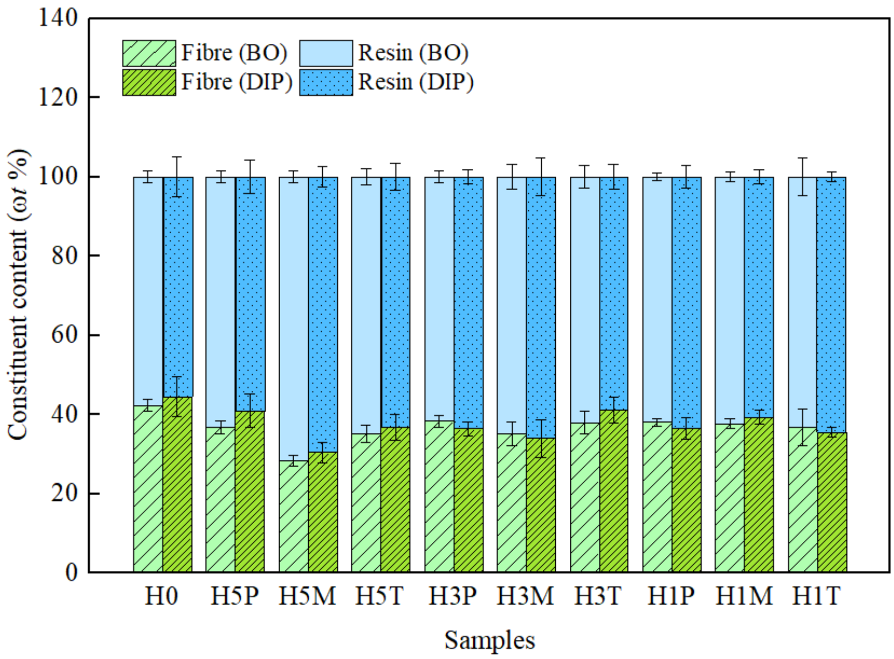

Figure 3.13 GFRP tube fibre and resin volume fractions, in percentage

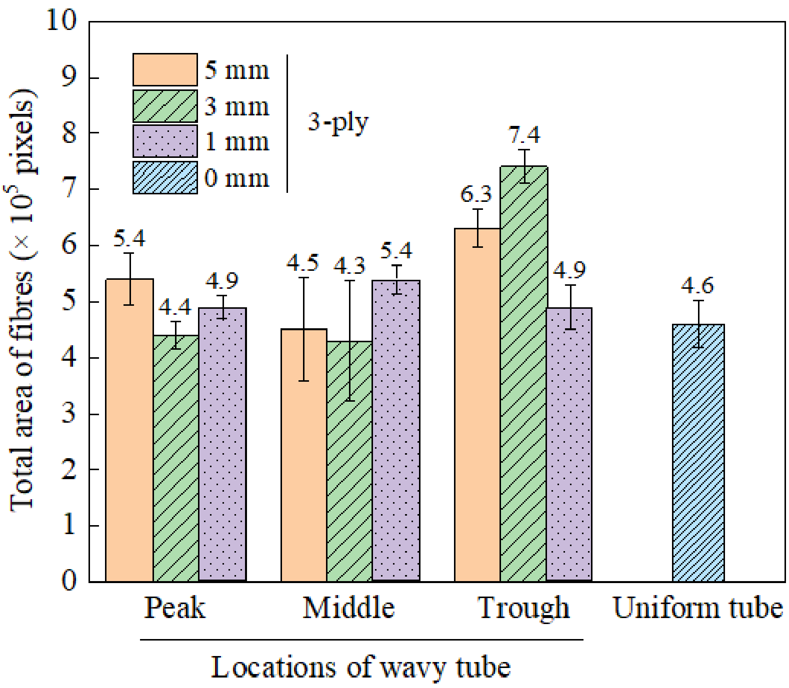

Figure 3.14 Total cross-section area of fibres (×10^5 pixels)

Figure 3.15 Failure modes of specimens in the split disk tests

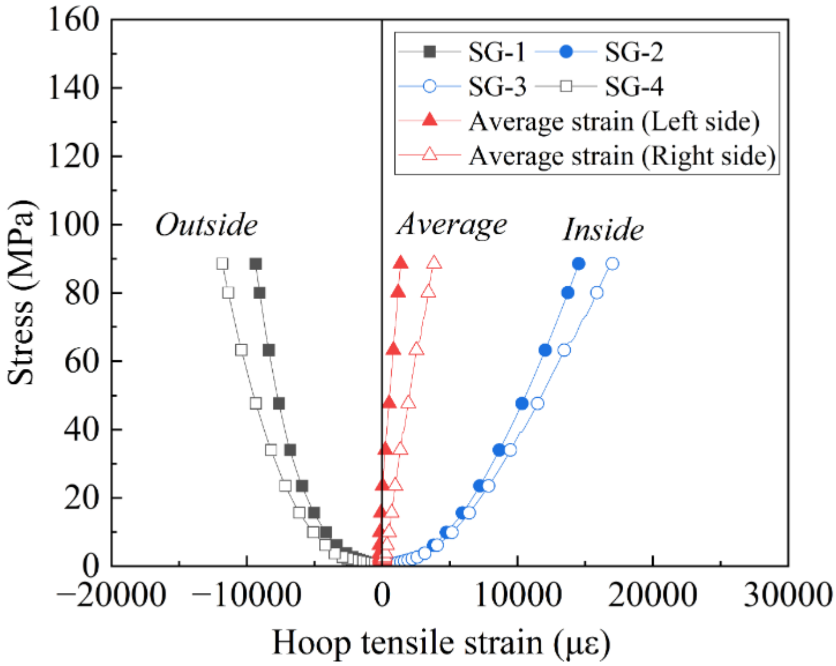

Figure 3.16 Typical stress-strain curves (from split disk tests, specimen S-H0L3-3)

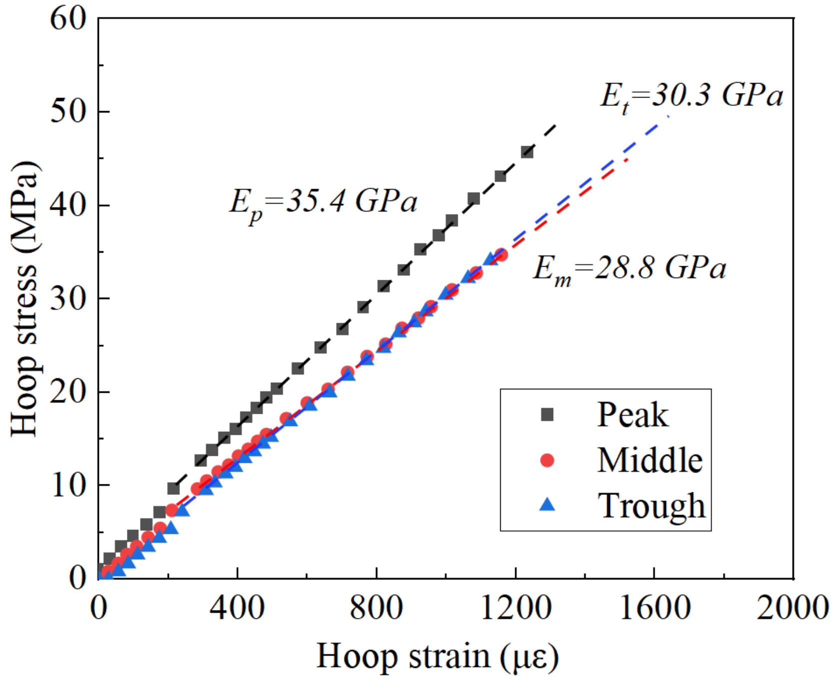

Figure 3.17 Typical stress-strain curves (from internal air pressure tests, specimen I-H5L3-3)

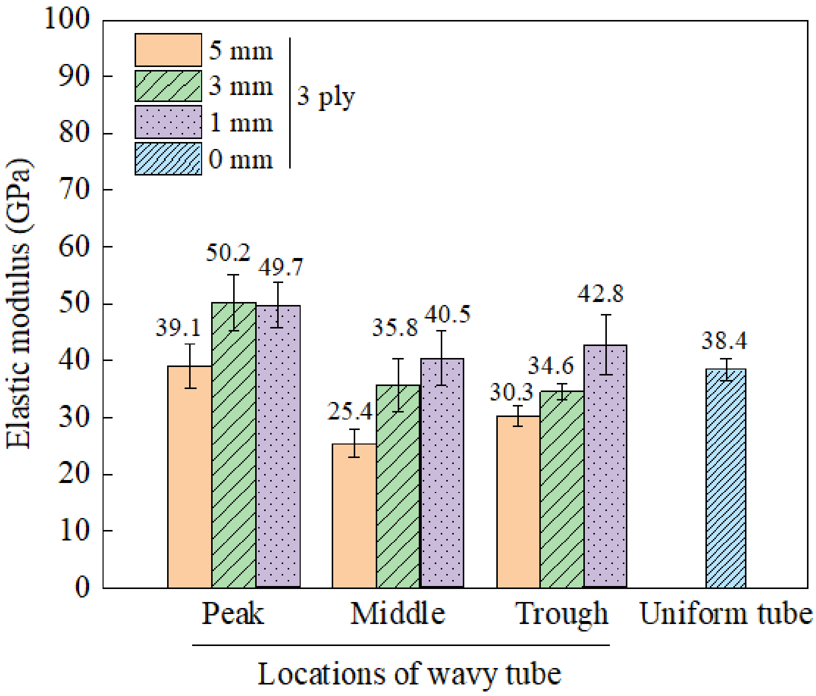

(a) 3-ply tubes

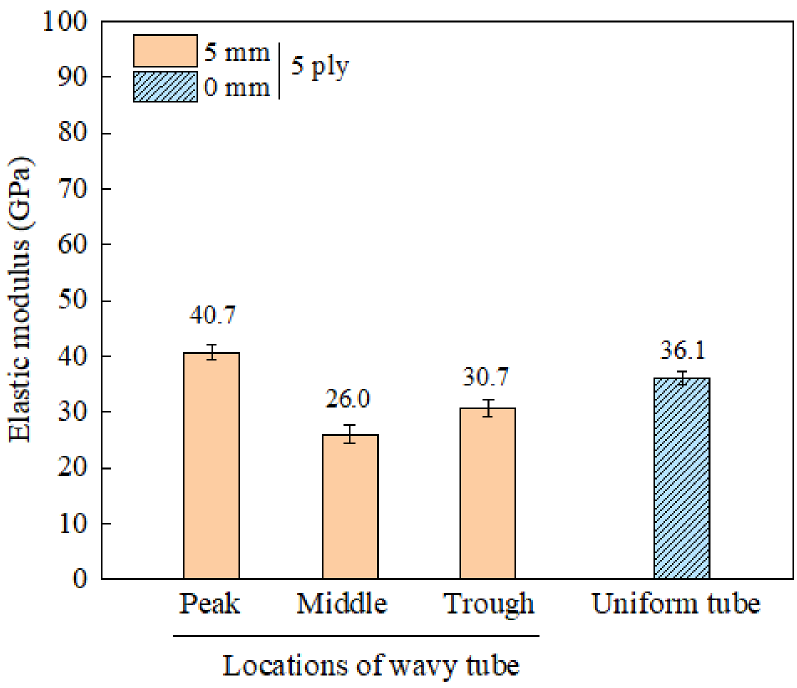

(b) 5-ply tubes

Figure 3.18 Elastic modulus of GFRP tubes

CHAPTER 4
COMPRESSIVE BEHAVIOUR OF FRP-CONFINED UHPC AND UHPFRC

4.1 INTRODUCTION

In a hybrid rebar, the ultra-high performance concrete (UHPC) annulus is confined by the FRP tube and is normally the primary bearer of the compressive load of the hybrid system. Hence, the compressive behaviour of FRP-confined UHPC plays a vital role in understanding the mechanical behaviour of hybrid rebars. However, as indicated by the review presented in Chapter 2, limited research has been conducted on FRP-confined UHPC and FRP-confined ultra-high performance fibre reinforced concrete (UHPFRC), especially for UHPC with a compressive strength exceeding 150 MPa. As a result, the present Ph.D. research programme first aimed at understanding the compressive behaviour of FRP-confined UHPC/UHPFRC through a systematic experimental study and theoretical analysis. In this chapter, instead of wavy-shaped FRP tubes, confinement was provided by FRP jackets formed from fibre sheets using the wet lay-up method. Compared to a wavy-shaped FRP tube, the elastic modulus of an FRP jacket can be more easily determined through tensile coupon tests. Furthermore, the elastic modulus of such an FRP jacket is highly uniform along the tube length while that of a wavy-shaped tube can vary much more significantly. This uniformity of hoop elastic modulus along the tube length means that the confinement mechanism in FRP-confined UHPC/UHPFRC can be better investigated using specimens confined with FRP jackets. Two types of FRP [i.e., glass FRP (GFRP) and carbon FRP (CFRP)] were used to achieve varying levels of confinement to the UHPC. The other investigated parameters for FRP-confined UHPC/UHPFRC included the thickness of

FRP jacket, the compressive strength of UHPC column, the specimen size, and the volume fraction of steel fibres. The failure mode, axial stress-axial strain behaviour, axial strain-lateral strain behaviour, FRP confinement efficiency, and the FRP hoop rupture strain were investigated in detail. Finally, the performance of an existing design-oriented stress-strain model originally developed for FRP-confined NSC/UHPC/UHPFRC was evaluated using the test data.

It should be noted that the experiments constituting Batch 1 in this chapter were carried out during my research assistantship period, under the supervision of Professor Teng, from September 2018 to August 2019, prior to the commencement of my Ph.D. studies. However, all the remaining work presented in this chapter, including the subsequent experiments, analyses, and discussions, was undertaken during my Ph.D. study period.

4.2 EXPERIMENTAL PROGRAMME

4.2.1 Test Specimens

A total of 68 UHPC or UHPFRC cylinders, including 22 plain UHPC/UHPFRC specimens and 46 FRP-confined UHPC/UHPFRC specimens, were fabricated and tested under concentric axial compression. The details of the test specimens are given in Table 4.1. The specimens were divided into three groups in terms of casting batches. For Batch 1 and Batch 3, all specimens were cast with UHPC, while Batch 2 included some UHPFRC specimens. The primary distinction between Batch 1 and Batch 3 lies in the compressive strength of UHPC. Batch 1 UHPC had a compressive strength of approximately 190 MPa, whereas Batch 3 UHPC possessed a compressive strength of around 150 MPa. Batch 3 UHPC served as a reference group for investigating the effect of UHPC compressive strengths on the compressive behaviour of FRP-confined UHPC. In Batch 2, three steel fibre volume fractions (i.e., 0%, 1% and 2%), denoted by "V0", "V1", and "V2", were examined. The specimens were confined with different layers of FRP, covering an FRP confinement stiffness ratio (ρ_K) ranging from 0 to 0.225, which is calculated in the following equation:

$$\rho_K = \frac{2E_{frp}t_f}{(f'_{co}/\varepsilon_{co})D} \tag{4.1}$$

where E_{frp}= elastic modulus of FRP jacket/tube in the hoop direction; t_f = thickness of FRP jacket/tube; f'_{co} = unconfined UHPC/UHPFRC compressive strength; ε_{co} = axial strain at peak axial stress of unconfined UHPC/UHPFRC; D = diameter of confined UHPC/UHPFRC cylinder.

Two types of FRP, namely CFRP and GFRP, with fibres oriented only in the hoop direction, were used to confine the UHPC/UHPFRC cylinders. The specimens in Batch 2 were further divided into three groups of different sizes, among which 12 specimens had a diameter of 50 mm and a height of 100 mm, 18 specimens had a diameter of 75 mm and a height of 150 mm, and the remaining specimens had a diameter of 100 mm and a height of 200 mm. For each specimen configuration, two nominally identical specimens were prepared and tested.

Each specimen was given a name which starts with "Sn" to distinguish the casting batch, "V0", "V1" or "V2" denoting the volume ratio of steel fibres (0%, 1%, and 2%) for specimens of Batch 2 only, followed by "D50", "D75" or "D100" representing the diameter (50 mm, 75 mm, and 100 mm) of cylinders. The name is then followed by "U" representing plain UHPC/UHPFRC specimens without FRP confinement, "C" or "G" representing the type of FRP for the FRP-confined UHPC/UHPFRC specimens, and a digital number representing the number of FRP layers. As the FRP jackets were formed by directly wrapping fibre sheets onto concrete columns using the wet lay-up method, it was challenging to accurately control and measure the thickness of an FRP jacket after fabrication. Furthermore, the confining effect was primarily attributed to the fibres, so the number of fibre or FRP layers is considered a more reliable and representative parameter in this thesis. The name ends with "1" or "2" to differentiate the two nominally identical specimens.

4.3 MATERIAL PROPERTIES

4.3.1 UHPC and UHPFRC

The mix proportions of the UHPC and UHPFRC are summarised in Table 4.2. The raw materials of the UHPC included tap water, white cement, silica fume (SF), quartz powder (QP), river sand, and superplasticizer (SP) (Teng et al., 2019). Two types of superplasticizers (SPs) with different solid contents, specifically 22% and 44%, were used. For S2 and S3 batches, the higher solid content means that the amount of SP used should be halved, and the quantities of other components in the mix proportions should be adjusted accordingly. The SP used in the S1 Batch was discontinued, and subsequently the other type of SP was used for S2 and S3 specimens. Straight copper-plated steel fibres with a length of 13 mm and a diameter of around 0.2 mm were added for UHPFRC. The tensile strength and elastic modulus of the steel fibres were 3000 MPa and 210 GPa, respectively. The compressive properties of UHPC/UHPFRC were obtained by compressing two unconfined cylinders for each mix design and sample size. The ends of the unconfined specimens were grounded in advance to ensure the flatness of the loading surfaces. Three 50-mm axial strain gauges were installed at 120° apart at the mid-height section to measure the axial strains. The average cylindrical compressive strengths (f'_{co}), the average axial strains at peak stress and the average elastic moduli (E_c) are listed in Table 4.3. The elastic moduli were calculated following ASTM C469 (2014).

4.3.2 FRP Jackets

To obtain the tensile properties of the CFRP or GFRP jacket, three one-layer CFRP or GFRP coupons were fabricated with unidirectional fibre sheets and tested under tension according to ASTM D3039 (2017). The tensile strength, tensile modulus, and tensile rupture strain of the CFRP jacket were obtained to be 3456 MPa, 240.8 GPa, and 1.67%, respectively. The corresponding values for the GFRP jacket were 1486 MPa, 87 GPa, and 1.76%, respectively. The tensile strengths and tensile moduli were obtained based on a nominal fibre thickness of 0.167 mm per layer for the CFRP jacket and 0.169 mm per layer for the GFRP jacket according to the manufacturer. The tensile moduli of the CFRP and GFRP jackets were obtained from the secant moduli corresponding to an FRP tensile strain of 1.16% and 1.14% (the average FRP hoop rupture strains measured in the compression tests of FRP-confined UHPC specimens), respectively, on the tensile stress-strain curves.

4.4 SPECIMEN PREPARATION

The mixing procedure of the UHPC/UHPFRC included the following steps: (1) mixing the white cement, SF, QP, and river sand for 5 minutes; (2) adding SP and water; (3) mixing for another 8 minutes; (4) for UHFRC, adding steel fibres to the mixture and continuing mixing for 3 minutes. The UHPC/UHPFRC specimens were cured in a thermostatic water tank at 22°C ± 3°C for at least 28 days. After curing, a single continuous fibre sheet impregnated with epoxy resin was wrapped around UHPC/UHPFRC cylinder using the wet lay-up method. An overlapping zone of 50 mm, 75 mm, and 100 mm between the finishing end and the starting end of the sheet was adopted for D50, D75, and D100 FRP-confined UHPC/UHPFRC specimens respectively. Each end of the FRP-confined specimen was strengthened with an additional CFRP or GFRP strip of three layers with a width of 10 mm, 15 mm, and 20 mm for D50, D75, and D100 specimens respectively to prevent unexpected failure at the two ends. Before the compression tests, the two ends of each FRP-confined UHPC specimen were capped with ultra-high strength paste (UHSP) (Xiang et al., 2021) to ensure the flatness of the two loading surfaces.

4.5 EXPERIMENTAL SET-UP AND INSTRUMENTATION

For each FRP-confined specimen, two mid-height LVDTs (LVDT-M1 and LVDT-M2) covering a mid-height length of 50/75/100 mm (i.e., half of the total height) were installed to measure the axial shortenings of the mid-height region; another two full-height LVDTs (LVDT-F1 and LVDT-F2) were installed between the top and bottom loading plates to measure the full-length shortenings of the specimen [Figure 4.1(a)]. Eight axial strain gauges and eight hoop strain gauges both with a gauge length of 5 mm were installed at 45° apart at the mid-height section for D75 and D100 specimens [Figure 4.1(b)]. Among the eight hoop strain gauges, three were installed in the overlapping zone with a length of 120 mm while the remaining five were installed outside the overlapping zone [Figure 4.1(b)].

For D50 specimens, four axial strain gauges and four hoop strain gauges, each with a gauge length of 5 mm, were installed 90° apart at the mid-height section. One gauge was installed in the overlapping zone, while the remaining three were positioned outside this zone. The compression tests were conducted using an MTS testing machine. Displacement control with a loading rate of 0.3 mm/min was adopted. Within this chapter, compressive stresses and strains of concrete as well as tensile stresses and strains of FRP jackets are designated as positive.

4.6 EXPERIMENTAL RESULTS

4.6.1 General Behaviour

Figure 4.2 illustrates the typical failure modes of tested specimens. The unconfined UHPC specimen (i.e., S2V0-D75-U-1) failed in a brittle manner with an explosive sound shortly after the peak stress [Figure 4.2(a)]. A cone-shape portion of the specimen was retained after the test, which aligns with the findings reported by other researchers (e.g., Liao et al. 2021, Naeimi and Moustafa, 2021). As shown in Figure 4.2(a), the unconfined UHPFRC specimens (i.e., S2V1 and S2V2) maintain an integrity after failure, with a major inclined crack through the full height of the specimen. Pulled-out steel fibres could be observed within the major cracks. For FRP-confined UHPC/UHPFRC specimens, a loud sound was heard when the unconfined UHPC/UHPFRC strength was reached, indicating the cracking of the inner UHPC/UHPFRC. For the specimens with a weak FRP confinement (i.e., S1-D75-G1-1, S1-D75-G2-1, and S1-D75-G3-1), after the cracking sound, the axial load dropped dramatically until an explosive sound of FRP hoop rupture; however, for the specimens with a relatively strong FRP confinement (i.e., S2V0-D100-C8-1, S2V1-D100-

C8-1, and S2V2-D100-C8-1), the axial load started to increase again after an abrupt load drop with the cracking sound, until an explosive sound of FRP hoop rupture, indicating the final failure of the specimen. All the FRP-confined UHPC/UHPFRC specimens failed by FRP hoop rupture near the specimen mid-height [Figures 4.2(b) and (c)].

4.6.2 Axial Stress-Strain Curves

The axial strains of the specimens can be obtained from the readings of either the mid-height LVDTs or the full-height LVDTs. However, it was found that the readings of the mid-height LDVTs were affected by the cracking of UHPC/UHPFRC inside the FRP jacket when the unconfined UHPC/UHPFRC strength was approximately reached. As a result, the readings of the full-height LVDTs were used to obtain the axial strains of the test specimens. The lateral strains (defined to be negative and equal to the hoop strains in magnitude) were averaged from the readings of the hoop strain gauges outside the overlapping zone at the specimen mid-height section.

Figure 4.3 shows the axial stress-axial strain curves of all the test FRP-confined UHPC/UHPFRC specimens. It should be noted that specimen S1-D75-G3-2 failed prematurely due to a possible local damage of the FRP jacket, and thus the axial stress-strain curves are much shorter than those of the nominally identical specimen. It is seen that, for the specimens with a relatively small FRP confinement level, the axial stress-strain curves feature an ascending first branch followed by a descending branch (i.e., a softening behaviour) with axial stress fluctuations (i.e., specimens S1-D75-G*n*, S1-D75-C1, 2, and S2V0-D75-C1, 2) [Figures 4.3(a) to (c)]. For the specimens with a relatively large FRP confinement level, the axial stress-strain curves feature an ascending first branch, followed by an axial stress drop and then a second ascending branch (i.e., a hardening behaviour) (i.e., specimens S1-D75-C2 to C7, S2V0-D75-C3 to C9, S2V*n*-D50, S2V*n*-D75, S2V*n*-D100, and S3-D50) [Figures 4.3(b) to (g)]. Specimens S1-D75-C2, S1-D75-C3, and S2V0-D75-C3 possessed some axial stress fluctuations in the second ascending branch and the scatters between the two nominally identical specimens are relatively large. However, as the FRP confinement level increases, the ascending third branch becomes very smooth and the scatters between the two nominally identical specimens become very small. For all the specimens, the first ascending branch features an almost linear curve due to the ultra-high strength of UHPC/UHPFRC.

The sudden axial stress drop after the first ascending branch of the axial stress-strain curve of FRP-confined UHPC/UHPFRC has also been reported by other researchers (e.g., Wang et al., 2018, Tian et al., 2019, Liao et al., 2021, Wang et al., 2022). This sudden axial stress drop is believed to be caused by the shrinkage of UHPC/UHPFRC which creates a micro gap between the UHPC/UHPFRC and the FRP jacket. When the specimen is under axial compression, micro cracks and damage occurred in the UHPC/UHPFRC when the unconfined concrete strength is reached at which the FRP confinement is not fully activated, leading to an axial stress drop. The axial stress drop results in a large expansion of UHPC/UHPFRC which induces large FRP confinement, leading to an ascending third branch for the specimens with a sufficiently large FRP confinement. It was also observed that the peak stresses of the FRP-confined UHPC/UHPFRC specimens with a softening behaviour and the first peak stresses at the axial stress drop of the specimens with a hardening behaviour are generally larger than the unconfined concrete strength. Similar observations have been reported by other researchers on UHPC/UHPFRC (e.g., Oliveira et al., 2019, Zeng et al., 2020). The larger peak stress than the unconfined concrete strength may be caused by the interaction between UHPC/UHPFRC and FRP jacket through the bonding of epoxy resin. However, further research with more test data is needed to clarify this issue in the future.

Figure 4.4 presents typical axial stress-strain curves of FRP-confined UHPC/UHPFRC with sufficient or insufficient FRP confinement. For sufficient FRP confinement, the stress-strain curve generally consists of an ascending first branch, an axial stress drop **branch** and an ascending second branch. The key test results of the FRP-confined UHPC/UHPFRC specimens, including average cylindrical compressive strengths (f'_{co}), the average axial strains at peak stress of unconfined concrete (ε_{co}), the compressive strengths (i.e., peak stresses) (f'_{cc}), the axial strains at peak stress (ε_{cc}), the ultimate axial stresses (f'_{cu}) and ultimate axial strains (ε_{cu}) at FRP rupture, the first peak axial stresses before stress reduction (f'_{c1}), the axial strains at the first peak stress (ε_{c1}), the axial stresses after stress reduction (f'_{c2}) and its corresponding axial strains (ε_{c2}), the FRP hoop rupture strain ($\varepsilon_{h,rup}$), and the FRP confinement stiffness ratios (ρ_K) are summarised in Table 4.4. The FRP hoop rupture strains ($\varepsilon_{h,rup}$) were averaged from the readings of the hoop strain gauges outside the overlapping zone when FRP rupture occurred.

4.6.3 FRP Confinement Efficiency

In Figure 4.5, the normalised ultimate compressive stresses (f'_{cu}/f'_{co}) are plotted against the FRP confinement stiffness ratios (ρ_k) for the FRP-confined UHPC/UHPFRC specimens tested in the present study as well as those tested by Zohrevand and Mirmiran (2011), Liao et al. (2021), Lam et al. (2021), Wang et al. (2023), and de Oliveira et al. (2019). The specimens with an unconfined concrete strength larger than 150 MPa (f'_{co} >150 MPa) and those with an unconfined concrete strength larger than 120 MPa and smaller than 150 MPa (120 MPa < f'_{co}<150 MPa) are respectively drawn in Figures 4.5(a) to (d). A ratio of f'_{cu}/f'_{co} larger than 1.0 generally indicates that the UHPC/UHPFRC is sufficiently confined with a hardening behaviour while a ratio smaller than 1.0 indicates insufficiently confined UHPC/UHPFRC. Figure 4.5(a) shows that a minimum value of ρ_k ≈ 0.036 should be used if an ultimate axial stress larger than the unconfined strength (i.e., a threshold value of ρ_k for a hardening behaviour) is anticipated for FRP-confined UHPC. This threshold value of ρ_k is much larger than the value of 0.01 for FRP-confined NSC, suggesting a reduced confinement efficiency in FRP-confined UHPC (Teng et al. 2009).The estimated threshold value of ρ_k is 0.015 for FRP-confined UHPFRC as indicated by the trend line of f'_{cu}/f'_{co} versus ρ_k in Figure 4.5(b), implying that steel fibres may be beneficial to the FRP confinement efficiency. Figure 4.5(c) shows that the estimated threshold value of ρ_k for the FRP-confined UHPC specimens with 120 MPa <f'_{co} <150 MPa is 0.022. For the FRP-confined UHPFRC specimens with 120 MPa <f'_{co} <150 MPa, the intercept for the trendline is larger than 1, indicating that the threshold value of ρ_k for FRP-confined UHPFRC could not be estimated by the trend line due to the limit of the database. The different observations in Figures 4.5(a-d) indicated that the FRP confinement efficiency of FRP-confined UHPC/UHPFRC is affected by both the concrete compressive strength and the steel fibre volume fraction. Further research is needed for a more accurate threshold value of ρ_k when more test data of FRP-confined UHPC/UHPFRC are available in the future.

4.6.4 FRP Hoop Rupture Strains

Figure 4.6 presents the variation of FRP hoop strain efficiency factor ($k_{\varepsilon} = \varepsilon_{h,rup}/\varepsilon_f$) with FRP jacket thickness for the test FRP-confined UHPC specimens, where the FRP hoop strain efficiency factor is defined as the ratio of the FRP hoop rupture strain from compression tests ($\varepsilon_{h,rup}$) and the ultimate tensile strain obtained from coupon tests (ε_f). Due to the unsatisfactory test results of FRP hoop rupture strains from the S2 and S3 batch specimens, this analysis will focus solely on comparing the test results of the S1 batch specimens. The hoop strain efficiency factor of specimen S1-D75-G3-2 was excluded due to the premature failure of this specimen. Figure 4.6 shows that the FRP hoop strain efficiency factors of the CFRP-confined UHPC specimens range from 0.547 to 0.894, with an average value of 0.686, and those of the GFRP-confined UHPC specimens range from 0.533 to 0.878, with an average value of 0.612. The former value (0.686) is larger than the value of 0.586 reported in Lam and Teng (2003) for CFRP-confined NSC, while the latter value (0.612) is close to the value of 0.624 for GFRP-confined NSC reported in Lam and Teng (2003). Liao et al. (2021) found that the average FRP hoop strain efficiency factors for CFRP-confined UHPC and UHPFRC specimens with a diameter of 50 mm and 100 mm were 0.77 and 0.65, respectively, also larger than the value of 0.586 reported in Lam and Teng (2003) for CFRP-confined NSC. However, more test data of FRP-confined UHPC are needed before any solid conclusions can be made. Besides, Figure 4.6 shows that the FRP jacket thickness does not seem to have an obvious effect on the FRP strain efficiency factor for either CFRP or GFRP-confined UHPC specimens. Liao et al. (2021) also found that the FRP strain efficiency factors for CFRP-confined UHPC/UHPFRC specimens maintained a high degree of independence from the FRP confinement level.

4.6.5 Effects of Different Parameters

4.6.5.1 Effect of FRP jacket thickness

All the CFRP-confined UHPC specimens with a diameter of 75 mm were selected for comparison for examining the effect of FRP jacket thickness on the compressive behaviour of FRP-confined UHPC. The axial stress-strain curves of these specimens are shown in Figures 4.3(b), (c) and (g). Generally, the ultimate axial stress, ultimate axial strain, and the slope of the final segment enhance with the increase of the FRP jacket thickness, which is consistent with the observations reported in existing studies (e.g., Wang et al., 2023, Liao et al., 2022). Figure 4.7 shows the effects of the FRP jacket thickness on the two characteristic points (f'_{cu},ε_{cu}), (f'_{c1},ε_{c1}), and the stress retention ratio (f'_{c2}/f'_{c1}). It is evident that the normalised ultimate axial stress and normalised ultimate axial strain increase with the FRP jacket thickness, which is consistent with the observations made in Figure 4.3. The largest average normalised ultimate axial stress and normalised ultimate axial strain among all specimens are 3.28 and 12.35, respectively, for C9 specimens. Moreover, it was found that both the normalised first peak axial stress and its corresponding axial strain exhibit a slightly positive trend with the FRP jacket thickness. For example, the average normalised first peak axial stress is 1.17 for C2 specimens and 1.48 for C9 specimens. As a result, the transition segment after the first peak stress is affected by the FRP jacket thickness. However, as shown in Figure 4.7(e), the stress retention ratio does not exhibit an obvious trend with the variation of the FRP jacket thickness, indicating that the increase of confinement cannot advance the activation of the FRP jacket before the crack of inside UHPC.

4.6.5.2 *Effect of steel fibre content*

The influence of steel fibre content on the compressive behaviour of FRP-confined UHPC/UHPFRC is shown in Figures 4.3(d-f) and Figure 4.8. As shown in Figures 4.3(d-f), the axial stress-strain curves for specimens with three steel fibre volume fractions are generally similar in the overall shape. The axial stress-strain curves for specimens with steel fibre addition are slightly higher than those without steel fibres, especially for specimens with diameters of 50 mm and 75 mm (i.e., D 50and D75 specimens). Figure 4.8 compares the characteristic values of selected specimens with different steel fibre volume fractions, including the normalised ultimate axial stresses, the normalised ultimate axial strains, the normalised first peak stresses and their corresponding axial strains, and the stress retention ratios. A slightly decreasing trend could be observed on the normalised ultimate stresses/strains with the increase of steel fibre volume. This also applies to the normalised first peak stresses and normalised axial strains at the first peak stress as shown in the figure. This phenomenon has also been observed by Wang et al. (2023), indicating that the bridging effect of steel fibres could not benefit the strength or stain enhancement ratio of FRP-confined specimens in the second ascending stage. However, Liao et al. (2021) found that the normalised first peak stresses and the normalised axial strains at the first peak stress were enhanced as the steel fibre volume fraction increased. The discrepancy may come from the difference in FRP jacket thickness between the two studies. The maximum FRP confinement stiffness ratio of the specimens (diameter = 100 mm) in Liao et al. (2021) was only around 0.1, while in Wang et al. (2023) and the present study, the FRP confinement stiffness ratio of the specimens of the same size were between 0.044 and 0.160. The bridging effect of steel fibres may be weakened by the strong confinement provided by FRP jackets. As illustrated in Figure 4.3 and Table 4.4, specimens S2V2-D50-C4-2 and S2V2-D75-C6-1 exhibited early failure compared to their identical counterparts, resulting in reduced ultimate axial stresses (i.e., 353.7 MPa and 332.0 MPa) and their corresponding axial strain. A potential explanation for this premature failure is the detrimental effect of the presence of steel fibres within the UHPC. These steel fibres may cluster together, and after the concrete cracks, such clustering could damage the FRP jackets, thereby causing the premature failure of the specimens. Further experiments are required to validate this conjecture.

4.6.5.3 Effect of specimen size

The effect of specimen size on the compressive strengths of UHPC/UHPFRC and FRP-confined UHPC/UHPFRC is illustrated in Figures 4.9(a) and (b), respectively. It is evident that the compressive strength of plain UHPC/UHPFRC substantially deceases with the enlargement of the specimen size. For example, for series S2V0 specimens, the average compressive strength reduces by 6.57% from 175.9 MPa for D50 specimens (diameter = 50 mm) to 164.4 MPa for D100 specimens (diameter = 100 mm). The corresponding reduction percentages are 10.02% and 7.16% for series S2V1 specimens and S2V2 specimens, respectively. The results reveal the sensitive size effect of unconfined UHPC/UHPFRC. It is also seen that the addition of steel fibres does not exhibit a significant impact on the size effect of unconfined concrete. For FRP-confined UHPC/UHPFRC specimens, the average compressive strength of series S2V0 specimens is decreased from 426.9 MPa to 383.8 MPa when the specimen diameter is increased from 50 mm to 100 mm. Nevertheless, there seems to be no significant correlation between the size of FRP-confined UHPFRC specimens (i.e., series S2V1 and S2V2 specimens) and their compressive strength. For series S2V1 specimens, the D75 specimens (diameter =75 mm) exhibit the highest average compressive strength, reaching 436.4 MPa. The average compressive strengths of D50 specimens (diameter = 50 mm) and D100 specimens (diameter = 100 mm) are 411.8 MPa and 359.9 MPa, respectively. For series S2V2 specimens, the compressive strength varies between 383.0 MPa for D75 specimens and 410.9 MPa for D100 specimens. Compared to the reduction percentages of 6.57% and 10.02% observed in the unconfined series S2V0 and S2V1 specimens when transitioning from D50 specimens (diameter = 50 mm) to D100 specimens (diameter = 100 mm), the corresponding reduction percentages for the series S2V0 and S2V1 specimens with FRP confinement are similar, at 10.1% and 12.6%, respectively. However, for the series S2V2 specimens with FRP confinement, an increase in specimen size from D50 (diameter = 50 mm) to D100 (diameter = 100 mm) results in an enhancement of the average compressive strength by 3.6%. The increase in compressive strength indicates a less significant size effect for FRP-confined UHPFRC with a steel fibre volume fraction of 2%. However, more test data are required for a more solid conclusion to be drawn.

The influence of specimen size on the normalised axial stress-strain curves of specimens of different sizes but similar FRP confinement ratios are shown in Figure 4.10 in three groups with three different steel fibre volume fractions. To eliminate the effect of concrete strength, the axial stresses and the axial strains were normalised with respect to the unconfined concrete compressive strength and the corresponding axial strain respectively. In general, the normalised axial stress-strain curves of the specimens are similar, with the exception of certain specimens that display a pronounced drop in axial stress following the attainment of the first peak axial stress. However, it can be found that, compared with series

D100 specimens, the stress drops after the first peak stress of series D50 and D75 specimens are less obvious in all three groups, implying that the reduction of specimen size (i.e., from D100 to D50 and D75 specimens) could relieve the stress reduction after the first peak stress. Note that the FRP confinement stiffness ratios of all these specimens were close to each other. As discussed in the preceding sections, the sudden axial stress drop is mainly attributed to the micro gap generated by the shrinkage of UHPC. The total shrinkage magnitude of the D100 specimens may be larger than that of the D50 specimens, resulting in a wider gap and a more obvious axial stress drop.

5.3.2.1 Effect of compressive strength

Figure 4.11 illustrated the influence of compressive strength on normalised axial stress-strain curves of FRP-confined UHPC specimens. As presented in Table 4.3, the unconfined UHPC specimens in series S1 exhibited an average compressive strength of 187.8 MPa, whereas those in series 2 and series 3 had average compressive strengths of 173.5 MPa and 149.7 MPa, respectively. In Figure 4.11(a) or 4.11(b), most of the observed curves are relatively similar. However, a few curves, such as those for specimens S1-D75-C3-1, S2V0-D75-C3-2, and S3-D75-C6-1, exhibit a significantly larger drop in stress after reaching the first peak stress, resulting in lower normalised axial stresses in the subsequent phase compared to the other curves. Since the three specimens are from three different batches, this can be regarded as variability and does not indicate a correlation between the stress drop and the concrete strength within the range of 150 MPa to 190 MPa. Therefore, it can be concluded that when the concrete strength exceeds 150 MPa, there is no significant difference in the axial compressive behaviour between concretes with strengths of 150 MPa and 190 MPa.

4.7 COMPARISON WITH EXISTING DESIGN-ORIENTED STRESS-STRAIN MODELS

Table 4.5 provides a summary of five existing design-oriented models that have been developed for predicting the characteristic points on the stress-strain curves (including the stresses and strains at ultimate condition) of FRP-confined NSC, UHPC and UHPFRC (Teng et al., 2009; Zohrevand and Mirmiran, 2013; Lam et al., 2021; Dang et al., 2022; Liao et al., 2022). Teng et al.'s (2009) model (i.e., Model 1) is a refined version of the model proposed by Lam and Teng (2003) for FRP-confined NSC. It is considered as one of the most representative models offering high accuracy. Zohrevand and Mirmiran's (2013) model (i.e., Model 2) was developed using their test results for FRP-confined UHPFRC based on the models of Lam and Teng (2003) and Samaan et al. (1998). The more recent axial stress-strain models (i.e., Models 3-5) of Lam et al. (2021), Dang et al. (2022) and Liao et al. (2022) are recalibrated models for FRP-confined UHPC/UHPFRC based on Lam and Teng's (2003) model and Teng et al.'s (2009) model. Among these four models for FRP-confined UHPC/UHPFRC, the models of Zohrevand and Mirmiran (2013) and Lam et al. (2021) are only applicable to FRP-confined UHPFRC, while those of Liao et al. (2022) and Dang et al. (2022) were proposed for both FRP-confined UHPC and FRP-confined UHPFRC. The database used for the development of the models of Lam et al. (2021), Dang et al. (2022) and Liao et al. (2022) for FRP-confined UHPC/UHPFRC included specimens with a compressive strength smaller than 150 MPa or even 130 MPa. Among the above five models, only Liao et al.'s (2022) model takes the steel fibre volume fraction as a criterion to select a proper ρ_k value. The performance of these models in predicting the compressive behaviour of FRP-confined UHPC/UHPFRC with an unconfined concrete strength larger than 150 MPa has never been evaluated. Therefore, a test database of FRP-confined UHPC/UHPFRC was collected from the open literature in the present study and the test results are compared with the predictions from the five stress-strain models. Note that only specimens with an unconfined concrete strength larger than 150 MPa were selected for the evaluation. The details of the selected specimens from different studies are summarised in Table 4.6. The performances of the five models were assessed using the mean value (Mean), the standard deviation (SD), and the coefficient of variation (CoV) of the values of ratios between the test results and the predictions, which are calculated in Eqs. 4.2, 4.3 and 4.4, respectively, where P_i is the i^{th} predicted value from a model; E_i is the i^{th} experimental value; and n is the total number of the specimens in the database.

$$\mathrm{Mean} = \frac{1}{n}\sum_{i=1}^{n}\frac{P_i}{E_i} \tag{4.2}$$

$$\mathrm{SD} = \sqrt{\frac{1}{n-1}\sum_{i=1}^{n}\left[\frac{P_i}{E_i} - \frac{1}{n}\sum_{i=1}^{n}\frac{P_i}{E_i}\right]^2} \tag{4.3}$$

$$\mathrm{CoV} = \frac{SD}{Mean} \tag{4.4}$$

The performance of the existing models in predicting the stress enhancement ratios of the specimens is shown in Figure 4.12. The values of Mean, SD, and CoV of each model are plotted in Figure 4.14(a). In general, Teng et al.'s (2009) model and Zohrevand and

Mirmiran's (2013) model overestimate the stress enhancement ratios of the test specimens by about 10% and 30%, respectively. Particularly, the model of Zohrevand and Mirmiran (2013) overestimates the stress enhancement ratios obviously when the FRP confinement stiffness ratio is relatively high (for those with large stress enhancement ratios). The inaccuracy of Zohrevand and Mirmiran's (2013) model may be attributable to the use of limited test data for developing the model. Note that Teng et al.'s (2009) model was originally developed for NSC. Lam et al.'s (2021) model and Dang et al.'s (2022) model provide more satisfactory predictions with mean values close to 1.0 [Figure 4.12(c) and (d)]. Note that the database used for the development of the two models mostly consisted of test results of FRP-confined UHPFRC. The model of Liao et al. (2022) is capable of predicting the stress enhancement ratios at the first characteristic points (i.e., f'_{c1}/f'_{co}) reasonably well, although it slightly overestimates the stress enhancement ratios at the second characteristic points(i.e., f'_{c2}/f'_{co}) [Figures 4.12(f) and (g)]. Furthermore, the model's tendency to underestimate the stress enhancement ratios at the ultimate condition (i.e., f'_{cu}/f'_{co}), particularly when the FRP confinement stiffness ratios are relatively high, is evident in Figure 4.12(e). As illustrated in Figures 4.12(c) and (d), the models proposed by Lam et al. (2021) and Dang et al. (2022) tend to slightly overestimate the stress enhancement ratios at the ultimate condition (i.e., f'_{cu}/f'_{co}) when the FRP confinement stiffness ratios for FRP-confined UHPC are low.

For the strain enhancement ratio, the performance of the five models is illustrated in Figure 4.13 and Figure 4.14(b). It can be seen that Teng et al.'s (2009) model overestimates the strain enhancement ratios by approximately 14%. Model 2 to 5, which were developed based on database of FRP-confined UHPC/UHPFRC, underestimate the strain enhancement ratios of the test specimens by 72%, 21%, 3%, and 14%, respectively. Among these models, Dang et al.'s (2022) model shows a mean value closest to 1 for predicting the ultimate strain enhancement ratios ($\varepsilon_{cu}/\varepsilon_{co}$), but it has slightly high SD and CoV values, which are 0.29 and 0.30, respectively. The model of Liao et al. 2022 has a mean value closet to 1 (i.e., 0.97) for $\varepsilon_{c1}/\varepsilon_{co}$ and $\varepsilon_{c2}/\varepsilon_{co}$, but the SD and CoV values of this model are relatively higher than those for the strength enhancement ratios. Similar findings are reported in Wang et al., (2023). The lower accuracy of the models in predicting the strain enhancement ratios compared with the stress enhancement ratios is believed to be partially caused by the significant variation in the methods used to obtain axial strains in different studies. Lam et al. (2021) and Wang et al. (2023) obtained the axial strains using mid-height LVDTs [i.e., LVDTs mounted at the mid-height region over a length of 80 mm (or 120 mm) of the 100 mm × 200 mm cylinders (or 150 mm×300 mm cylinders)], while full-height LVDTs (i.e., LVDTs capturing the full-height shortenings of the specimens) were used in the other studies. For FRP-confined NSC, the full-height LVDTs and mid-height LVDTs readings are generally close to each other (Vincent and Ozbakkaloglu 2013; Lim and Ozbakkaloglu 2015; Vincent and Ozbakkaloglu 2015). However, Pour et al. (2018) found that the axial strains obtained from mid-height LVDTs were generally smaller than those obtained from full-height LVDTs for FRP-confined HSC specimens after the first peak axial stress (f'_{c1}). Compared to HSC, UHPC/UHPFRC possesses a larger level of brittleness. As a result, the impact of different measurement methods on the obtained strain data may be more significant for FRP-confined UHPC/UHPFRC than FRP-confined NSC or HSC.

4.8 NEW EQUATIONS FOR ULTIMATE CONDITION

New predictive equations of two versions for FRP-confined UHPC and UHPFRC, respectively, are proposed in this section. Based on the test results from the present database, the following equations for the ultimate failure point (f'_{cu}, ε_{cu}) of FRP-confined UHPC with an unconfined concrete strength larger than 150 MPa are proposed:

$$\frac{f'_{cu}}{f'_{co}} = 1 + 4.6(\rho_k - 0.036)\rho_\varepsilon \tag{4.5}$$

$$\frac{\varepsilon_{cu}}{\varepsilon_{co}} = 1 + 22.5\rho_k^{0.81}\rho_\varepsilon^{0.45} \tag{4.6}$$

$$\rho_\varepsilon = \frac{\varepsilon_{h,rup}}{\varepsilon_{co}} \tag{4.7}$$

where ρ_ε is the strain ratio. For FRP-confined UHPFRC with an unconfined concrete strength larger than 150 MPa, the following equations are proposed for predicting the ultimate axial stress and the corresponding strain:

$$\frac{f'_{cu}}{f'_{co}} = 1 + 3.4(\rho_k - 0.015)\rho_\varepsilon \tag{4.8}$$

$$\frac{\varepsilon_{cu}}{\varepsilon_{co}} = 1 + 20.2\rho_k\rho_\varepsilon^{0.83} \tag{4.9}$$

The proposed equations adopted the original forms of equations proposed by Teng et al. (2009). The constants 0.036 and 0.015 are the minimum value of ρ_k of FRP-confined UHPC/UHPFRC below which FRP confinement is assumed to result in no enhancement in the compressive strength of concrete, as proposed in Section 4.6.3. The other constants in the proposed equations represent the parameters that have been optimally fitted. Figure 4.15 shows the performance of the proposed equations in predicting the experimental results in the present database. The mean, SD, and CoV values of the proposed equations in predicting the stress enhancement ratios are 1.0, 0.1, and 0.1, respectively. For the strain enhancement ratios, the mean, SD, and CoV values of the proposed equations are 1.06, 0.25, and 0.24, respectively. In comparison to the existing models in Table 4.5, the proposed equations demonstrate mean values close to 1.0, along with smaller SD and CoV values than those of the existing models for both the predicted stress enhancement ratios and strain enhancement ratios.

4.9 CONCLUSIONS

This chapter has presented the results of a systematic experimental study on FRP-confined UHPC/UHPFRC with an unconfined compressive strength of over 150 MPa. The effects of FRP confinement stiffness ratio and steel fibre content on the behaviour of FRP-confined UHPC/UHPFRC were examined in detail. Based on the test results and discussions presented in this chapter, the following conclusions can be drawn:

(1) For FRP-confined UHPC/UHPFRC specimens with a relatively small FRP confinement stiffness, the axial stress-strain curves feature an ascending first branch followed by a descending branch, while for specimens with a relatively large FRP confinement stiffness, the axial stress-strain curves feature an ascending first branch, followed by an axial stress drop and then an ascending third branch.

(2) A minimum value of $\rho_k \approx 0.036$ (or 0.015) was identified to achieve a compressive strength larger than the unconfined concrete strength for FRP-confined UHPC (or FRP-confined UHPFRC). This threshold value of ρ_k is much larger than the value of 0.01 for FRP-confined NSC reported by Teng et al. (2009), indicating that a greater amount of FRP material is needed to effectively confine UHPC/UHPFRC due to its brittle nature.

(3) The average FRP hoop strain efficiency factor of CFRP-confined UHPC was 0.686 and that of GFRP-confined UHPC was 0.612. The former (0.686) is larger than the value of 0.586 reported in Lam and Teng (2003) for CFRP-confined NSC, while the latter (0.612) is close to the value of 0.624 for GFRP-confined NSC reported in Lam and Teng (2003).

(4) Dang et al.'s (2022) stress-strain model provided reasonably accurate predictions for the axial stresses and strains at ultimate condition of the FRP-confined UHPC/UHPFRC specimens collected in the database. Liao et al.'s (2022) model is capable of predicting the stress/strain enhancement ratios at the first characteristic point reasonably well.

(5) New equations for predicting the compressive strengths and the ultimate axial strains of FRP-confined UHPC and UHPFRC were proposed, which were demonstrated to perform better than the existing models in predicting the test results of the collected database.

4.10 REFERENCES

ACI 318-08 (2008). *Building Code Requirements for Structural Concrete and Commentary*, American Concrete Institute, Farmington Hills, Michigan, USA.

ASTM D3039/D3039M (2017). *Standard Test Method for Tensile Properties of Polymer Matrix Composite Materials*, ASTM International, West Conshohocken, PA.

ASTM C469/C469M (2014). *Standard Test Method for Static Modulus of Elasticity and Poisson's Ratio of 659 Concrete in Compression*, ASTM International, West Conshohocken, PA.

Berthet, J.F., Ferrier, E. and Hamelin, P. (2005). "Compressive behaviour of concrete externally confined by composite jackets. Part A: experimental study", *Construction and Building Materials*, 19(3), 223-232.

De Larrard, F. and Sedran, T. (1994). "Optimization of ultra-high-performance concrete by the use of a packing model", *Cement and Concrete Research*, 24(6), 997-1009.

De Oliveira, D.S., Raiz, V. and Carrazedo, R. (2019). "Experimental study on normal-strength, high-strength and ultrahigh-strength concrete confined by carbon and glass FRP laminates", *Journal of Composites for Construction*, ASCE, 23(1), 04018072.

Graybeal, B. and Tanesi, J. (2007). "Durability of an ultrahigh-performance concrete", *Journal of Materials in Civil Engineering*, ASCE, 19(10), 848-854.

Guler, S. (2014). "Axial behaviour of FRP-wrapped circular Ultra-High Performance Concrete specimens", *Structural Engineering and Mechanics*, 50(6), 709-722.

Jiang, T. and Teng, J.G. (2007). "Analysis-oriented stress–strain models for FRP–confined concrete", *Engineering Structures*, 29(11), 2968-2986.

Krahl, P.A., Gidrão, G.D.M.S. and Carrazedo, R. (2019). "Cyclic behaviour of UHPFRC under compression", *Cement and Concrete Composites*, 104, 103363.

Lam, L. and Teng, J.G. (2003). "Design-oriented stress–strain model for FRP-confined concrete", *Construction and Building Materials*, 17(6-7), 471-489.

Lam, L. and Teng, J.G. (2004). "Ultimate condition of fibre reinforced polymer-confined concrete", *Journal of Composites for Construction*, ASCE, 8(6), 539-548.

Lee, C.S. and Hegemier, G.A. (2009). "Model of FRP-confined concrete cylinders in axial compression", *Journal of Composites for Construction*, ASCE, 13(5), 442-454.

Liao, J., Yang, K. Y., Zeng, J.J., Quach, W.M., Ye, Y.Y. and Zhang, L. (2021). "Compressive behaviour of FRP-confined ultra-high performance concrete (UHPC) in circular columns", *Engineering Structures*, 249, 113246.

Lim, J.C., and Ozbakkaloglu, T. (2014a). "Confinement model for FRP-confined high-strength concrete", *Journal of Composites for Construction*, ASCE, 18(4), 04013058.

Lim, J.C. and Ozbakkaloglu, T. (2014b). "Influence of silica fume on stress–strain behaviour of FRP-confined HSC", *Construction and Building Materials*, 63, 11-24

Lim, J. C. and Ozbakkaloglu, T. (2015). "Influence of concrete age on stress–strain behavior of FRP-confined normal-and high-strength concrete", *Construction and Building Materials*, 82, 61-70.

Naeimi, N. and Moustafa, M.A. (2021). "Compressive behaviour and stress–strain relationships of confined and unconfined UHPC", *Construction and Building Materials*, 272, 121844.

Ozbakkaloglu, T. (2013). "Compressive behaviour of concrete-filled FRP tube columns: Assessment of critical column parameters", *Engineering Structures*, 51, 188-199.

Pour, A.F., Gholampour, A. and Ozbakkaloglu, T. (2018). "Influence of the measurement method on axial strains of FRP-confined concrete under compression", *Composite Structures*, 188, 415-424.

Richard, P. and Cheyrezy, M. (1995). "Composition of reactive powder concretes", *Cement and Concrete Research*, 25(7), 1501-1511.

Samaan, M., Mirmiran, A., Shahawy, M. (1998). "Model of concrete confined by fibre composites", *Journal of Structural Engineering*, ASCE, 124(9), 1025-31.

Shi, C., Wu, Z., Xiao, J., Wang, D., Huang, Z. and Fang, Z. (2015). "A review on ultra high performance concrete: Part I. Raw materials and mixture design", *Construction and Building Materials*, 101, 741-751.

Teng, J.G., Jiang, T., Lam, L., and Luo, Y.Z. (2009). "Refinement of a design-oriented stress-strain model for FRP-confined concrete", *Journal of Composites for Construction*, ASCE, 13(4), 269.

Teng, J.G., Xiang, Y., Yu, T. and Fang, Z. (2019). "Development and mechanical behaviour of ultra-high-performance seawater sea-sand concrete", *Advances in Structural Engineering*, *22*(14), 3100-3120.

Tian, H., Zhou, Z., Wei, Y., Wang, Y. and Lu, J. (2019). "Experimental investigation on axial compressive behavior of ultra-high performance concrete (UHPC) filled glass FRP tubes", *Construction and Building Materials*, 225, 678-691.

Vincent, T. and Ozbakkaloglu, T. (2013). "Influence of fiber orientation and specimen end condition on axial compressive behavior of FRP-confined concrete", *Construction and Building Materials*, 47, 814-826.

Vincent, T. and Ozbakkaloglu, T. (2015). "Influence of shrinkage on compressive behaviour of concrete-filled FRP tubes: An experimental study on interface gap effect", *Construction and Building Materials*, 75, 144-156.

Wang, W., Wu, C., Liu, Z. and Si, H. (2018). "Compressive behaviour of ultra-high performance fibre-reinforced concrete (UHPFRC) confined with FRP", *Composite Structures*, 204, 419-437.

Wille, K., El-Tawil, S. and Naaman, A.E. (2014). "Properties of strain hardening ultra high performance fibre reinforced concrete (UHP-FRC) under direct tensile loading", *Cement and Concrete Composites*, 48, 53-66.

Wille, K., Naaman, A.E. and Parra-Montesinos, G.J. (2011). "Ultra-high performance concrete with compressive strength exceeding 150 MPa (22 ksi): A Simpler Way", *ACI Materials Journal*, 108(1), 46-54.

Wang, J.J., Zhang, S.S., Nie, X.F. and Yu, T. (2023). "Compressive behaviour of FRP-confined ultra-high performance concrete (UHPC) and ultra-high performance fibre reinforced concrete (UHPFRC)", *Composite Structures*, 312, 116879.

Wu, Y.F. and Jiang, J.F. (2013). "Effective strain of FRP for confined circular concrete columns", *Composite Structures*, 95, 479-491.

Xiang, Y., Teng, J.G. and Jiang, C. (2021). "Manufacture and levelling methods for a new cementitious capping material for compression tests of high strength and ultra-high strength concrete (Chinese Patent No. 202011596226.4), China National Intellectual Property Administration.

Zhang, Y.S., Sun, W., Liu, S.F., Jiao, C.J. and Lai, J.Z. (2008). "Preparation of C200 green reactive powder concrete and its static–dynamic behaviours", *Cement and Concrete Composites*, *30*(9), 831-838.

Zeng, J.J., Ye, Y.Y., Gao, W.Y., Smith, S.T. and Guo, Y.C. (2020). "Stress-strain behaviour of polyethylene terephthalate fibre-reinforced polymer-confined normal-, high-and ultra high-strength concrete", *Journal of Building Engineering*, 101243.

Zohrevand, P. and Mirmiran, A. (2011). "Behaviour of ultrahigh-performance concrete confined by fibre-reinforced polymers", *Journal of Materials in Civil Engineering*, ASCE, 23(12), 1727-1734.

Table 4.1 Summary of unconfined and FRP-confined specimens

Batch No.	Specimen	FRP type	Diameter (mm)	No. of FRP layers	FRP nominal thickness (mm)	Steel fibre fraction V_f (%)
1	S1-D75-U-1,2	-	75	-	-	0
	S1-D75-G1-1,2	GFRP	75	1	0.169	0
	S1-D75-G2-1,2	GFRP	75	2	0.338	0
	S1-D75-G3-1,2	GFRP	75	3	0.507	0
	S1-D75-G4-1,2	GFRP	75	4	0.676	0
	S1-D75-C1-1,2	CFRP	75	1	0.167	0
	S1-D75-C2-1,2	CFRP	75	2	0.334	0
	S1-D75-C3-1,2	CFRP	75	3	0.501	0
	S1-D75-C5-1,2	CFRP	75	5	0.835	0
	S1-D75-C7-1,2	CFRP	75	7	1.169	0
2	S2V0-D50-U-1,2	-	50	-	-	0
	S2V1-D50-U-1,2	-	50	-	-	1
	S2V2-D50-U-1,2	-	50	-	-	2
	S2V0-D50-C4-1,2	CFRP	50	4	0.668	0
	S2V1-D50-C4-1,2	CFRP	50	4	0.668	1
	S2V2-D50-C4-1,2	CFRP	50	4	0.668	2
	S2V0-D75-U-1,2	-	75	-	-	0
	S2V1-D75-U-1,2	-	75	-	-	1
	S2V2-D75-U-1,2	-	75	-	-	2

Table 4.1 *(Continued)*

Batch No.	Specimen	FRP type	Diameter (mm)	No. of FRP layers	FRP nominal thickness (mm)	Steel fibre fraction V_f (%)
2	S2V0-D75-C1-1,2	CFRP	75	1	0.167	0
	S2V0-D75-C3-1,2	CFRP	75	3	0.501	0
	S2V0-D75-C6-1,2	CFRP	75	6	1.002	0
	S2V0-D75-C9-1,2	CFRP	75	9	1.503	0
	S2V1-D75-C6-1,2	CFRP	75	6	1.002	1
	S2V2-D75-C6-1,2	CFRP	75	6	1.002	2
	S2V0-D100-U-1,2	-	100	-	-	0
	S2V1-D100-U-1,2	-	100	-	-	1
	S2V2-D100-U-1,2	-	100	-	-	2
	S2V0-D100-C8-1,2	CFRP	100	8	1.336	0
	S2V1-D100-C8-1,2	CFRP	100	8	1.336	1
	S2V2-D100-C8-1,2	CFRP	100	8	1.336	2
3	S3-D75-U-1,2	-	75	-	-	0
	S3-D75-C3-1,2	CFRP	75	3	0.501	0
	S3-D75-C6-1,2	CFRP	75	6	1.002	0

Table 4.2 UHPC/UHPFRC mix proportion

Raw material	S1	S2V0	S2V1	S2V2	S3
White cement (kg/m^3)	852	851	842	834	836
Silica fume (kg/m^3)	213	213	211	208	209
Quartz powder (kg/m^3)	213	213	211	208	209
River sand (kg/m^3)	938	936	926	917	920
Superplasticizer-44% (kg/m^3)	-	21	21	21	21
Superplasticizer-22% (kg/m^3)	43	-	-	-	-
Water (kg/m^3)	162	184	182	180	197
Steel fibre (kg/m^3)	0	0	79	157	0

Table 4.3 Material properties of unconfined UHPC and UHPFRC

Unconfined UHPC and UHPFRC	Average compressive strength (MPa)	Axial strain at peak stress (%)	Elastic modulus (GPa)
S1-D75	187.8	0.41	49.9
S2V0-D50	175.9	0.40	43.4
S2V1-D50	177.7	0.43	44.2
S2V2-D50	188.3	0.43	43.0
S2V0-D75	173.5	0.42	42.9
S2V1-D75	168	0.41	43.5
S2V2-D75	169.7	0.43	44.0
S2V0-D100	164.4	0.41	43.4
S2V1-D100	159.9	0.39	43.1
S2V2-D100	174.8	0.41	45.1
S3-D75	149.7	0.40	39.1

Table 4.4 Key results of test specimens

Specimen	f'_{co}(MPa)	ε_{co}(%)	f'_{cc}(MPa)	ε_{cc} (%)	f'_{cu}(MPa)	ε_{cu} (%)	f'_{c1}(MPa)	ε_{c1} (%)	f'_{c2}(MPa)	ε_{c2} (%)	$\varepsilon_{h,rup}$ (%)	ρ_K
S1-D75-G1-1	187.8	0.41	206.4	0.57	104.6	1.11	-	-	-	-	1.17	0.009
S1-D75-G1-2	187.8	0.41	212.5	0.58	137.8	0.78	-	-	-	-	1.58	0.009
S1-D75-G2-1	187.8	0.41	217.9	0.61	93.1	1.52	-	-	-	-	0.96	0.017
S1-D75-G2-2	187.8	0.41	199.1	0.66	150.7	1.25	-	-	-	-	1.1	0.017
S1-D75-G3-1	187.8	0.41	230.7	0.63	142.7	1.52	-	-	-	-	1.47	0.026
S1-D75-G3-2	187.8	0.41	196.0	0.66	195.0	0.69	-	-	-	-	0.3	0.026
S1-D75-G4-1	187.8	0.41	197.6	0.64	154.2	1.41	-	-	-	-	1.24	0.034
S1-D75-G4-2	187.8	0.41	231.9	0.62	141.1	0.99	-	-	-	-	0.99	0.034
S1-D75-C1-1	187.8	0.41	228.9	0.65	199.5	0.94	-	-	-	-	0.93	0.023
S1-D75-C1-2	187.8	0.41	232.5	0.75	177.3	1.19	-	-	-	-	1.52	0.023
S1-D75-C2-1	187.8	0.41	238.4	1.51	238.4	1.51	224.80	0.68	211.30	0.78	1.11	0.047
S1-D75-C2-2	187.8	0.41	220.6	1.53	220.6	1.53	214.30	0.64	180.30	0.75	1.2	0.047
S1-D75-C3-1	187.8	0.41	262.3	1.69	262.3	1.69	242.00	0.70	222.70	0.97	1.03	0.070
S1-D75-C3-2	187.8	0.41	311.2	1.91	311.2	1.91	256.60	0.71	234.70	0.83	1.22	0.117
S1-D75-C5-1	187.8	0.41	357.0	3.50	357.0	3.5	205.60	0.87	187.90	0.91	1.1	0.117
S1-D75-C5-2	187.8	0.41	333.8	3.11	333.8	3.11	210.50	0.83	183.10	0.88	1.16	0.117
S1-D75-C7-1	187.8	0.41	439.8	4.05	439.8	4.05	270.00	1.10	232.60	1.15	1.36	0.164
S1-D75-C7-2	187.8	0.41	412.2	3.72	412.2	3.72	254.30	1.00	218.60	1.07	1.03	0.164
S2V0-D50-C4-1	175.9	0.40	430.0	4.03	430.0	4.03	261.83	0.82	257.03	0.89	1.41	0.146
S2V0-D50-C4-2	175.9	0.40	423.9	3.87	423.9	3.87	266.69	0.79	257.39	0.91	1.05	0.146
S2V1-D50-C4-1	177.7	0.43	431.0	3.01	431.0	3.01	263.54	0.70	260.41	0.71	1.32	0.156
S2V1-D50-C4-2	177.7	0.43	392.6	3.08	392.6	3.08	231.67	0.73	230.77	0.76	-	0.156
S2V2-D50-C4-1	188.3	0.43	439.4	4.13	439.4	4.13	233.71	0.64	233.40	0.65	1.1	0.147

Specimen	f'_{co}(MPa)	ε_{co}(%)	f'_{cc}(MPa)	ε_{cc} (%)	f'_{cu}(MPa)	ε_{cu} (%)	f'_{c1}(MPa)	ε_{c1} (%)	f'_{c2}(MPa)	ε_{c2} (%)	$\varepsilon_{h,rup}$ (%)	ρ_K
S2V2-D50-C4-2	188.3	0.43	353.7	3.25	353.7	3.25	212.50	0.47	204.75	0.53	-	0.147
S2V0-D75-C1-1	173.5	0.42	183.2	0.58	124.6	1.07	-	-	-	-	-	0.026
S2V0-D75-C1-2	173.5	0.42	202.1	0.62	156.4	0.66	-	-	-	-	0.6	0.026
S2V0-D75-C3-1	173.5	0.42	249.4	1.39	249.4	1.39	218.4	0.58	178.6	0.54	0.95	0.078
S2V0-D75-C3-2	173.5	0.42	247.7	1.57	247.7	1.57	217.4	0.71	197.5	0.88	1.13	0.078
S2V0-D75-C6-1	173.5	0.42	448.3	4.02	448.3	4.02	244.68	0.71	235.83	0.81	1.05	0.156
S2V0-D75-C6-2	173.5	0.42	390.0	3.34	390.0	3.34	249.89	0.80	245.94	0.88	1.22	0.156
S2V0-D75-C9-1	173.5	0.42	570.0	4.41	570.0	4.41	246.0	0.94	244.6	0.97	-	0.234
S2V0-D75-C9-2	173.5	0.42	566.9	5.96	566.9	5.96	267.8	0.93	253.1	0.99	-	0.234
S2V1-D75-C6-1	168.0	0.41	431.2	3.69	431.2	3.69	241.47	0.78	242.68	0.94	1.08	0.157
S2V1-D75-C6-2	168.0	0.41	441.6	3.11	441.6	3.11	256.46	0.75	254.20	0.76	-	0.157
S2V2-D75-C6-1	169.7	0.43	332.0	1.95	332.0	1.95	245.76	0.71	234.38	0.80	-	0.163
S2V2-D75-C6-2	169.7	0.43	434.0	3.37	434.0	3.37	237.30	0.62	232.86	0.63	-	0.163
S2V0-D100-C8-1	164.4	0.41	358.6	3.12	358.6	3.12	213.7	0.74	177.5	0.80	0.98	0.160
S2V0-D100-C8-2	164.4	0.41	408.9	3.49	408.9	3.49	235.2	0.66	222.5	0.74	-	0.160
S2V1-D100-C8-1	159.9	0.39	344.2	3.22	344.2	3.22	209.9	0.65	171.2	0.55	1.12	0.157
S2V1-D100-C8-2	159.9	0.39	374.9	3.43	374.9	3.43	215.5	0.58	204.2	0.62	1.02	0.157
S2V2-D100-C8-1	174.8	0.41	432.0	3.55	432.0	3.55	248.8	0.74	241.0	0.96	1	0.151
S2V2-D100-C8-2	174.8	0.41	389.7	3.14	389.7	3.14	245.2	0.72	205.5	0.81	0.92	0.151
S3-D75-C3-1	149.7	0.40	256.4	1.93	256.4	1.93	194.40	0.62	191.20	0.59	1.02	0.086
S3-D75-C3-2	149.7	0.40	238.5	1.46	238.5	1.46	192.90	0.63	183.90	0.65	1.08	0.086
S3-D75-C6-1	149.7	0.40	379.0	3.58	379.0	3.58	232.90	0.77	175.30	0.80	0.85	0.172
S3-D75-C6-2	149.7	0.40	391.4	4.06	391.4	4.06	228.70	0.73	211.50	0.85	-	0.172

Note: “-” ——not available.

Table 4.5 Summary of selected existing stress-strain models

Number	Model	Ultimate axial stress	Ultimate axial strain
1	Teng et al., 2009	$\frac{f'_{cu}}{f'_{co}} = 1 + 3.5(\rho_k - 0.01)\rho_\varepsilon$	$\frac{\varepsilon_{cu}}{\varepsilon_{co}} = 1.75 + 6.5\rho_k^{0.8}\rho_\varepsilon^{1.45}$
2	Zohrevand and Mirmiran, 2013	$\frac{f'_{cu}}{f'_{co}} = 1 + 0.107\frac{f_{l,a}^2}{f'_{co}}$	$\frac{\varepsilon_{cu}}{\varepsilon_{co}} = \frac{f'_{cu} - f_o}{E_2\varepsilon_{co}}$ $f_o = 0.7862f'_{cu} + 0.455f_{l,a}$ $E_2 = 1350.76{f'_{co}}^{0.2} + 5.675\frac{E_{frp}t_{frp}}{D}$
3	Lam et al., 2021	$\frac{f'_{cu}}{f'_{co}} = 1 + 2.8\frac{f_{l,a}}{f'_{co}}$	$\frac{\varepsilon_{cu}}{\varepsilon_{co}} = 1 + 8.3\frac{f_{l,a}}{f'_{co}}(\frac{\varepsilon_{h,rup}}{\varepsilon_{co}})^{0.45}$
4	Dang et al., 2022	$\frac{f'_{cu}}{f'_{co}} = 1 + 2.74\frac{f_{l,a}}{f'_{co}}$	$\frac{\varepsilon_{cu}}{\varepsilon_{co}} = 1 + 17.4\rho_k^{0.9}\rho_\varepsilon^{0.73}$
5	Liao et al., 2022	For CFRP confinement, if $V_{sf} = 0\%$, $\rho_k < 0.075$; if $V_{sf} = 2\%$, $\rho_k < 0.036$. For GFRP confinement, if $V_{sf} = 0\%$, $\rho_k < 0.083$; if $V_{sf} = 2\%$, $\rho_k < 0.06$. $\frac{f'_{c1}}{f'_{co}} = 1 + 0.254\left(\frac{f_{l,a}}{f'_{co}}\right)^{0.6}\left(\frac{\varepsilon_{h,rup}}{\varepsilon_{co}}\right)$ $\frac{f'_{c2}}{f'_{co}} = 0.827 + 1.224\left(\frac{f_{l,a}}{f'_{co}}\right)^{0.8}\left(\frac{\varepsilon_{h,rup}}{\varepsilon_{co}}\right)^{0.2}$ $\frac{f'_{cu}}{f'_{co}} = 0.56 + 2.35(\frac{f_{l,a}}{f'_{co}})^{0.6}(\frac{\varepsilon_{h,rup}}{\varepsilon_{co}})^{0.1}$ $\frac{\varepsilon_{c1}}{\varepsilon_{co}} = 1 + 1.922\left(\frac{f_{l,a}}{f_{co}}\right)^{0.8}(\frac{\varepsilon_{h,rup}}{\varepsilon_{co}})^{0.1}$ $\frac{\varepsilon_{c2}}{\varepsilon_{co}} = 1.153 + 0.359\left(\frac{f_{l,a}}{f_{co}}\right)^{0.1}(\frac{\varepsilon_{h,rup}}{\varepsilon_{co}})^{0.8}$ $\frac{\varepsilon_{cu}}{\varepsilon_{co}} = 1.263 + 1.809(\frac{f_{l,a}}{f'_{co}})^{0.1}(\frac{\varepsilon_{h,rup}}{\varepsilon_{co}})^{0.7}$ For CFRP confinement, if $V_{sf} = 0\%$, $\rho_k \geq 0.075$; if $V_{sf} = 2\%$, $\rho_k \geq 0.036$. For GFRP confinement, if $V_{sf} = 0\%$, $\rho_k \geq 0.083$; if $V_{sf} = 2\%$, $\rho_k \geq 0.06$. $\frac{f'_{cu}}{f'_{co}} = 1 + 0.606(\frac{f_{l,a}}{f'_{co}})^{0.6}(\frac{\varepsilon_{h,rup}}{\varepsilon_{co}})^{0.7}$ $\frac{\varepsilon_{cu}}{\varepsilon_{co}} = 1 + 0.595(\frac{f_{l,a}}{f'_{co}})^{0.1}(\frac{\varepsilon_{h,rup}}{\varepsilon_{co}})^{1.45}$	

Table 4.6 Summary of database

Reference	No. of selected specimens	f'_{co} (MPa)	Steel fibre volume fraction V_f (%)
de Olivera et al., 2019	17	161, 204	0
Zohrevand and Mirmiran, 2011	6	188	2
Lam et al., 2021	3	151.1	2
Liao et al., 2021	14	151.75, 156.44	1, 2
Wang et al., 2023	16	158.11	2
Present study	42	159.9-187.8	0, 1, 2

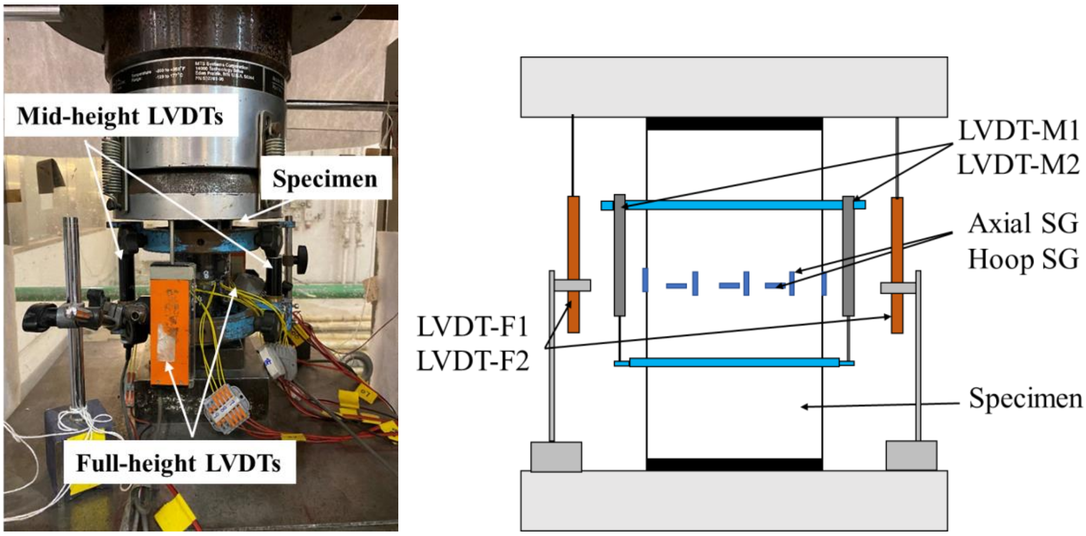

(a) Test set-up and layout of LVDTs

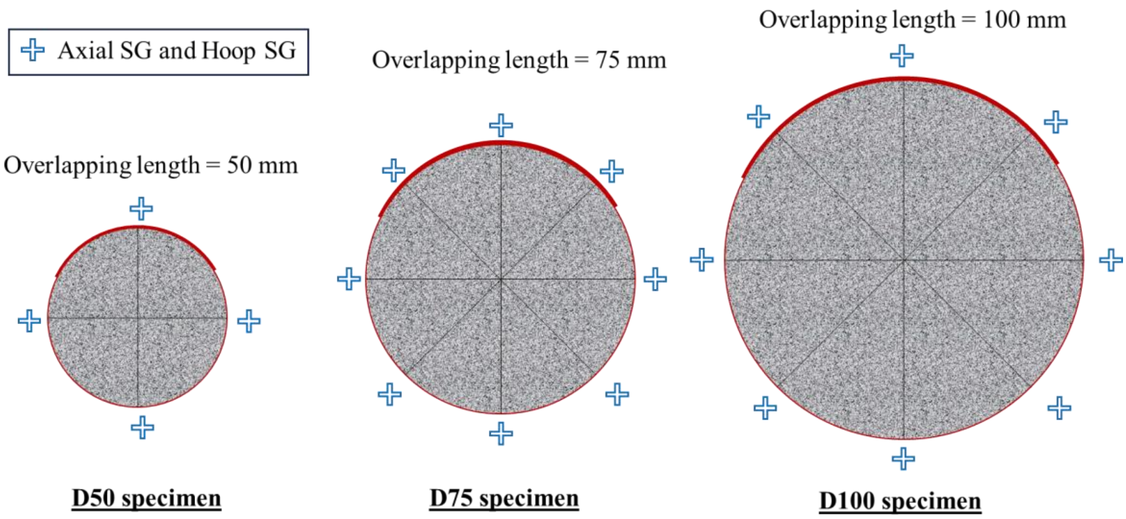

(b) Layout of axial and hoop strain gauges

Figure 4.1 Test set-up and instrumentation

S2V0-D75-U-1 S2V1-D75-U-1 S2V2-D75-U-1

(a) Unconfined specimens

S2V0-D100-C8-1 S2V1-D100-C8-1 S2V2-D100-C8-1

(b) CFRP-confined specimens

S1-D75-G1-1 S1-D75-G2-1 S1-D75-G3-1

(c) GFRP-confined specimens

Figure 4.2 Failure modes of representative specimens

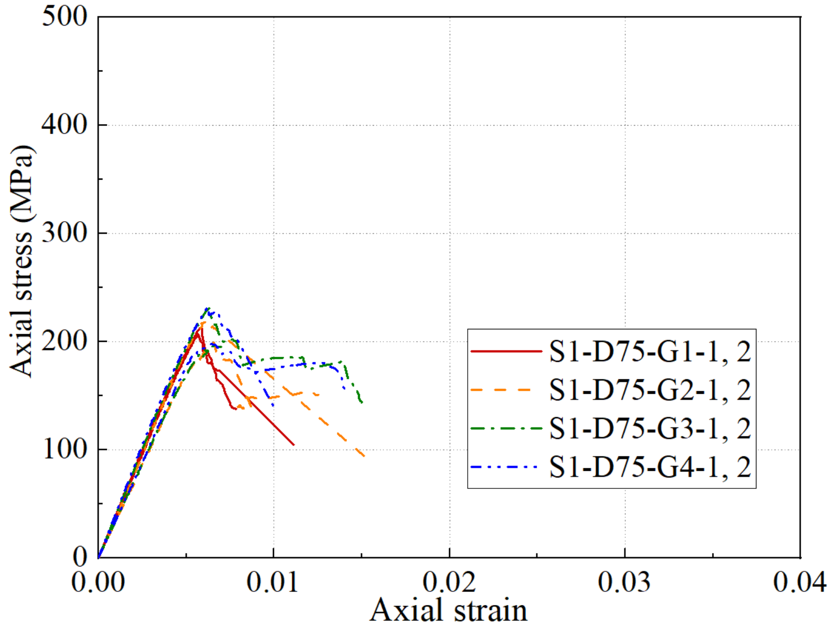

(a) S1-D75-G*n* specimens

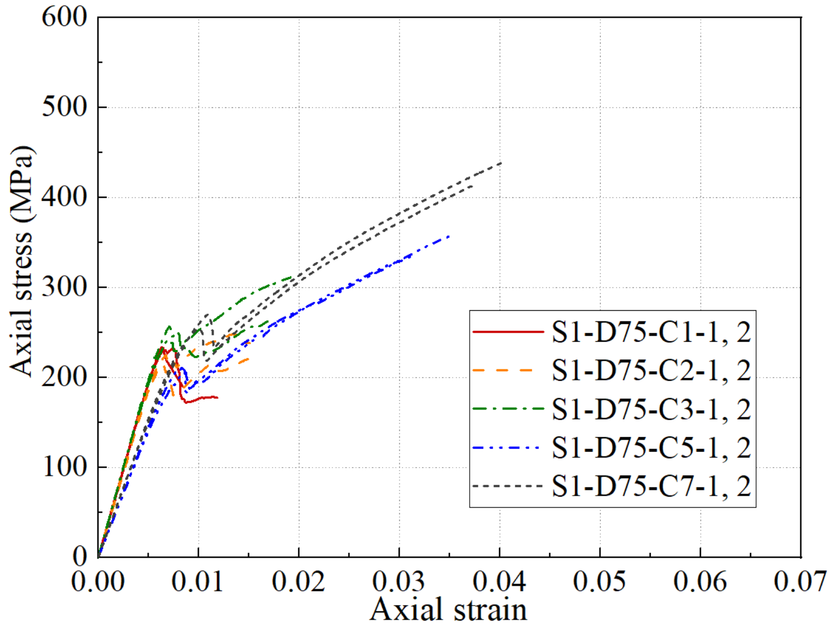

(b) S1-D75-C*n* specimens

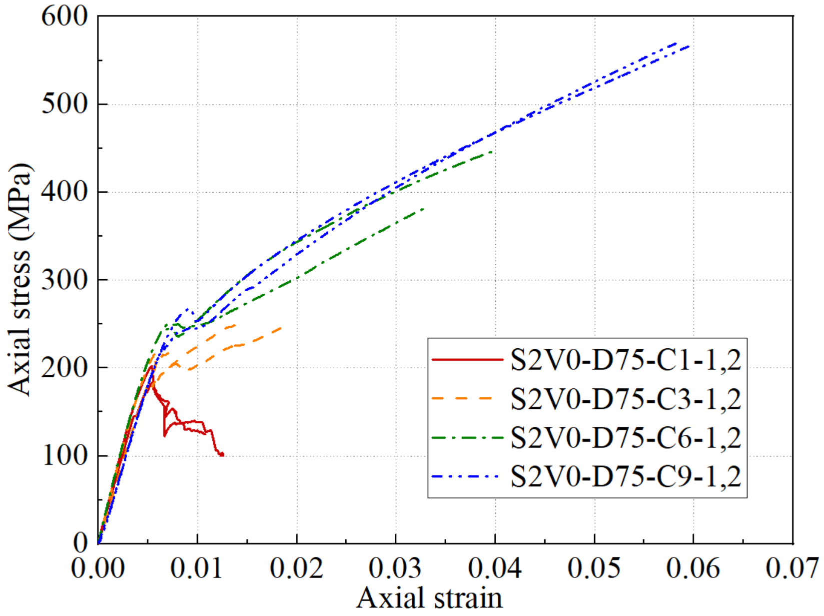

(c) S2V0-D75 specimens

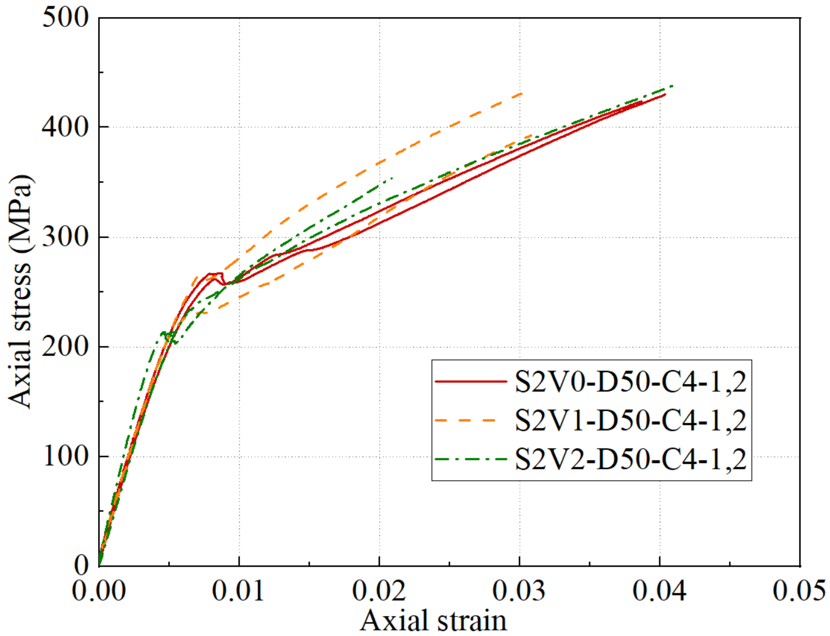

(d) S2V*n*-D50 specimens

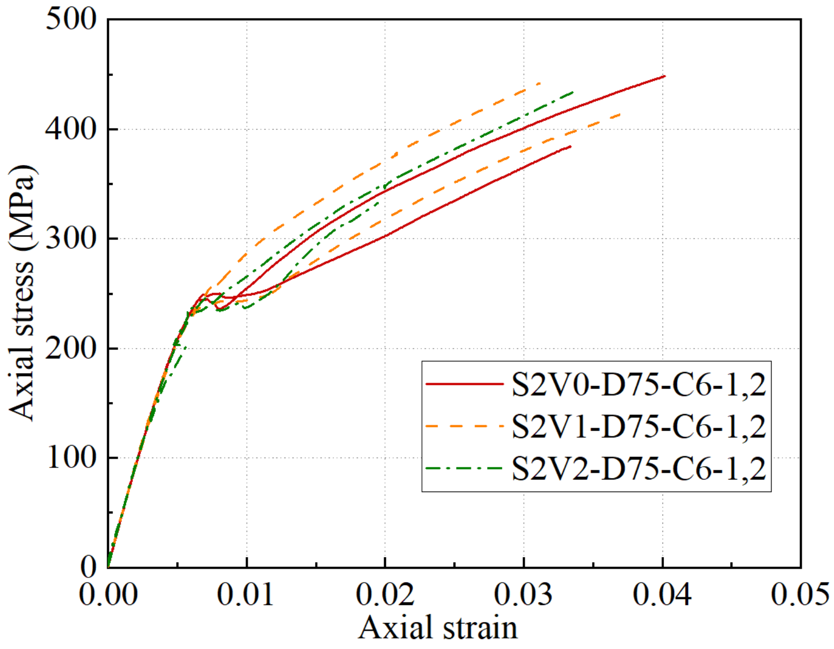

(e) S2Vn-D75 specimens

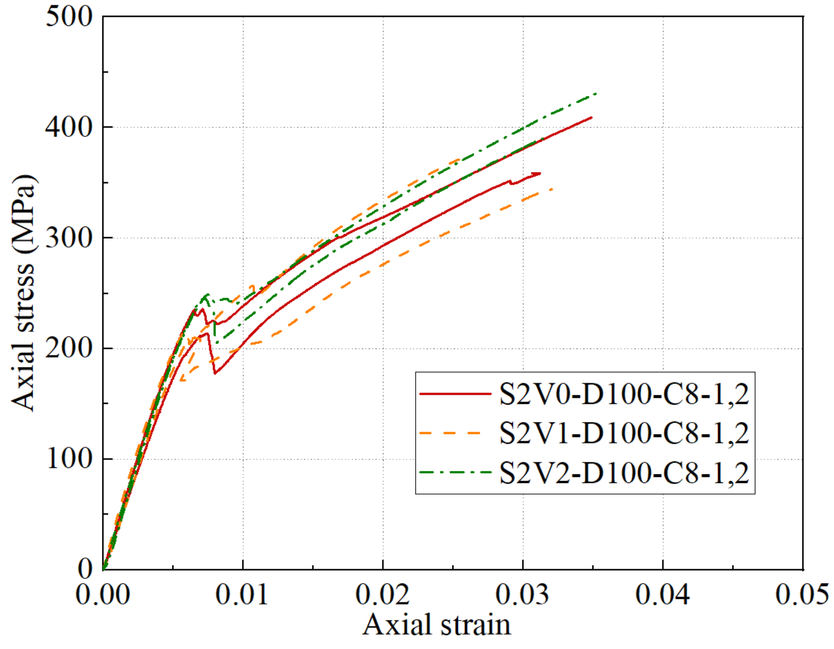

(f) S2Vn-D100 specimens

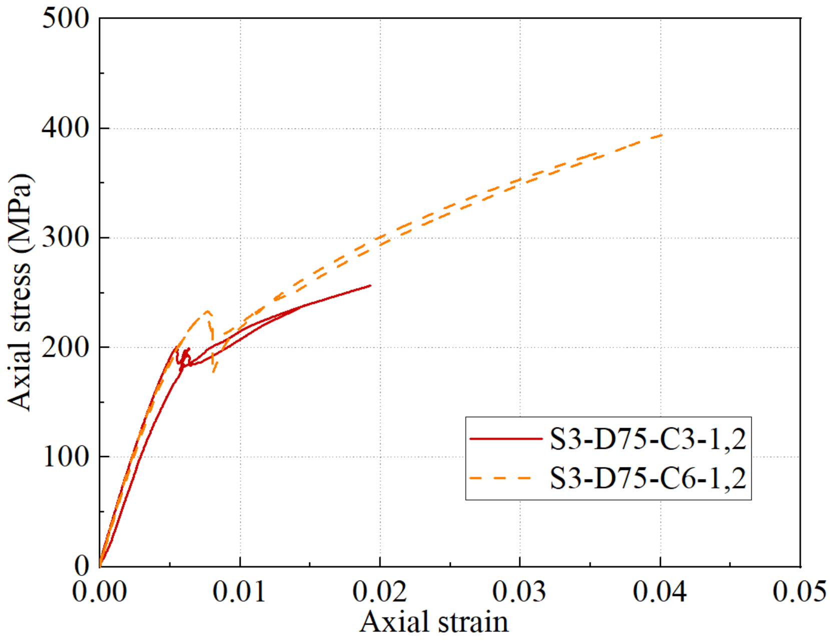

(g) S3-D75 specimens

Figure 4.3 Axial stress-strain curves of FRP-confined UHPC/UHPFRC

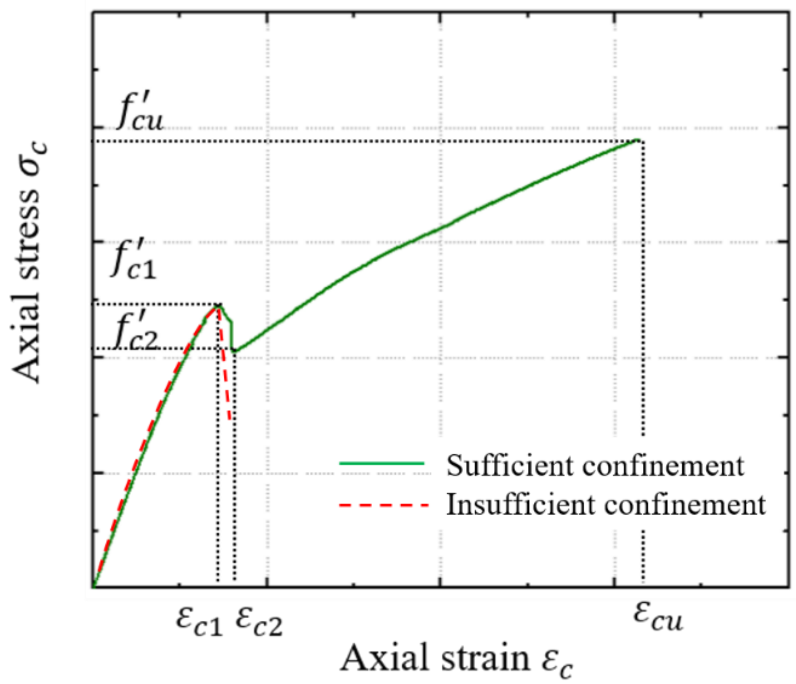

Figure 4.4 A typical axial stress-strain curve of FRP-confined UHPC/UHPFRC

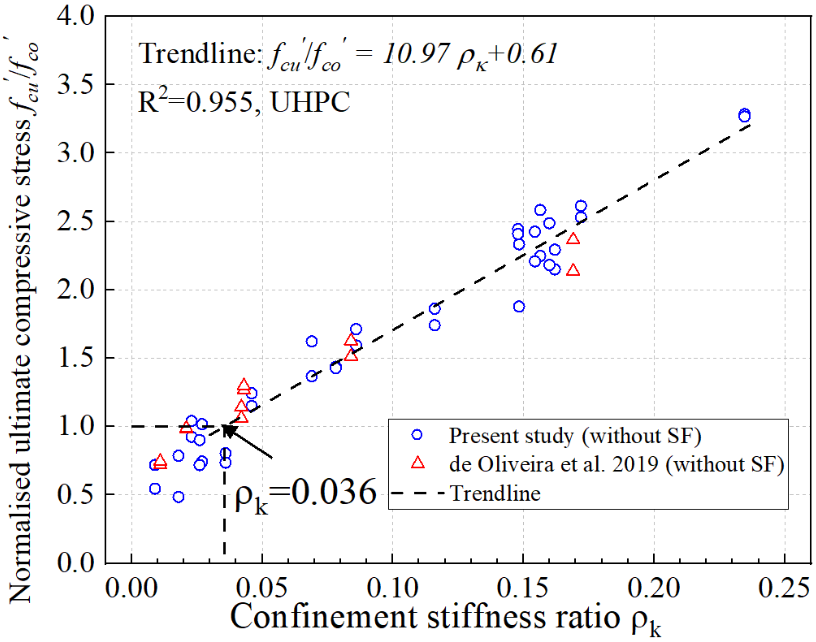

(a) $f'_{co} > 150\ MPa$, UHPC

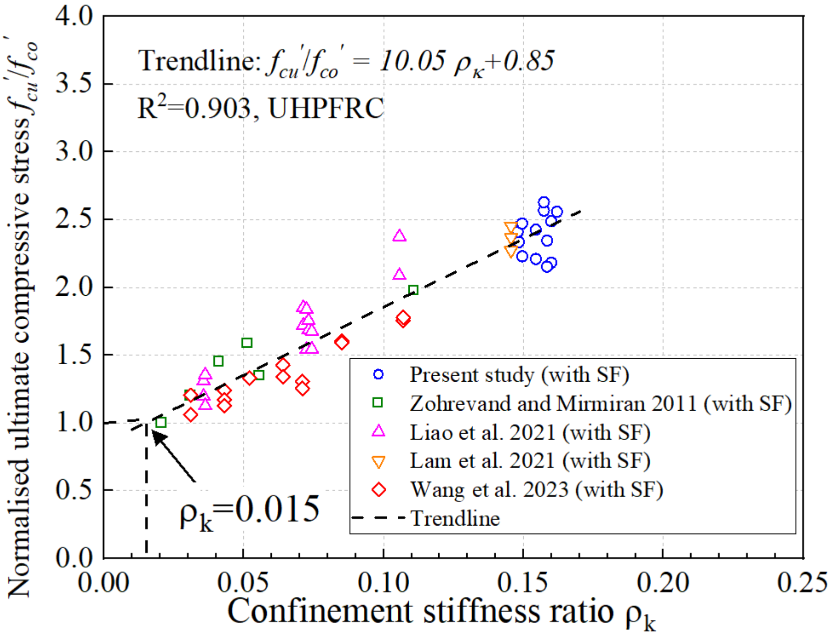

(b) $f'_{co} > 150\ MPa$, UHPFRC

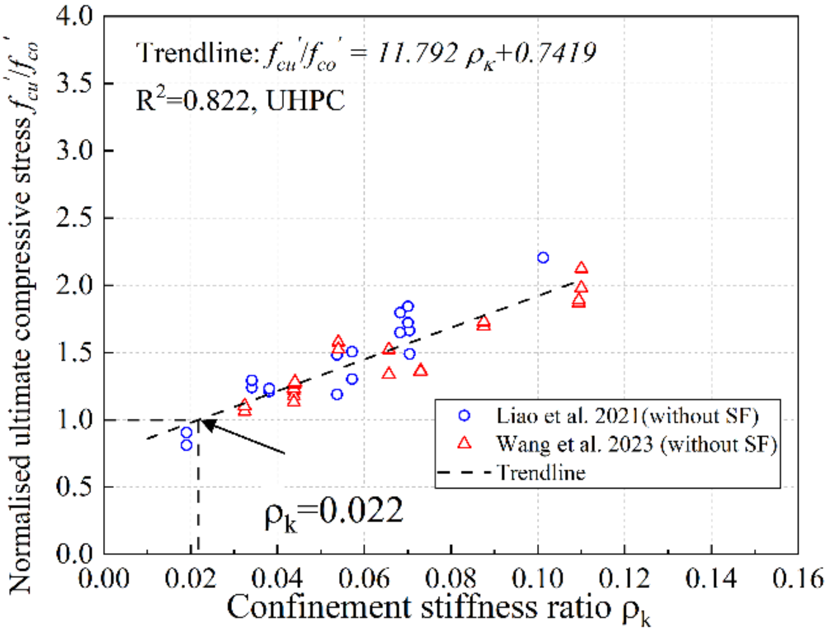

(c) $120\ MPa < f'_{co} < 150\ MPa$, UHPC

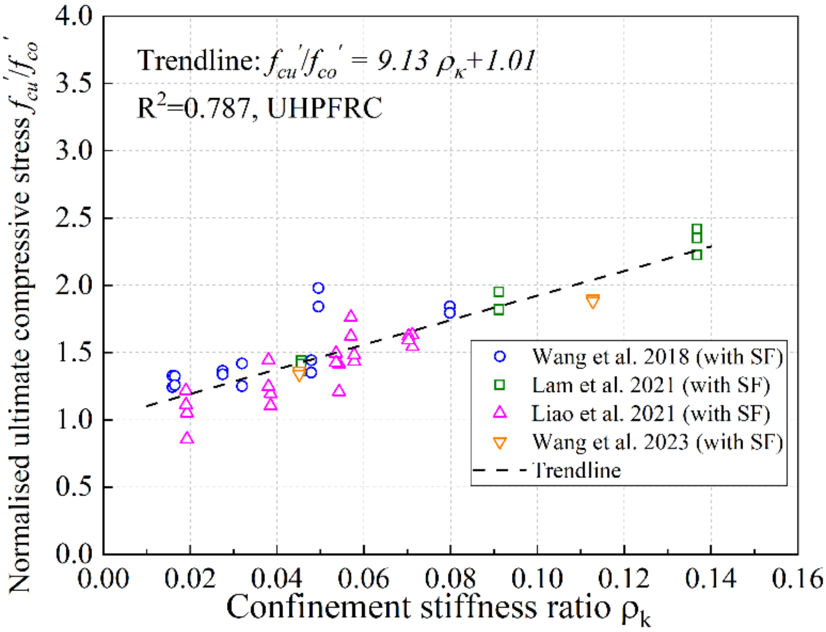

(d) $120\ MPa < f'_{co} < 150\ MPa$, UHPFRC

Figure 4.5 Threshold value of FRP confinement stiffness ratio for sufficiently confined UHPC/UHPFRC

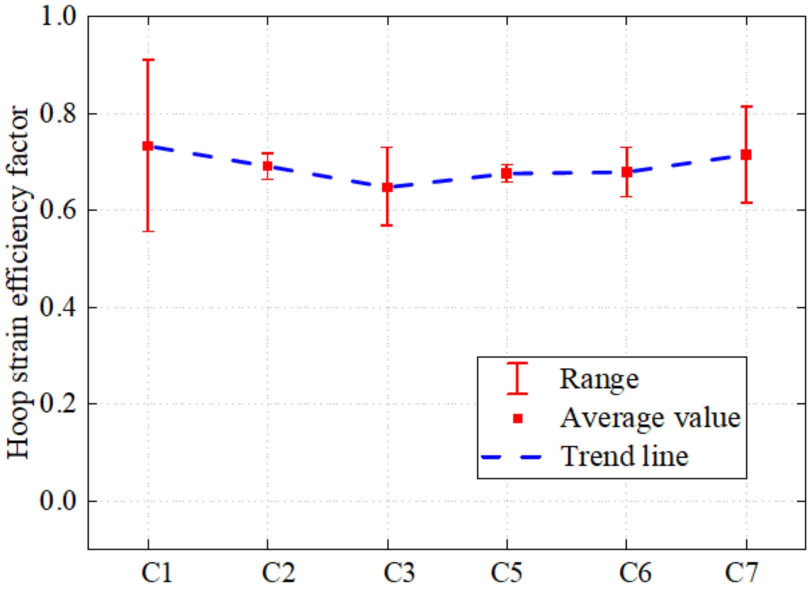

(a) CFRP-confined UHPC specimens

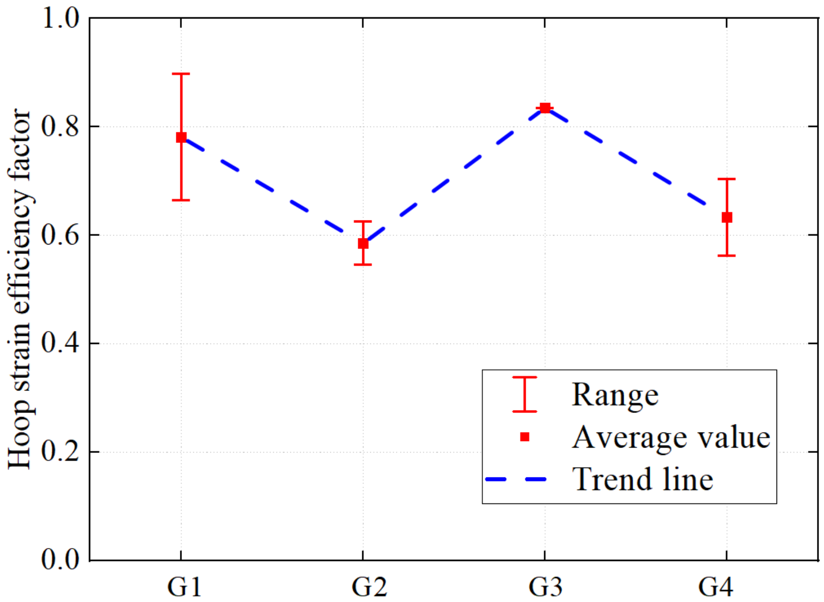

(b) GFRP-confined UHPC specimens

Figure 4.6 Variation of FRP hoop strain efficiency factor with FRP jacket thickness

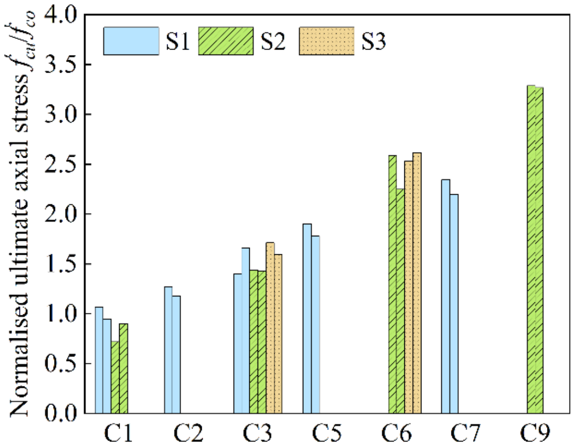

(a) Normalised ultimate axial stress

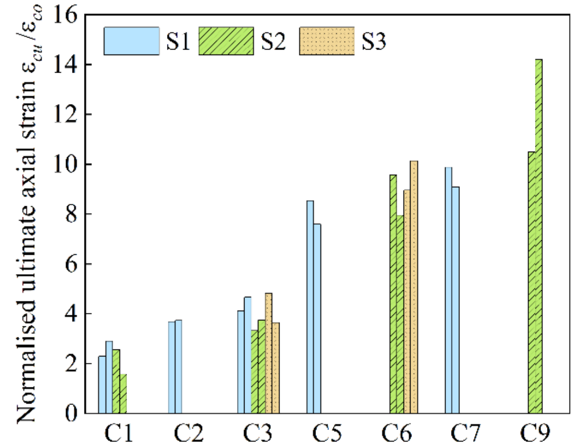

(b) Normalised ultimate axial strain

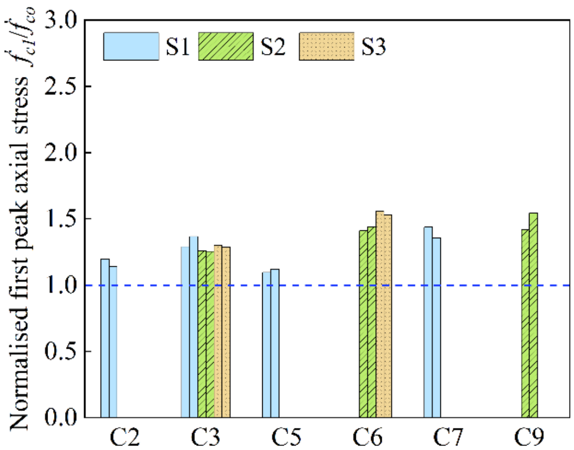

(c) Normalised first peak stress

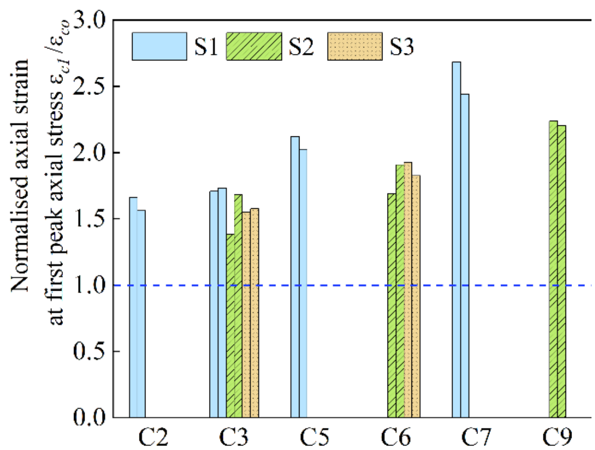

(d) Normalised axial strain at first peak stress

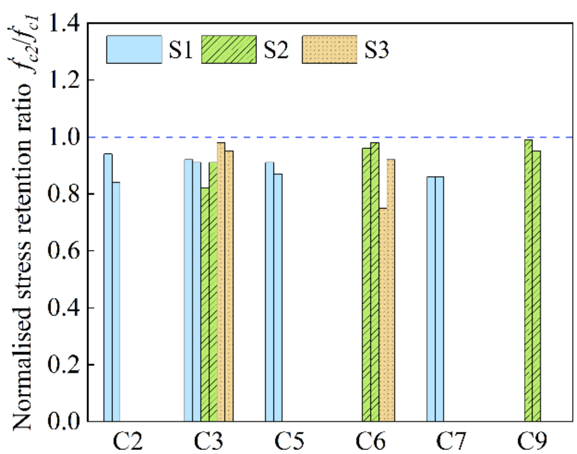

(e) Stress retention ratio

Figure 4.7 Influence of FRP jacket thickness

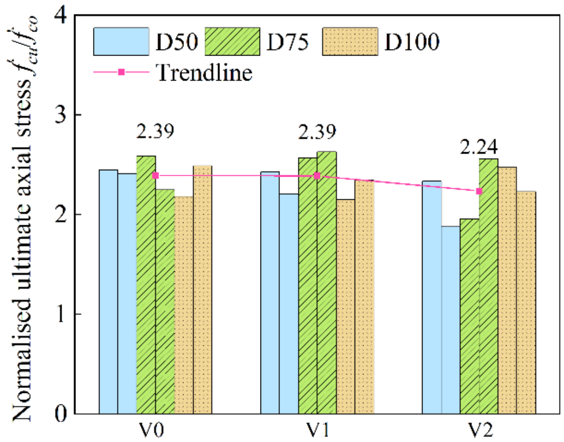

(a) Normalised ultimate axial stress

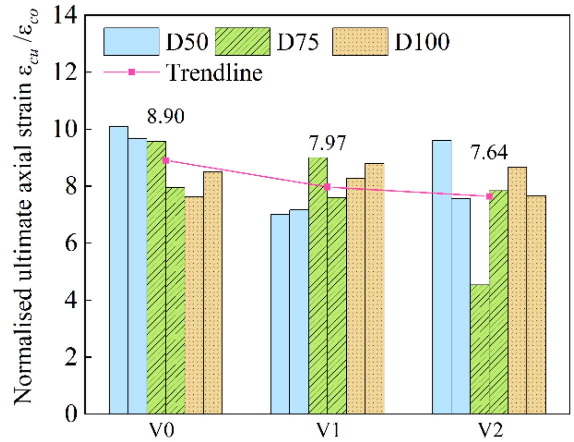

(b) Normalised ultimate axial strain

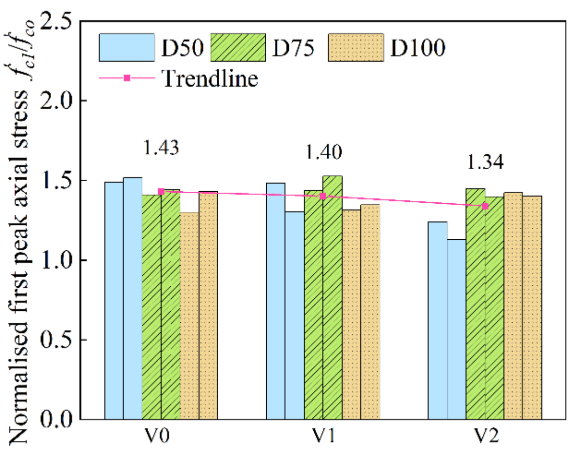

(c) Normalised first peak stress

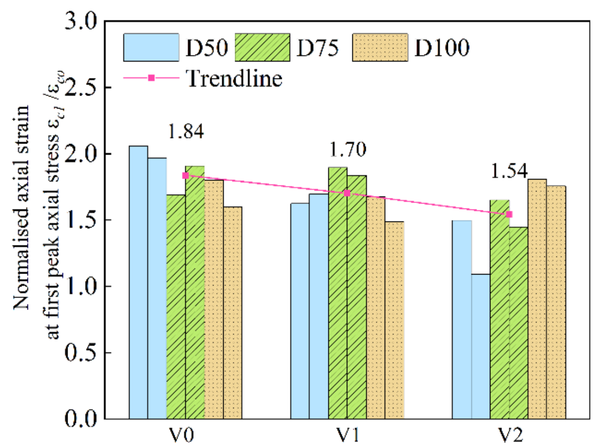

(d) Normalised axial strain at first peak stress

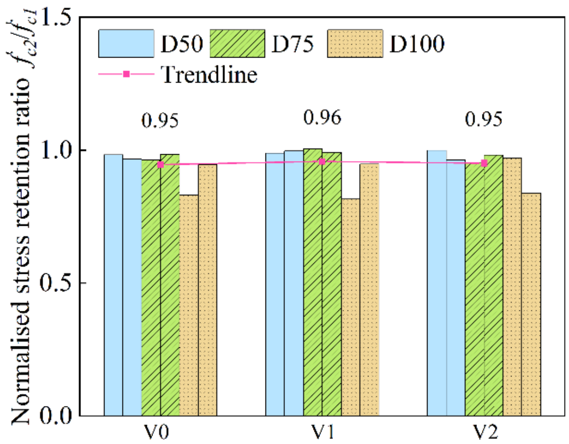

(e) Stress retention ratio

Figure 4.8 Influence of steel fibre content (S2 series specimens)

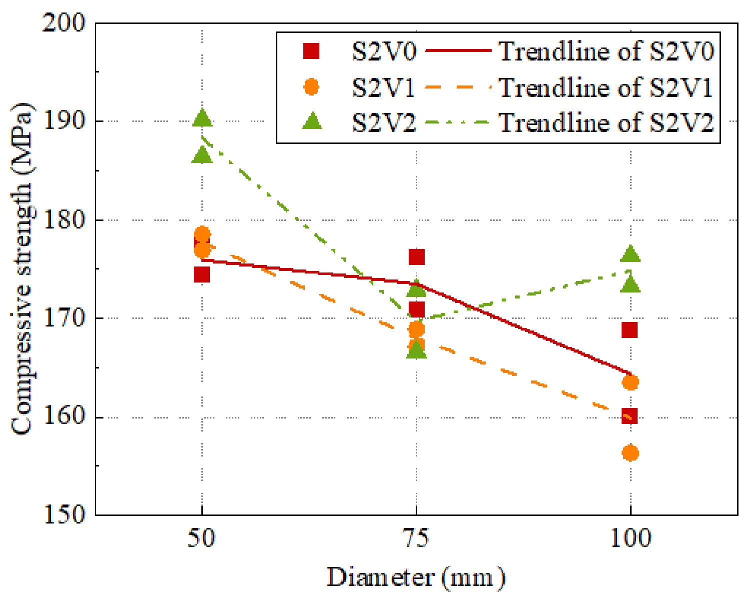

(a) Unconfined specimens

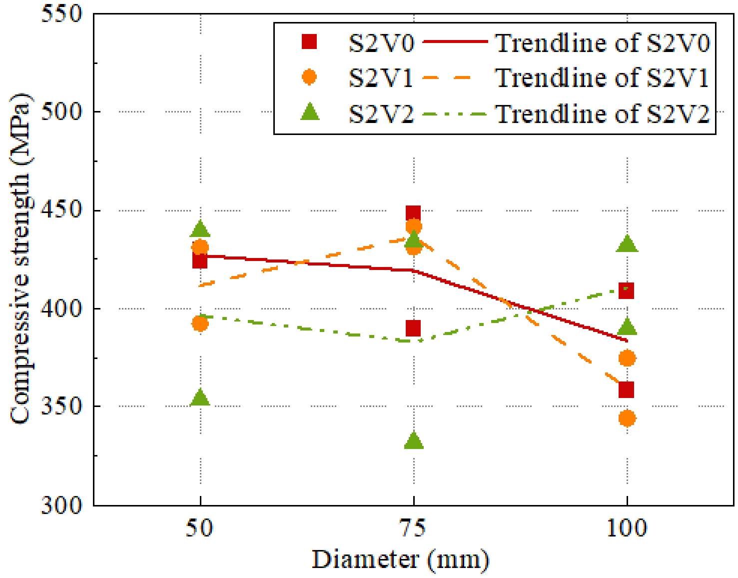

(b) Confined specimens

Figure 4.9 Influence of specimen size on compressive strength of unconfined UHPC/UHPFRC and FRP-confined UHPC/UHPFRC

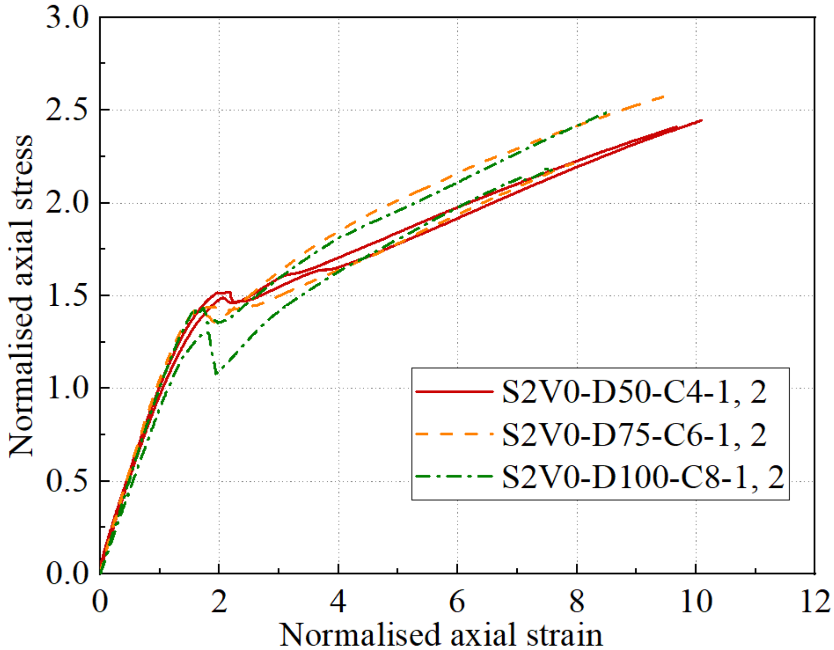

(a) S2V0-D*n* specimens

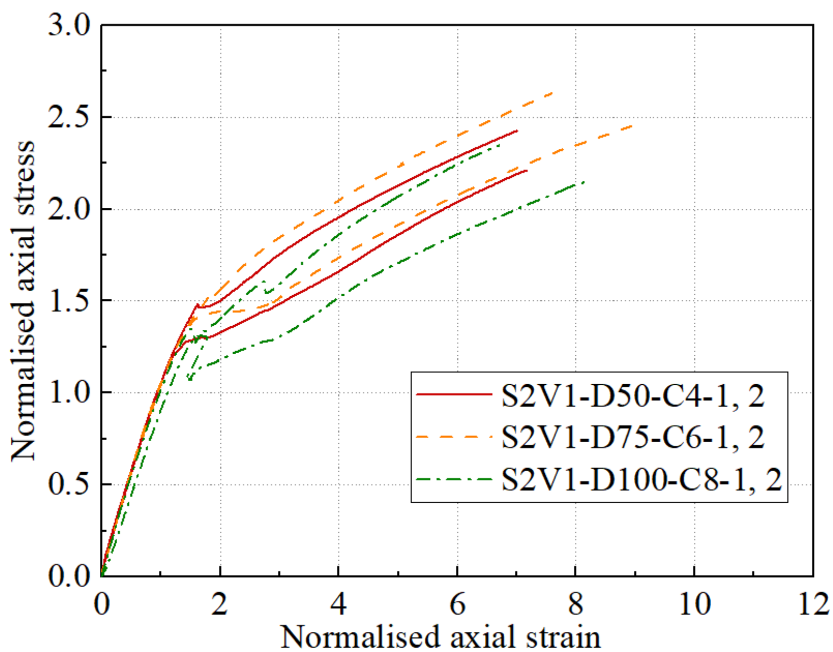

(b) S2V1-D*n* specimens

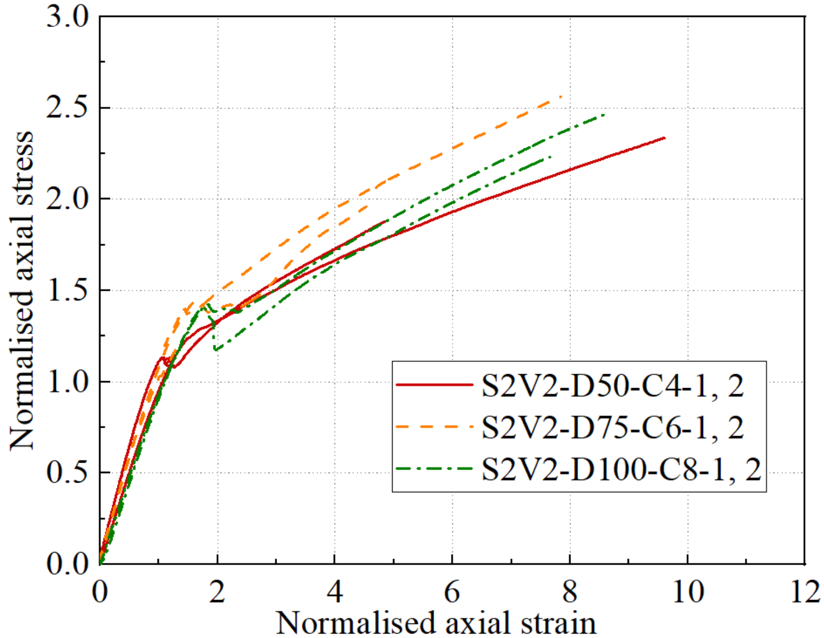

(c) S2V2-D*n* specimens

Figure 4.10 Influence of specimen size on normalised axial stress-strain curves

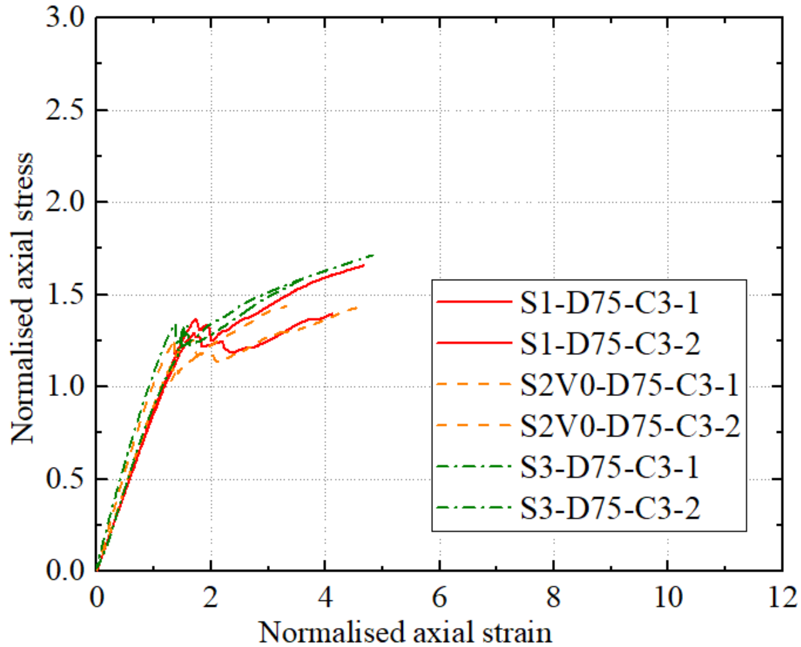

(a) S*n*-D75-C3 specimens

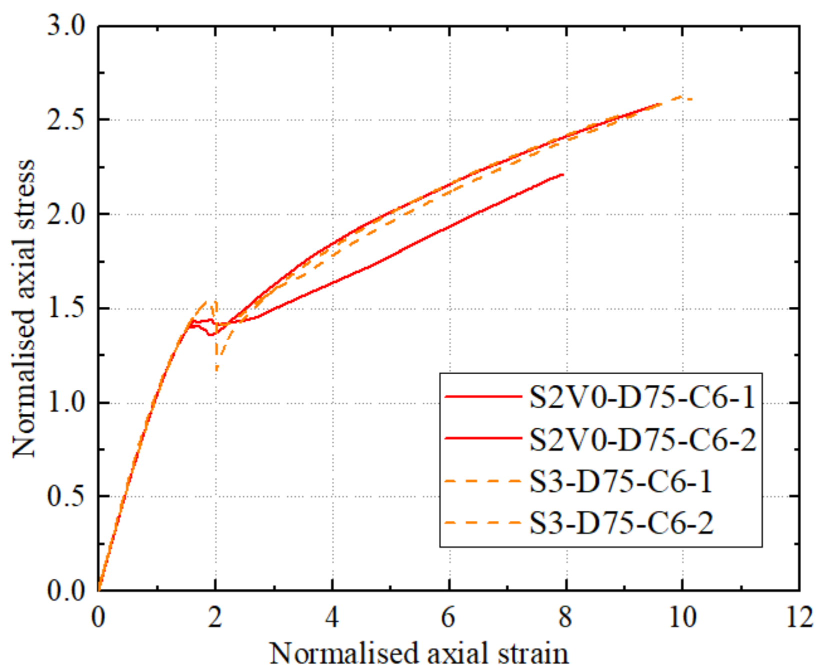

(b) S*n*-D75-C6 specimens

Figure 4.11 Influence of compressive strength on normalised axial stress-strain curves

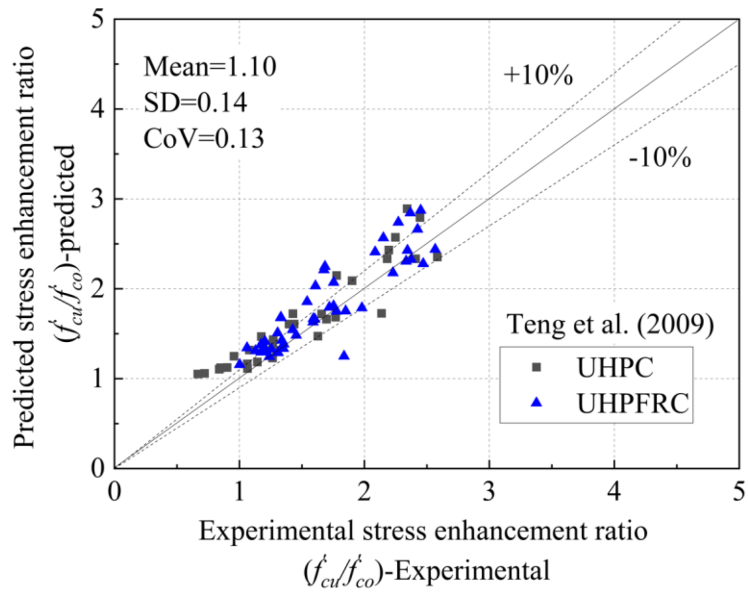

(a) Teng et al. (2009)

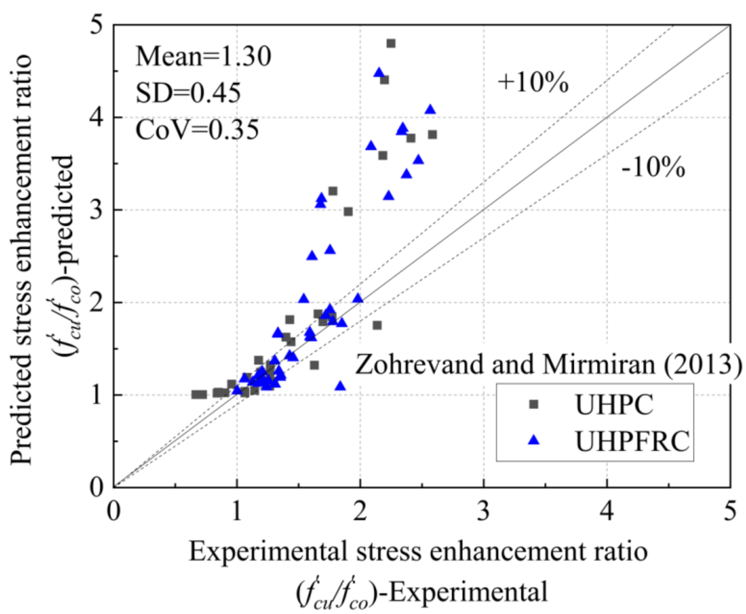

(b) Zohrevand and Mirmiran (2013)

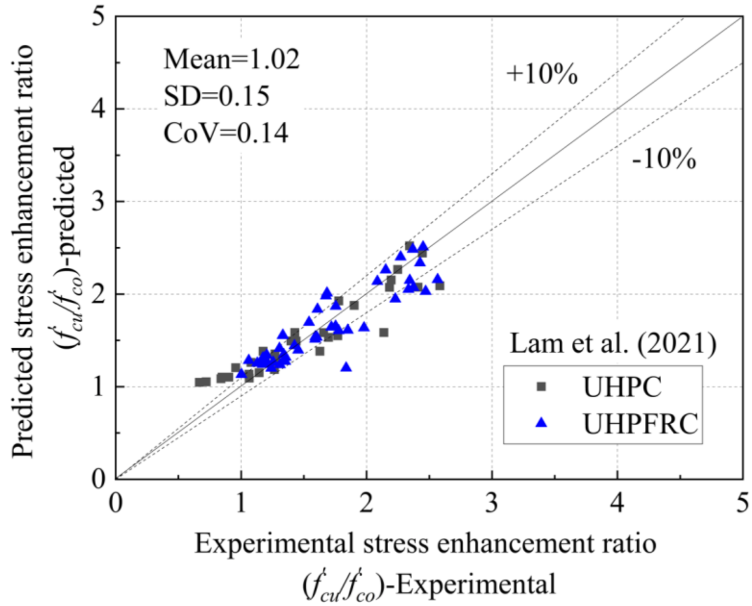

(c) Lam et al. (2021)

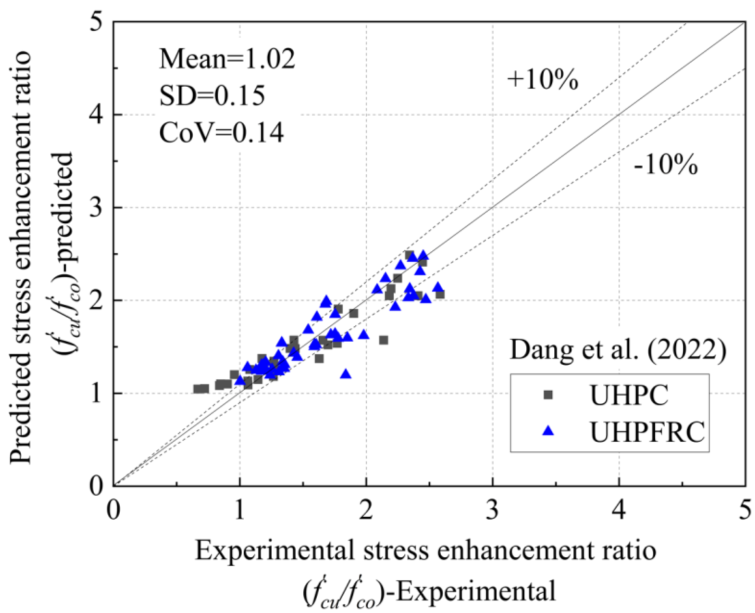

(d) Dang et al. (2022)

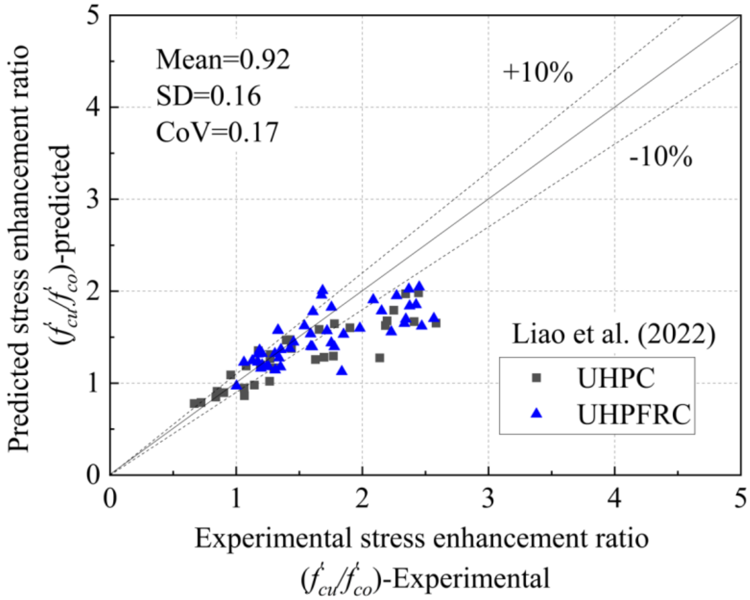

(e) Liao et al. (2022) - f'_{cu}/f'_{co}

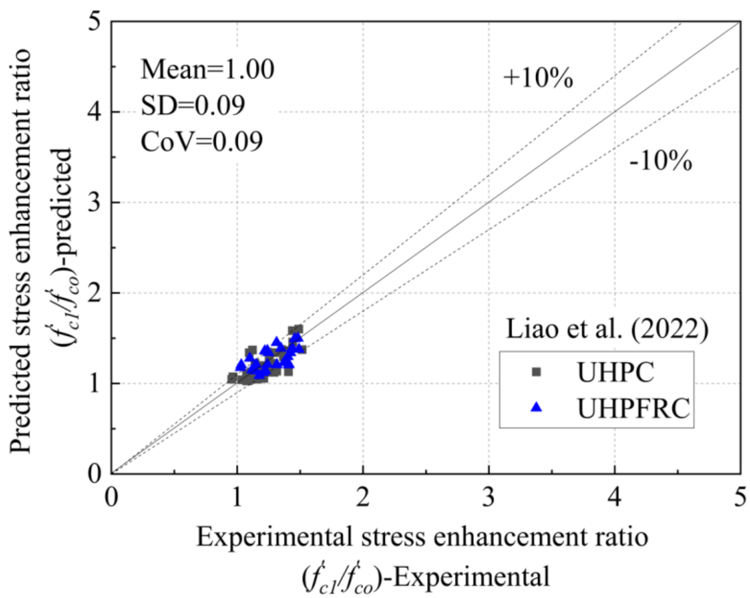

(f) Liao et al. (2022) - f'_{c1}/f'_{co}

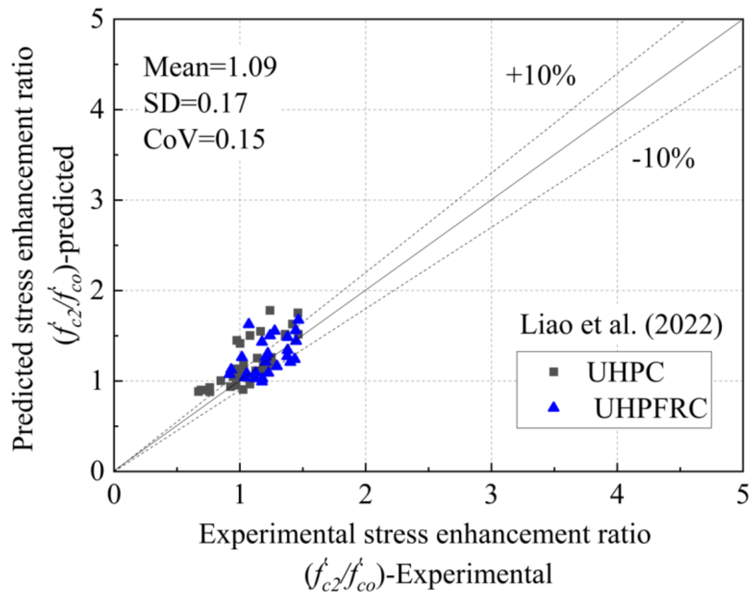

(g) Liao et al. (2022)-f'_{c2}/f'_{co}

Figure 4.12 Performance of existing models in predicting stress enhancement ratios

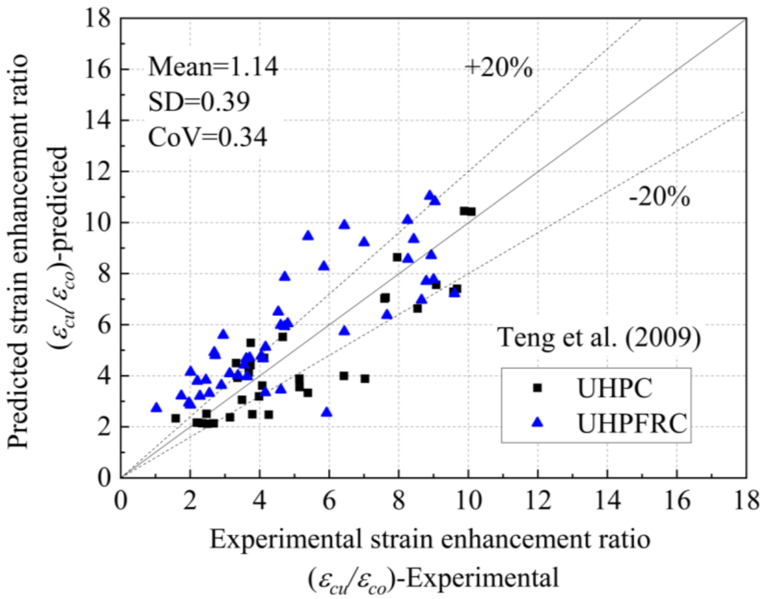

(a) Teng et al. (2009)

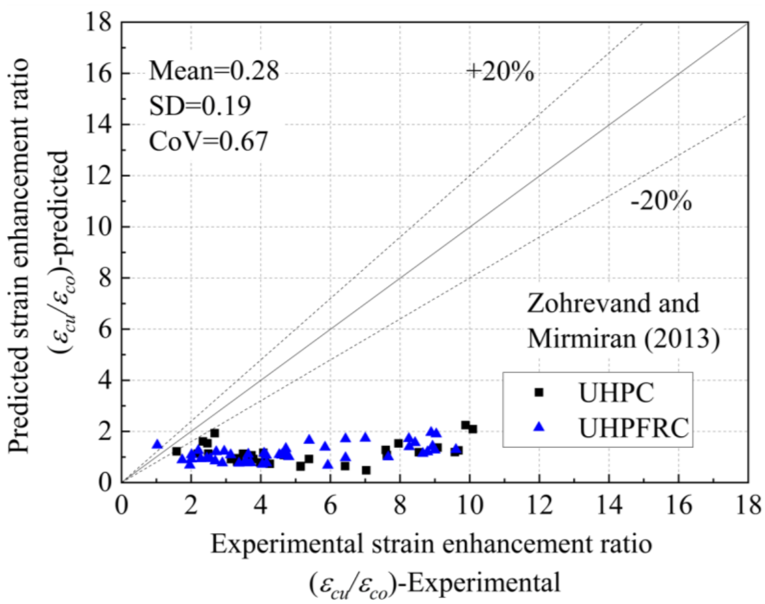

(b) Zohrevand and Mirmiran (2013)

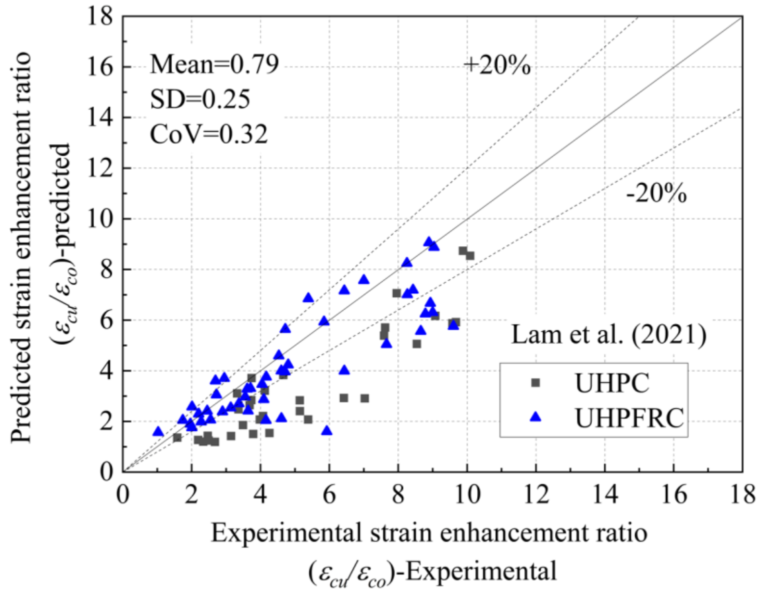

(c) Lam et al. (2021)

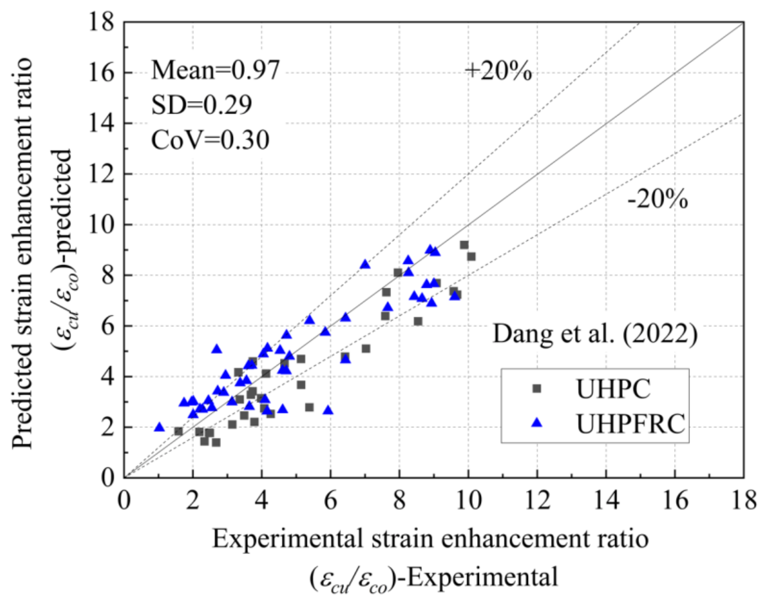

(d) Dang et al. (2022)

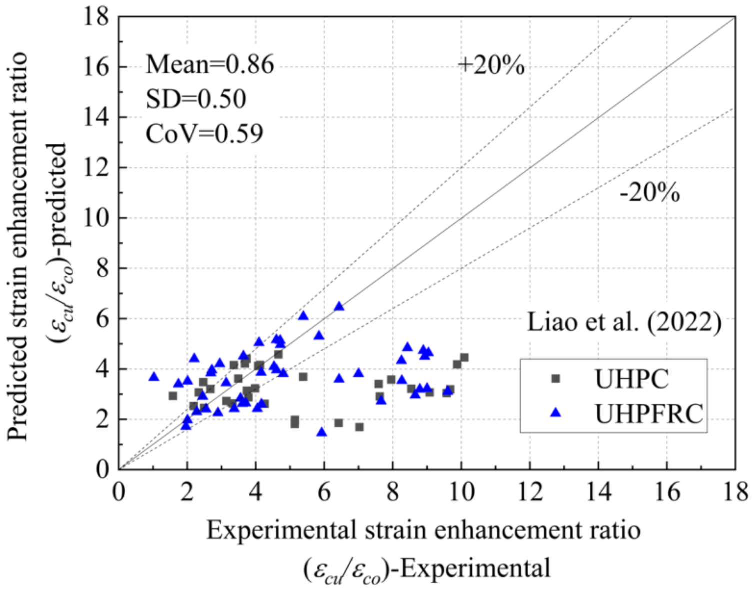

(e) Liao et al. (2022) - $\varepsilon_{cu}/\varepsilon_{co}$

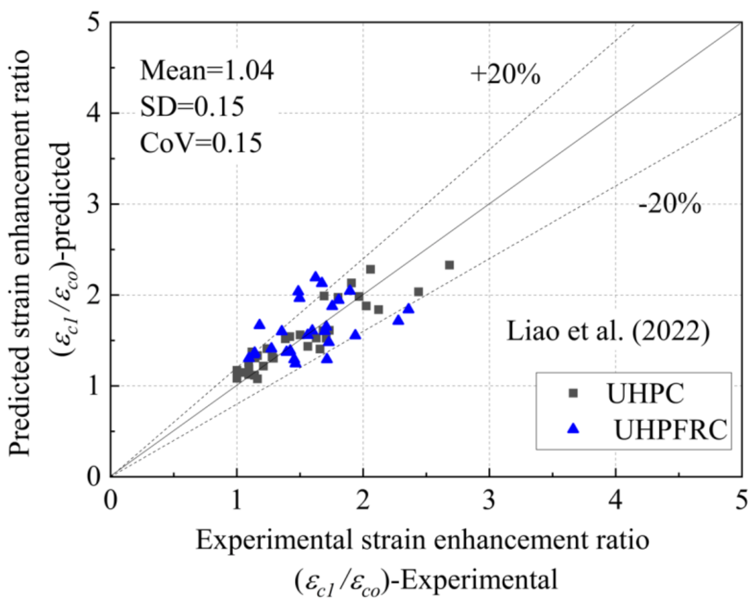

(f) Liao et al. (2022) - $\varepsilon_{c1}/\varepsilon_{co}$

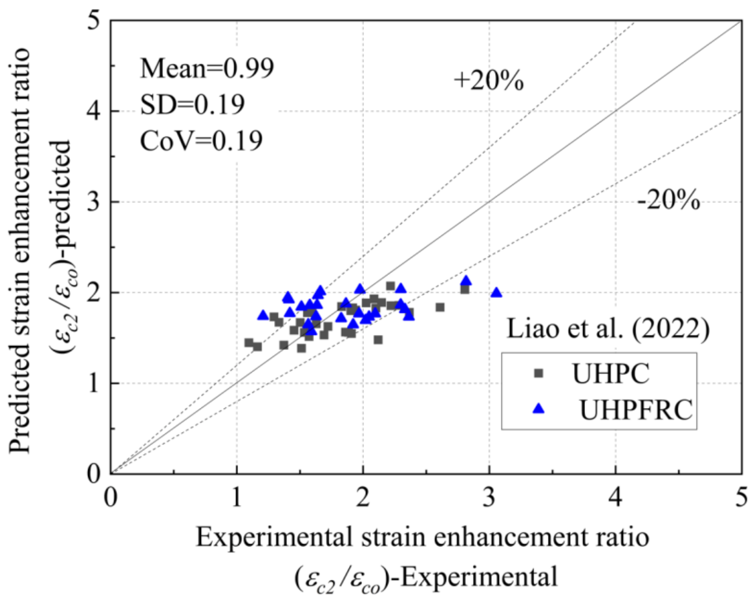

(g) Liao et al. (2022) - $\varepsilon_{c2}/\varepsilon_{co}$

Figure 4.13 Performance of existing models in predicting strain enhancement ratios

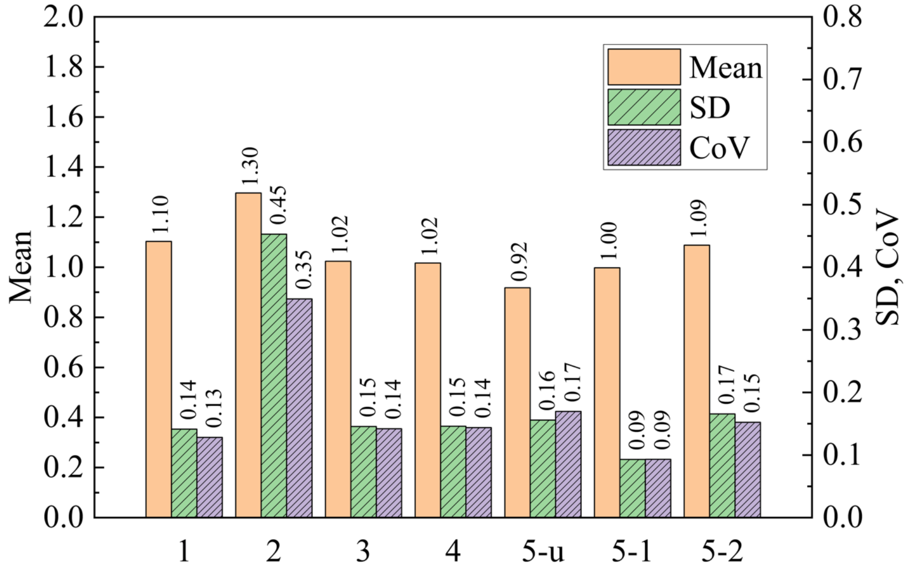

(a) Stress enhancement ratio

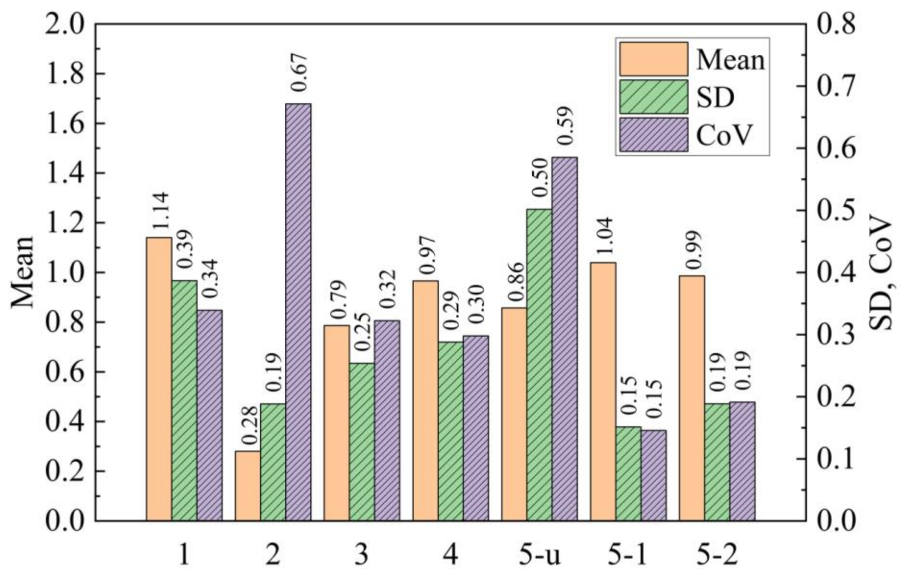

(b) Strain enhancement ratio

Figure 4.14 Accuracy of existing design-oriented models

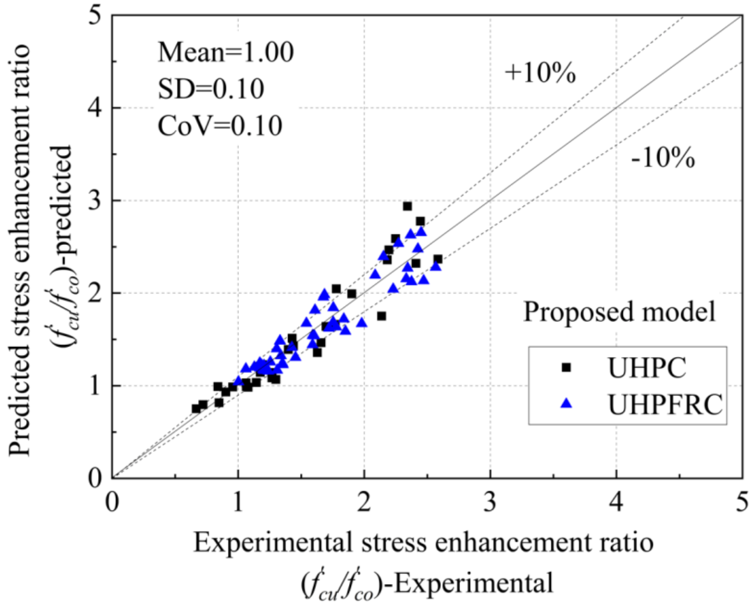

(a) Stress enhancement ratio

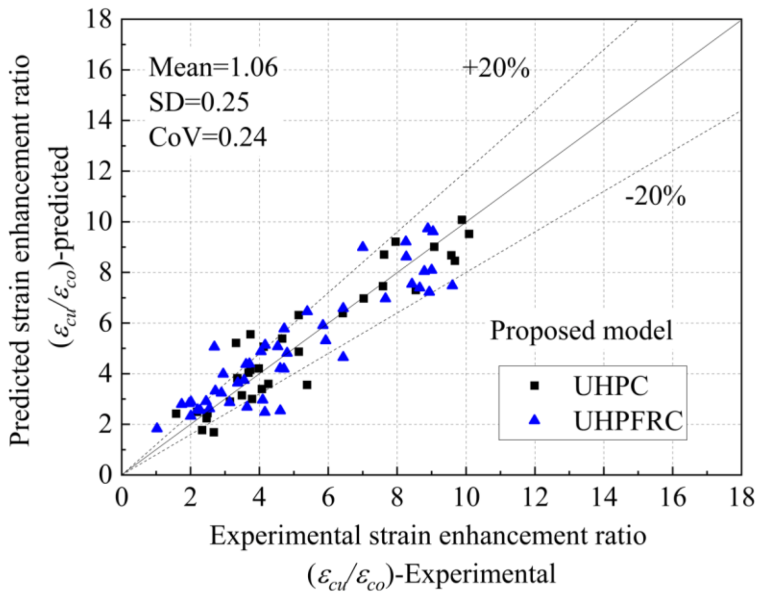

(b) Strain enhancement ratio

Figure 4.15 Performance of new equations for predicting the ultimate condition of FRP-confined UHPC and UHPFRC

CHAPTER 5
COMPRESSIVE BEHAVIOUR OF WAVY-SHAPED HYBRID REBARS UNDER MONOTONIC AXIAL COMPRESSION

5.1 INTRODUCTION

As explained in Chapter 1, the bond between the conventional uniform hybrid rebars and the surrounding concrete, as well as that between the uniform FRP tubes and the inner UHPC is comparatively weak. To address the bonding deficiencies of the conventional uniform hybrid rebars, a novel form of hybrid rebars with a wavy shape was proposed in this Ph.D. research programme. Such novel hybrid rebars were fabricated and tested firstly under monotonic axial compression to examine their compressive behaviour. The key test variables included the wave height and the thickness of the wavy-shaped GFRP tubes. The failure modes, axial load-axial strain curves, and axial strain-hoop strain curves of the test hybrid rebars were investigated in detail. A prediction method based on an existing stress-strain model for FRP-confined concrete was proposed to predict the performance of wavy-shaped hybrid rebars under compression.

5.2 FABRICATION OF A WAVY-SHAPED HYBRID REBAR

Figure 5.1 shows the schematic diagram of a segment of a typical wavy-shaped hybrid rebar. Three representative diameters of the wavy-shaped GFRP tube are indicated, namely the maximum inner diameter D_{max}, the average inner diameter D_{avg}, and the minimum inner diameter D_{min}. The thickness of the wavy-shaped GFRP tube is denoted by t and the wavelength (i.e., the distance between adjacent troughs or peaks) is denoted by λ. The wave height h is defined by the vertical distance between the peak and the trough of the wave.

The manufacturing process of a wavy-shaped hybrid rebar generally follows that for a unform hybrid rebar as demonstrated in Figure 5.2. Firstly, a wavy-shaped GFRP tube and a central GFRP rebar were fixed on a base plate. The GFRP rebar was positioned at the centre of the GFRP tube. Subsequently, a positioning plate was placed on the top of the GFRP tube. UHPC was casted into the GFRP tube through the holes drilled on the top positioning plate. During casting, the UHPC was slowly filled into the space between the GFRP rebar and the GFRP tube. The top positioning plate and the base plate were removed once the UHPC had hardened. Then, the hybrid rebars were cured in a water tank at 22°C ± 3°C for more than 28 days.

5.3 EXPERIMENTAL PROGRAMME

5.3.1 Specimen Details

To investigate the compressive properties of hybrid rebars, a long hybrid rebar was cut into several specimens with a height of approximately three times the average diameter. A total of 32 specimens were fabricated and tested under axial compression, including 16 FRP tube-confined UHPC specimens and 16 hybrid rebar specimens. Figure 5.3 shows the hybrid rebar specimens with different wave heights. For the 50-mm-diameter hybrid rebars, the diameter of the GFRP rebar was chosen as 25 mm. The wavelength λ was designed as 80 mm. Three types of wave height (i.e., 5 mm, 3 mm, and 1 mm) and two types of fibre layers (i.e., 3-ply and 5-ply) were included to fabricate the hybrid rebars. The clear height of the 50-mm-diameter specimens was 160 mm, twice the wavelength of the wavy shape (i.e., 80 mm). As shown in Figure 5.4, specimens of two sizes (D_{avg} = 33 mm and 50 mm) were tested (the smaller specimens were uniform hybrid rebars only). Thirteen-mm-diameter GFRP rebars were adopted as the internal rebars of the 33-mm small-scale hybrid rebar specimens. All the 33-mm-diameter specimens had a uniform outer GFRP tube without a wavy shape and the clear height was 100 mm, around three times the average diameter. In the existing literature, a height-to-diameter ratio of 2 to 3 is typically adopted for short concrete column tests (Ozbakkaloglu et al., 2013; Wang et al., 2017; Liu et al., 2018). The height-to-diameter ratio of 3 is long enough to avoid the end effect and short enough to avoid the slenderness effect. This study also aims to investigate the cross-sectional performance of short columns; therefore, specimens with a height-to-diameter ratio of 3 were adopted. The specimen details are summarized in Table 5.2.

The specimens were named as follows: (a) “FU” and “HR” representing the type of specimens (“FU” for FRP-confined UHPC specimens; “HR” for hybrid rebar specimens); (b) a digital number after “H” representing the wave height in mm; (c) a digital number after “L” representing the number of layers of the FRP tube; (d) letter “D” and the subsequent number denoting the average diameter (only for specimens with an average diameter of 33 mm); (e) letter “M” representing the monotonic loading pattern; (f) “1” or “2” to differentiate two nominally identical specimens. For example, specimen “HR-H5L5-M1” is one of the two nominally identical hybrid rebar specimens confined with a 5-layer GFRP tube with a wave height of 5 mm; specimen “FU-H0L1D33-M1” is one of the two nominally identical 1-layer GFRP tube confined UHPC specimens with a wave height of 0 mm.

5.3.2 Material Properties

5.3.2.1 UHPC

The UHPC mix proportion is shown in Table 5.1. The constituent raw materials and mixing procedure of the UHPC have been introduced in Section 4.4. The compressive properties of unconfined UHPC were determined based on compression tests conducted on two plain UHPC cylinders (diameter × height = 75 mm × 150 mm), following the guidelines outlined in ASTM C469/C469M-22 (2022) and ASTM C1856/C1856M-17 (2017) . The average compressive strength, elastic modulus, and the axial strain at peak stress of the plain UHPC were obtained to be 187.9 MPa, 46.9 GPa, and 0.45%, respectively.

5.3.2.2 FRP rebars

The GFRP rebars purchased from Dextra Group Co., Ltd. were used in this research. For 25-mm-diameter FRP rebars, six short FRP rebar specimens were tested under axial compression in accordance with the test method proposed by AlAjarmeh et al. (2019) (Figure 5.5). Both ends of the FRP rebar were confined with steel caps of Q355 steel with a thickness of 4 mm and the gaps between the steel caps and the FRP rebar were filled with ultra-high strength paste (UHSP) (Xiang, 2021) to avoid end failure and the loading surfaces of the specimens were capped with UHSP to ensure the flatness of the loading ends. Figure 5.5(c) shows the dimensions of the FRP rebars and the steel caps. Two free lengths (i.e., the clear length between the end steel tubes) of 50 mm and 100 mm were examined to investigate the effect of specimen length [Figures 5.5(a) and (c)]. Two strain gauges with a gauge length of 5 mm were installed at the mid-height section of each FRP rebar at an interval of 180°. PS glue was used to provide a smooth surface of the FRP rebar where the strain gauges were to be installed. The FRP rebars were loaded with a displacement rate of 0.5 mm/min until the failure according to Khorramian and Sadeghian (2019). The 13-mm-diameter FRP rebars were in the same batch as that used in Lin and Zhang (2023); therefore, the compressive properties of the FRP rebars reported in Lin and Zhang (2023) were directly used. The average compressive strength, elastic modulus, crushing strains were 585.3 MPa, 55.8 GPa, 1.048%, respectively, for the 13-mm-diameter FRP rebars.

5.3.2.3 Filament wound GFRP tubes

The filament-wound GFRP tubes were manufactured in the laboratory of the Hong Kong Polytechnic University. The detailed design of the mandrel and the fabrication process of the wavy-shaped GFRP tubes have been detailed in Chapter 3. The raw materials for the GFRP tubes remained consistent with those described in Chapter 3. The FRP tubes had average inner diameters of 33 mm and 50 mm, both featuring a consistent fibre winding angle of 89°. The elastic moduli of the 50-mm-diameter GFRP tubes, including uniform tubes and wavy-shaped tubes, were obtained through split-disk tests or internal air pressure tests as presented in Chapter 3. The values of elastic moduli for wavy-shaped GFRP tubes with different wave heights and different numbers of fibre layers can be found in Table 3.4 and Table 3.5 of Chapter 3. Although material property tests were not specifically conducted for the 33-mm-diameter uniform FRP tubes, it could be inferred that their hoop moduli should be similar to those of the 50-mm-diameter uniform tubes.

5.3.3 Test Set-Up and Instrumentation

All the compression tests were carried out on an MTS machine with a consistent displacement control rate of 0.3 mm/min. The test set-up is shown in Figure 5.6. For the specimens with an average diameter of 50 mm or 33 mm, two LVDTs covering a mid-height region of 3/4 of the total height of the specimen (i.e., gauge length = 120 mm or 75 mm) were used to measure the axial shortenings of each specimen. Apart from the mid-height LVDTs, another two LVDTs were installed between the top and bottom steel plates for measuring the full-height axial shortenings of each specimen. Four strain gauges with a gauge length of 5 mm were installed at the trough and peak sections respectively of each wavy-shaped specimen to measure the hoop strains (Figure 5.7). The same strain gauge layout was adopted for the conventional uniform hybrid rebar specimens with a diameter of 50 mm; for the uniform hybrid specimens with a diameter of 33 mm, only the mid-height section was installed with four strain gauges. To ensure the flatness of the contacting surfaces between the steel plates and the specimen, both ends of the specimen were capped with the aforementioned UHSP.

5.4 TEST RESULT AND DISCUSSION

5.4.1 General Observation

The typical failure modes of hybrid rebar specimens and FRP-confined UHPC specimens are shown in Figures 5.8(a-d). As shown in Figures 5.8(a-c), the hybrid rebar specimens generally failed with the rupture of the outer FRP tube in the hoop direction as well as the crushing of the internal UHPC and the FRP rebar. After removing the outer GFRP tube, a substantial amount of crushed UHPC was observed at the rupture location of the GFRP tube. With the crushed UHPC removed, the central FRP rebar exhibited an inclined failure plane. Figure 5.9(c) shows that the FRP-confined UHPC specimens failed by the GFRP tube rupture in the hoop direction and localized crushing of UHPC. For FRP-confined UHPC specimens, only one explosive sound was heard at the end of the testing, an indicator of the GFRP tube rupture and the crushing of UHPC. However, for some hybrid rebars (i.e., HR-H0L3-M1, HR-H5L3-M1/M2, HR-H0L5-M2, and HR-H5L5-M1/M2), two sounds were heard during the loading process. The first sudden sound was heard shortly before the final failure of the specimens. The sudden sound was accompanied by a significant decrease in the axial load, which should be attributed to the failure of the internal FRP rebar. The typical failure mode of FRP rebars can be found in Figure 5.8(e). The bare FRP rebar specimens with either a free length of 2D and 4D failed by splitting or crushing of the FRP rebar. By comparing the failure modes of the FRP rebar in hybrid rebar specimens with the bare FRP rebar specimens, it could be observed that the splitting behaviour of the FRP rebars was prevented by the external confinement provided by the UHPC and GFRP tube. The key test results of the compression tests of FRP rebars are summarised in Table 5.3. For specimens with a free length of 2D, the compression tests yielded a peak stress of 744.5 MPa, an elastic modulus of 55.1 GPa and an ultimate strain of 1.26%. Similarly, for specimens with a free length of 4D, the compression tests resulted in a peak stress of 685.2 MPa, an elastic modulus of 56.3 GPa and an ultimate strain of 1.13%. AlAjarmeh et al. (2019) found that FRP rebars with a free length smaller than 8D generally failed by crushing under axial compression. Therefore, both these two types of specimens (i.e., 2D and 4D) fall within the range of crushing failure zone. Previous experimental results have demonstrated that the compressive properties for those specimens within this range is independent of the free length of the specimens (Bruun, 2014; AlAjarmeh et al., 2019). Since the results of shorter 2D specimens may better represent the material properties of the FRP rebars under compression, in subsequent analyses, the compressive properties of the 2D specimens with a larger ultimate strain of 1.26% were used, along with the corresponding peak stress of 744.5 MPa and the elastic modulus of 55.1 GPa.

5.4.2 Axial Load-Axial Strain Curves

In this chapter, axial compressive stresses and strains are defined to be positive while hoop tensile stresses and strains are defined to be negative, unless otherwise specified. The axial strains were obtained from the mid-height LVDTs to illuminate the influence of deformations of the specimen ends. The axial load-axial strain curves of the hybrid rebars and the bare FRP rebars under axial compression are presented in Figure 5.9. Compared to the 3-ply hybrid rebars, the 5-ply hybrid rebars exhibited a less pronounced load drop at the transition region between the two branches of the axial load-axial strain curves. Figure 5.10 presents two typical diagrammatic average axial stress-strain curves of hybrid rebars. The average axial stresses were calculated by dividing the axial loads by the cross-sectional area of the specimen corresponding to the average diameter (D_{avg}) of the wavy-shaped GFRP tube. As shown in Figure 5.10, the stress-strain curves of hybrid rebars can be classified into two types: for specimens in which FRP rebars did not experience premature failure, the experiments terminated with the rupture of the outer GFRP tube, exhibiting a three-stage stress-strain curve; in the case of specimens in which FRP rebars failed prior to the failure of the outer GFRP tube, the stress-strain curve demonstrates four stages.

For both types of curves, the stress-strain curves exhibited an initial linear elastic portion (i.e., Stage 1). After the axial stress reached approximately the peak stress of the corresponding unconfined UHPC, a sudden stress drop occurred (i.e., Stage 2). The axial stress continued increasing until the rupture of the GFRP tube or the failure of the internal FRP rebar (i.e., Stage 3). If the FRP rebar failed before the rupture of the GFRP tube, the axial stress experienced a significant drop and then gradually increased again until the rupture of the outer GFRP tube [i.e., Stage 4 in Figure 5.10 (b)]. The critical values f_1/f_{co}, f_2/f_{co}, f_3/f_{co}, f_4/f_{co}, E_3/E_1, and ε_3 of the teste specimens are summarized in Table 5.4, where the values of E_1 were calculated by taking the slope of the secant line between the point corresponding to an axial strain of 50 microstrains and the point corresponding to 40% of the compressive strength of unconfined UHPC according to ASTM C469/C469M-22 (2022); the values of E_3 were obtained through a linear regression with the test stress and strain data points during Stage 3.

Evidently, Figure 5.9 shows that the axial load-axial strain curves of hybrid rebars are above the curves of the corresponding bare FRP rebars. Due to the difference in cross-sectional area, the corresponding average axial stress in the hybrid rebar is lower than that in the FRP rebar. For instance, the cross-sectional area of the H0L5 hybrid rebar is four times that of the FRP rebar. The load-bearing capacity of the hybrid rebar is approximately 750 kN, which equates to a compressive strength of around 381 MPa, while the compressive strength of the FRP rebar is 744.5 MPa. Besides, the ultimate strains corresponding to the rupture of the external GFRP tube are obviously larger than the ultimate strains of the bare FRP rebars. The results indicate that the ductility values of the test hybrid rebars are significantly larger than those of the corresponding bare FRP rebars. The increase in ultimate strain can be attributed to the excellent ductility of the confined UHPC.

5.4.3 Effect of Specimen Size

In addition to the aforementioned hybrid rebar with an average diameter of 50 mm, four small-scale uniform hybrid rebars and four small-scale uniform GFRP tube confined UHPC specimens with a diameter of 33 mm were also tested. Figures 5.11(a) and (b) show the axial stress-strain curves of these small-scale specimens. According to Eq. (4.1) in Chapter 4, the confinement stiffness ratios for the H0L1D33 specimens and the H0L2D33 specimens were approximately 0.027 and 0.055, respectively. In Chapter 4, it was found that the critical confinement stiffness ratio for ensuring a hardening stress-strain behaviour (i.e., strong confinement) for UHPC with a strength greater than 150 MPa is 0.036. Therefore, the H0L1D33 series specimens were expected to possess weak FRP confinement. The H0L2D33 series specimens exhibited superior ductility and much larger compressive strength than the corresponding FRP-confined UHPC specimens.

In Figure 5.11(c), a comparison is made between the axial stress-strain curves of the H0L2D33 series specimens and the H0L3 series specimens. The diameter and the tube thickness of the H0L3 series specimens were 1.5 times those of the smaller-scale H0L2D33 series specimens. According to Eq. (4.1) in Chapter 4, the confinement stiffness ratios of the specimens of the two sizes were close to each other. Figure 5.11(c) shows that the stress-strain curves of the 50-mm-diameter FRP-confined UHPC specimens are generally lower than those of the 33-mm-diameter FRP-confined UHPC specimens, which may be attributed to the size effect of FRP-confined UHPC. Besides, in Chapter 4, it was found that a reduction of specimen size could relieve the stress reduction after the first peak stress of FRP-confined UHPC. However, it can be seen that the stress-strain curves of the 50-mm-diameter hybrid rebars are higher than those of the 33-mm-diameter hybrid rebars. It is possible that the concrete layer and the external GFRP tube of the 33-mm-diameter hybrid rebars were too thin, leading to some defects that affected the effectiveness of FRP confinement.

5.4.4 Effect of Wave Height

Figure 5.12 shows the influence of wave height of the wavy shape on the critical parameters (as summarised in Table 5.4) of the 50-mm-diameter hybrid rebars. It can be observed that the parameters f_1/f_{co}, f_2/f_{co} f_3/f_{co}, E_3/E_1 do not exhibit an obvious trend with an increase in the wave height. It is known that the first portion of the stress-strain curve of FRP-confined concrete follows that of unconfined concrete due to the passive confinement nature of FRP confinement, while the slope in the third stage depends greatly on the FRP confinement stiffness. The average axial strain at the end of the third stage (ε_3) of all the test specimens was 1.57%, which is larger than the ultimate compressive strain of 1.26% of the bare FRP rebar, indicating that the confinement provided by the outer UHPC and the wavy tube may be helpful in preventing of the fibre-micro buckling of the FRP rebar.

5.4.5 Confinement Mechanism

The hoop strain-axial strain curves of wavy-shaped hybrid rebars and their corresponding wavy-shaped GFRP tube-confined UHPC specimens are plotted and compared in Figure 5.13. Since the wavy-shaped FRP tubes had varied diameters, the hoop strains were compared at two locations: (a) the peak location with the maximum diameter (D_{max}); and (b) the trough location with the minimum diameter (D_{min}). The general trend shows that the absolute values of the hoop strains of the wavy-shaped FRP tube confined UHPC specimens were larger than those of the wavy-shaped hybrid rebar specimens at both the peak and trough locations when the axial strains exceeded the ultimate axial strain of UHPC. The difference in dilation behaviour between the wavy-shaped hybrid rebars and the wavy-shaped GFRP tube-confined UHPC specimens may be explained by the distinct expansion characteristics of FRP rebars and UHPC. Previous studies have commonly reported or assumed the Poisson's ratios of FRP rebars to be within a range of 0.22 to 0.3 (Nanni et al., 1993; Castro and Carino, 1998; Gooranorimi et al., 2017). Teng et al. (2019) reported a Poisson's ratio of 0.21 for unconfined UHPC. While UHPC possesses a slightly lower Poisson's ratio compared to FRP rebars in the elastic range, the dilation of the former increases dramatically during the later loading stage. The inclusion of an FRP rebar in the hybrid rebar results in a smaller volume of UHPC compared with a GFRP tube-confined solid UHPC specimen, leading to a less pronounced dilation behaviour in the former.

As the wavy tubes had different diameters along the tube axis, the hoop strain distributions along the axial direction should be different from those of conventional uniform FRP tube-confined concrete. Figure 5.14 presents the relationships of the hoop strains between the peak and trough locations of the wavy-shaped specimens and uniform specimens, including GFRP tube-confined UHPC and hybrid rebar specimens. For a direct comparison, the hoop strains of the uniform specimens at the same locations as the peak and trough locations of wavy-shaped specimens are compared. As shown in Figures 5.14(a) and 5.14(b), the curves are generally distributed near the bi-sector, indicating a close similarity in the hoop strains at different heights for uniform specimens. More specifically, for wavy-shaped specimens, including both GFRP tube-confined UHPC and hybrid rebar specimens, the absolute values of hoop strains at the peak are generally larger than those at the trough during the early loading stage. It was also found that the distance between the plotted curves and the diagonal line during the early loading stage is generally proportional to the wave height, indicating that as the wave height increases, the difference in hoop strains between the peak and trough locations also increases. The difference in geometrical properties (i.e., diameter) and mechanical properties at the peak and trough locations may be the reasons for the above phenomenon. Taking specimen HR-H5L5-M1 as an example, the diameter at the peak location was 1.22 times that at the trough location. If the same amount of fibres was assumed to be applied at the two locations, the confinement level at the peak location should be lower than that at the trough location. The second reason is that the actual thickness of fibres at the peak location was smaller than that at the trough location. Although the winding process with varied carriage speeds had been adopted in this research programme for achieving uniform properties of the wavy-shaped FRP tubes at different locations as presented in Chapter 3, fibre sliding still slightly occurred during the winding process, leading to smaller amount of fibres at the peak location.

After the initial loading stage, the relationship between the hoop strains at the peak location and those at the trough location becomes unclear. Several curves intersect with the diagonal line, indicating that the absolute values of the hoop strains at the peak locations are less than those at the trough locations. This may be attributed to the development of non-uniform damage in UHPC. To gain a clearer understanding of the distribution of hoop strains in wavy-shaped specimens, the hoop strains at the peak and trough locations are plotted against the axial strains respectively, and compared on the same graph, as shown in Figure 5.15. It can be observed that, during the initial loading stage of wavy-shaped specimens, when the axial strain is smaller than the ultimate strain of UHPC, the curve at the peak location is clearly below that at the trough location. When the axial strain exceeds the ultimate strain of UHPC, the curves at peak locations of most wavy-shaped specimens remains significantly below those at trough locations. Only a small number of curves exhibit a change in slope, resulting in lower absolute values of hoop strains at peak locations than those at trough locations. Theoretically, the specimen tended to fail due to FRP tube rupture at the peak location with larger hoop strains. However, the test results indicated that the rupture of the FRP tube occurred not only at the peak locations. The FRP tube rupture may also be affected by the cracking of the internal UHPC in the specimens. The failure of UHPC resulted in large diagonal cracks, which occurred relatively randomly. Consequently, after these diagonal cracks formed, the hoop strains near the cracks suddenly increased. Ultimately, the FRP tube fails at the locations of these diagonal cracks. The formation of such cracks altered the original distribution pattern of the hoop strains.

5.4.6 Comparison with FRP-Confined Solid UHPC

In the present study, the fibre orientation of the GFRP tubes was close to the tube hoop direction (i.e., ±89°); therefore, the contribution of the GFRP tubes to the axial load-bearing capacity of a hybrid rebar could be neglected. The axial load resisted by a hybrid rebar at a given axial strain (ε) is equal to the summation of the loads resisted by the UHPC annulus and the internal FRP rebar. The loads resisted by the UHPC annulus and the FRP rebar can be calculated by the following equations:

$$F_a = \frac{A_a}{A_u} F_u \tag{5.1}$$

$$F_b = E_b \varepsilon A_b \tag{5.2}$$

$$F_h = F_a + F_b \tag{5.3}$$

where F_a is the load resisted by the FRP-confined UHPC annulus in the hybrid rebar; F_h is the summed load resistance of the FRP-confined UHPC annulus and the FRP rebar; E_b is the compressive elastic modulus of the FRP rebar, obtained from the compression tests of bare FRP rebars; A_u, A_b, and A_a are the cross-sectional areas of the UHPC in the corresponding FRP-confined solid UHPC specimen, the FRP rebar, and the UHPC annulus in the hybrid rebar, respectively. The calculated axial load-strain curves and the tested curves of the hybrid rebars are shown in Figure 5.16. The calculated curves terminated at the ultimate axial strains of the corresponding FRP rebars under compression. Therefore, it is evident that the hybrid rebars exhibited better deformation capacities compared to the theoretically calculated values. The calculated curves are very close to the experimental curves, including the slopes of the curves in the first and third stages (i.e., Stage 1 and Stage 3). Therefore, it may be concluded that the stress-strain curve of a wavy-shaped hybrid rebar could be accurately predicted by the summation of the curves of the UHPC annulus and the internal FRP rebar.

5.5 THEORETICAL ANALYSIS

5.5.1 Jiang and Teng's Model

As shown in Figure 5.16, the axial load resistance of a hybrid rebar generally consists of the resistances of the FRP-confined UHPC annulus and the inner FRP rebar. As a result, the axial load-axial strain curves of a hybrid rebar could be predicted if the curves of the two constituent materials are known. The axial stress-strain behaviour of FRP-confined UHPC annulus is assumed to be identical to that of FRP-confined solid UHPC; the later may be predicted with Jiang and Teng (2007) analysis-oriented model. Jiang and Teng (2007) model was originally proposed based on a large database of FRP-confined normal strength concrete (NSC) specimens. Previous studies showed that this model is capable of providing close predictions for the axial stress-strain curves and the axial strain-hoop strain curves for FRP-confined NSC (Zohrevand and Mirmiran, 2011; Ozbakkaloglu, 2013; Chen et al., 2016; Zeng et al., 2020).

It is assumed that the behaviour of FRP-confined concrete is independent on the stress path in Jiang and Teng's (2007) model, which means that the axial stress and axial strain of FRP-confined concrete at a given hoop strain are equal to those of the same concrete confined with a constant confining pressure corresponding to that lateral strain. The key components of Jiang and Teng's (2007) model are summarized below.

Confining pressure:

$$f_l = -\frac{2E_{frp}t\varepsilon_h}{D} \tag{5.4}$$

where f_l = confining pressure; E_{frp} and t are the elastic modulus and the thickness of FRP jacket/tube, respectively; ε_h represents the hoop strain of the FRP jacket/tube; D is the diameter of the concrete cross section.

Active-confinement base model:

$$\frac{\sigma_c}{f_{cc}^{\prime *}} = \frac{(\varepsilon_c/\varepsilon_{cc}^*)r}{r-1+(\varepsilon_c/\varepsilon_{cc}^*)^r} \tag{5.5}$$

$$r = \frac{E_c}{E_c - f_{cc}^{\prime *}/\varepsilon_{cc}^*} \tag{5.6}$$

$$\frac{f_{cc}^{\prime *}}{f_{co}^{\prime}} = 1 + 3.5\frac{f_l}{f_{co}^{\prime}} \tag{5.7}$$

$$\frac{\varepsilon_{cc}^*}{\varepsilon_{co}} = 1 + 17.5\left(\frac{f_l}{f_{co}^{\prime}}\right)^{1.2} \tag{5.8}$$

where $f_{co}^{\prime}$ and E_c are the peak axial stress and the elastic modulus of unconfined concrete respectively; σ_c and ε_c are the axial stress and the axial strain of concrete, respectively; f_l is confining pressure; $f_{cc}^{\prime *}$ and ε_{cc}^* represent the peak axial stress and its corresponding axial strain at a given lateral confining pressure; ε_{co} is the axial strain at peak stress of unconfined concrete.

Hoop strain-axial strain relationship:

$$\frac{\varepsilon_c}{\varepsilon_{co}} = 0.85\left(1 + 8\frac{f_l}{f'_{co}}\right)\left\{\left[1 + 0.75\left(\frac{-\varepsilon_h}{\varepsilon_{co}}\right)\right]^{0.7} - exp\left[-7\left(\frac{-\varepsilon_h}{\varepsilon_{co}}\right)\right]\right\} \tag{5.9}$$

5.5.2 Comparisons and Discussions

The comparisons of the axial load-axial strain curves between the predictions and the test results are shown in Figure 5.17. The hoop elastic moduli of the GFRP tubes obtained from the air pressure tests were used in the predictions; the compressive strength (f'_{co}), the corresponding axial strain (ε_{co}) and the elastic modulus ($E_c = 46.9\ GPa$) of UHPC were obtained from compression tests of the unconfined UHPC specimens. The predicted curves terminated at the measured hoop rupture strains averaged from two nominally identical specimens. For the wavy-shaped GFRP tube-confined UHPC specimens and hybrid rebar specimens, the average inner diameters (i.e., D_{avg}) and the hoop elastic moduli of the GFRP tubes at the of the middle location were used. The onset point of Stage 4 (see Figure 5.10) was assumed to be at an axial strain of 0.015, which is equal to the average value of test results of specimens with four stages of stress-strain curves. It should be noted that this value is only applicable to the hybrid rebars in the present study. Further research is needed to better predict this axial strain when more test data are available in the future. As discussed in the preceding sections, the load drop in Stage 4 was caused by the damage of the FRP rebar. After the load drop, the axial load of the FRP rebar did not reduce to zero due to the confinement provided by surrounding UHPC and FRP tube. It was found from the test results that the residual loads of the FRP rebars after the load drop (i.e., the loads at the onset point of Stage 4) were approximately 60% of their load-bearing capacities. Therefore, a 40% load loss of FRP rebars was assumed in the prediction of the load-strain curves in Stage 4 in the present study.

Figure 5.17 shows that the predicted load-strain curves generally agree well with the experimental curves in Stage 1. The curves of some specimens in Stage 2, characterized by a sudden load drop after the first peak load, could not be accurately predicted. However, for specimens HR-H0L5-M1, HR-H5L5-M1, and HR-H5L5-M2 whose load drops in Stage 2 are not significant, the predicted curves in Stage 2 are close to the test curves. For the other specimens with obvious load drops, the predicted loads in Stage 2 are generally larger than the test results.

5.6 CONCLUSIONS

This chapter has presented the results of an experimental programme on the stress-strain behaviour of wavy-shaped hybrid rebars in which the wavy-shaped GFRP tubes with fibres oriented near the hoop direction were fabricated and used to provide confinement to the UHPC and the central FRP rebar. Through testing 16 wavy-shaped GFRP tube confined UHPC specimens and 16 wavy-shaped hybrid rebar specimens, the influences of wave height, FRP tube thickness, and specimen size have been examined. The results and discussions presented in this chapter may lead to the following conclusions:

(1) The presence of a wavy shape in the GFRP tube did not have an obvious effect on the failure modes of hybrid rebars. Two failure modes of hybrid rebars were observed: (a)

failure due to GFRP tube rupture which occurred before the failure of the internal GFRP rebar; and (b) failure of the internal GFRP rebar prior to the rupture of the GFRP tube, leading to a significant load drop.

(2) The wavy-shape GFRP tubes fabricated in this research programme could provide sufficient confinement to the internal UHPC and FRP rebar. When sufficient confinement was provided (i.e., $\rho_k > 0.036$), the hybrid rebars demonstrated high efficacy in improving the compressive performance of FRP rebars ranging from 13 mm to 25 mm in diameter. Compared to FRP rebars, significant enhancements in ductility were observed for hybrid rebars.

(3) The axial stress-strain behaviours of wavy-shaped hybrid rebars with wave heights ranging from 1 mm to 5 mm are similar, indicating that the wave height within the studied range had a limited effect on the confinement mechanism in hybrid rebars.

(4) The theoretical method based on Jiang and Teng's (2007) model for FRP-confined concrete predicts reasonably well the axial load-strain curves of the test wavy-shaped hybrid rebars, especially when there is no significant load drop after the first peak axial load.

5.7 REFERENCES

AlAjarmeh, O., Manalo, A., Benmokrane, B., Vijay, P., Ferdous, W. and Mendis, P. (2019). "Novel testing and characterization of GFRP bars in compression", *Construction and Building Materials*, 225, 1112-1126.

ASTM C1856, C1856M (2017a). *Standard Practice for Fabricating and Testing Specimens of Ultra-High Performance Concrete*, American Society for Testing and Materials (ASTM), West Conshohocken, PA.

ASTM C469/C469M (2022). *Standard Test Method for Static Modulus of Elasticity and Poisson Ratio of Concrete in Compression*, American Society for Testing and Materials (ASTM), West Conshohocken, PA.

Bruun, E. (2014). "GFRP bars in structural design: Determining the compressive strength versus unbraced length interaction curve", *Journal of Student Science and Technology*, 7(1).

Castro, P.F. and Carino, N.J. (1998). "Tensile and nondestructive testing of FRP bars", *Journal of Composites for Construction*, ASCE, 2(1), 17-27.

Chen, G., He, Y., Jiang, T. and Lin, C. (2016). "Behavior of CFRP-confined recycled aggregate concrete under axial compression", *Construction and Building Materials*, 111, 85-97.

Gooranorimi, O., Suaris, W. and Nanni, A. (2017). "A model for the bond-slip of a GFRP bar in concrete", *Engineering Structures*, 146, 34-42.

ISO 7509 (2015). *Plastics Piping Systems - Glass-Reinforced Thermosetting Plastics (GRP) Pipes-Determination of Time to Failure under Sustained Internal Pressure*, International Organization for Standardization, Geneva, Switzerland.

Jiang, T. and Teng, J.G. (2007). “Analysis-oriented stress–strain models for FRP–confined concrete”, *Engineering Structures*, 29(11), 2968-2986.

Khorramian, K. and Sadeghian, P. (2019). “Material characterization of GFRP bars in compression using a new test method”, *Journal of Testing and Evaluation*, 49(2), 1037-1052.

Lin, G. and Zhang, S. (2023). “Contribution of longitudinal GFRP bars in concrete filled FRP tubular (CFFT) cylinders under monotonic or cyclic axial compression”, *Engineering Structures*, 281, 115766.

Liu, J., Teng, Y., Zhang, Y., Wang, X. and Chen, Y.F. (2018). “Axial stress-strain behavior of high-strength concrete confined by circular thin-walled steel tubes”, *Construction and Building Materials*, 177, 366-377.

Nanni, A., Okamoto, T., Tanigaki, M. and Osakada, S. (1993). “Tensile properties of braided FRP rods for concrete reinforcement”, *Cement and Concrete Composites*, 15(3), 121-129.

Ozbakkaloglu, T. (2013). “Compressive behavior of concrete-filled FRP tube columns: Assessment of critical column parameters”, *Engineering Structures*, 51, 188-199.

Ozbakkaloglu, T., Lim, J.C. and Vincent, T. (2013). “FRP-confined concrete in circular sections: Review and assessment of stress–strain models”, *Engineering Structures*, 49, 1068-1088.

Teng, J.G., Xiang, Y., Yu, T. and Fang, Z. (2019). “Development and mechanical behaviour of ultra-high-performance seawater sea-sand concrete", *Advances in Structural Engineering*, 22(14), 3100-3120.

Wang, J., Feng, P., Hao, T. and Yue, Q. (2017). "Axial compressive behavior of seawater coral aggregate concrete-filled FRP tubes", *Construction and Building Materials*, 147, 272-285.

Zeng, J.J., Gao, W.Y., Duan, Z.J., Bai, Y.L., Guo, Y.C. and Ouyang, L.J. (2020). "Axial compressive behavior of polyethylene terephthalate/carbon FRP-confined seawater sea-sand concrete in circular columns", *Construction and Building Materials*, 234, 117383.

Zohrevand, P. and Mirmiran, A. (2011). "Behavior of ultrahigh-performance concrete confined by fiber-reinforced polymers", *Journal of Materials in Civil Engineering*, ASCE, 23(12), 1727-1734.

Table 5.1 UHPC mix proportions

Material	White cement	Silica fume	Quartz powder	River sand	HRWR	Water	Total
Mix proportions (kg/m^3)	830	208	208	913	42	185	2386

Table 5.2 Test matrix

Specimen	Diameter of FRP rebar (mm)	Average diameter of hybrid rebar (mm)	Number of layers of GFRP tube	Wave height (mm)
FU-H0L3-M1,2	25	50	3-ply	0
FU-H1L3-M1,2	25	50	3-ply	1
FU-H3L3-M1,2	25	50	3-ply	3
FU-H5L3-M1,2	25	50	3-ply	5
FU-H0L5-M1,2	25	50	5-ply	0
FU-H5L5-M1,2	25	50	5-ply	5
HR-H0L3-M1,2	25	50	3-ply	0
HR-H1L3-M1,2	25	50	3-ply	1
HR-H3L3-M1,2	25	50	3-ply	3
HR-H5L3-M1,2	25	50	3-ply	5
HR-H0L5-M1,2	25	50	5-ply	0
HR-H5L5-M1,2	25	50	5-ply	5
FU-H0L1D33-M1,2	13	33	1-ply	0
FU-H0L2D33-M1,2	13	33	2-ply	0
HR-H0L1D33-M1,2	13	33	1-ply	0
HR-H0L2D33-M1,2	13	33	2-ply	0

Table 5.3 Compression test results of bare FRP rebars

Specimens ID	Actual diameter (mm)	Peak stress (MPa)	Ultimate strain (%)	Elastic modulus (GPa)
2D-1	24.80	764.4	1.17	57.2
2D-2	24.90	733.0	1.26	55.2
2D-3	24.68	736.3	1.35	52.9
Average	24.82	744.5	1.26	55.1
4D-1	24.69	661.2	1.16	52.5
4D-2	24.87	753.3	1.21	59.8
4D-3	24.93	641.2	1.02	56.7
Average	24.83	685.2	1.13	56.3

Table 5.4 Compression test results of hybrid rebars

Specimen ID	Wave height (mm)	Number of layers of GFRP tube	f_1/f_{co}	f_2/f_{co}	f_3/f_{co}	f_4/f_{co}	E_3/E_1	ε_3 (%)
HR-H0L3-M1	0	3	1.08	0.95	1.59	1.08	0.24	1.59
HR-H0L3-M2	0	3	1.02	0.97	1.50	-	0.43	1.15
HR-H1L3-M1	1	3	1.13	1.00	1.69	-	0.33	1.87
HR-H1L3-M2	1	3	1.04	0.95	1.70	-	0.44	1.60
HR-H3L3-M1	3	3	1.06	1.10	1.83	-	0.37	1.88
HR-H3L3-M2	3	3	1.00	1.07	1.73	-	0.35	1.47
HR-H5L3-M1	5	3	1.12	1.18	1.73	1.34	0.27	1.64
HR-H5L3-M2	5	3	1.05	1.17	1.70	1.00	0.43	1.68
HR-H0L5-M1	0	5	1.19	1.00	2.19	-	0.31	1.76
HR-H0L5-M2	0	5	1.20	0.98	1.92	1.44	0.27	1.72
HR-H5L5-M1	5	5	1.06	1.20	1.78	1.38	0.4	1.35
HR-H5L5-M2	5	5	1.10	1.23	1.63	1.42	0.46	1.11

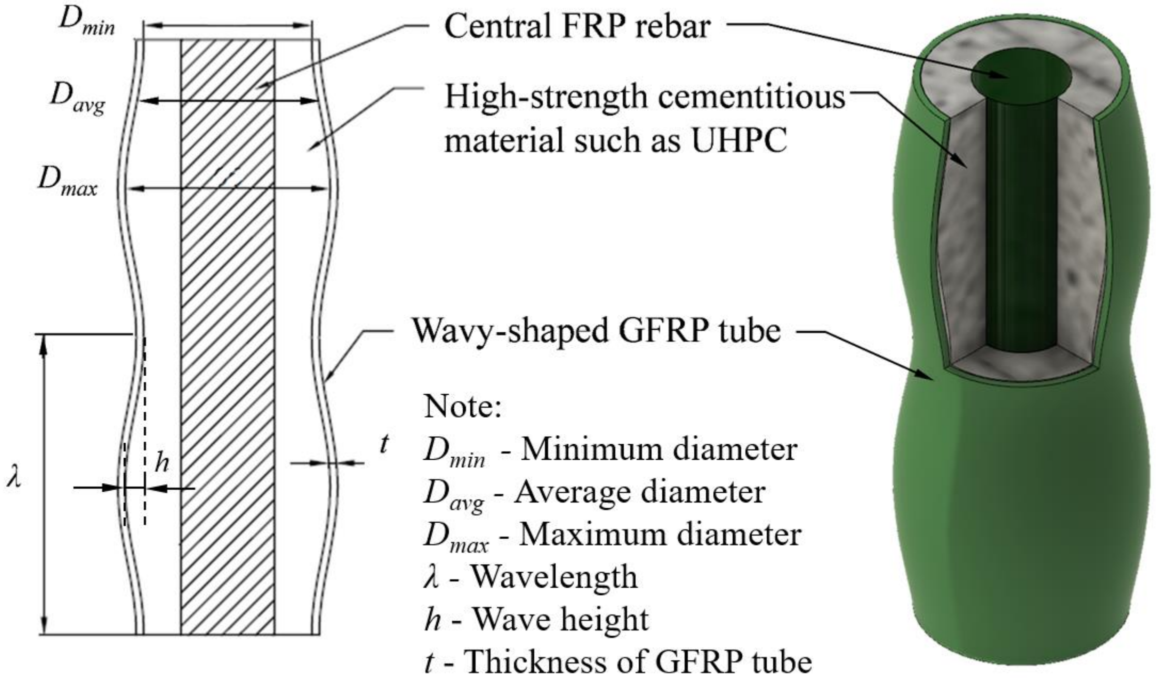

Figure 5.1 Schematic diagram of a wavy-shaped hybrid rebar

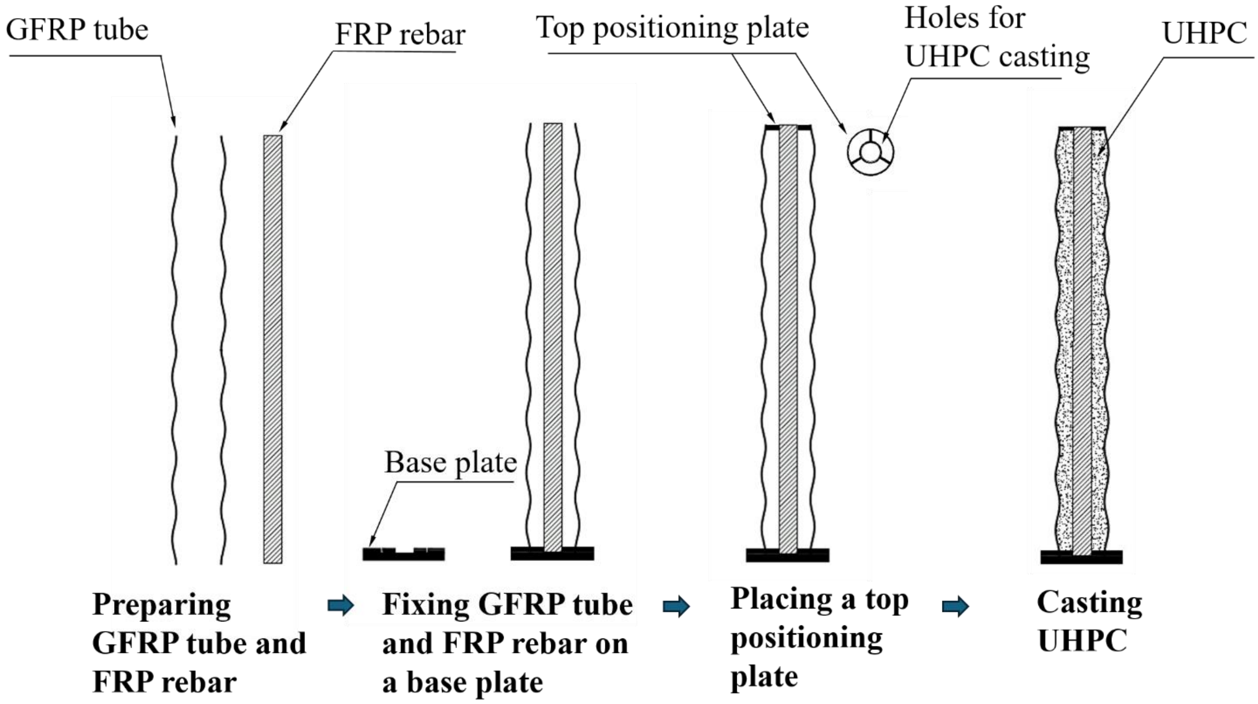

Figure 5.2 Manufacturing process of a hybrid rebar

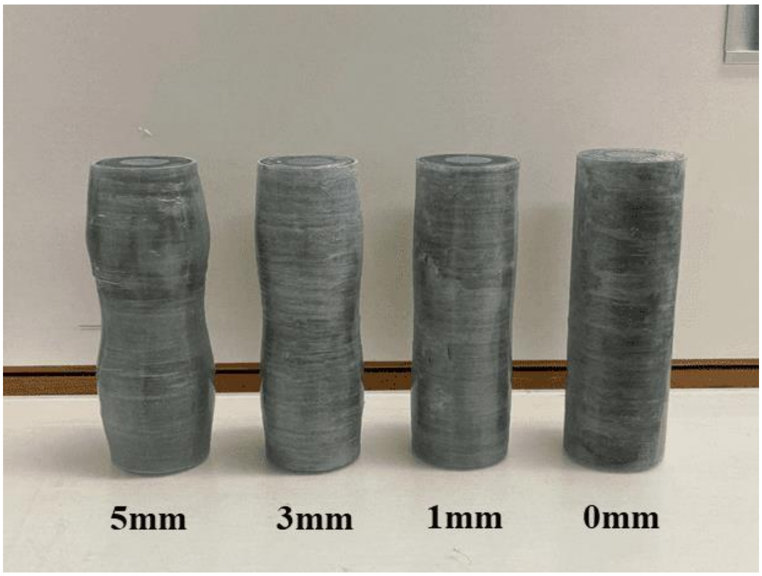

Figure 5.3 Hybrid rebars fabricated in this research project with different wave heights

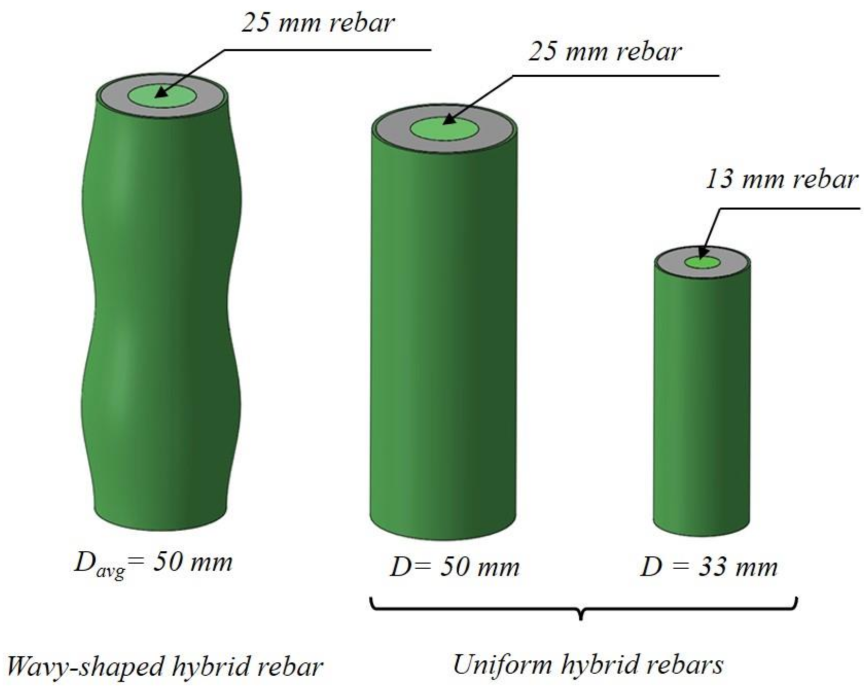

Figure 5.4 Schematic of hybrid rebars with a diameter of 50 or 33 mm

(a) Test specimens

(b) Set-up of compression test

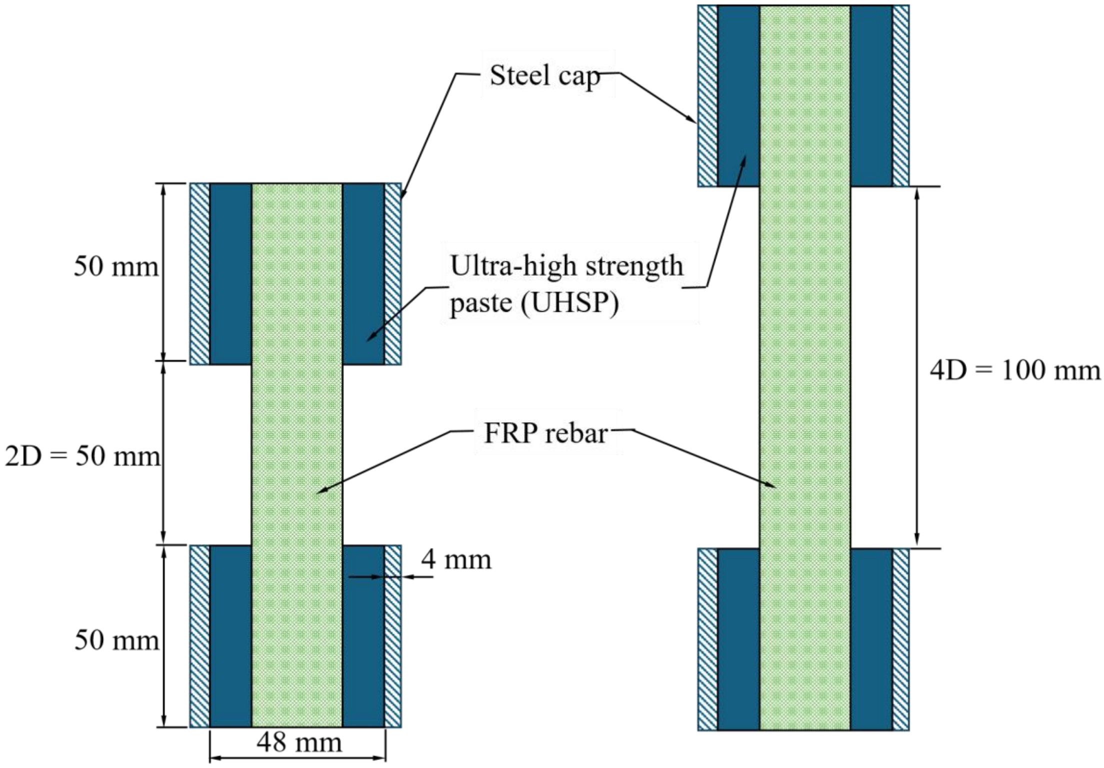

(c) Dimensions of FRP rebar specimens and steel tubes

Figure 5.5 Compression test of FRP rebars

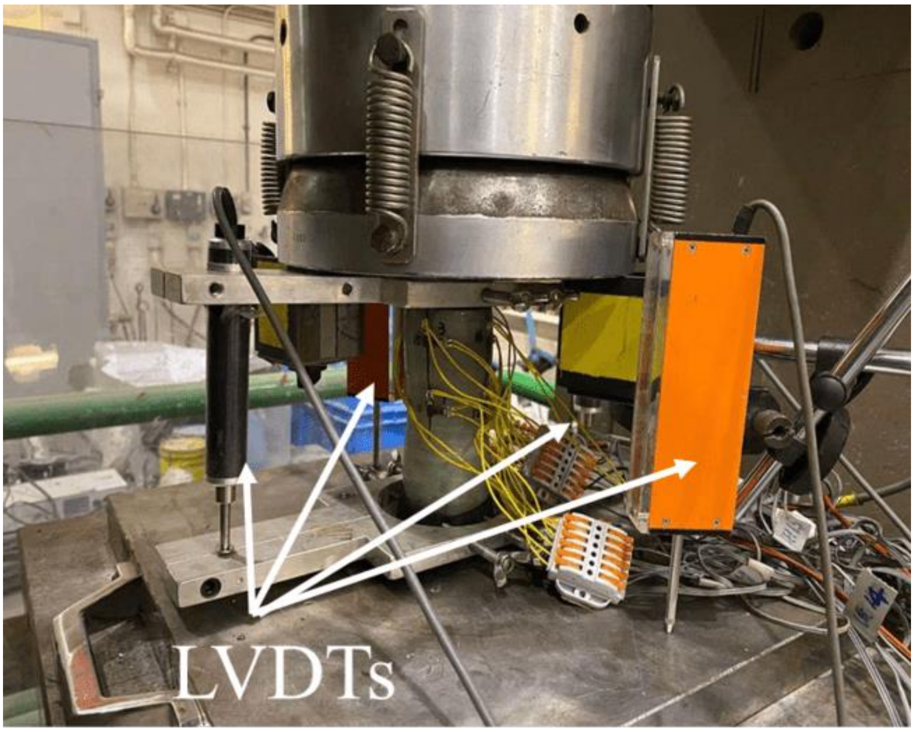

Figure 5.6 Test set-up

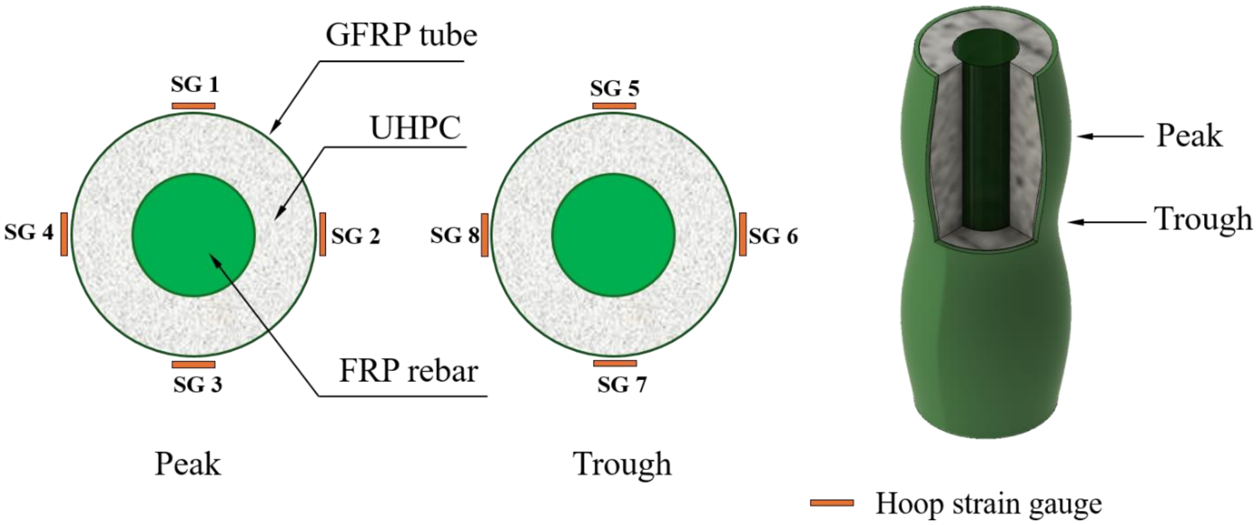

Figure 5.7 Layout of strain gauges

(a) HR-H5L3-M1

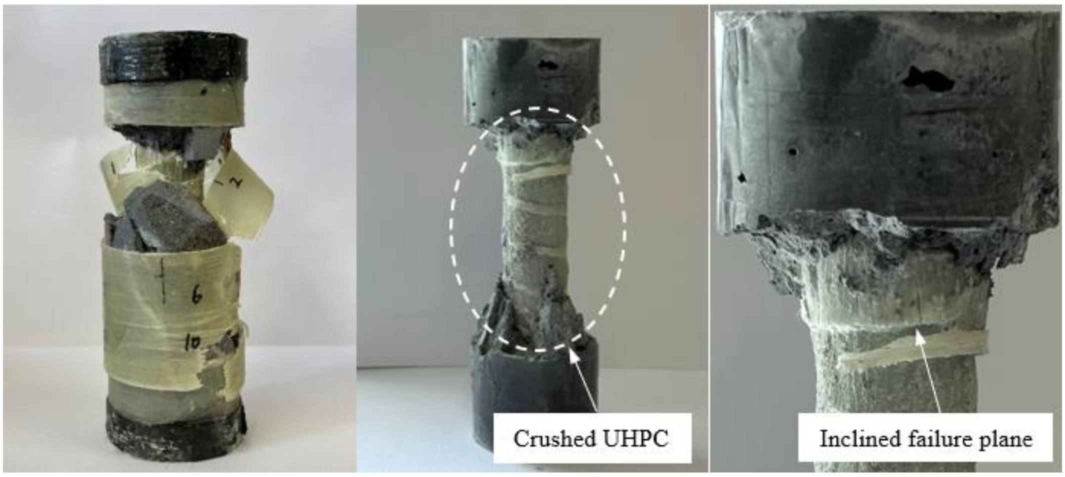

(b) HR-H0L3-M1

(c) HR-H0L3-M2

(d) FU-H5L3-M2

(e) FRP rebars

Figure 5.8 Failure modes

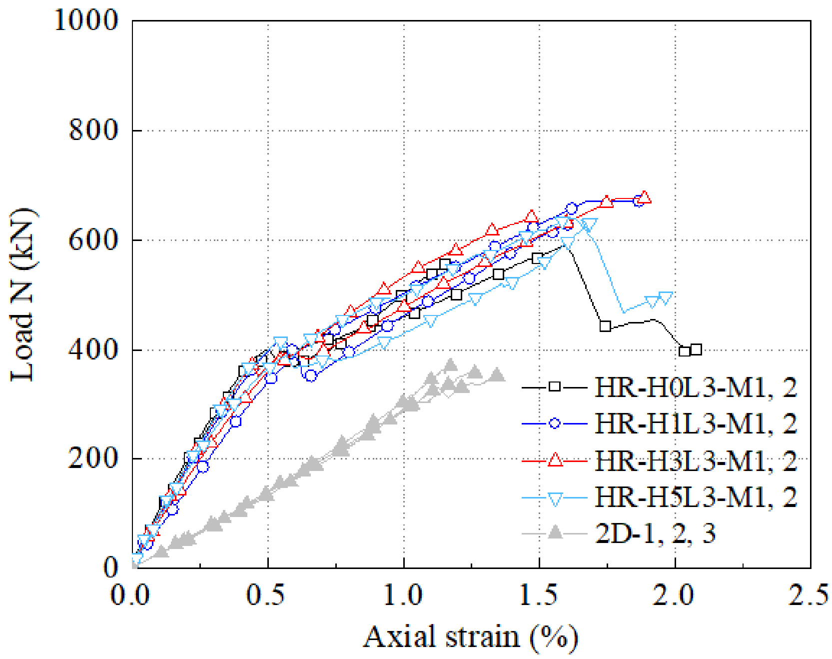

(a) 3-ply hybrid rebars

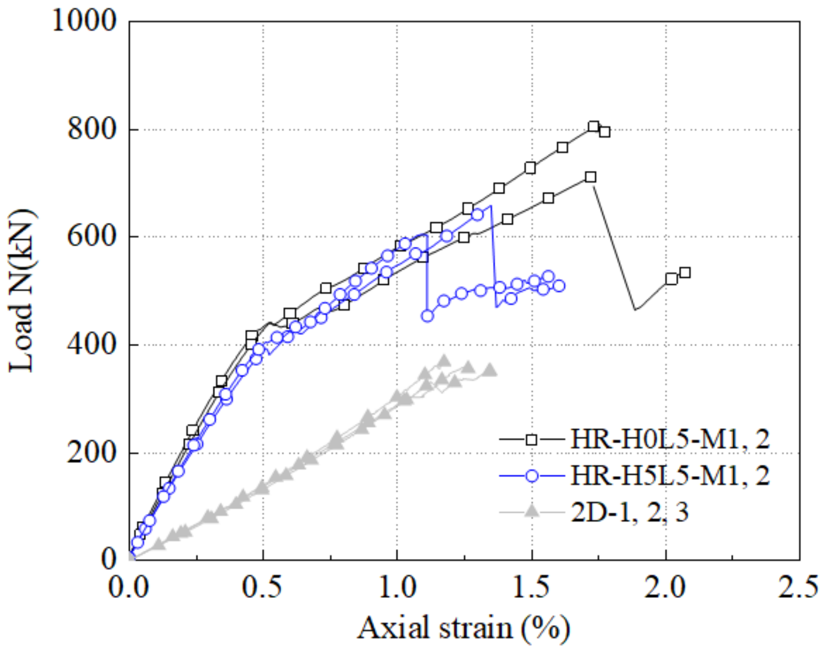

(b) 5-ply hybrid rebars

Figure 5.9 Axial load-axial strain curves of hybrid rebar specimens

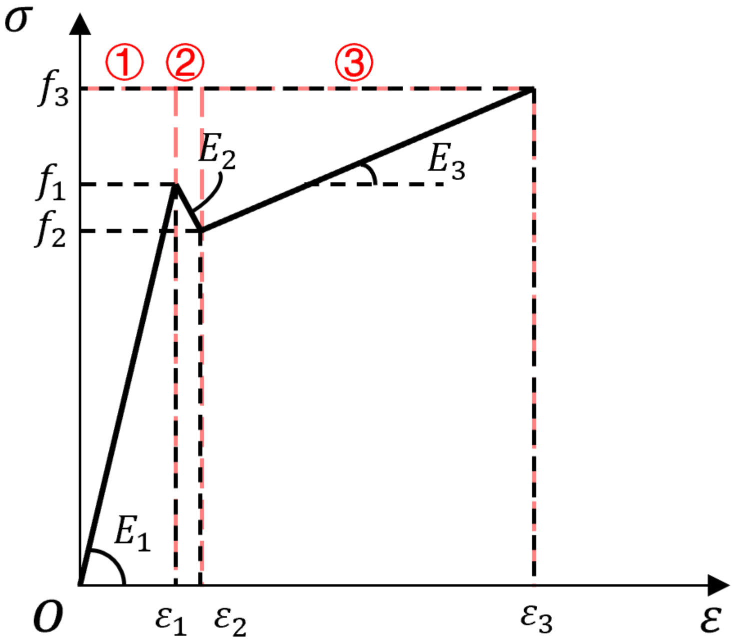

(a) Three-stage curve

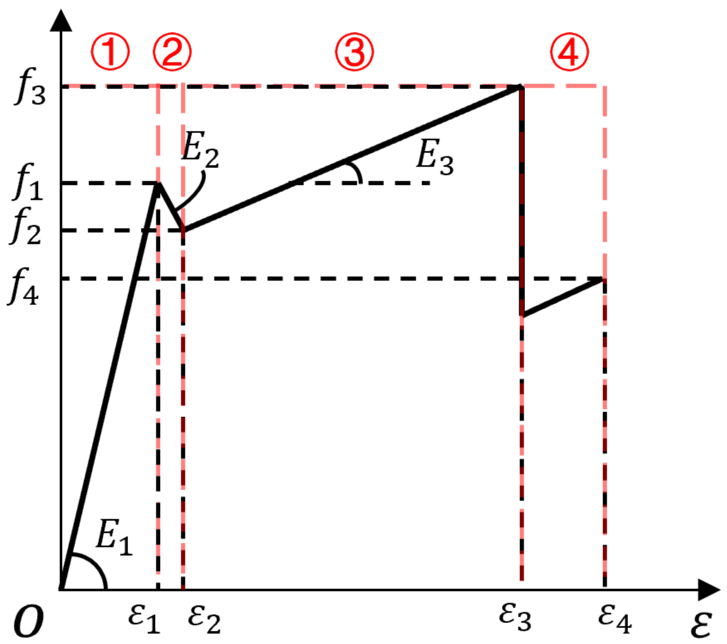

(b) Four-stage curve

Figure 5.10 Typical average axial stress-strain curves of hybrid rebars

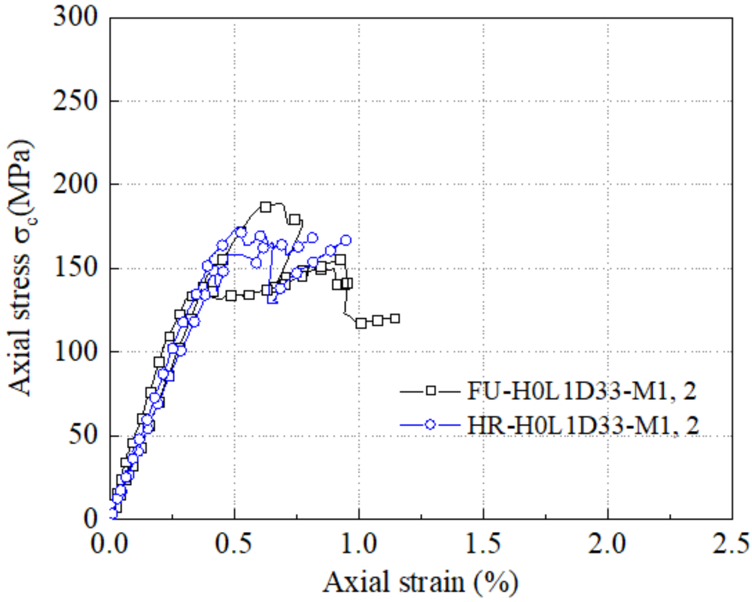

(a) H0L1D33

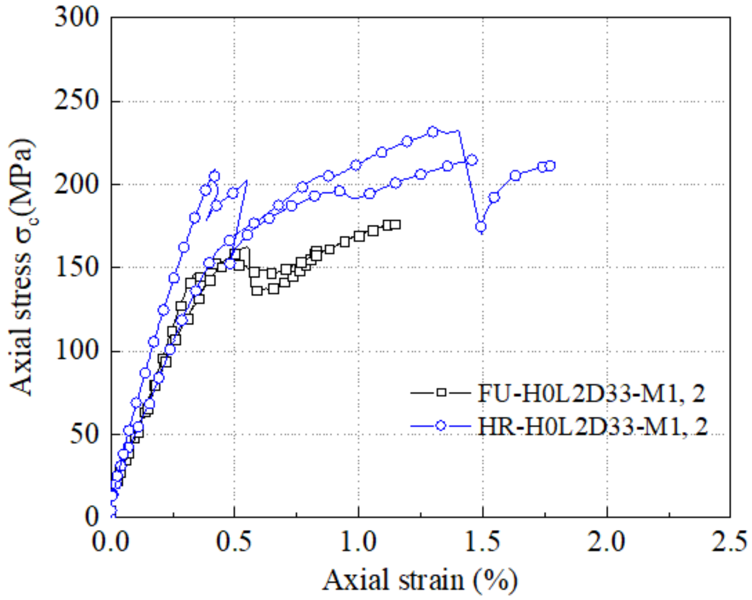

(b) H0L2D33

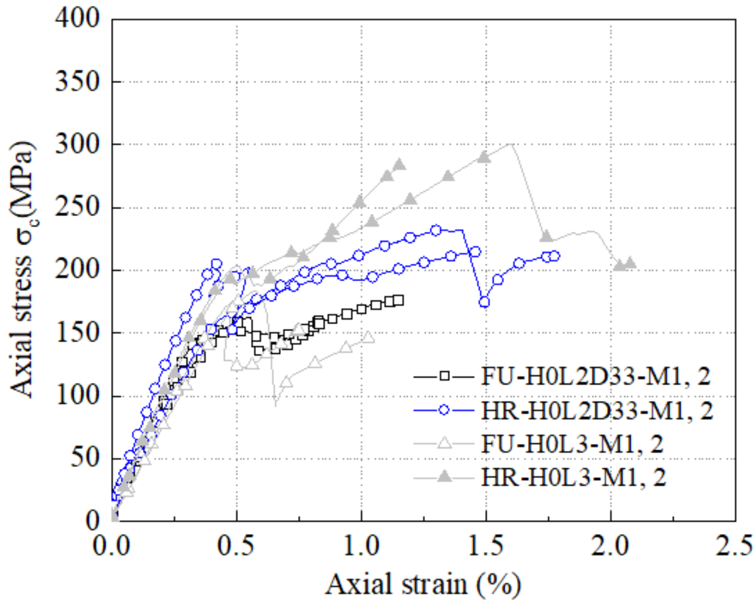

(c) Comparison between H0L2D33 and H0L3 specimens

Figure 5.11 Axial stress-strain curves of small-scale specimens

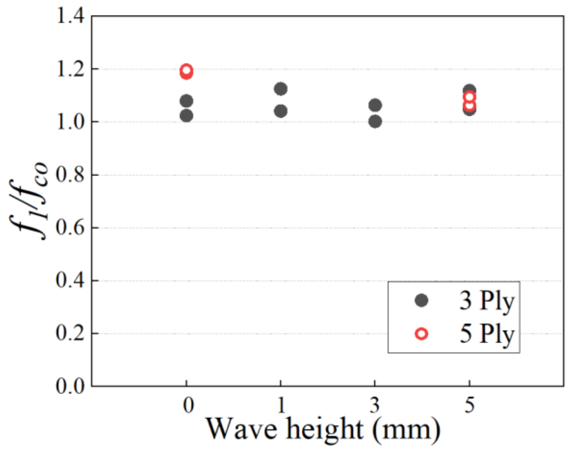

(a) f_1/f_{co}

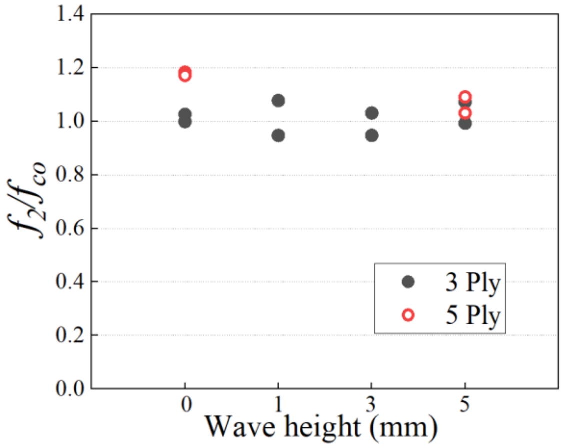

(b) f_2/f_{co}

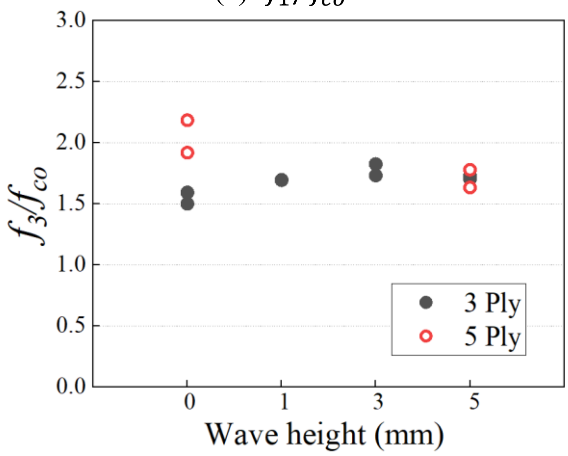

(c) f_3/f_{co}

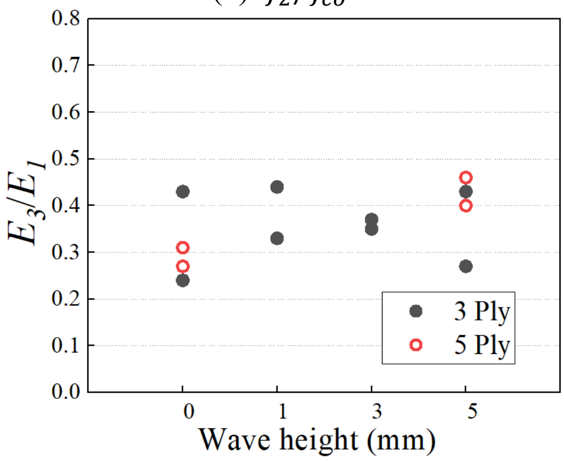

(d) E_3/E_1

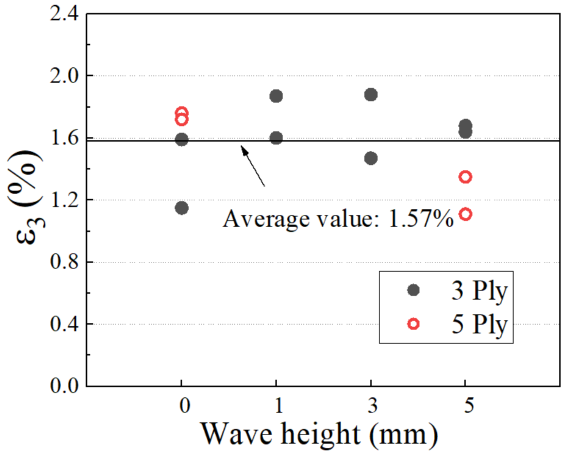

(e) ε_3

Figure 5.12 Effects of wave height on critical parameters

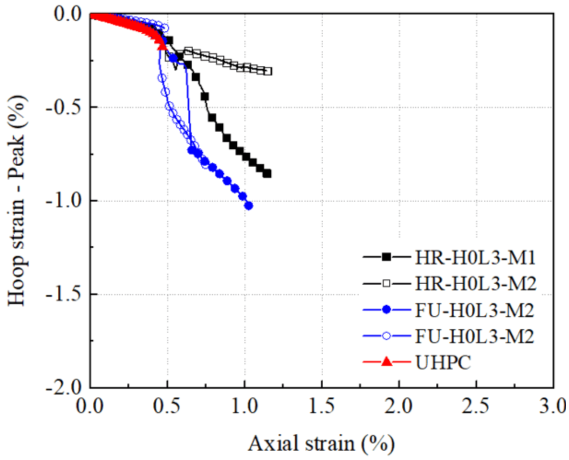

(a) H0L3 series at peak location

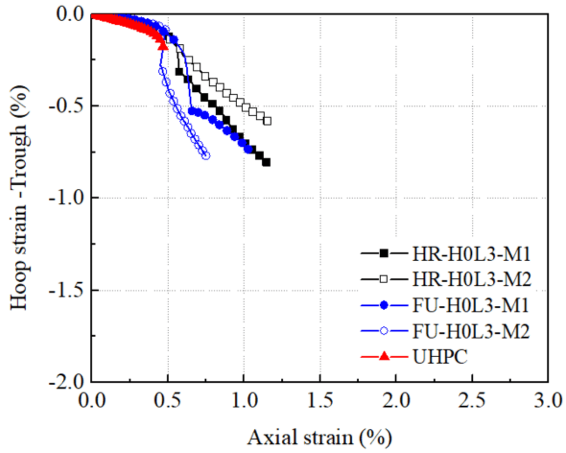

(b) H0L3 series at trough location

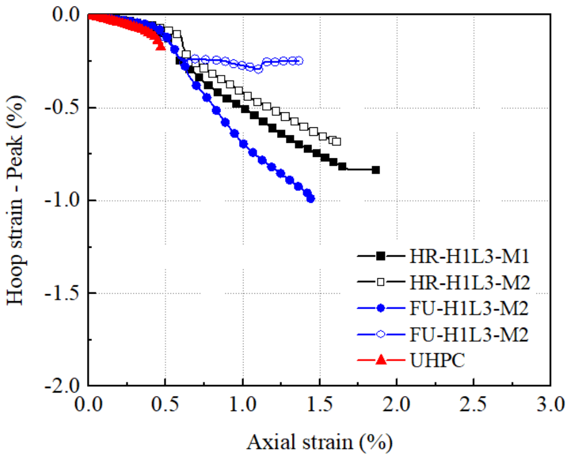

(c) H1L3 series at peak location

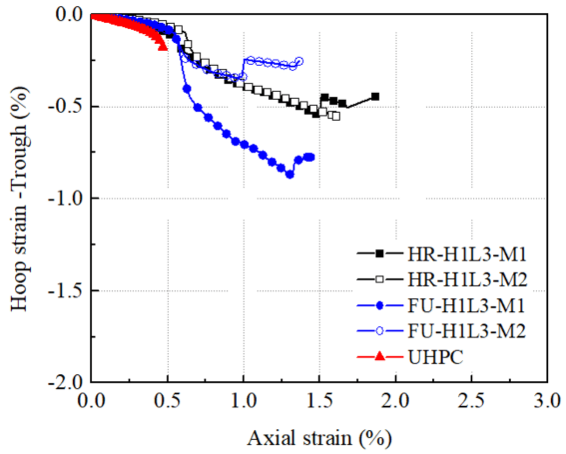

(d) H1L3 series at trough location

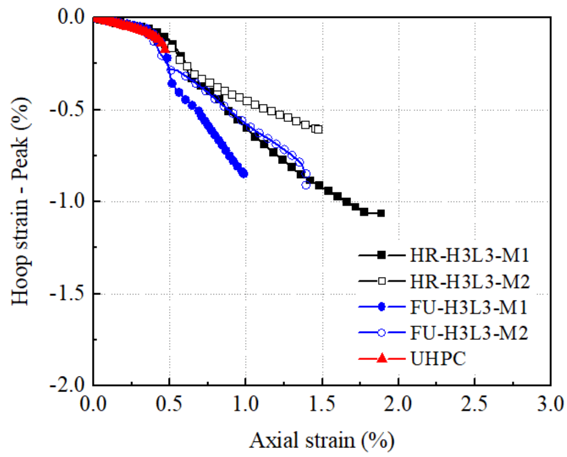

(e) H3L3 series at peak location

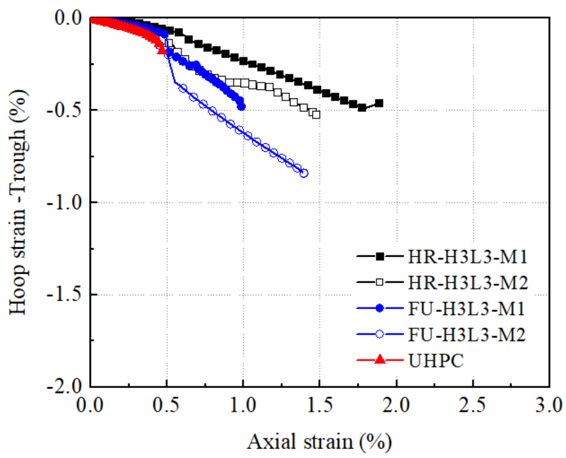

(f) H3L3 series at trough location

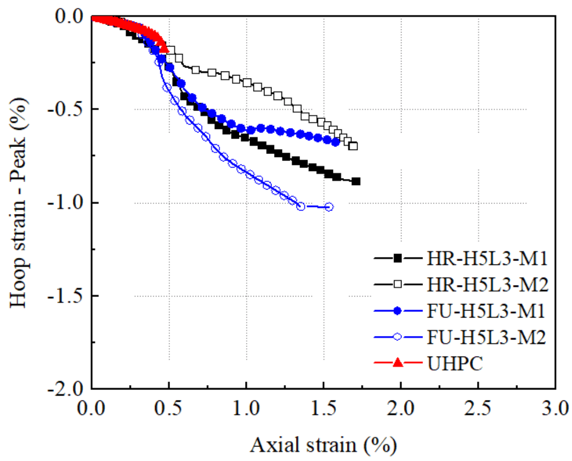

(g) H5L3 series at peak location

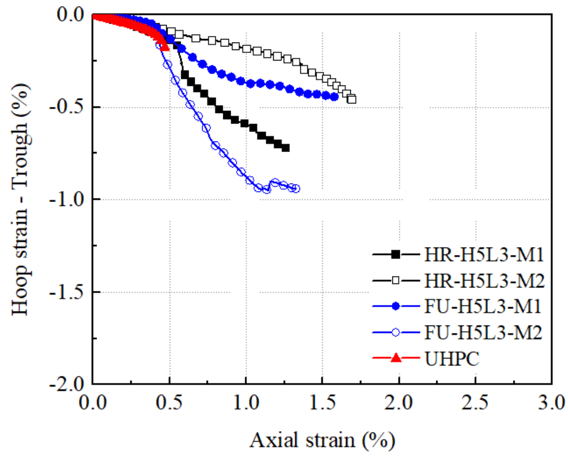

(h) H5L3 series at trough location

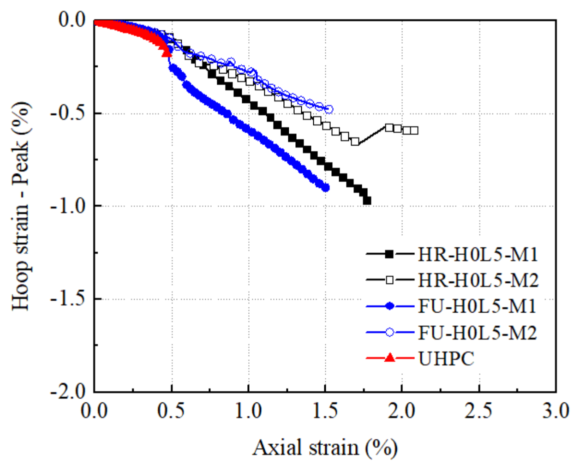

(i) H0L5 series at peak location

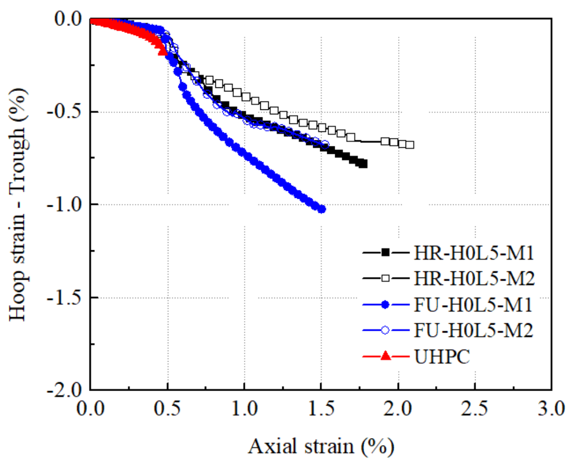

(j) H0L5 series at trough location

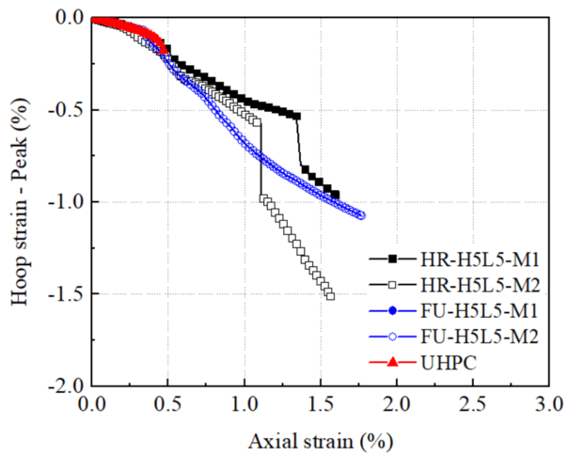

(k) H5L5 series at peak location

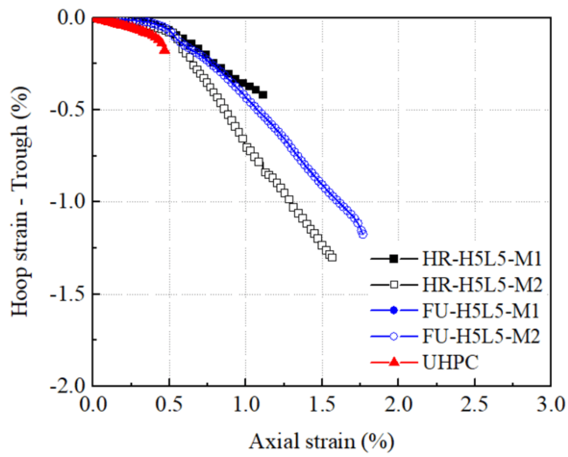

(l) H5L5 series at trough location

Figure 5.13 Hoop strain-axial strain relationships at different locations

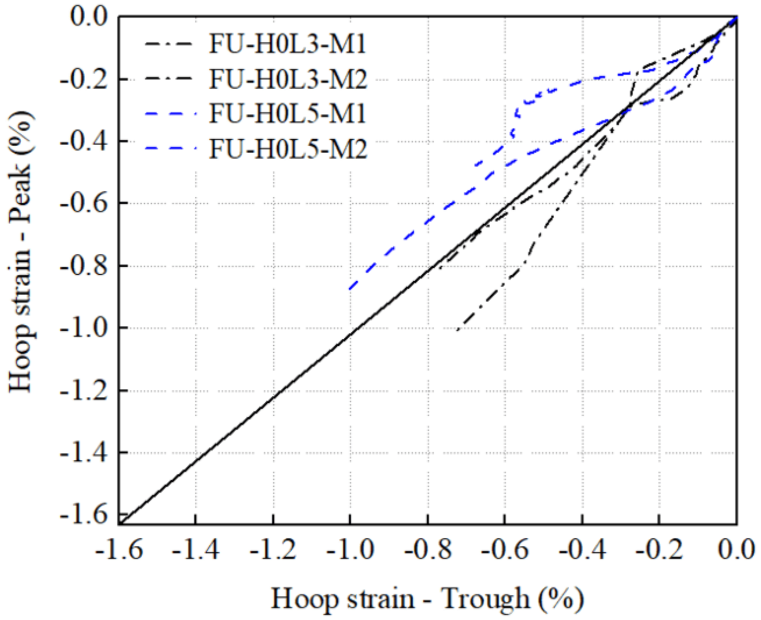

(a) Uniform GFRP tube-confined UHPC

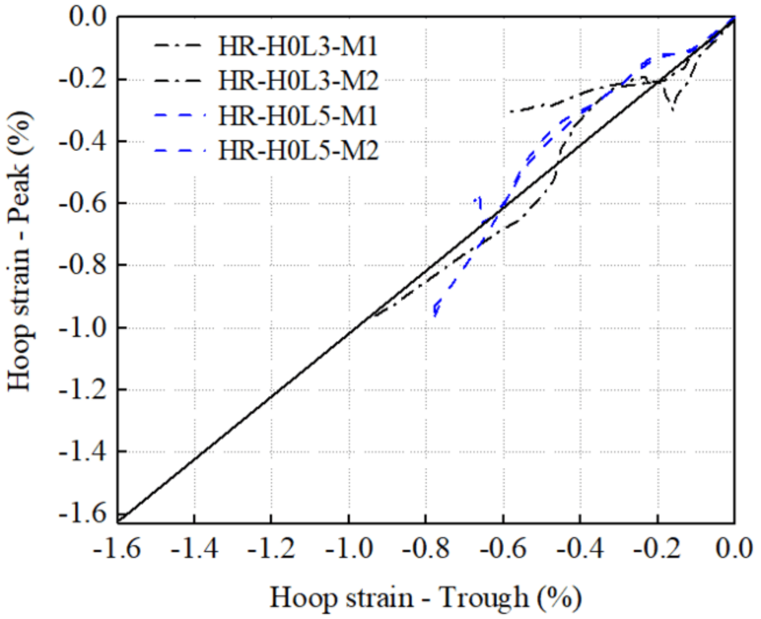

(b) Uniform hybrid rebars

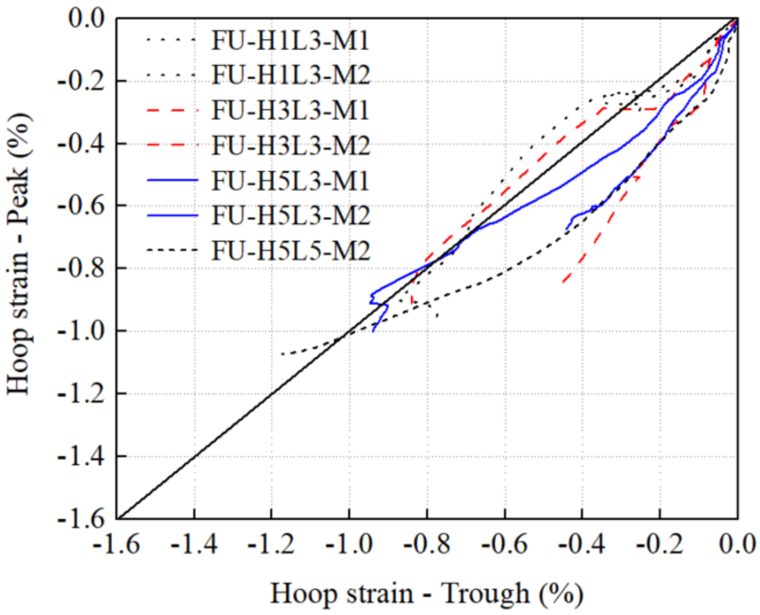

(c) Wavy-shaped GFRP tube-confined UHPC

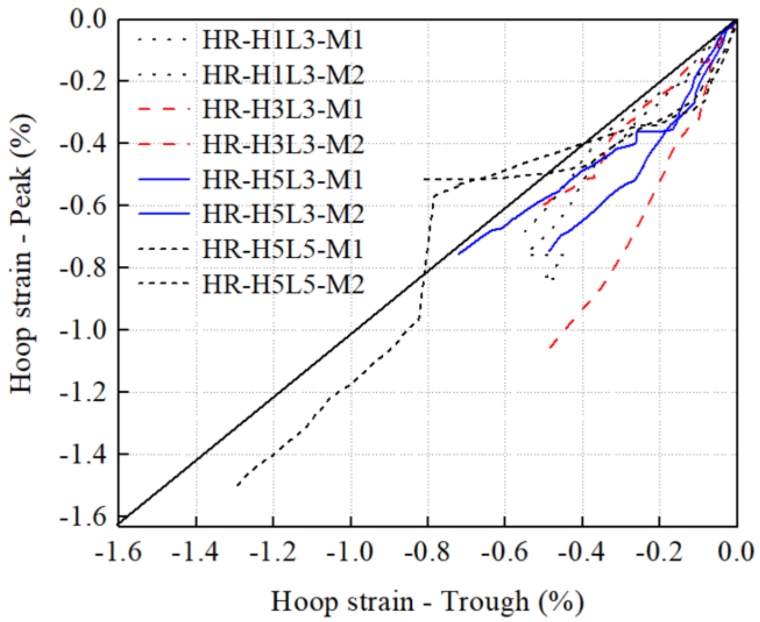

(d) Wavy-shaped hybrid rebars

Figure 5.14 Peak-trough hoop strain relationship

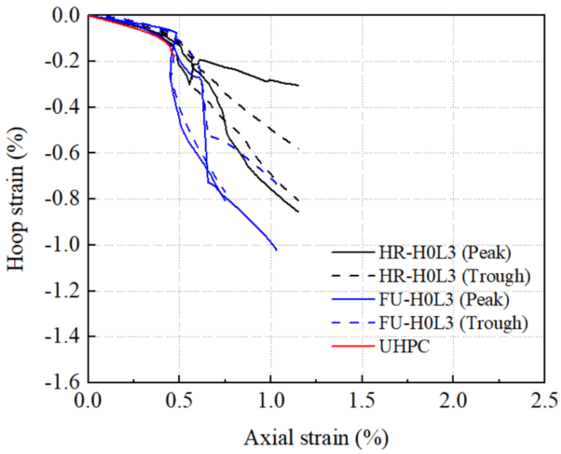

(a) H0L3

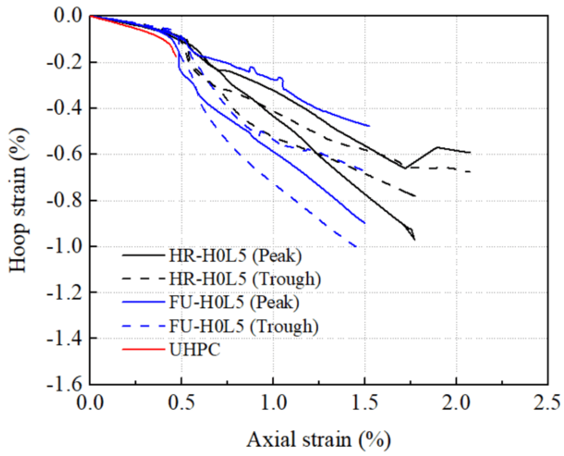

(b) H0L5

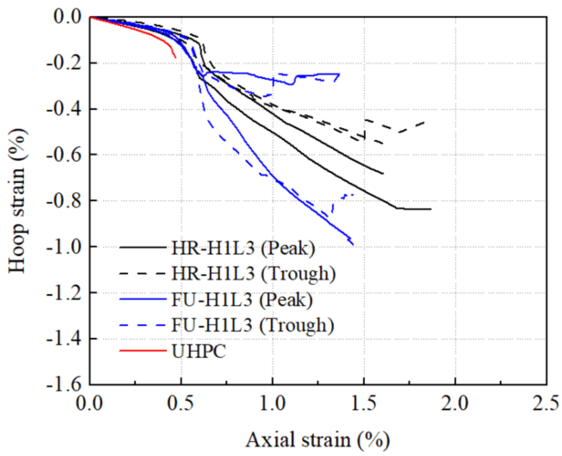

(c) H1L3

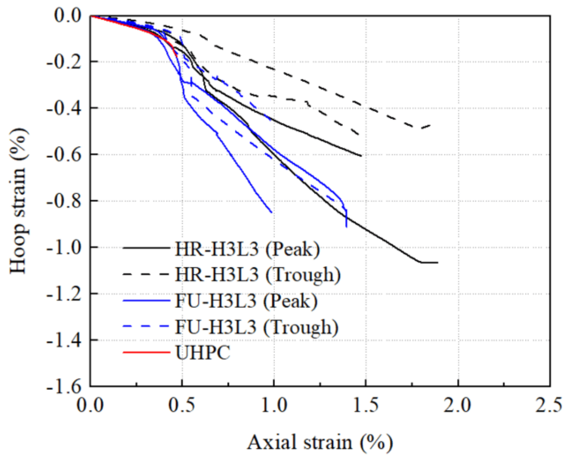

(d) H3L3

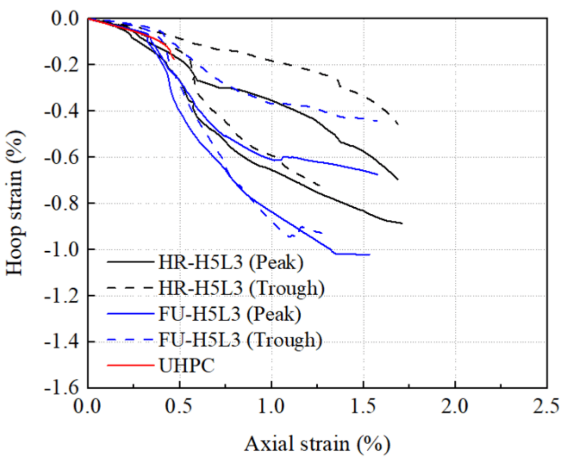

(e) H5L3

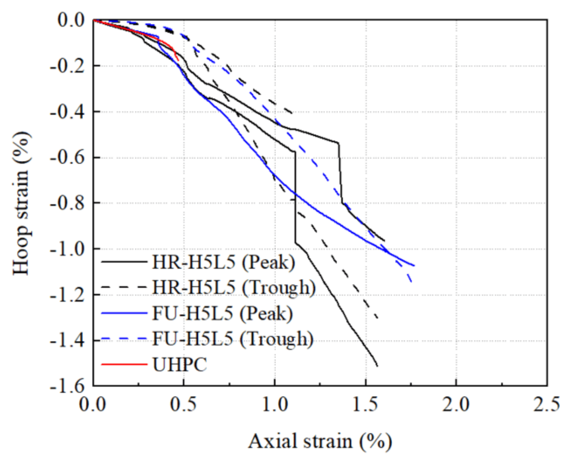

(f) H5L5

Figure 5.15 Hoop strain-axial strain relationships

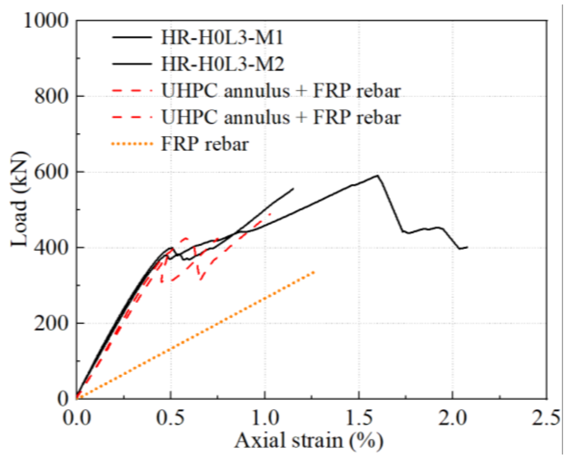

(a) H0L3

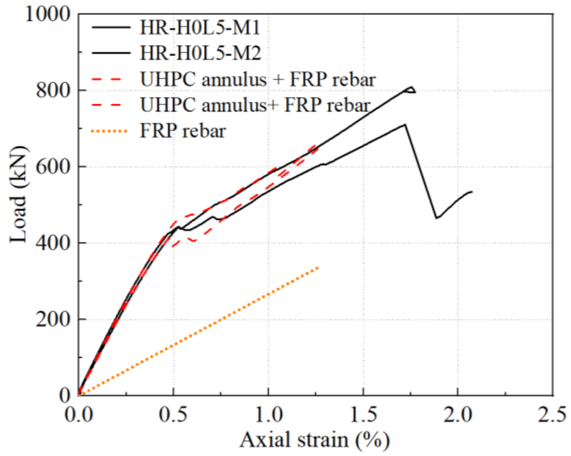

(b) H0L5

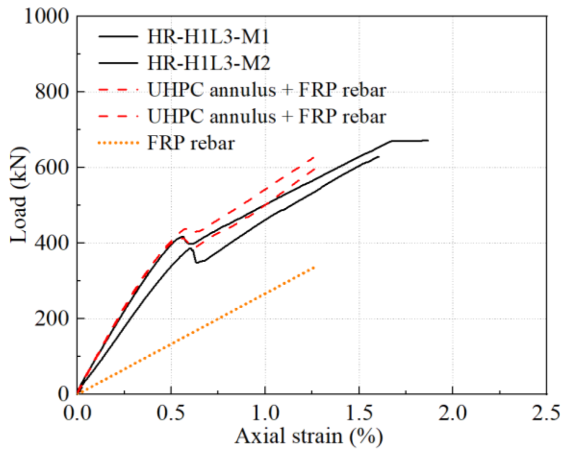

(c) H1L3

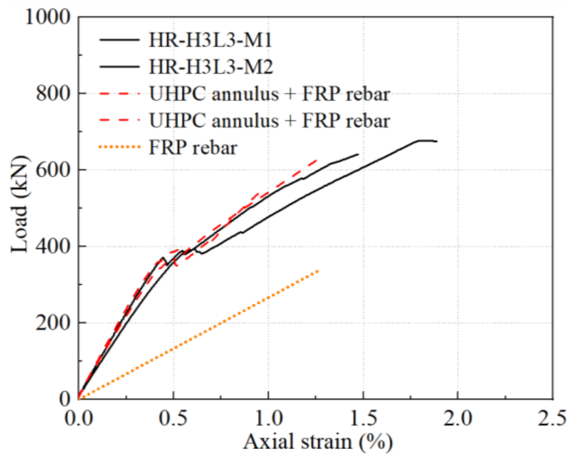

(d) H3L3

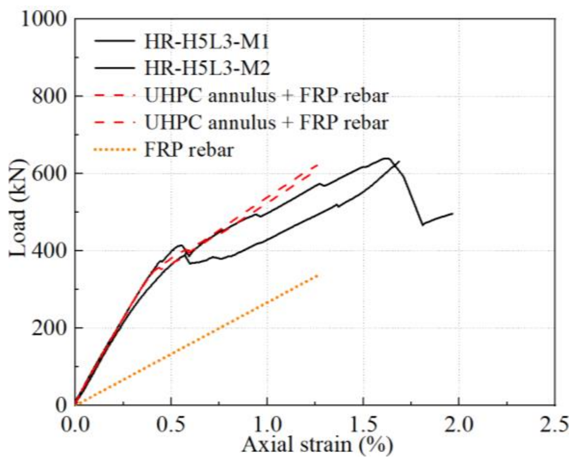

(e) H5L3

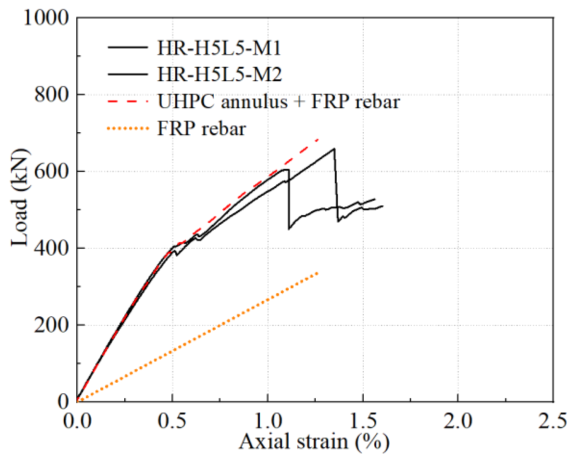

(f) H5L5

Figure 5.16 Comparison between test results and predictions

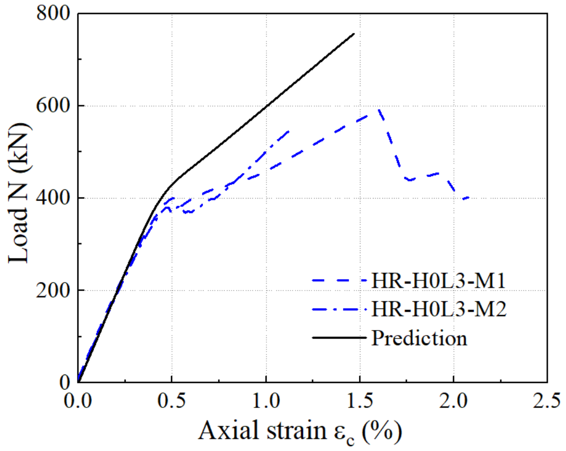

(a) HR-H0L3

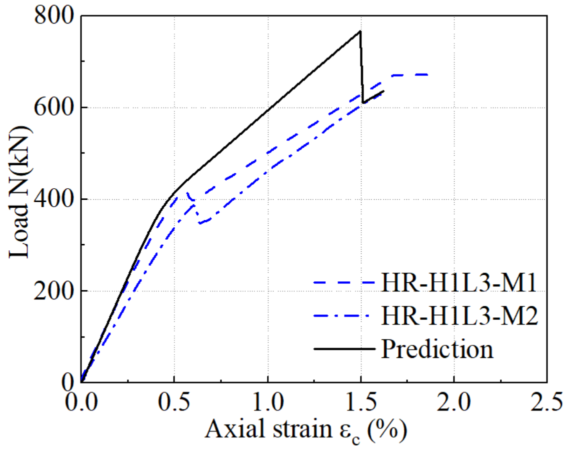

(b) HR-H1L3

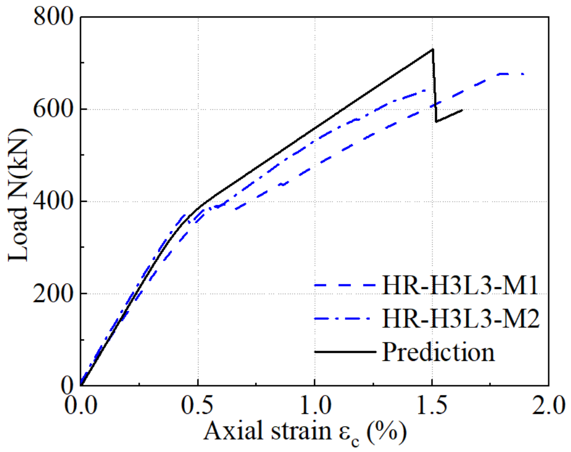

(c) HR-H3L3

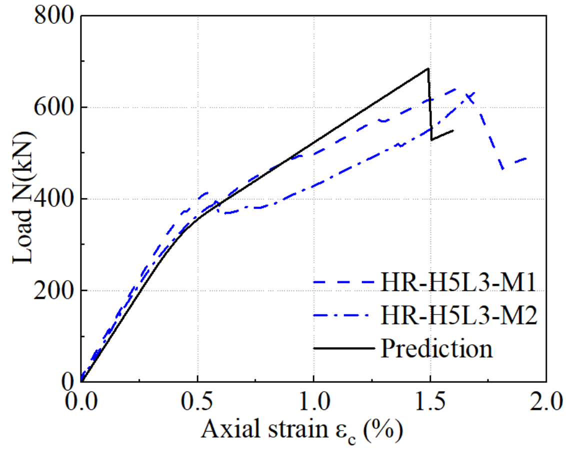

(d) HR-H5L3

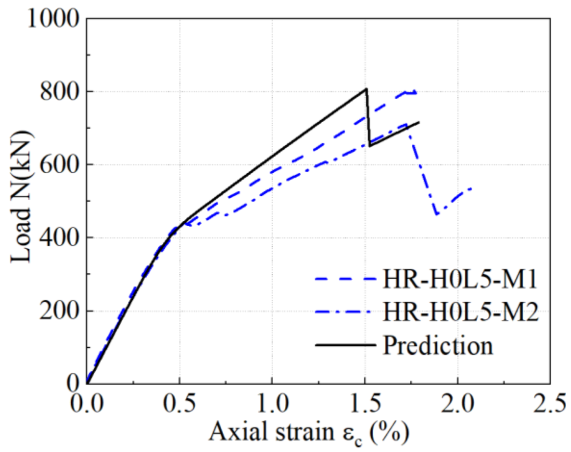

(e) HR-H0L5

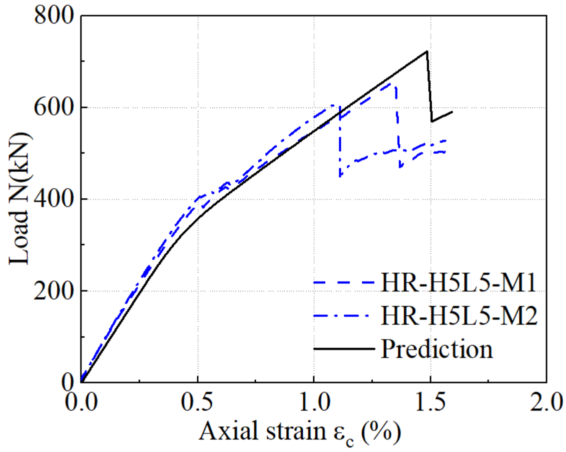

(f) HR-H5L5

Figure 5.17 Predicted versus test load-axial strain curves of hybrid rebars

CHAPTER 6
MECHANICAL BEHAVIOUR OF WAVY-SHAPED HYBRID REBARS UNDER CYCLIC AXIAL COMPRESSION

6.1 INTRODUCTION

In Chapter 5, it was demonstrated that wavy-shaped hybrid rebars could exhibit good compressive performance under monotonic axial compression. As a reinforcing component for concrete structures with promising potential applications in seismic regions, the behaviour of hybrid rebars subject to cyclic loading is of particular importance. As a result, this chapter presents an experimental study on wavy-shaped hybrid rebars under cyclic axial compression. Wavy-shaped GFRP tube-confined UHPC specimens (without an internal GFRP bar) were also prepared and tested for a direct comparison with the wavy-shaped hybrid rebar specimens.

As revealed by the review presented in Chapter 2, numerous cyclic stress-strain models have been proposed for FRP-confined concrete in columns under cyclic axial compression (Shao et al., 2006; Lam and Teng, 2009; Yu et al., 2015; Tian et al., 2020; Huang et al., 2021). However, the majority of these models have been focused on FRP-confined normal strength concrete (NSC) and high-strength concrete (HSC), while only limited research was dedicated to investigating the cyclic axial behaviour of FRP-confined UHPC. In this Ph.D. research project, a comprehensive assessment of typical cyclic stress-strain models in predicting the cyclic behaviour of wavy-shaped hybrid rebar specimens and wavy-shaped GFRP tube-confined UHPC specimens was conducted. To capture the cyclic characteristics of these specimens, the original equations for plastic strains and stress deterioration were modified. The axial load-strain curves of wavy-shaped hybrid rebar specimens were compared with the predicted curves obtained by summing the axial load-strain curves of different constituent components within the specimen.

6.2 EXPERIMENTAL PROGRAMME

6.2.1 Specimen Details

A total of 12 wavy-shaped FRP tube-confined UHPC specimens (without an FRP bar inside) (Series 1) and 12 wavy hybrid rebar specimens (Series 2) were prepared and tested under cyclic axial compression. All the specimens had an average diameter of 50 mm and a height of 160 mm. The details of the specimens are listed in Table 6.1. In the table, the 12 wavy-shaped FRP tube-confined UHPC specimens and the 12 wavy-shaped hybrid rebar specimens tested under monotonic compression are also included for the ease of comparison. Their detailed test results have been presented in Chapter 5. Each specimen was given a name, which starts with two letters "FU" or "HR" representing an "FRP-confined UHPC specimen" or a "hybrid rebar", followed by a letter "H" and a number "0", "1", "3" or "5" denoting a weight height of 0 mm, 1 mm, 3 mm or 5 mm for the FRP tube, together with a letter "L" and a number "3" or "5" standing for a 3-ply or 5-ply GFRP tube. The name is then followed by a letter "M" or "C" representing "Monotonic" or "Cyclic" axial compression, and the final number "1" or "2" is used to differentiate two nominally identical specimens.

6.2.2 Specimen Preparation

The preparation process for the specimens subject to cyclic axial compression was the same as that for the specimens subject to monotonic axial compression as described in Chapter 5; thus, it is not described again in this chapter. The mixing proportion of UHPC and the manufacturing method of hybrid rebars can be referred to Table 5.1 and Figure 5.2, respectively. Chapter 5 has already detailed the compressive properties of the UHPC, which exhibits an average compressive strength (f'_{co}) of 187.9 MPa, an elastic modulus (E_c) of 46.9 GPa, and an axial strain at peak stress (ε_{co}) of 0.45%.

6.2.3 Test Set-Up and Loading Scheme

The test set-up and the instrumentations are the same as those for the specimens in Chapter 5 (see Figure 5.6). The specimens were tested on an MTS machine with a consistent displacement rate of 0.3 mm/min. A cyclic compressive loading scheme was applied on each specimen as shown in Figure 6.1. In each loading cycle, a prescribed compressive strain was first applied followed by unloading to an approximately zero stress. The prescribed compressive strain was increased with an interval of 2000 με until the failure of the specimen. The unloading/reloading cycles were controlled manually based on the displacements averaged from the two LVDTs amounted at the mid-height covering a gauge length of 3/4 of the total height of each specimen (i.e., MLVDTs) and the loads recorded by the MTS system.

6.3 TEST RESULTS AND DISCUSSIONS

6.3.1 General Observations

After the axial strain exceeded ε_{co}, white patches became visible on the outer surface of the GFRP tubes, indicating resin cracking of the GFRP tubes, which is a common observation for FRP tube-confined concrete specimens under axial compression (Zhang et al. 2014). During the final stage of loading, one explosive sound could be heard in some hybrid rebar specimens. This phenomenon is consistent with that of hybrid rebars under monotonic axial compression as reported in Chapter 5. Typical failed GFRP tube-confined UHPC specimens and hybrid rebar specimens are shown in Figure 6.2. All specimens ultimately failed with the rupture of GFRP tubes due to hoop tension as shown in Figure 6.2. It could also be observed that the FRP tube fracture locations in the hybrid rebar specimens (e.g., specimens HR-H0L3-C1, HR-H0L5-C1, HR-H1L3-C1 and HR-H5L3-C1) were more concentrated compared to those of the FRP-confined UHPC specimens (e.g., specimens FU-H0L3-C1, FU-H0L5-C1, FU-H1L3-C1 and FU-H5L3-C1). As shown in Figure 6.2(b), localized diagonal cracks could be observed at the middle or peak location of the wavy-shaped GFRP tubes.

6.3.2 Axial Load-Axial Strain Curves

Figures 6.3 and 6.4 present the axial load-axial strain curves of test specimens under both monotonic loading and cyclic loading. The axial strains were obtained from the average readings of the two MLVDTs. A noticeable load drop could be observed at an axial strain of around 0.5% for both FRP-confined UHPC specimens and hybrid rebars specimens. The envelope curves of the cyclically loaded specimens generally agree well with the stress-strain curves of the corresponding monotonically loaded specimens. This phenomenon is consistent with those reported for FRP-confined NSC and HSC in the literature (Lam and Teng, 2009; Yu et al., 2015). Additionally, it can be observed that for hybrid rebars, the envelope curves of the cyclically loaded specimens could also be divided into three or four stages, similar to the stress-strain curves of monotonically loaded specimens, as detailed in Chapter 5.

As shown in Figure 6.4, the plastic strains of hybrid rebar specimens are relatively small before the failure of the internal FRP rebar, which is different from FRP-confined concrete (Zhang et al., 2015) or FRP-confined UHPC (Figure 6.3). The lower plastic strains of hybrid rebars were mainly due to the linear elastic characteristic of the central FRP rebar. Since the 25 mm FRP rebar occupied at least 25% of the cross-sectional area of a hybrid rebar, the compressive behaviour of the hybrid rebar is heavily affected by the internal FRP rebar. After the failure of the internal FRP rebar, a significant increase in the plastic strains from approximately 0.1% to 0.5% of the hybrid rebars could be observed. In comparison to FRP tube-confined UHPC specimens, hybrid rebar specimens appear to exhibit a reduced plastic strain at a specified unloading strain, even at the stage subsequent to the failure of the internal FRP rebar. This indicates that the effect of FRP rebars on the cyclic behaviour of hybrid rebars retained at the final stage (i.e., Stage 4). As illustrated in Figure 6.3, an increase in wave height results in the axial load-axial strain curves of FRP tube-confined UHPC specimens exhibiting a less pronounced reduction in load at the transition region. However, the influence of wave height on the axial load-axial strain curves of the hybrid rebar specimens is not particularly significant.

6.4 CYCLIC STRESS-STRAIN MODELS OF FRP-CONFINED UHPC

6.4.1 General

A cyclic axial stress-axial strain model for FRP-confined concrete generally consists of equations for an envelope curve, an unloading curve, and a reloading curve as presented in Figure 6.5. The axial strain and the axial stress at Point *a* are defined as the unloading strain ε_{un} and the unloading stress σ_{un}, respectively. The unloading curve starts from Point *a* (ε_{un}, σ_{un}) and exhibits a decrease in axial stress and axial strain, eventually ending at Point

b. Meanwhile, Point b also serves as the start of the reloading curve. The coordinate of Point b is donated by (ε_{pl}, σ_{re}), where the abscissa value is defined as the plastic strain. For the reloading curve, the axial stress continuously increases until the axial strain reaches ε_{ref}, which is equal to the value of unloading strain ε_{un} in the same loading cycle. It should be noted that Point c (ε_{ref}, σ_{new}) is lower than Point a (ε_{un}, σ_{un}), which reflects the stress deterioration phenomenon due to concrete damage. The reloading curve finally intersects with the envelope curve at Point d. At this point, the axial strain and the axial stress are denoted by $\varepsilon_{ret,env}$ and $\sigma_{ret,env}$, respectively.

The experimental cyclic axial load-strain curves of FRP tube-confined UHPC are compared with the predictions based on three typical existing cyclic stress-strain models for FRP-confined concrete, namely, the models of Lam and Teng (2009), Yu et al. (2015), and Huang et al. (2021). Lam and Teng's (2009) model was originally developed for capturing the cyclic stress-strain behaviour of FRP-confined NSC. The model has been demonstrated to be capable of accurately predicting the cyclic stress-strain behaviour of FRP-confined NSC. Yu et al. (2015) and Huang et al. (2021) further improved Lam and Teng's (2009) model to be applicable to FRP-confined HSC and FRP-confined UHPC, respectively. Note that the average compressive strength of UHPC for developing the model of Huang et al. (2021) was 137.7 MPa. Table 6.2 summarises the equations of the three existing cyclic stress-strain models. To assess the performance of these models in predicting the unloading/reloading paths of FRP-confined UHPC in the present study, the experimental envelope curves, including the experimental values of unloading strain ε_{un}, unloading stress σ_{un}, and plastic strain ε_{pl} were directly used in generating the predicted unloading/reloading stress-strain curves. This approach allowed a direct comparison between the predicted unloading/reloading paths and the test results, eliminating the influence of the accuracy of an envelope stress-strain model. Besides, the axial stress contribution of the GFRP tubes was ignored due to their negligible axial stiffnesses.

6.4.2 Unloading Curves

Figure 6.6 shows the comparison between the predictions based on Lam and Teng (2009), Yu et al. (2015), Huang et al. (2021) and the test results in terms of the unloading curves for the test FRP-confined UHPC specimens. Yu et al.'s (2015) model provides reasonably accurate predictions for the unloading curves, while the curves of Lam and Teng's (2009) model and Huang et al.'s (2021) model deviate from the test curves significantly. Both Lam and Teng's (2009) model and Yu et al.'s (2015) model were developed based on a large test database including both FRP-confined NSC and HSC. However, the HSC specimens used for the development of Lam and Teng's (2009) model were from one single source (Rousakis, 2001), which may lead to a low accuracy of this model for predicting FRP-confined HSC. Yu et al. (2015) modified Lam and Teng's (2009) model based on a larger database containing more experimental results of FRP-confined HSC specimens as well as concrete in filament-wound FRP tubes (i.e., CFFTs). As a result, Yu et al.'s (2005) model provided accurate predictions for the GFRP tube-confined UHPC specimens (including wavy-shaped specimens) in the present study. Huang et al.'s (2021) model was developed based on Lam and Teng's (2009) model but the test database they used consisted of only their own test results of CFRP-confined UHPC specimens. The average 28-day compressive strength of UHPC in Huang et al. (2021) was 137.7 MPa. As shown in Figure 6.6, the degree of non-linearity of the unloading curves predicted by Huang et al. (2021) was smaller than that observed in the experimental curves. The relatively low accuracy of Huang et al.'s (2021) model may be attributable to its database with limited test results. Based on the above observations, the following equation of parameter η in Yu et al.'s (2015) model which controls the shape of the unlading path was adopted in the present study for predicting the unloading paths of FRP-confined UHPC:

$$\eta = 40(350\varepsilon_{un} + 3)/f'_{co} \tag{6.1}$$

in which, ε_{un} is the unloading strain; f'_{co} is the compressive strength of unconfined concrete.

6.4.3 Plastic Strains

Figure 6.7 illustrates the influence of various parameters, such as GFRP tube thickness and wave height, on the relationship between plastic strain ε_{pl} and corresponding unloading strain ε_{un}. It could be observed that a linear relationship generally exists between the values of ε_{un} and ε_{pl}; thus, the linear trend lines regressed based on the test result of different groups of specimens are also presented in the figures. As shown in Figure 6.7(a), the increase in GFRP tube thickness leads to a slight decrease in the plastic strain. This is consistent with the observations reported in the literature for FRP-confined UHPC which revealed that FRP confinement would affect the relationships between ε_{un} and ε_{pl} (Tian et al. 2020, Huang et al. 2021).

Figures 6.7(b) and 6.7(c) illustrate the effect of wave height on the relationship between ε_{un} and ε_{pl} for FRP-confined UHPC specimens with three-ply and five-ply GFRP tubes, respectively. Compared with specimens with uniform GFRP tubes, those with wavy-shaped

GFRP tubes seem to possess a smaller plastic strain at a given unloading strain. Besides, for the wavy-shaped specimens with 3-ply GFRP tubes, it can be observed that the linear trend lines of different wave heights are close to each other. Further observations revealed that the higher trend lines of the uniform specimens (i.e., H0 series specimens) are attributed to the higher plastic strains exhibited by two specimens, i.e., FU-H0L3-C1 and FU-H0L5-C1. As shown in Figures 6.3(a) and 6.3(b), the axial load-axial strain curves of specimens FU-H0L3-C1 and FU-H0L5-C1 exhibit significantly larger load drops after the first peak load compared to the other specimens. Therefore, it can be inferred that this load drop affected the relationship between the unloading strain and the plastic strain. Except these two specimens, the other specimens (i.e., FU-H0L3-C2 and FU-H0L5-C2) sharing the same geometric and material properties of the above two specimens closely align with the data from the UHPC specimens confined by wavy-shaped GFRP tubes. Therefore, it can be concluded that the wave height of wavy-shaped GFRP tubes does not directly impact the relationship between plastic strains and corresponding unloading strains for FRP-confined UHPC specimens, but it might prevent the occurrence of load drops, thus indirectly influencing the relationship.

In Yu et al.'s (2015) model, a linear relationship between plastic strains ε_{pl} and unloading strains ε_{un} was adopted, whereas Lam and Teng's (2009) model incorporates the influence of concrete strength $f_{co}^{'}$. Huang et al. (2021) developed a model with both the concrete strength f_{co}' and the confining pressure f_{lu} taken into account. These equations are summarised in Table 6.2. Figure 6.8 shows the comparisons between the test results and the predictions with these three models. It can be observed that the models of Yu et al. (2015) and Huang et al. (2021) slightly overestimate the plastic strains, whereas the model of Lam and Teng (2009) underestimates the plastic strains dramatically. As a result, to better predict the plastic strains of FRP-confined UHPC, a new model of the relationship between unloading strains ε_{un} and plastic strains ε_{pl} should be proposed.

Figure 6.9 presents the plastic strains ε_{pl} against the corresponding envelope unloading strains ε_{un} for all FRP-confined UHPC specimens in the present study. It is evident that there is a linear relationship between ε_{pl} and ε_{un} when the latter is larger than 0.0065. Regression analysis was conducted for the data points of each FRP-confined UHPC specimens in the present research project. The statistical characteristics of the linear trendlines are summarised in Table 6.3. By averaging coefficients a and b for all specimens in Table 6.3, the following equations are obtained for the plastic strain:

$$\varepsilon_{pl} = 0.758\varepsilon_{un} - 0.0032 \tag{6.2}$$

As discussed earlier, the relationship between ε_{pl} and ε_{un} depends on the FRP confinement and the load drops after the first peak load. To further improve the accuracy of predictions, the following equation is also proposed to predict the plastic strain:

$$\varepsilon_{pl} = 0.682\varepsilon_{un} - 0.0179\frac{f_l}{f'_{co}} + 0.00368\frac{f_d}{f'_{co}} - 0.00046 \tag{6.3}$$

where f_d= the stress drops after the first peak stress. Note that the unloading strains of the test specimens used in the regression analysis for Eqs. 6.2 and 6.3 were all larger than 0.0065. More test data are needed in the future for more accurate predictions with wider ranges of parameters. Table 6.4 lists the mean values and the Coefficients of Variation (CoVs) of the ratios between test results and predicted results for the aforementioned models and the proposed equation (Eqs. 6.2 and 6.3). In Table 6.4, the mean and CoV for the model proposed by Lam and Teng (2009) are negative, as this model is not suitable for UHPC. The proposed Eqs. 6.2 and 6.3 demonstrate better performance, as evidenced by mean values of 1.08 and 1.02, and CoVs of 0.137 and 0.106, respectively. To simplify the calculations, Eq. 6.2 is used in the subsequent analysis to predict plastic strains for FRP-confined UHPC.

6.4.4 Stress Deterioration

As shown in Figures 6.5, it is evident that the new stress on the reloading path at the envelope unloading strain is lower than the envelope unloading stress. To describe this stress deterioration behaviour, a parameter referred to as stress deterioration ratio φ is defined as

$$\varphi = \frac{\sigma_{new}}{\sigma_{un,env}} \tag{6.4}$$

The experimental stress deterioration ratios for the FRP-confined UHPC specimens are presented in Figure 6.10. The average values for all the FRP-confined UHPC specimens is 0.953, which is slightly larger than the value of 0.92 for uniform FRP-confined NSC reported by Lam and Teng (2009), but similar to the values of 0.95 and 0.967 for uniform FRP-confined UHPC proposed by Tian et al. (2020) and Huang et al. (2021), respectively. Therefore, the stress deterioration ratio of FRP-confined UHPC is proposed to be calculated in the following equation:

$$\varphi = f(x) = \begin{cases} 1, & \varepsilon_{un} < 0.0045 \\ 0.953, & \varepsilon_{un} \geq 0.0045 \end{cases} \tag{6.5}$$

6.4.5 Reloading Curves

A reloading path generally consists of a linear portion and a parabolic portion. For FRP-confined UHPC specimens, the linear first portion is a straight line between the point at the plastic strain (Point b in Figure 6.5) and the point at the unloading strain (referred to as the junction point, Point c in Figure 6.5). Therefore, the axial stress of the junction point (σ_{new}) can be expressed as follows:

$$\sigma_{new} = \varphi \sigma_{un} \tag{6.6}$$

The linear first portion is depicted by:

$$\sigma_c = \sigma_{re} + E_{re}(\varepsilon_c - \varepsilon_{re})\left(\varepsilon_{re} \leq \varepsilon_c \leq \varepsilon_{ref}\right) \tag{6.7}$$

where the slope of the linear first portion E_{re} can be calculated as follow:

$$E_{re} = \frac{\sigma_{new} - \sigma_{re}}{\varepsilon_{ref} - \varepsilon_{re}}\left(\varepsilon_{re} \leq \varepsilon_c \leq \varepsilon_{ref}\right) \tag{6.8}$$

The parabolic second portion can be depicted by the following expression proposed by Lam and Teng (2009):

$$\sigma_c = A{\varepsilon_c}^2 + B\varepsilon_c + C\left(\varepsilon_{ref} \leq \varepsilon_c \leq \varepsilon_{ret,env}\right) \tag{6.9}$$

where A, B and C are constants to be determined. Once A is defined, the values of B and C can be determined using the following equations:

$$B = E_{re} - 2A\varepsilon_{ref} \tag{6.10}$$

$$C = \sigma_{new} - A\varepsilon_{ref}{}^{2} - B\varepsilon_{ref} \tag{6.11}$$

The envelope returning strain $\varepsilon_{ret,env}$ is calculated by the following equation:

$$\varepsilon_{ret,env} = \frac{E_c - B}{2A + \frac{(E_C - E_2)^2}{f'_{c0}}} \tag{6.12}$$

where E_C and f'_{c0} are the elastic modulus and the compressive strength of unconfined concrete. The start strain at the transition point (i.e., the start strain of the second linear path) of the envelope curve is given by:

$$\varepsilon_t = \frac{2f'_{co}}{(E_c - E_2)} \tag{6.13}$$

for $\varepsilon_{ret,env} < \varepsilon_t$,

$$A = \frac{(E_C - E_2)^2(E_{re}\varepsilon_{ref} - \sigma_{new}) + (E_C - E_{re})^2 f'_{c0}}{4(\sigma_{new} - E_c\varepsilon_{ref})f'_{c0} + (E_C - E_2)^2\varepsilon_{ref}{}^2} \tag{6.14}$$

for $\varepsilon_{ret,env} \geq \varepsilon_t$,

$$A = \frac{(E_{re} - E_2)^2}{4(\sigma_{new} - f'_{co} - E_2\varepsilon_{ref})} \tag{6.15}$$

$$\varepsilon_{ret,env} = \frac{E_2 - B}{2A} \tag{6.16}$$

With Eq. 6.5, a stress deterioration ratio of 0.953, and Eqs. 6.6-6.16, the unloading/reloading curves could be predicted as shown in Figure 6.11. Again, in making the predicted reloading curves, the experimental unloading strains and stresses in the envelope curves were directly adopted. As shown in Figure 6.11, the proposed method could provide reasonably accurate predictions for the unloading/reloading curves for the FRP-confined UHPC specimens, including both uniform specimens and wavy-shaped specimens, tested in the present study.

6.5 THEORETICAL ANALYSIS OF WAVY-SHAPED HYBRID REBARS

6.5.1 General

The load-strain curves of a wavy-shaped hybrid rebar could be obtained by summing the load-strain curves of three different constituent components of the hybrid rebar. The axial load of the hybrid rebar F_h at a given axial strain is calculated in the following equation:

$$F_h = A_b\sigma_b + A_a\sigma_a + A_t\sigma_t \tag{6.17}$$

in which A_b, A_a, and A_t are the cross-sectional areas of the central FRP rebar, concrete filled between the rebar and the outer GFRP tube, and the outer GFRP tube, respectively; σ_b and σ_t are the axial compressive stresses of the central FRP rebar and the outer GFRP tube; σ_c is the axial compressive stress of the confined concrete filled between the rebar and the outer GFRP tube. The GFRP tubes of the test specimens possessed a fibre orientation of approximately 89 degrees, leading to negligibly small axial stiffnesses; therefore, the axial contribution of the GFRP tubes was ignored in the calculations.

6.5.2 Unloading Curves

Based on the discussion in Section 6.4.2, Eq. 6.1 of parameter η in Yu et al.'s (2015) model which controls the shape of the unlading path was adopted in the present study for predicting the unloading paths of FRP-confined UHPC. The unloading curves of the hybrid rebar specimens were calculated based on Eq. 6.17 by summing the load-strain curves of different constituent components of a hybrid rebar.

6.5.3 Plastic Strains

Figure 6.12 presents the relationship between the unloading strains and plastic strains for the uniform and wavy-shaped hybrid rebars. Based on linear regression analyses, the following equations are proposed for hybrid rebars before (Stage 3) and after (Stage 4) the failure of the central FRP rebar, respectively:

$$\varepsilon_{pl,stage\ 3} = 0.0665\varepsilon_{un} + 0.0004 \tag{6.18}$$

$$\varepsilon_{pl,stage\ 4} = 0.4478\varepsilon_{un} - 0.0015 \tag{6.19}$$

As defined in Chapter 5, Stage 3 starts at the load drop at the corresponding peak load of the unconfined UHPC and ends at the failure of the central FRP rebar or the rupture of the FRP tube whichever occurred first. If the FRP rebar failed before the rupture of the FRP tube, the hybrid rebar can still resist a certain level of load due to the confinement provided by the FRP tube. In such case, a Stage 4 exists for the process after the failure of the FRP rebar until the rupture of the FRP tube.

During the unloading/reloading process, it should be noted that the axial strains of different components (i.e., FRP rebar and UHPC) at a zero axial force may be different in a hybrid rebar. It is known that the FRP rebar is an elastic material while the concrete possesses plasticity due to damage; therefore, the former exhibits smaller residual axial strains than the latter. Figure 6.13 shows the comparisons of plastic strains between hybrid rebars and FRP-confined UHPC specimens. It is evident that the plastic strains of hybrid rebars are lower than those of FRP-confined UHPC specimens. A typical unloading/reloading load-strain curve for a wavy-shaped hybrid rebar is shown in Figure 6.14, the unloading load-axial strain relationship is nearly linear when the load is relatively low. A theoretical axial load-axial strain curve of the FRP rebar is drawn from the plastic strain ε_{pl}, the slope of which was obtained based on the average value of elastic moduli of the FRP rebars in the coupon tensile tests. It can be observed that the unloading curve almost coincides with the curve of the FRP rebar when the load is close to zero, which means that the axial strain $\varepsilon_{pl,co}$ at which the unloading curve and the curve of the FRP rebar separate could be regarded as the plastic strain of UHPC. Therefore, $\varepsilon_{pl,co}$ should be adopted for UHPC in making predictions for hybrid rebars. Figure 6.15 presents the relationship between the plastic strains $\varepsilon_{pl,co}$ and the corresponding unloading strains for all hybrid rebar specimens. The following equation could be obtained to calculate $\varepsilon_{pl,co}$ for UHPC:

$$\varepsilon_{pl,co} = 0.7646\varepsilon_{un} - 0.0037 \tag{6.20}$$

6.5.4 Stress Deterioration

The experimental stress deterioration ratios for the hybrid rebar specimens are shown in Figure 6.16. The average values for the hybrid rebar specimens are 0.965, which is slightly larger than that for the FRP-confined UHPC specimens in the present study. The deterioration of stress is attributed to the inner damage of concrete under cyclic loading (Bai et al., 2021). In a hybrid rebar, the existence of FRP rebar results in a lower proportion of UHPC compared to the corresponding FRP-confined UHPC. Consequently, the stress deterioration due to UHPC damage is more pronounced in FRP-confined UHPC than in the hybrid rebar. Therefore, the stress deterioration ratio of a hybrid rebar is proposed by:

$$\varphi = f(x) = \begin{cases} 1, & \varepsilon_{un} < 0.0045 \\ 0.965, & \varepsilon_{un} \geq 0.0045 \end{cases} \tag{6.21}$$

6.5.5 Reloading Curves

The reloading curves of hybrid rebars also consist of a linear first portion and a parabolic second portion, which could be depicted with Eqs. 6.6-6.16. Thus, with the stress deterioration ratio of 0.965 and the plastic strain of Eqs. 6.18-6.20, as well as Eqs. 6.6-6.16, the reloading curves of the test hybrid rebar specimens could be predicted.

6.5.6 Predicted Cyclic Load-Strain Curves for Hybrid Rebars

The equation of parameter η (Eq. 6.1) in Yu et al.'s (2015) model which controls the shape of the unlading path was adopted in the present study for predicting the unloading paths of FRP-confined UHPC in hybrid rebars due to its satisfactory performance in predicting the cyclic behaviour of FRP-confined UHPC as shown in Section 6.4.2. The equations of plastic strains for hybrid rebars (i.e., Eqs. 6.18-6.19) and for FRP-confined UHPC proposed in Section 6.5.3 (i.e., Eq. 6.2) were utilised in combination with Eq. 6.1 of Yu et al.'s (2015) model. The overall performance of the cyclic stress-strain model proposed in this section was evaluated in Figure 6.17. In the predictions, the experimental unloading strains were used to predict the plastic strains (ε_{pl}) and the experimental unloading stresses were used to predict the new stresses on the reloading path at the envelope unloading strains (σ_{new}).

It is evident that the proposed model in this study can provide reasonably accurate predictions for the envelope unloading/reloading curves of the hybrid rebars.

In Chapter 5, an envelope load-strain model was proposed for the prediction of hybrid rebars under monotonic axial compression. This model was adopted herein to generate the envelope load-strain curves of hybrid rebars under cyclic axial compression. As shown in Figure 6.18, the predicted load-strain curves are plotted and compared with the experimental load-strain curves for hybrid rebar specimens. As shown in Figure 6.17, the predicted curves show good agreement with the experimental curves, indicating the good performance of the proposed method in the prediction of the compressive behaviour of wavy-shaped hybrid rebars under cyclic compression.

6.6 CONCLUSIONS

This chapter has presented a systematic experimental study on the compressive behaviour of wavy-shaped FRP tube-confined UHPC specimens and wavy-shaped hybrid rebar specimens under cyclic axial compression. A stress-strain model modified from Yu et al.'s (2015) model was developed to predict the cyclic load-strain curves of wavy-shaped FRP tube-confined UHPC specimens and wavy-shaped hybrid rebar specimens. The following conclusions can be made based on the experimental results and the theoretical analyses presented in this chapter:

(1) All wavy-shaped FRP tubes confined UHPC specimens and wavy-shaped hybrid rebars ultimately failed with the rupture of GFRP tubes due to hoop tension. The envelope curves of the cyclically loaded wavy-shaped hybrid rebars could also be divided into three or four stages, similar to the stress-strain curves of monotonically loaded wavy-

shaped hybrid rebars. The envelope load-strain curves of wavy-shaped FRP tube-confined UHPC specimens and wavy-shaped hybrid rebars under cyclic axial compression were close to the load-strain curves of their corresponding specimens under monotonic axial compression.

(2) The equation for parameter η (i.e., Eq. 6.1) in Yu et al.'s (2015) model could provide accurate predictions for the shape of unloading paths of wavy-shaped FRP tube-confined UHPC specimens.

(3) New equations for plastic strains and stress deteriorations for both wavy-shaped FRP tube-confined UHPC specimens and wavy-shaped hybrid rebars were proposed and they could provide reasonably accurate predictions for the present test results.

(4) The proposed stress-strain model is reasonably accurate in predicting the compressive behaviour of wavy-shaped FRP tube-confined UHPC specimens and wavy-shaped hybrid rebars under cyclic axial compression.

6.7 REFERENCES

Bai, Y.L., Mei, S.J., Li, P.D. and Xu, J.J. (2021). "Cyclic stress-strain model for large-rupture strain fiber-reinforced polymer (LRS FRP)-confined concrete", *Journal of Building Engineering*, 42, 102459.

Huang, L., Xie, J.H., Li, L.M., Xu, B.Q., Huang, P.Y. and Lu, Z.Y. (2021). "Compressive behaviour and modelling of CFRP-confined ultra-high performance concrete under cyclic loads", *Construction and Building Materials*, 310, 124949.

Lam, L. and Teng, J. (2009). "Stress–strain model for FRP-confined concrete under cyclic axial compression", *Engineering Structures*, 31(2), 308-321.

Rousakis, T.C. (2001). *Experimental Investigation of Concrete Cylinders Confined by Carbon FRP Sheets, under Monotonic and Cyclic Axial Compressive Load*, Research Report 01:2, Division of building technology, Chalmers University of Technology, Gothenburg, Sweden.

Shao, Y., Zhu, Z. and Mirmiran, A. (2006). "Cyclic modeling of FRP-confined concrete with improved ductility", *Cement and Concrete Composites*, 28(10), 959-968.

Tian, H.W., Zhou, Z., Wei, Y. and Lu, J. (2020). "Behavior and modeling of ultra-high performance concrete-filled FRP tubes under cyclic axial compression", *Journal of Composites for Construction*, ASCE, 24(5), 04020045.

Yu, T., Zhang, B. and Teng, J.G. (2015). "Unified cyclic stress–strain model for normal and high strength concrete confined with FRP", *Engineering Structures*, 102, 189-201.

Zhang, B., Yu, T. and Teng, J.G. (2015). "Behavior of concrete-filled FRP tubes under cyclic axial compression", *Journal of Composites for Construction*, ASCE, 19(3),

04014060.

Table 6.1 Details of specimens

Series	Specimen	Loading scheme	Thickness of GFRP tube	Wave height (mm)
Series 1	FU-H0L3-M1,2[a]	Monotonic	3-ply	0
	FU-H1L3-M1,2[a]	Monotonic	3-ply	1
	FU-H3L3-M1,2[a]	Monotonic	3-ply	3
	FU-H5L3-M1,2[a]	Monotonic	3-ply	5
	FU-H0L3-C1,2	Cyclic	3-ply	0
	FU-H1L3-C1,2	Cyclic	3-ply	1
	FU-H3L3-C1,2	Cyclic	3-ply	3
	FU-H5L3-C1,2	Cyclic	3-ply	5
	FU-H0L5-M1,2[a]	Monotonic	5-ply	0
	FU-H5L5-M1,2[a]	Monotonic	5-ply	5
	FU-H0L5-C1,2	Cyclic	5-ply	0
	FU-H5L5-C1,2	Cyclic	5-ply	5
Series 2	HR-H0L3-M1,2[a]	Monotonic	3-ply	0
	HR-H1L3-M1,2[a]	Monotonic	3-ply	1
	HR-H3L3-M1,2[a]	Monotonic	3-ply	3
	HR-H5L3-M1,2[a]	Monotonic	3-ply	5
	HR-H0L3-C1,2	Cyclic	3-ply	0
	HR-H1L3-C1,2	Cyclic	3-ply	1
	HR-H3L3-C1,2	Cyclic	3-ply	3
	HR-H5L3-C1,2	Cyclic	3-ply	5
	HR-H0L5-M1,2[a]	Monotonic	5-ply	0
	HR-H5L5-M1,2[a]	Monotonic	5-ply	5
	HR-H0L5-C1,2	Cyclic	5-ply	0
	HR-H5L5-C1,2	Cyclic	5-ply	5

[a] Specimens subject to monotonic compression which have been reported in Chapter 5

Table 6.2 Existing cyclic stress-strain models for FRP-confined concrete

	Lam and Teng (2009)	Yu et al. (2015)	Huang et al. (2021)
Unloading model	$\sigma_c = a\varepsilon_c^{\eta} + b\varepsilon_c + c$ $a = \frac{\sigma_{un} - E_{un,0}(\varepsilon_{un} - \varepsilon_{pl})}{\varepsilon_{un}^{\eta} - \varepsilon_{pl}^{\eta} - \eta\varepsilon_{pl}^{\eta-1}(\varepsilon_{un} - \varepsilon_{pl})}$ $b = E_{un,0} - \eta\varepsilon_{pl}^{\eta-1}a$ $c = -a\varepsilon_{pl}^{\eta} - b\varepsilon_{pl}$ $E_{un,0} = \min\left(\frac{0.5f'_{c0}}{\varepsilon_{un}}, \frac{\sigma_{un}}{\varepsilon_{un} - \varepsilon_{pl}}\right)$ $\eta = 350\varepsilon_{un} + 3$	Same as Lam and Teng (2009) except for η $\eta = 40(350\varepsilon_{un} + 3)/f'_{c0}$	Same as Lam and Teng (2009) except for $E_{un,0}$ and η $E_{un,0} = 40f'_{co}/\varepsilon_{un}^{0.3}$ $\eta = 100(350\varepsilon_{un} + 3)/f'_{c0}$
Plastic strain	for $0 < \varepsilon_{un} \leq 0.001$, $\varepsilon_{pl} = 0$ for $0.001 < \varepsilon_{un} < 0.0035$, $\varepsilon_{pl} = [1.4(0.87 - 0.004f'_{c0}) - 0.64](\varepsilon_{un} - 0.001)$ for $0.0035 \leq \varepsilon_{un} \leq \varepsilon_{cu}$, $\varepsilon_{pl} = (0.87 - 0.004f'_{c0})\varepsilon_{un} - 0.0016$	for $0 < \varepsilon_{un} \leq 0.001$, $\varepsilon_{pl} = 0$ for$0.001 < \varepsilon_{un} \leq 0.0035$, $\varepsilon_{pl} = 0.184\varepsilon_{un} - 0.0002$ for $0.0035 < \varepsilon_{un} \leq \varepsilon_{cu}$, $\varepsilon_{pl} = 0.703\varepsilon_{un} - 0.002$	for$0 < \varepsilon_{un} \leq 0.0035$, $\varepsilon_{pl} = 0$ for $0.0035 < \varepsilon_{un} \leq \varepsilon_{cu}$, $\varepsilon_{pl} = 0.72\varepsilon_{un} - 0.005(f_{lu}/f'_{co})^{0.5}$
Stress deteriorati on	for $0 < \varepsilon_{un} \leq 0.001$, $\varphi = 1$ for $0.001 < \varepsilon_{un} < 0.002$,$\varphi = 1 - 80(\varepsilon_{un} - 0.001)$ for $0.002 \leq \varepsilon_{un} \leq \varepsilon_{cu}$, $\varphi = 0.92$	for $0 < \varepsilon_{un} \leq 0.001$, $\varphi = 1$ for $0.001 < \varepsilon_{un} \leq 0.0035$, $\varphi = 1 - 32(\varepsilon_{un} - 0.001)$ for $0.0035 < \varepsilon_{un} \leq \varepsilon_{cu}$, $\varphi = 0.92$	for $\varepsilon_{un} < 0.0035$, $\varphi = 1$ for $0.0035 < \varepsilon_{un}$ $\varphi = 0.967$

Table 6.2 *(Continued)*

Objects	Lam and Teng (2009)	Yu et al. (2015)	Huang et al. (2021)
Reloading model	for $\varepsilon_{re} \leq \varepsilon_c \leq \varepsilon_{ref}$, $\sigma_c = \sigma_{re} + E_{re}(\varepsilon_c - \varepsilon_{re})$ for $\varepsilon_{ref} \leq \varepsilon_c \leq \varepsilon_{ret,env}$, $\sigma_c = A{\varepsilon_c}^2 + B\varepsilon_c + C$ $E_{re} = (\sigma_{new} - \sigma_{re})/(\varepsilon_{ref} - \varepsilon_{re})$ $\sigma_{new} = \varphi\sigma_{un}$ $B = E_{re} - 2A\varepsilon_{ref}$ $C = \sigma_{new} - A{\varepsilon_{ref}}^2 - B\varepsilon_{ref}$ for $\varepsilon_{ret,env} < \varepsilon_t$, $A = \frac{(E_C - E_2)^2\left(E_{re}\varepsilon_{ref} - \sigma_{new}\right) + (E_C - E_{re})^2 f'_{c0}}{4\left(\sigma_{new} - E_c\varepsilon_{ref}\right)f'_{c0} + (E_C - E_2)^2{\varepsilon_{ref}}^2}$ $\varepsilon_{ret,env} = \frac{E_c - B}{2A + \frac{(E_C - E_2)^2}{f'_{c0}}}$ for $\varepsilon_{ret,env} \geq \varepsilon_t$, $A = \frac{(E_{re} - E_2)^2}{4(\sigma_{new} - f'_{co} - E_2\varepsilon_{ref})}$ $\varepsilon_{ret,env} = \frac{E_2 - B}{2A}$	Same as Lam and Teng (2009)	for $\varepsilon_{re} \leq \varepsilon_c \leq \varepsilon_{ref}$, $\mathrm{D} = 1 - 200 \times (\varepsilon_{ref} - \varepsilon_c)^{1.25}$ $\sigma_c = \sigma_{re} + DE_{re}(\varepsilon_c - \varepsilon_{re})$ for $\varepsilon_{ref} \leq \varepsilon_c \leq \varepsilon_{ret,env}$, $\sigma_c = A{\varepsilon_c}^2 + B\varepsilon_c + C$ $E_{re} = (\sigma_{new} - \sigma_{re})/(\varepsilon_{ref} - \varepsilon_{re})$ $\sigma_{new} = \varphi\sigma_{un}$ $B = E_{re} - 2A\varepsilon_{ref}$ $C = \sigma_{new} - A{\varepsilon_{ref}}^2 - B\varepsilon_{ref}$ $f'_o = \exp\,[1.97(\frac{2E_{frp}t_{frp}}{E_{seco}d})]$ for $\varepsilon_{ret,env} < \varepsilon_t$, $A = \frac{4(E_C - E_2)^2\left(E_{re}\varepsilon_{ref} - \sigma_{new}\right) + 7.}{28.8f'_o\left(\sigma_{new} - E_c\varepsilon_{ref}\right) + 4(E_C}$ $\varepsilon_{ret,env} = \frac{E_c - B}{2A + \frac{(E_C - E_2)^2}{3.6f'_o}}$ for $\varepsilon_{ret,env} \geq \varepsilon_t$, $A = \frac{(E_{re} - E_2)^2}{4(\sigma_{new} - f'_o - E_2\varepsilon_{ref})}$, $\varepsilon_{ret,env} = \frac{E_2 - B}{2A}$

Table 6.3 Regression analysis for plastic strains of FU specimens

Specimen	$\varepsilon_{pl} = a\varepsilon_{un} + b$		R^2
	a	b	
FU-H0L5-C1	0.760	-0.0026	0.992
FU-H0L5-C2	0.655	-0.0029	1.000
FU-H5L5-C1	0.658	-0.0031	1.000
FU-H5L5-C2	0.614	-0.0027	0.992
FU-H0L3-C1	1.058	-0.0048	1.000
FU-H0L3-C2	0.836	-0.0036	0.998
FU-H1L3-C1	0.731	-0.0023	1.000
FU-H1L3-C2	0.798	-0.0042	1.000
FU-H3L3-C1	0.760	-0.0032	0.999
FU-H3L3-C2	0.810	-0.0039	0.992
FU-H5L3-C1	0.603	-0.0016	0.996
FU-H5L3-C2	0.814	-0.0036	0.997

Table 6.4 Statistical evaluation of different models

Model	Mean	CoV
Lam and Teng (2009)	-0.09	-1.467
Yu et al. (2015)	1.20	0.176
Huang et al. (2021)	1.28	0.177
Eq. 6.2	1.08	0.137
Eq. 6.3	1.02	0.106

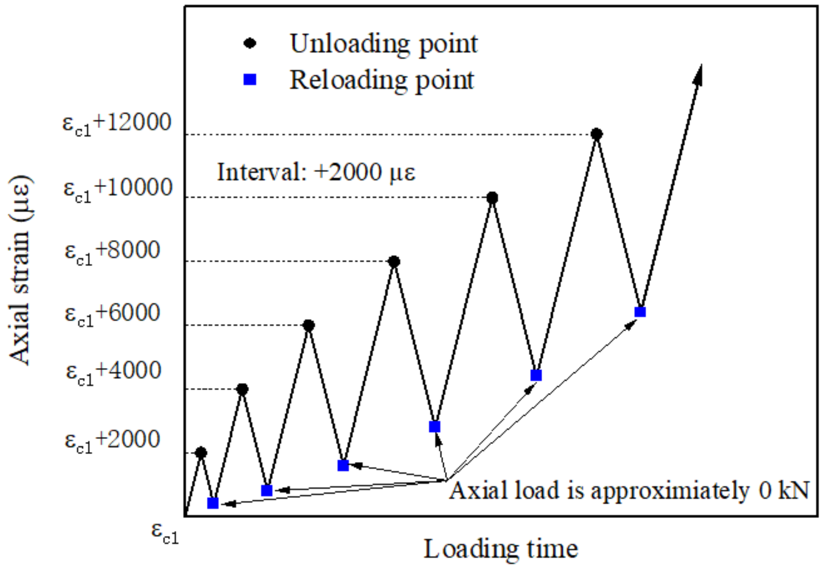

Figure 6.1 Cyclic loading scheme

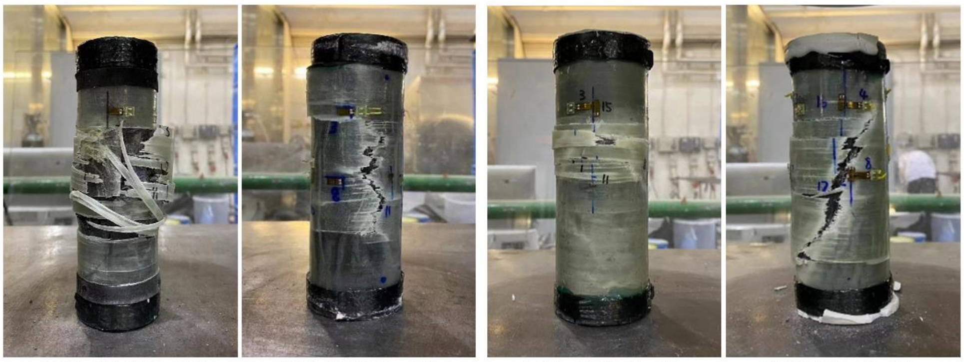

HR-H0L3-C1 FU-H0L3-C1 HR-H0L5-C1 FU-H0L5-C1

(a) Uniform specimens

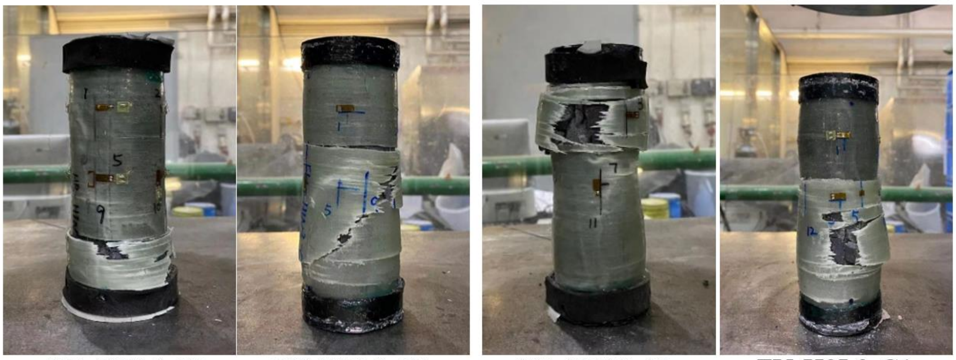

HR-H1L3-C1 FU-H1L3-C1 HR-H3L3-C1 FU-H3L3-C1

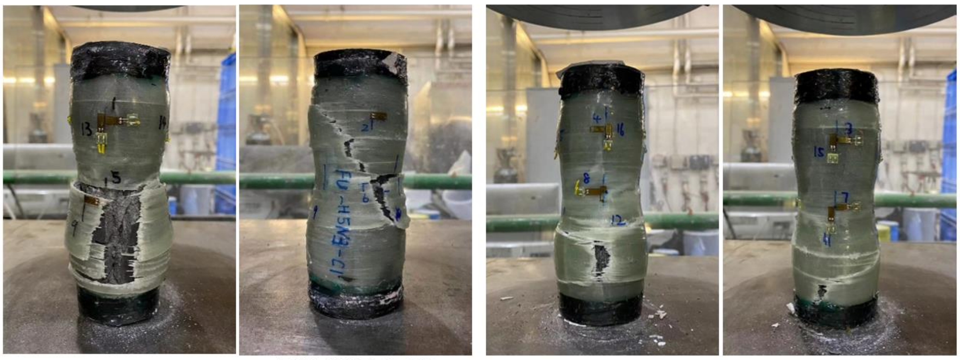

HR-H5L3-C1 FU-H5L3-C1 HR-H5L5-C1 FU-H5L5-C1

(b) Wavy-shaped specimens

Figure 6.2 Typical failed specimens

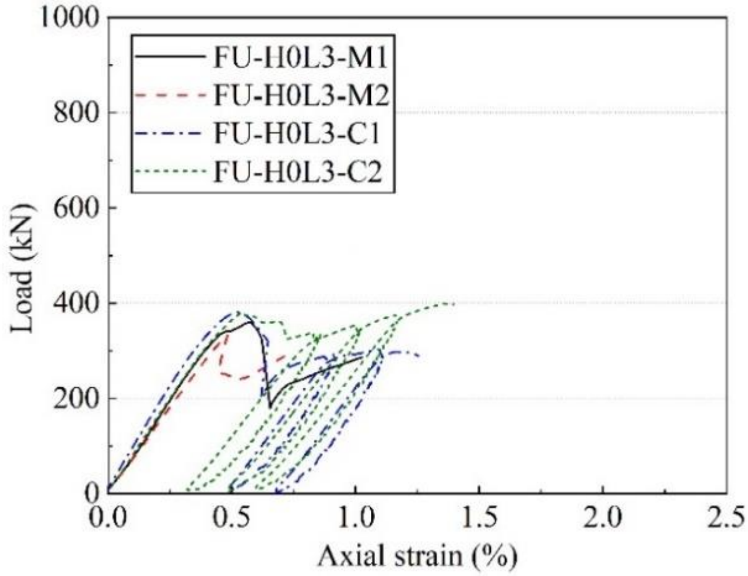

(a) FU-H0L3 specimens

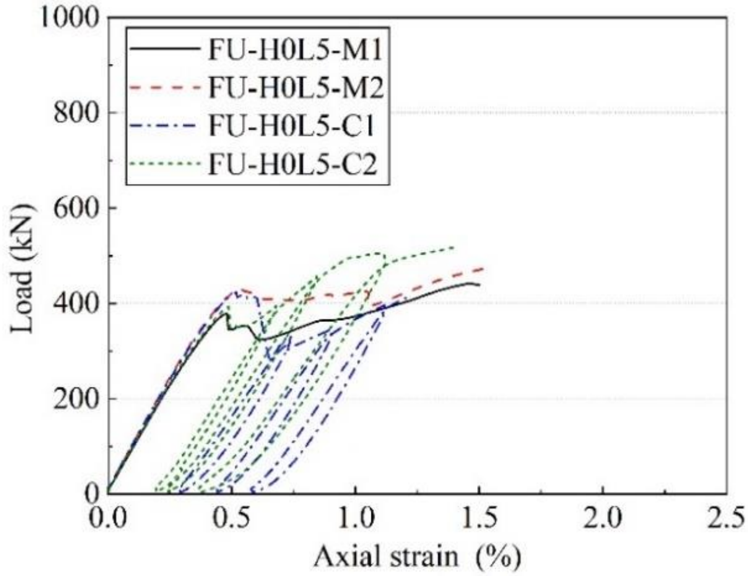

(b) FU-H0L5 specimens

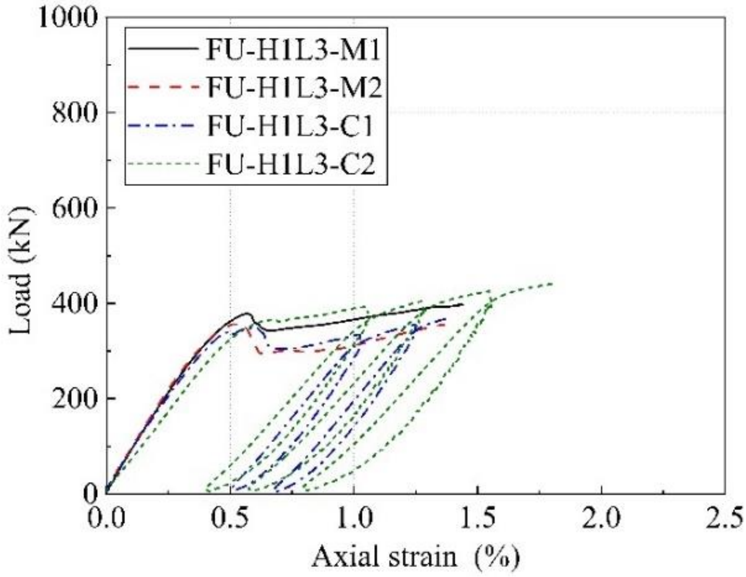

(c) FU-H1L3 specimens

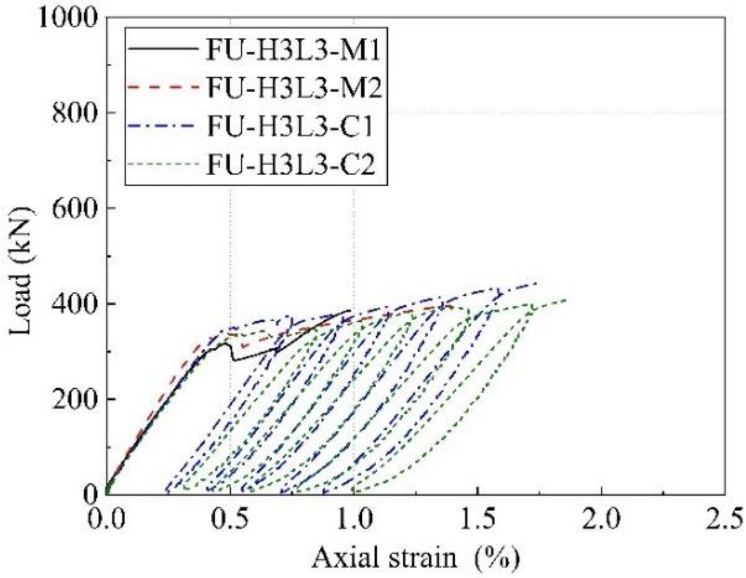

(c) FU-H3L3 specimens

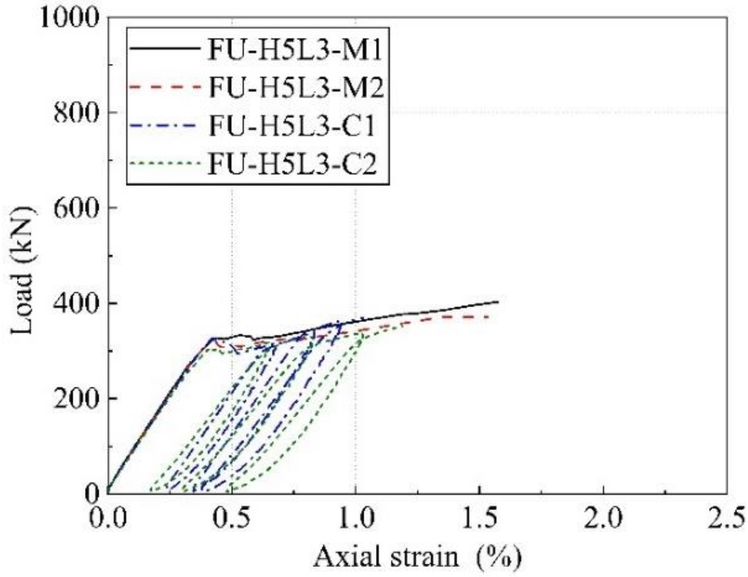

(e) FU-H5L3 specimens

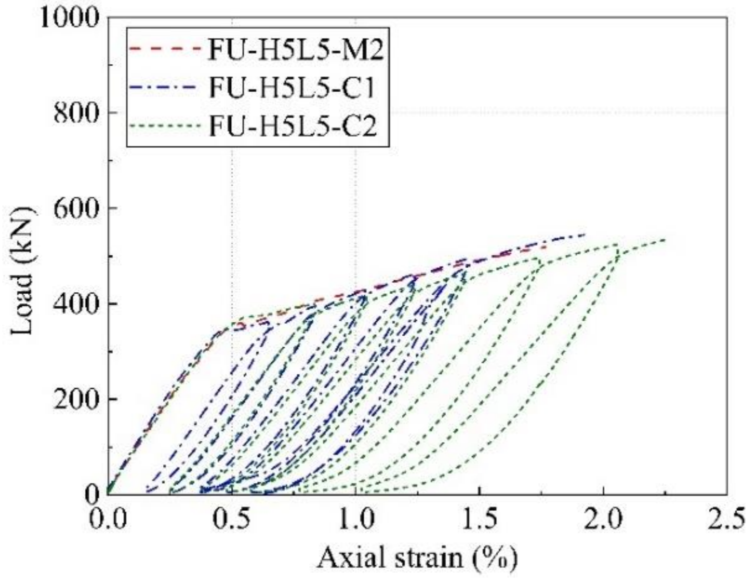

(f) FU-H5L5 specimens
Figure 6.3 Load-axial strain curves for specimens of Series 1

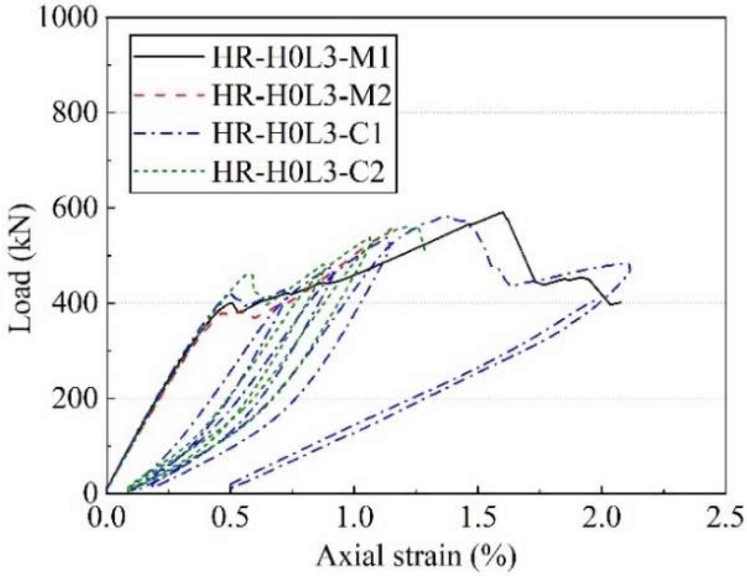

(a) HR-H0L3 specimens

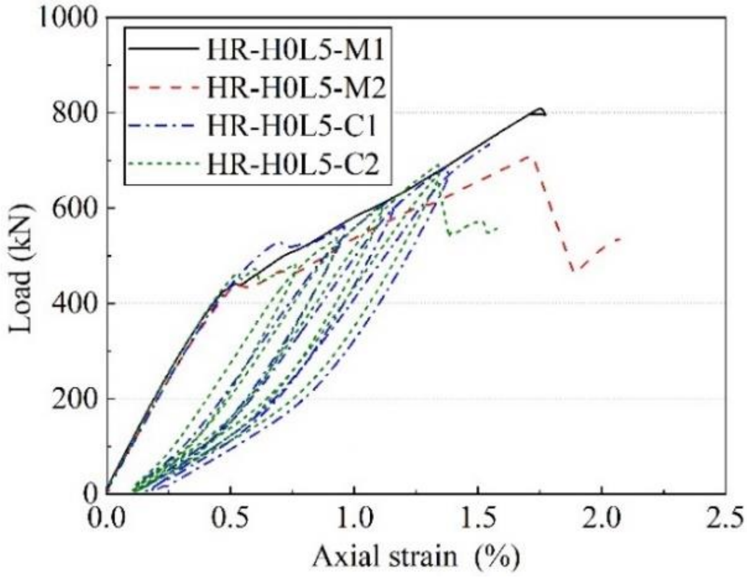

(b) HR-H0L5 specimens

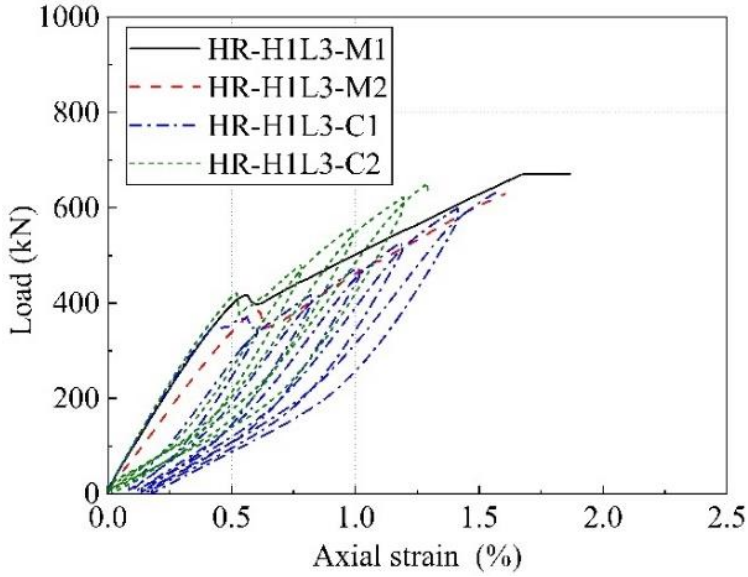

HR-H1L3 specimens

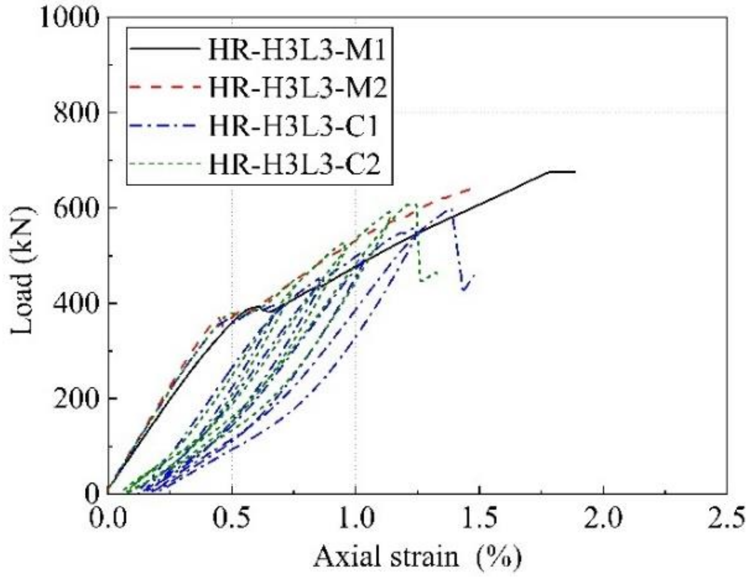

HR-H3L3 specimens

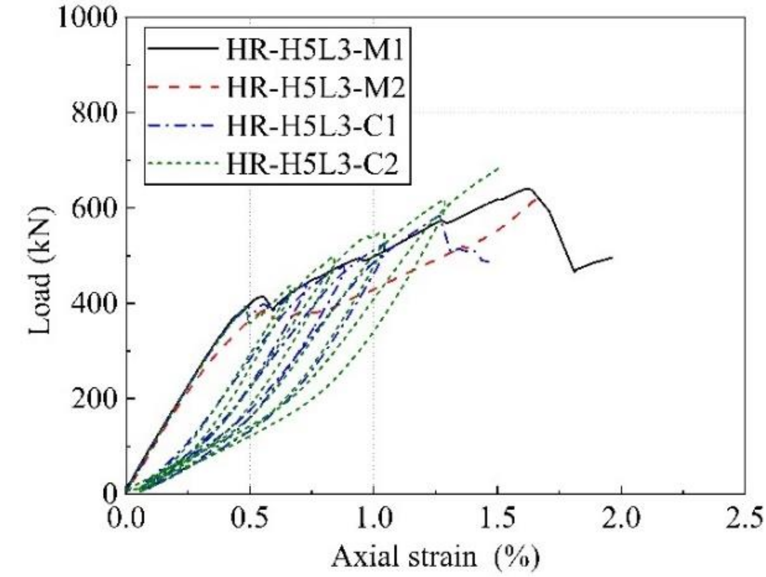

HR-H5L3 specimens

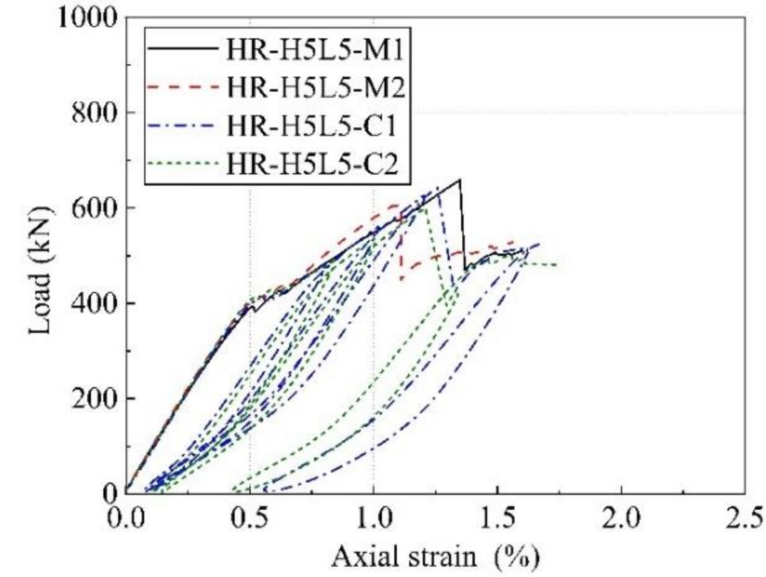

(f) HR-H5L5 specimens

Figure 6.4 Load-axial strain curves for specimens of Series 2

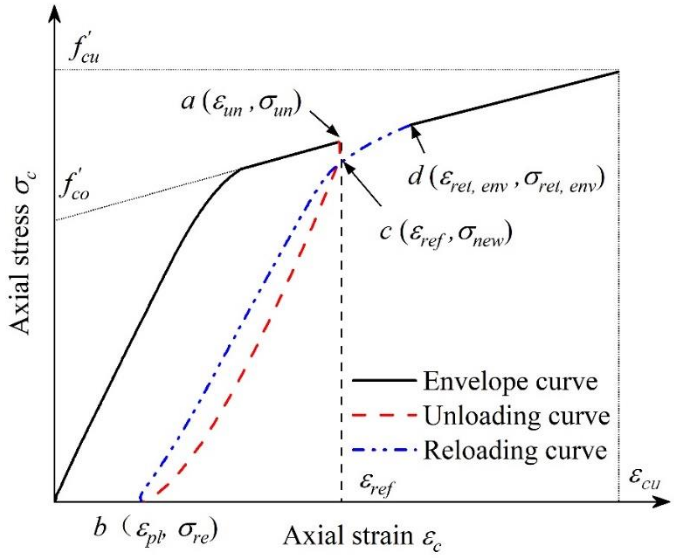

Figure 6.5 Typical envelope and unloading/reloading curves [drawn with some modifications to that of Lam and Teng (2009)]

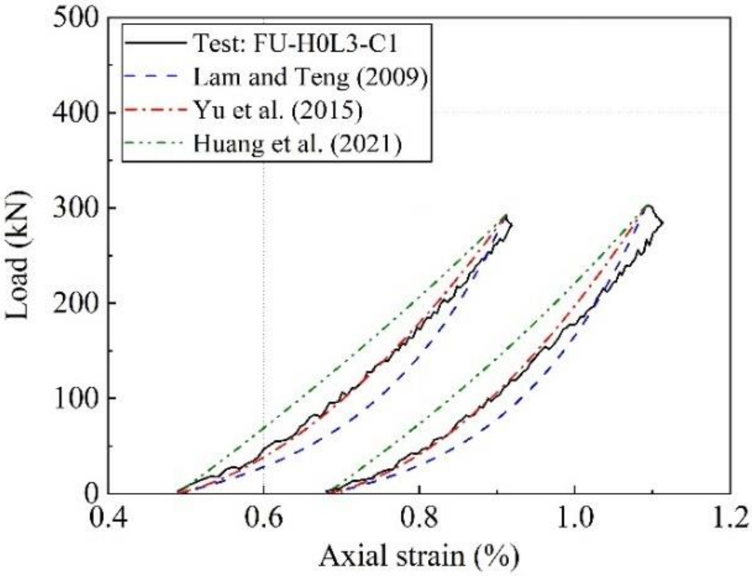

(a) FU-H0L3-C1

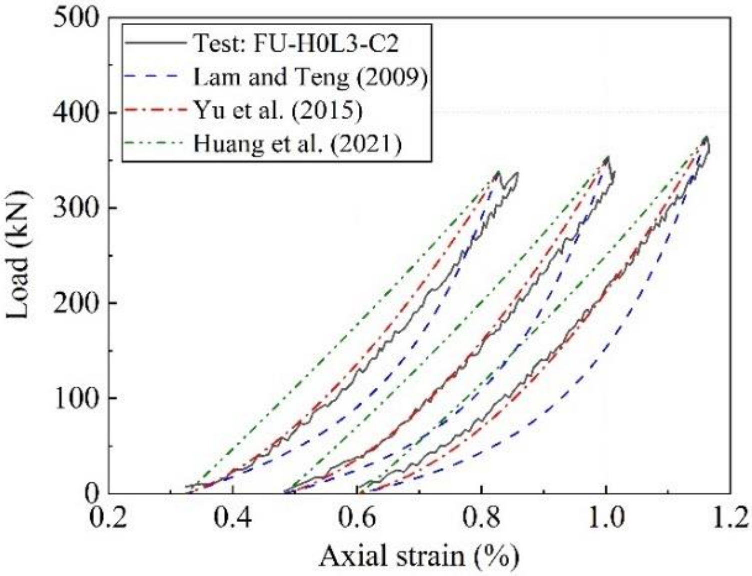

(b) FU-H0L3-C2

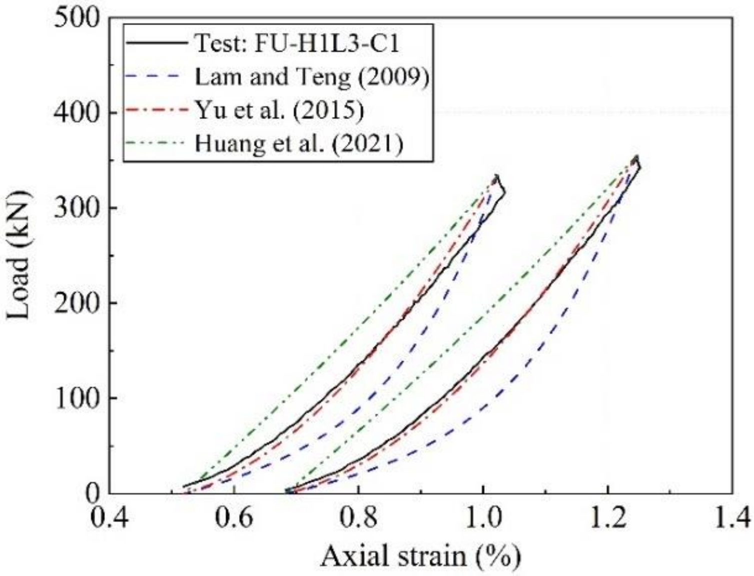

(c) FU-H1L3-C1

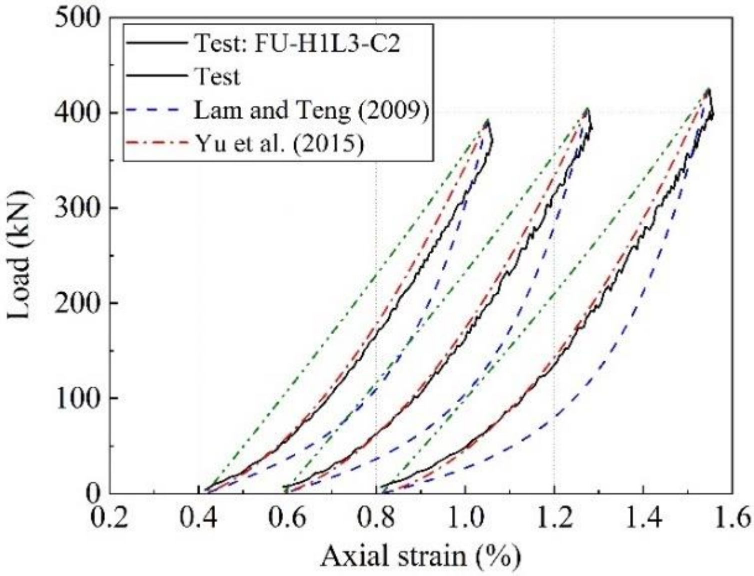

(d) FU-H1L3-C2

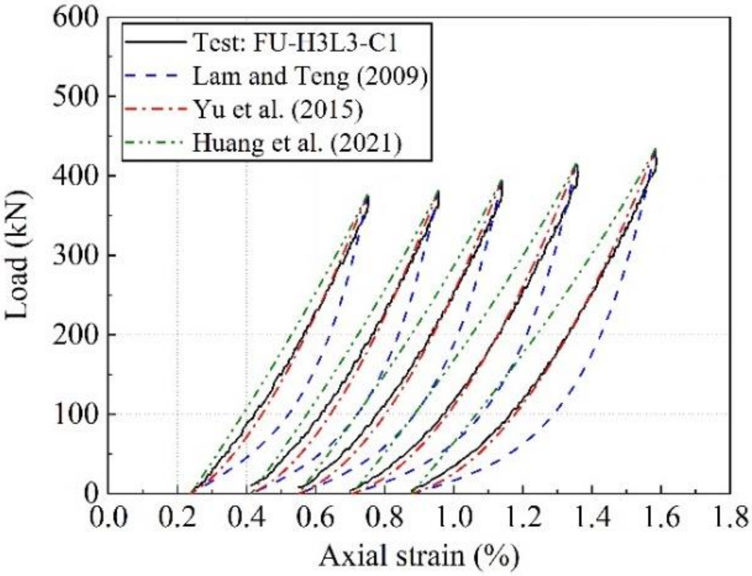

(e) FU-H3L3-C1

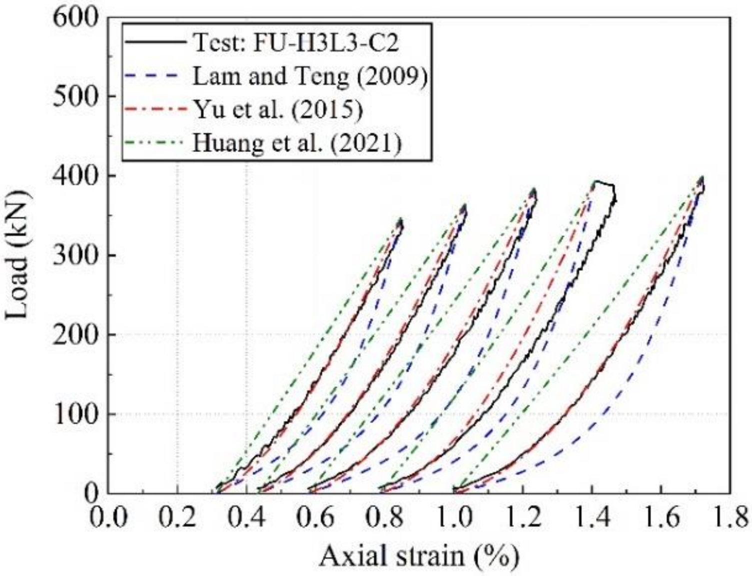

(f) FU-H3L3-C2

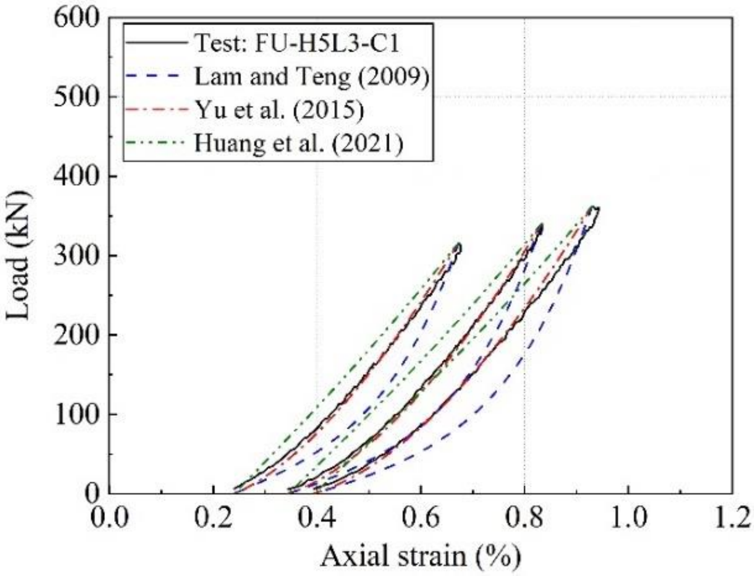

(g) FU-H5L3-C1

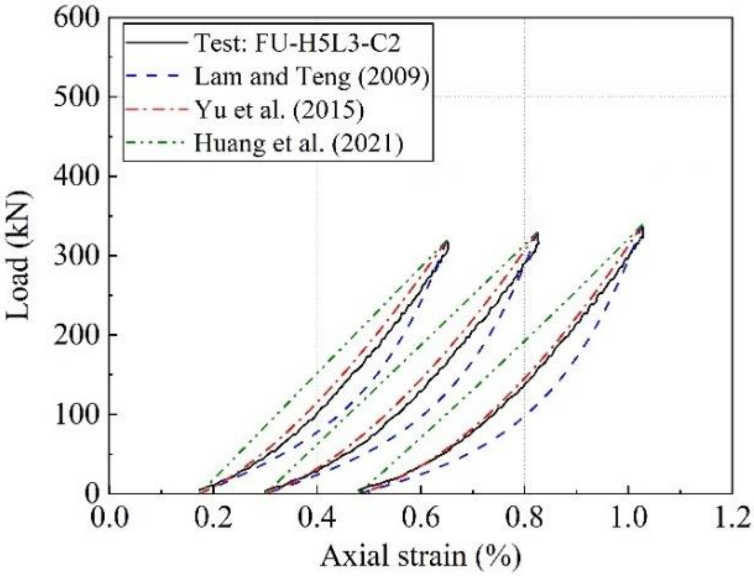

(h) FU-H5L3-C2

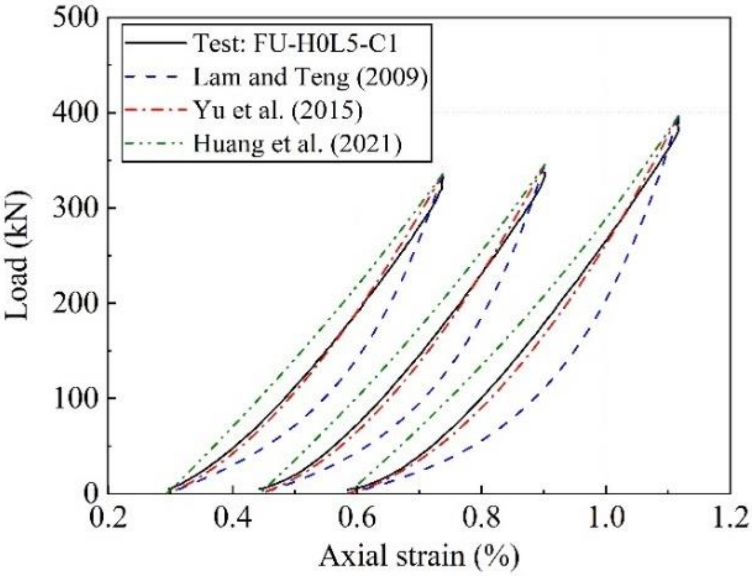

(i) FU-H0L5-C1

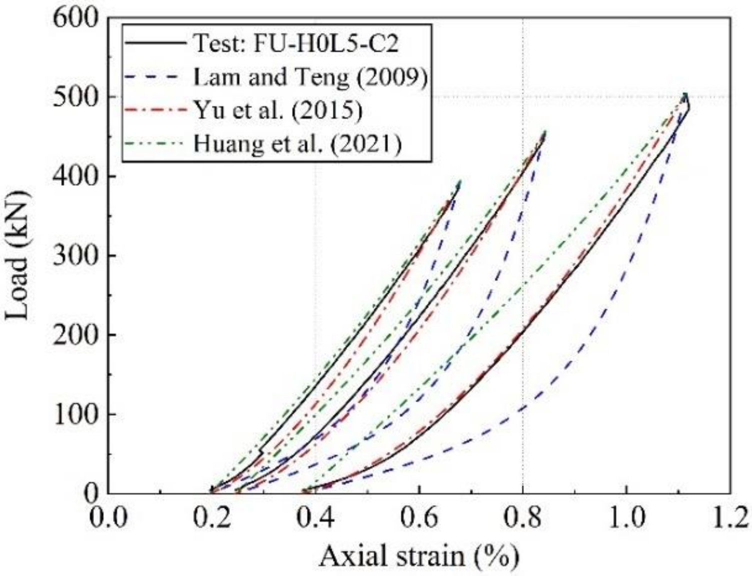

(j) FU-H0L5-C2

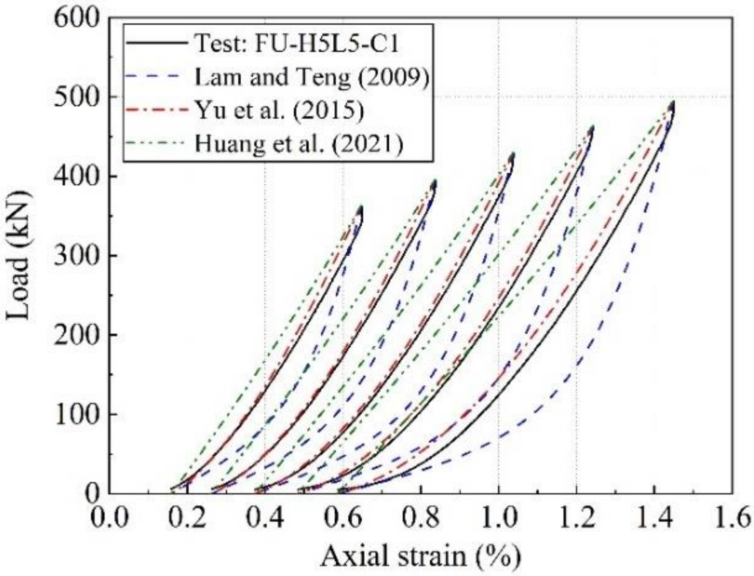

(k) FU-H5L5-C1

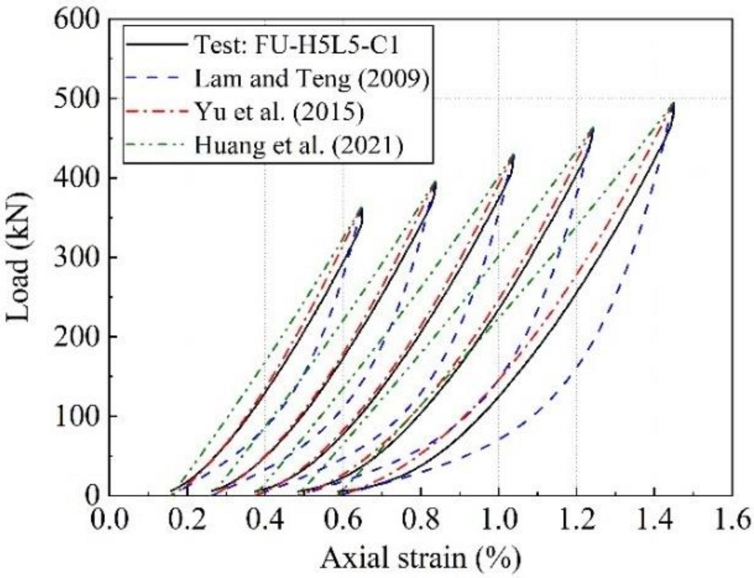

(l) FU-H5L5-C2

Figure 6.6 Comparisons of unloading curves between test results and predictions

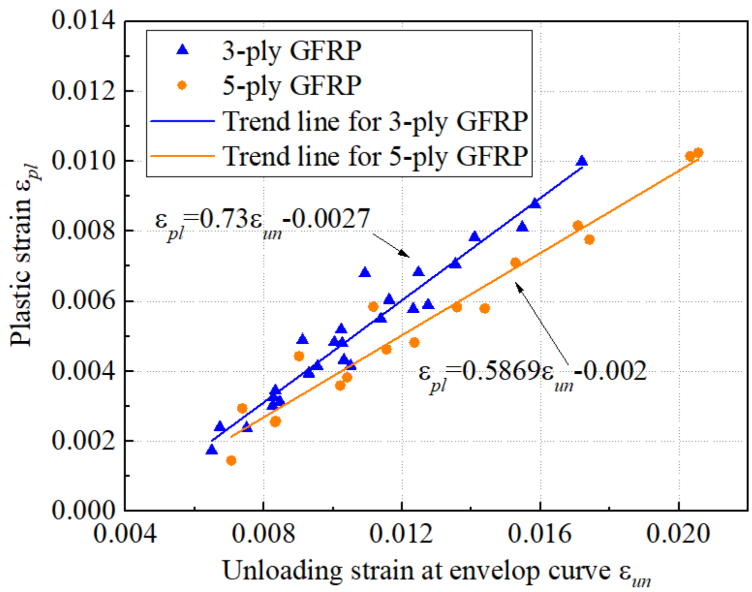

(a) Effect of GFRP tube thickness

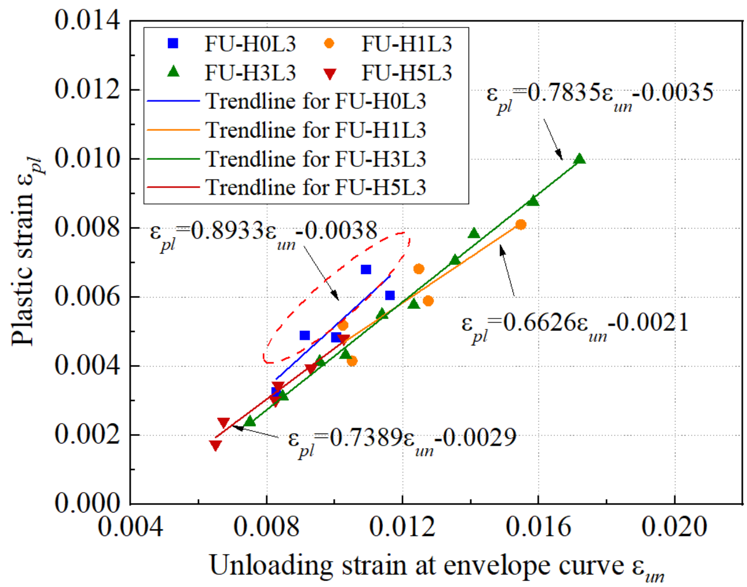

(b) Effect of wave height for L3 specimens

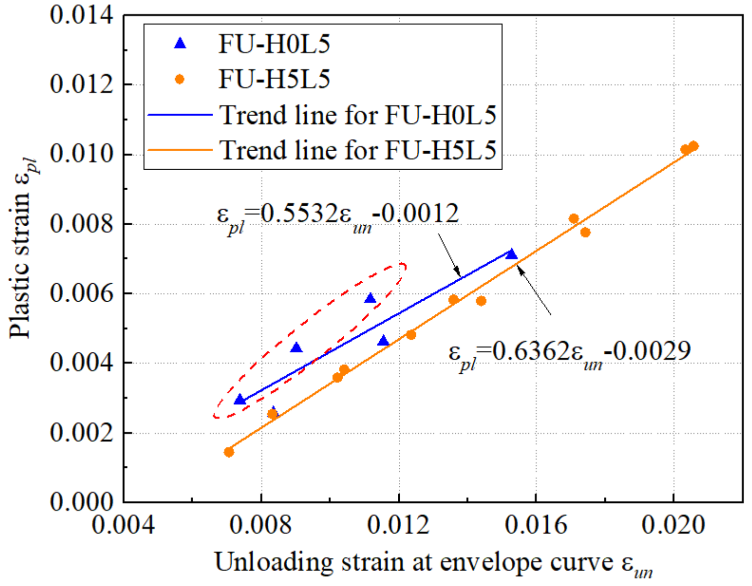

(c) Effect of wave height for L5 specimens

Figure 6.7 Effect of different parameters on the relationship between plastic strains and corresponding unloading strains for FRP-confined UHPC specimens

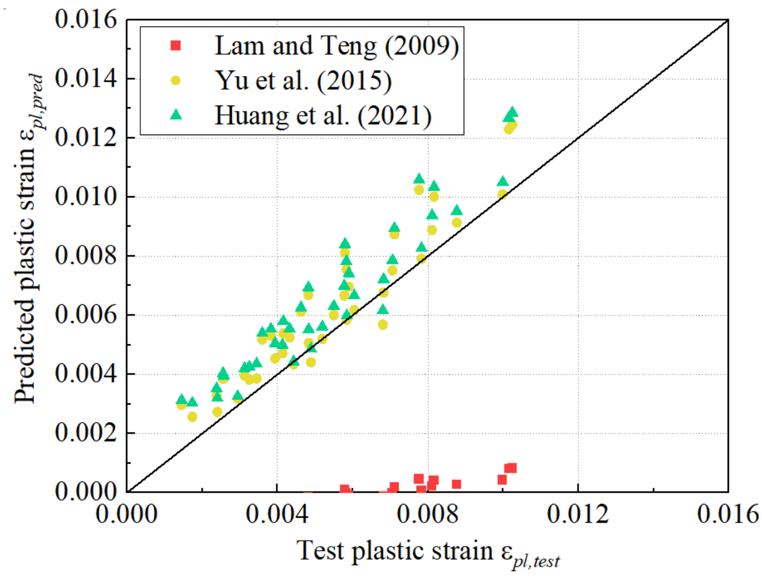

Figure 6.8 Predicted versus test values for the plastic strains of test specimens

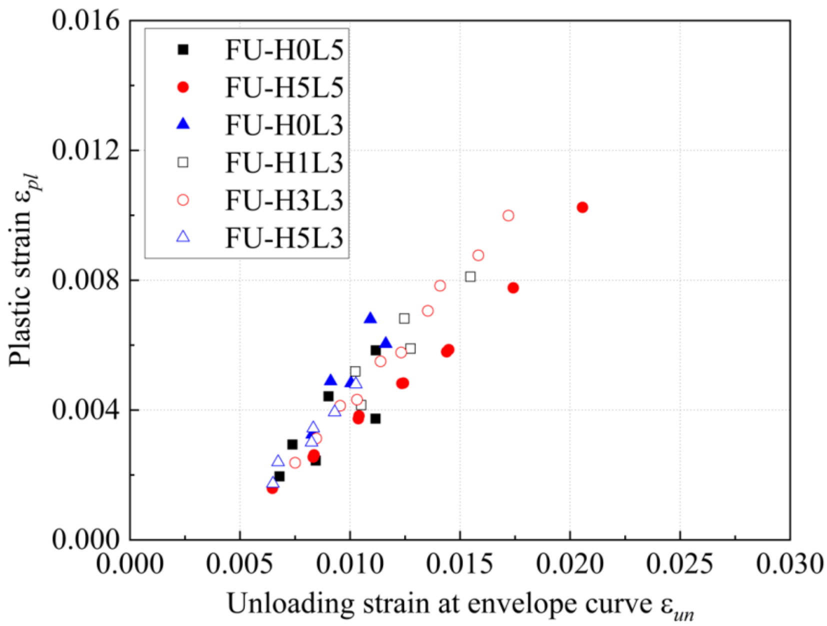

Figure 6.9 Relationship between plastic strains and unloading strains for FRP-confined UHPC specimens

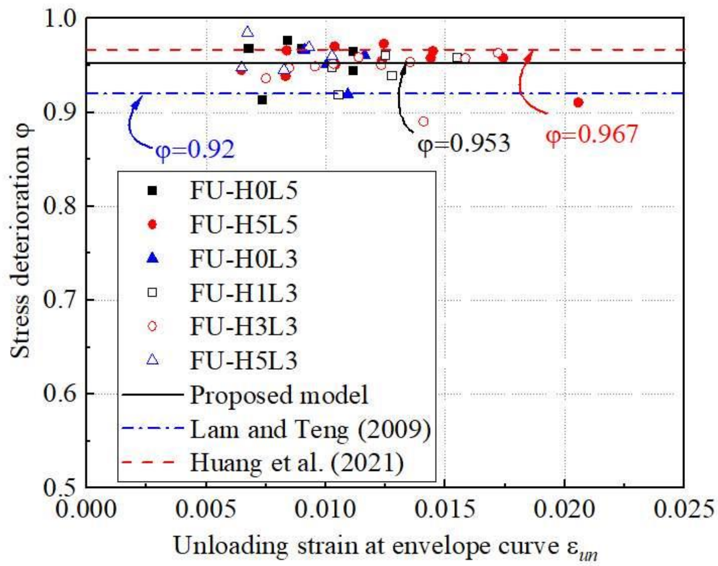

Figure 6.10 Stress deterioration ratios for different unloading strains for FRP-confined UHPC specimens

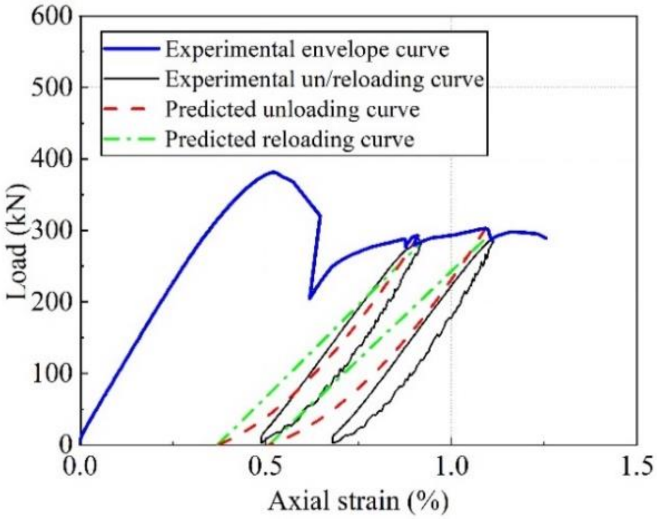

(a) FU-H0L3-C1

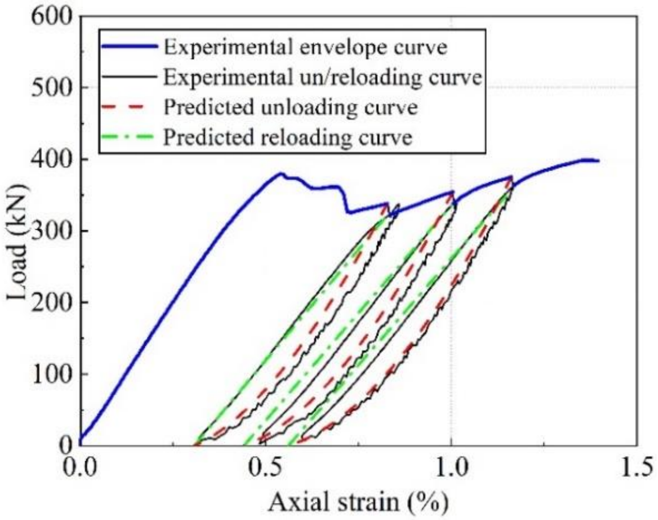

(b) FU-H0L3-C2

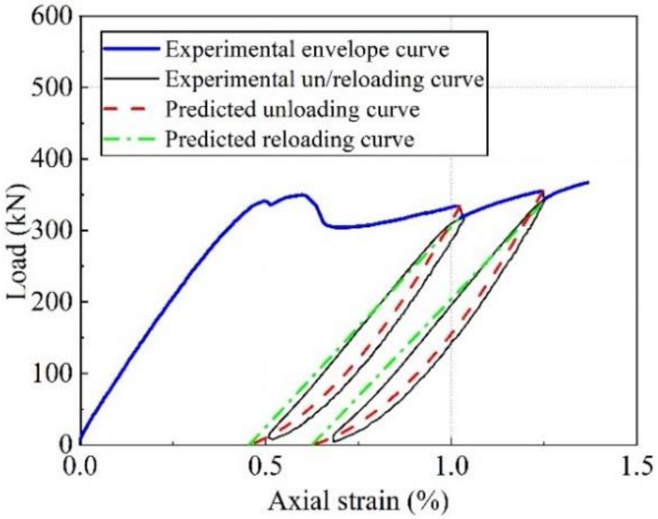

(c) FU-H1L3-C1

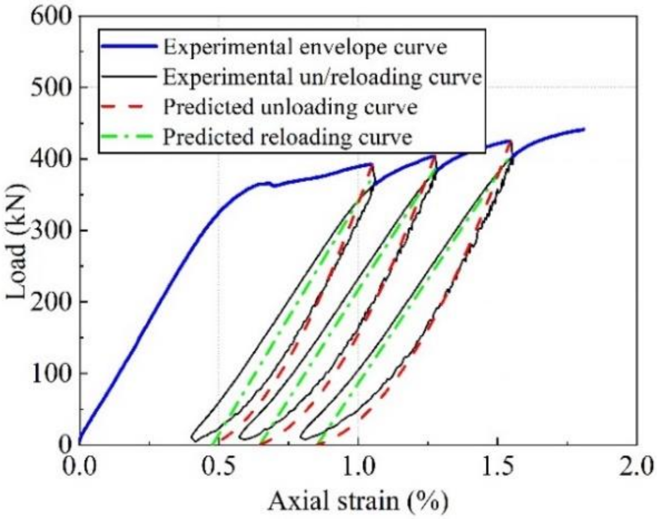

(d) FU-H1L3-C2

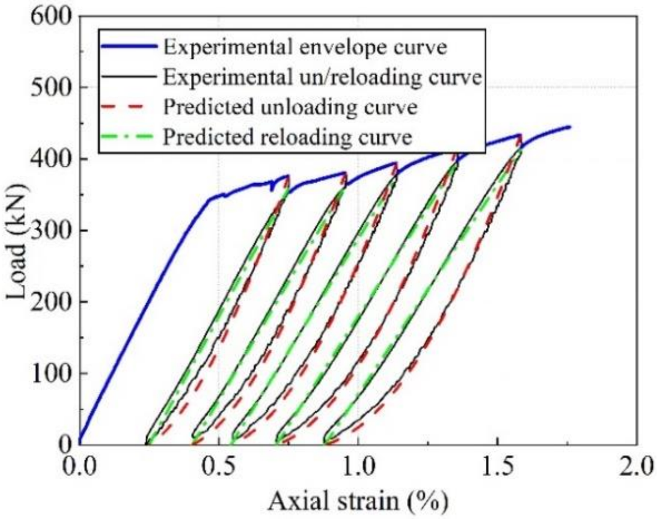

(e) FU-H3L3-C1

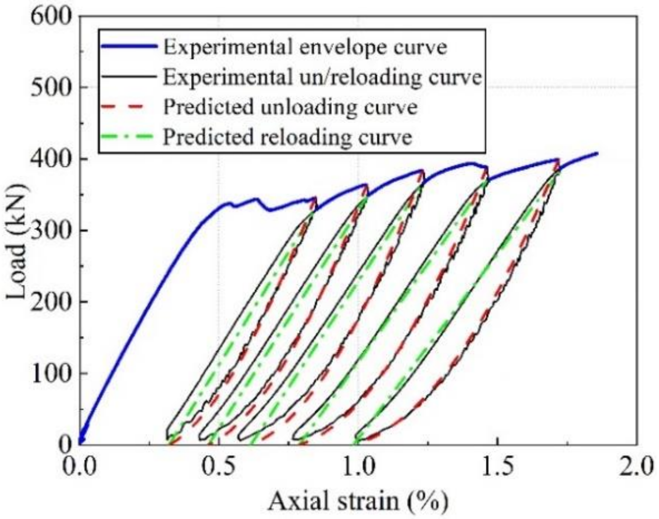

(f) FU-H3L3-C2

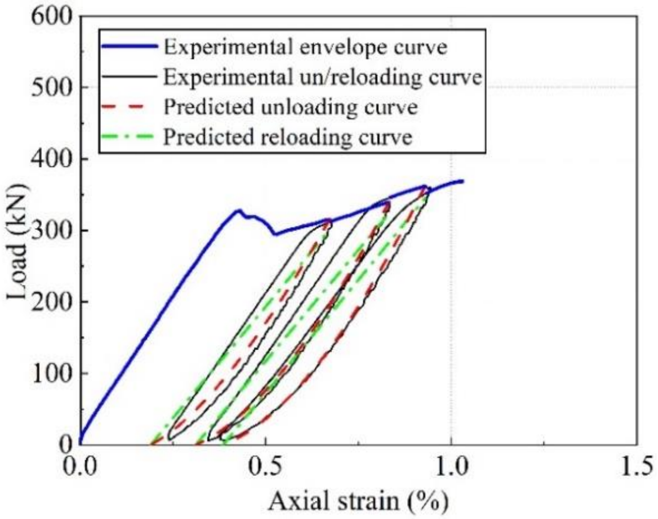

(d) FU-H5L3-C1

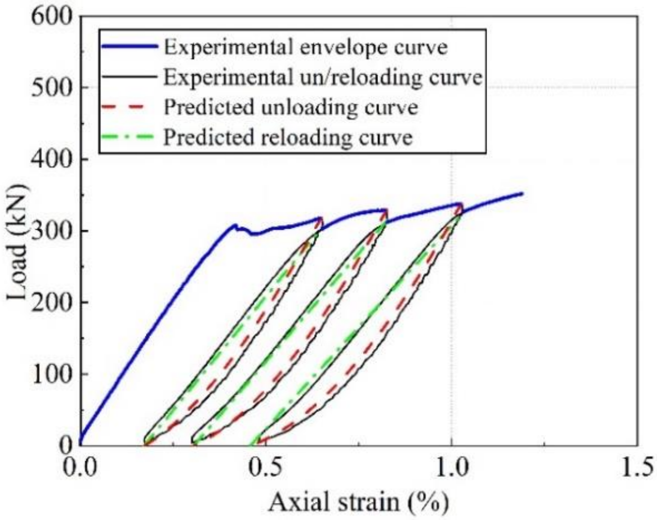

(h) FU-H5L3-C2

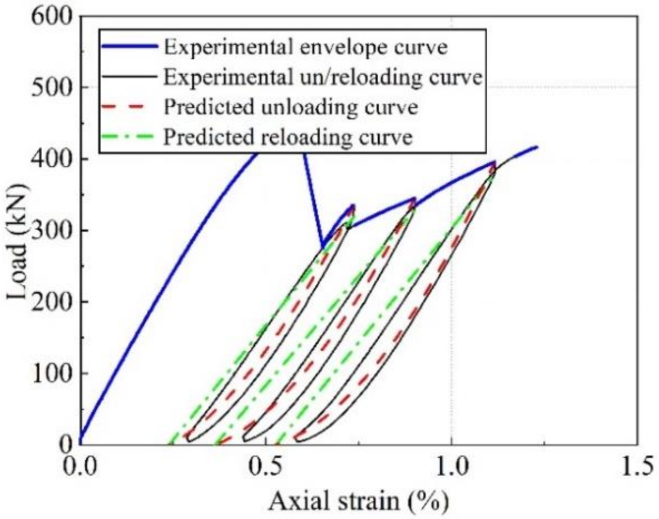

(i) FU-H0L5-C1

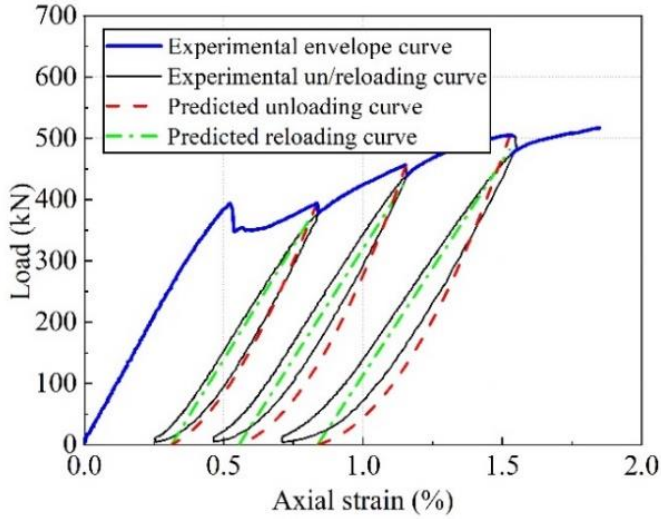

(j) FU-H0L5-C2

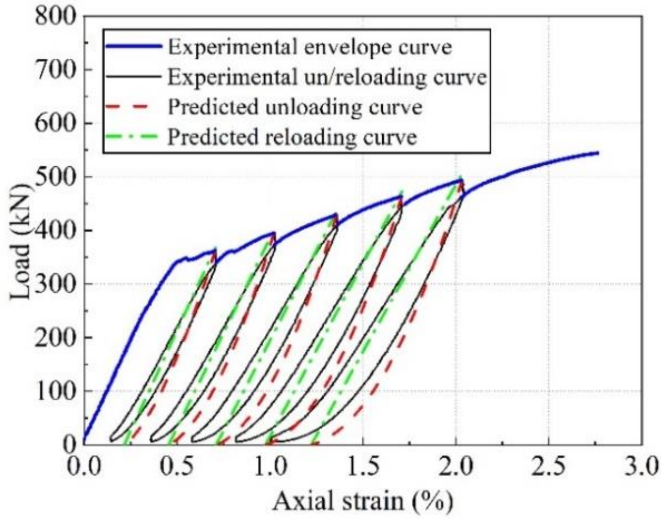

(k) FU-H5L5-C1

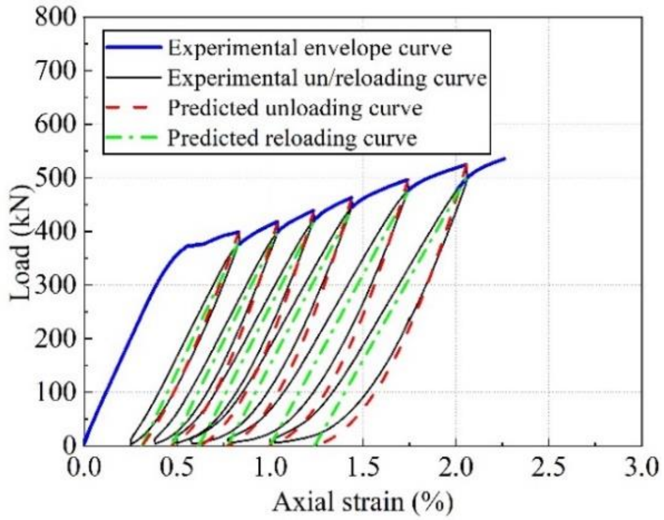

(l) FU-H5L5-C2

Figure 6.11 Comparisons of envelope unloading/reloading curves between test results and predictions for FRP-confined UHPC specimens

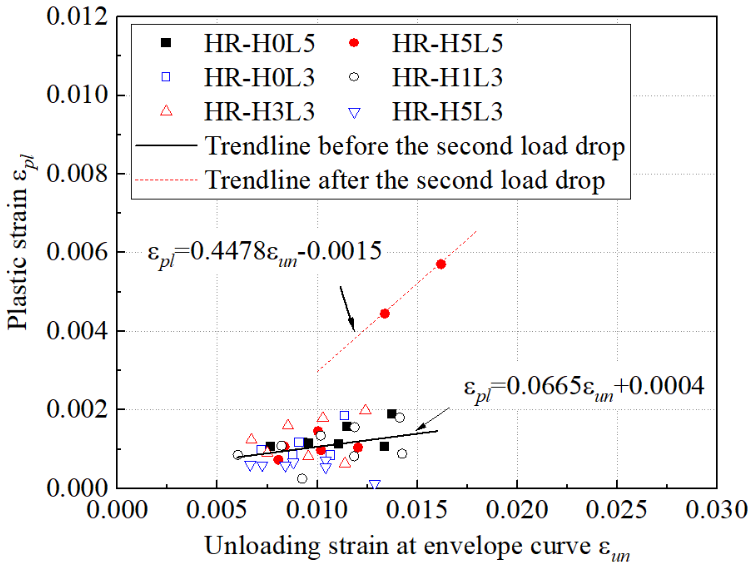

Figure 6.12 Plastic strains for different unloading strains for hybrid rebar specimens

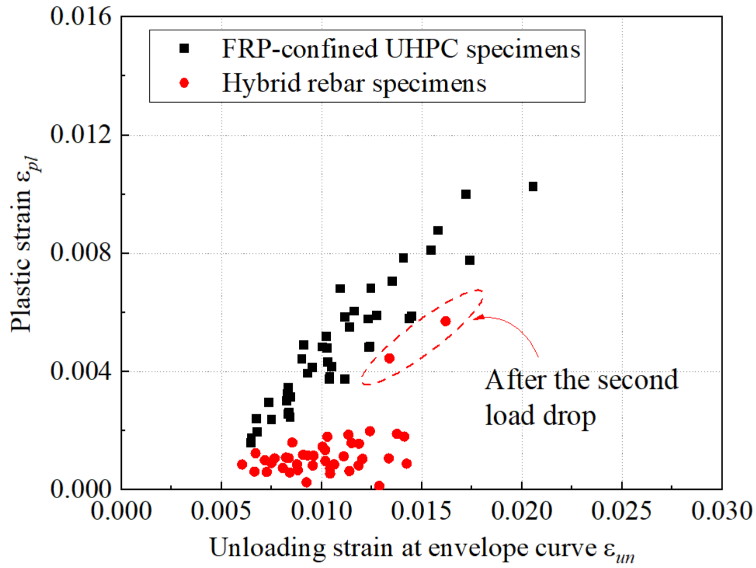

Figure 6.13 Comparisons of plastic strains between hybrid rebars and FRP-confined UHPC specimens

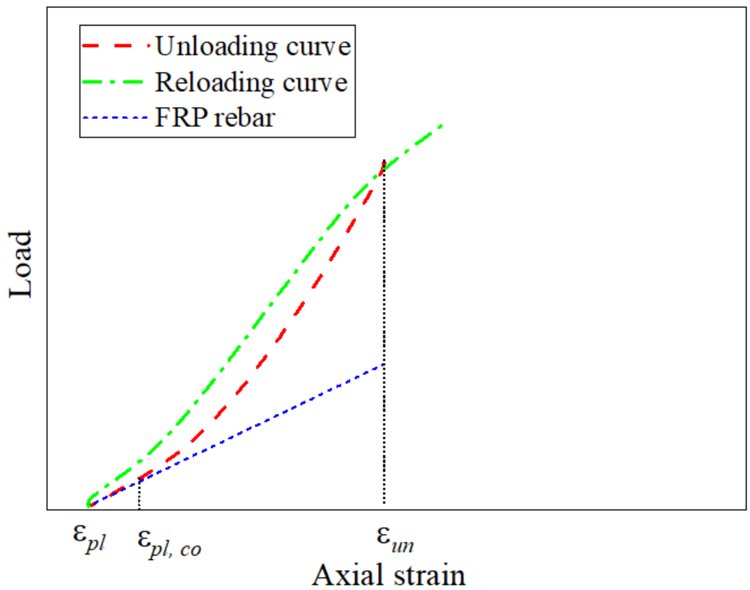

Figure 6.14 Typical unloading and reloading curves for a wavy-shaped hybrid rebar

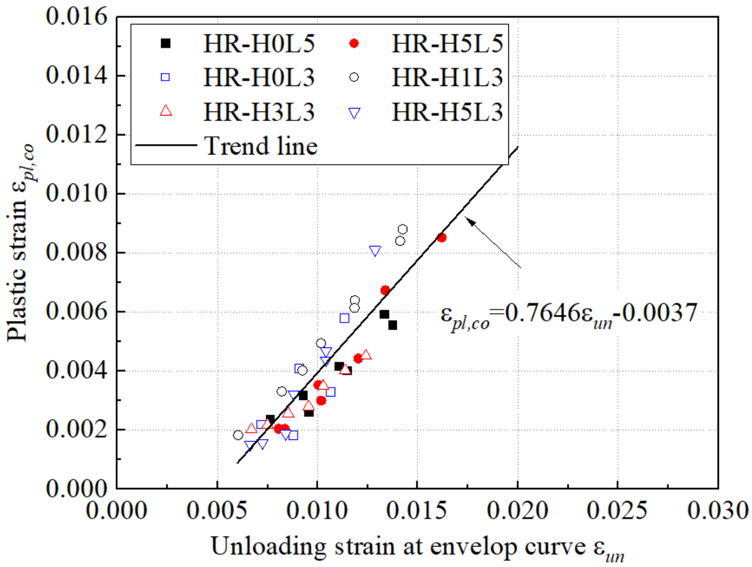

Figure 6.15 Relationship between plastic strains $\varepsilon_{pl,co}$ and the corresponding unloading strains for hybrid rebar specimens

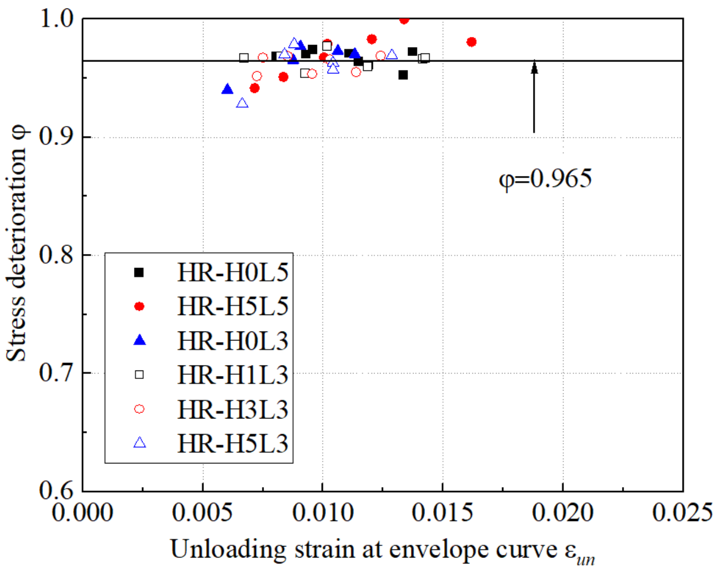

Figure 6.16 Stress deterioration ratios for hybrid rebar specimens with different unloading strains

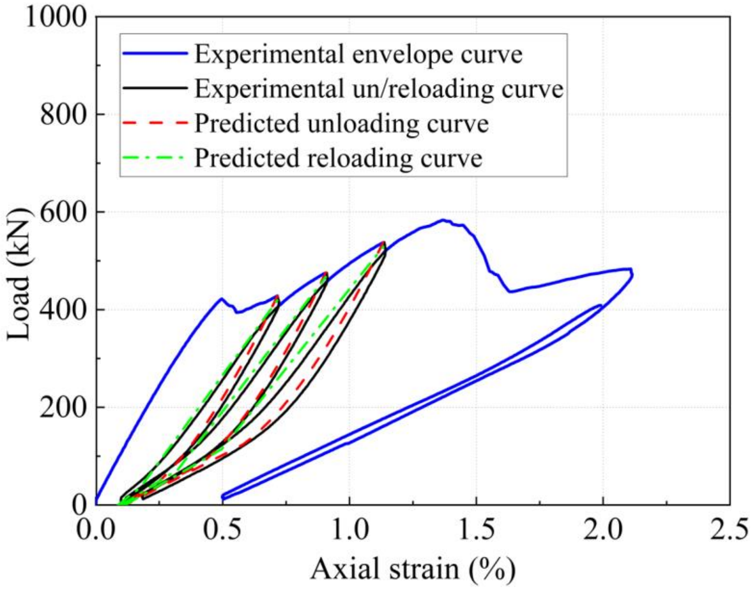

(a) HR-H0L3-C1

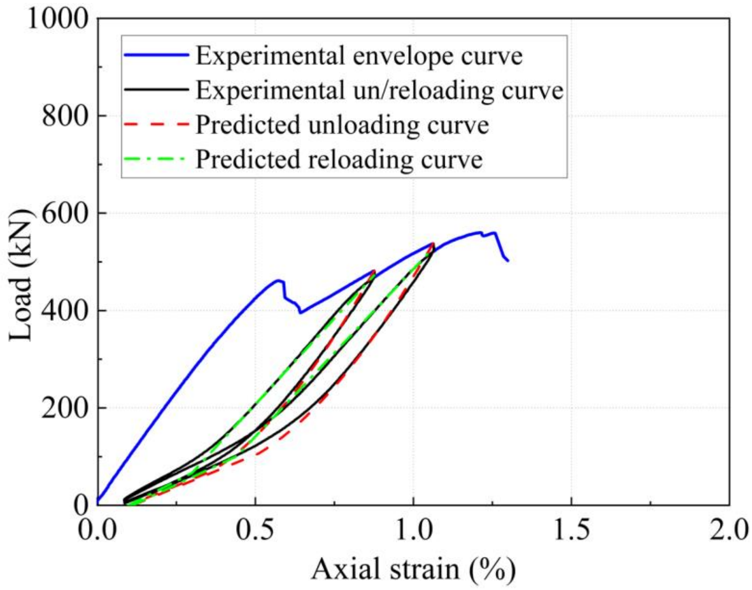

(b) HR-H0L3-C2

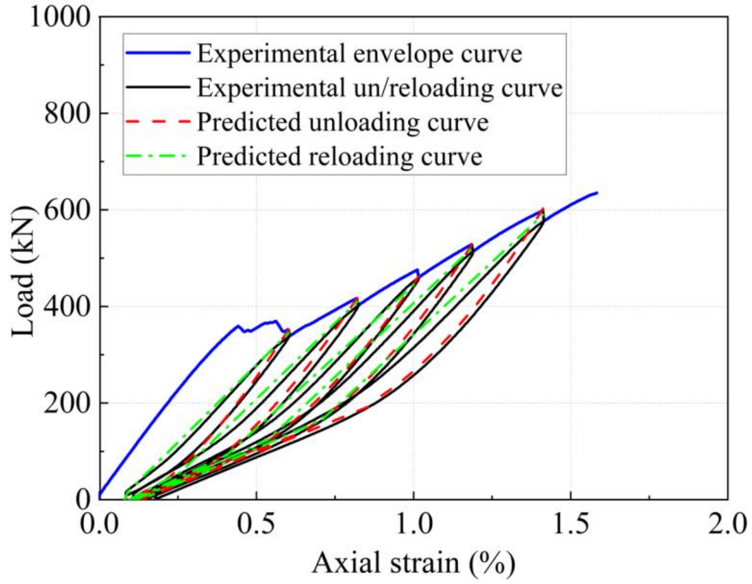

(c) HR-H1L3-C1

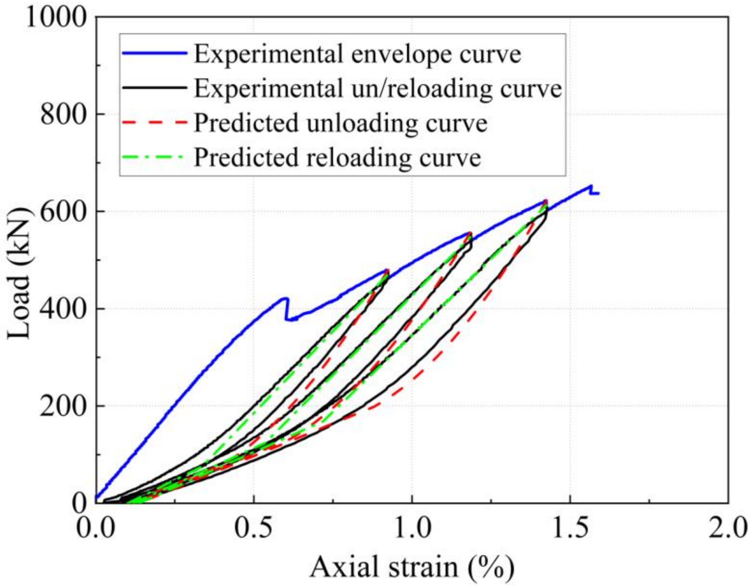

(d) HR-H1L3-C2

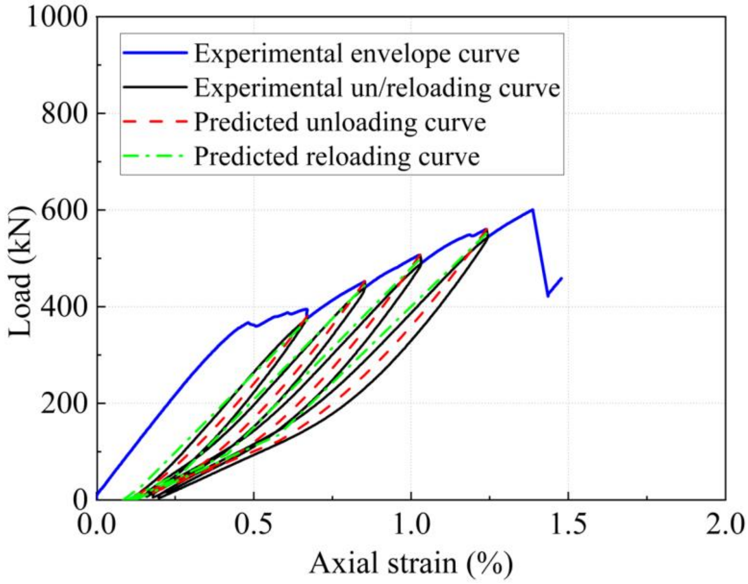

(e) HR-H3L3-C1

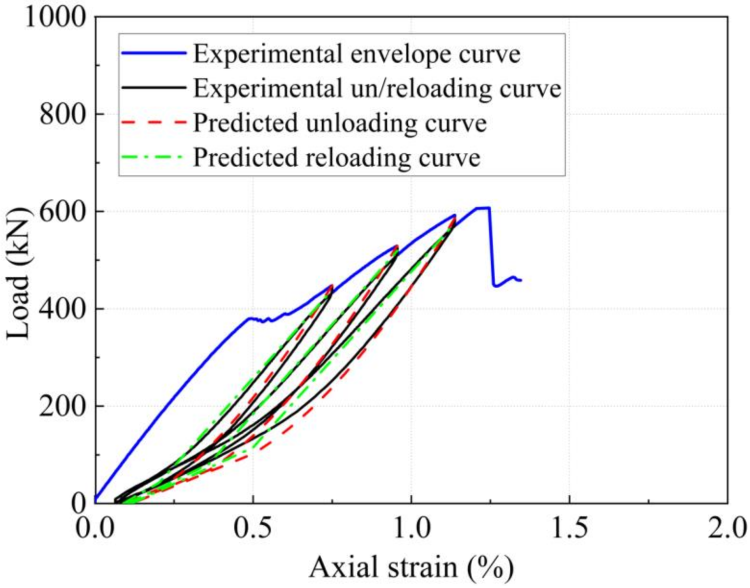

(f) HR-H3L3-C2

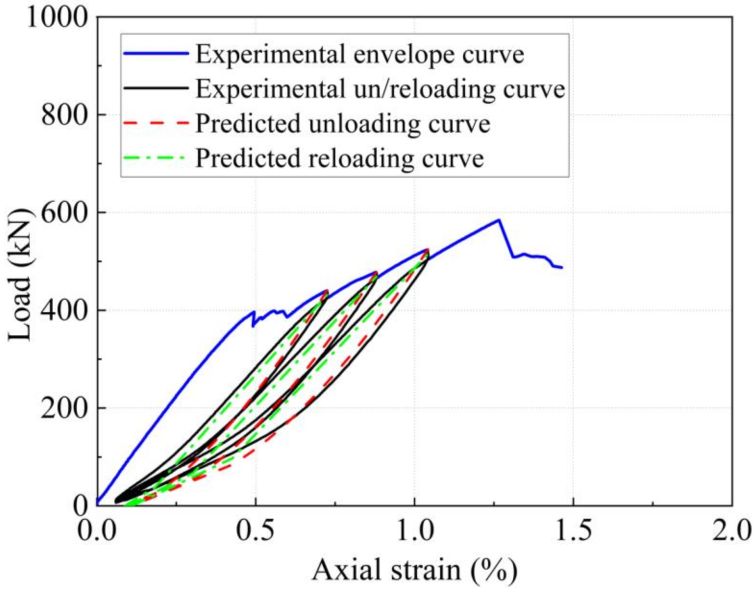

(g) HR-H5L3-C1

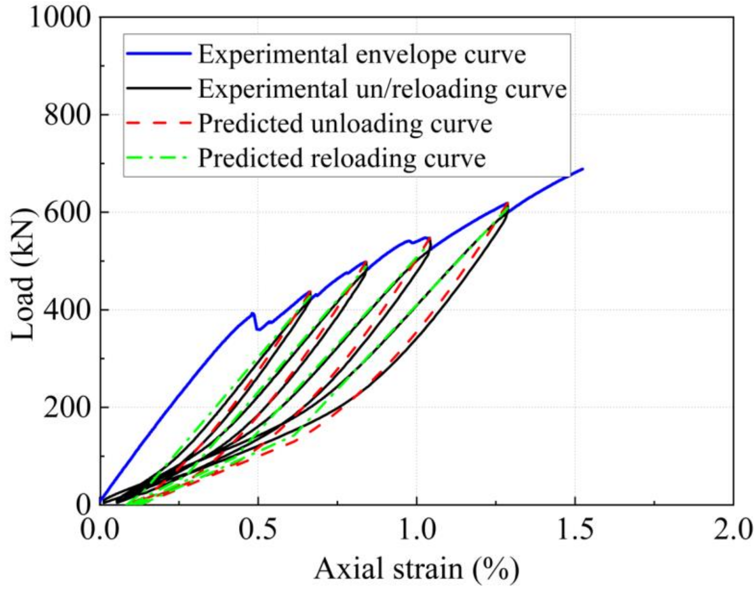

(h) HR-H5L3-C2

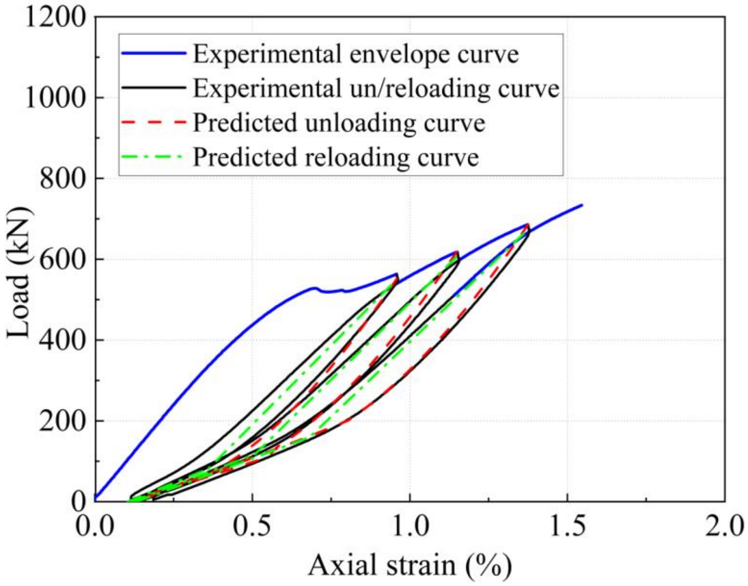

(i) HR-H0L5-C1

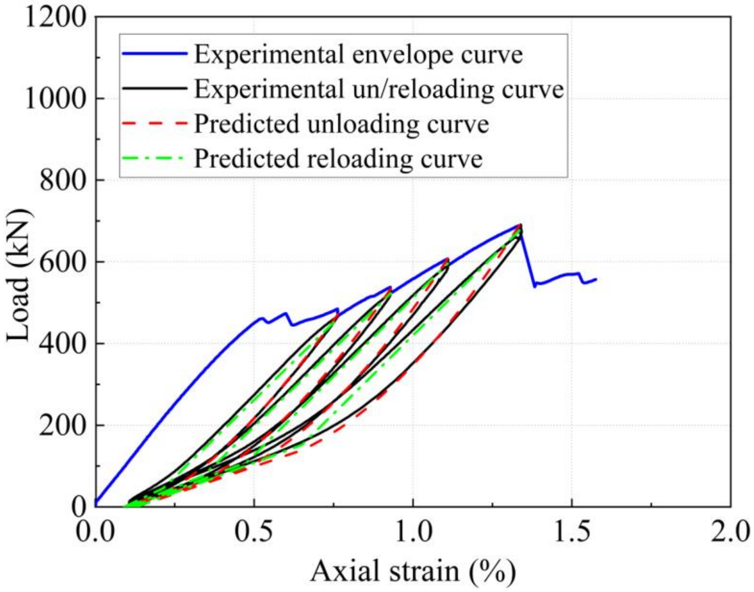

(j) HR-H0L5-C2

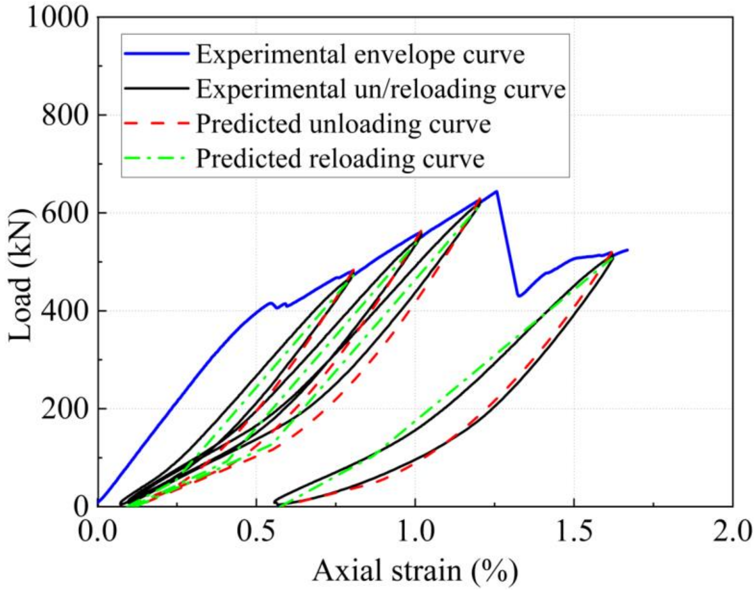

(k) HR-H5L5-C1

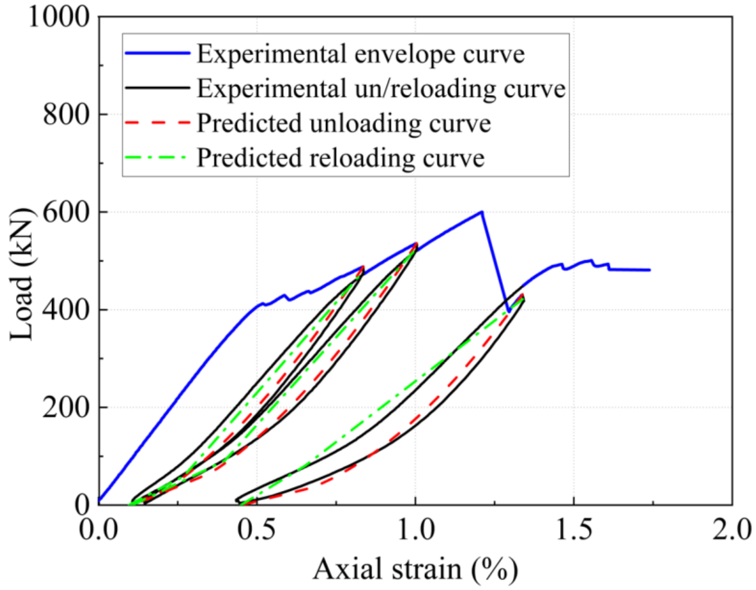

(l) HR-H5L5-C2

Figure 6.17 Performance of equations for envelope unloading/reloading curves for hybrid rebar specimens

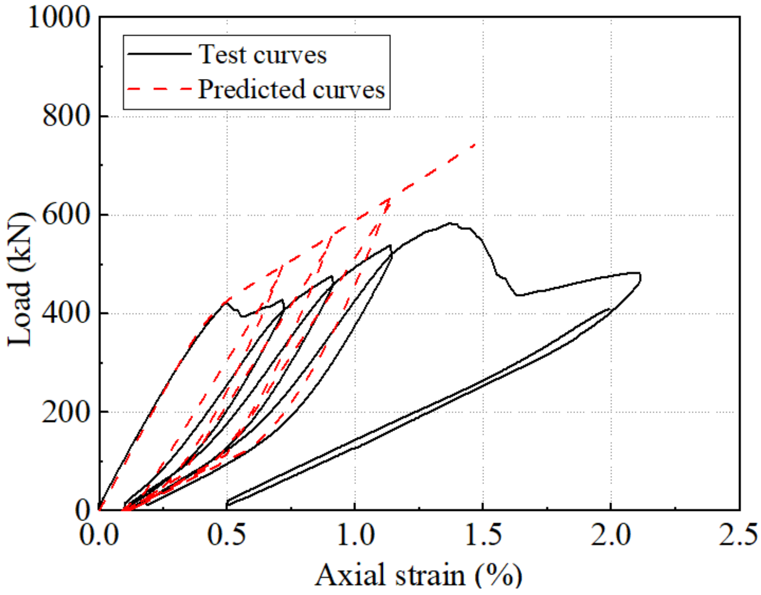

(a) HR-H0L3-C1

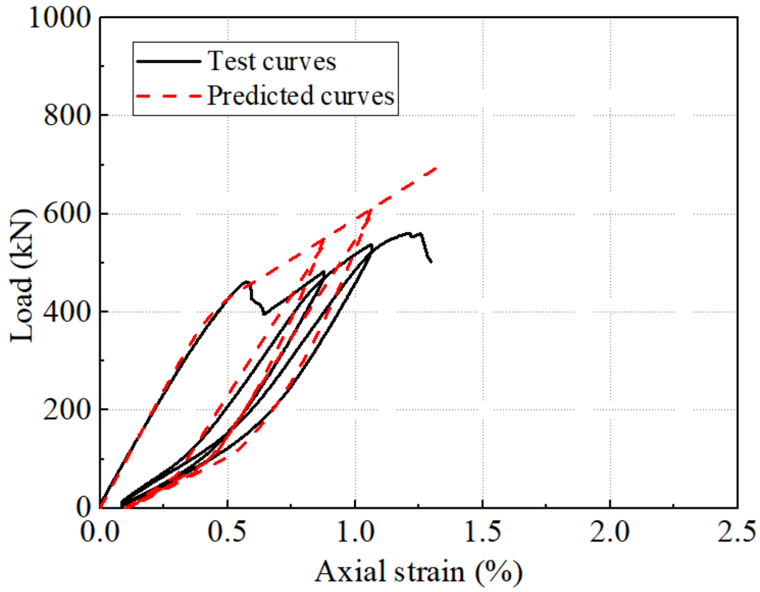

(b) HR-H0L3-C2

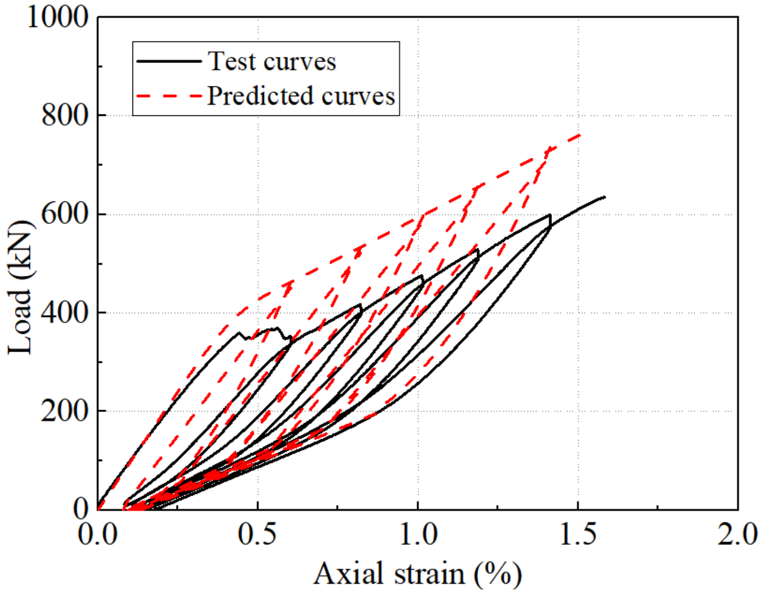

(c) HR-H1L3-C1

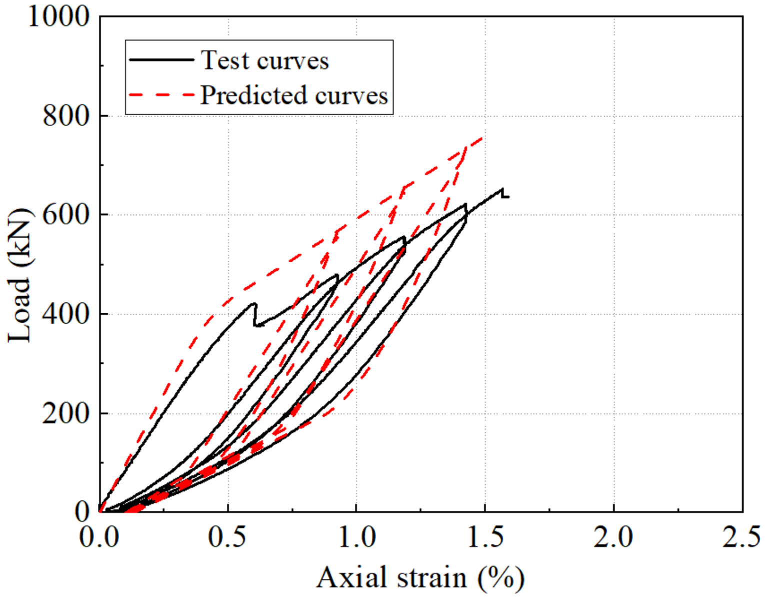

(d) HR-H1L3-C2

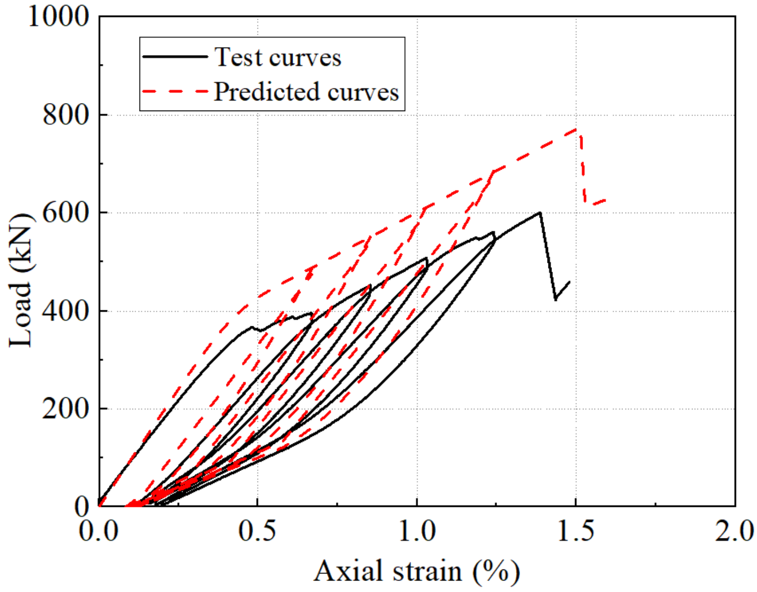

(e) HR-H3L3-C1

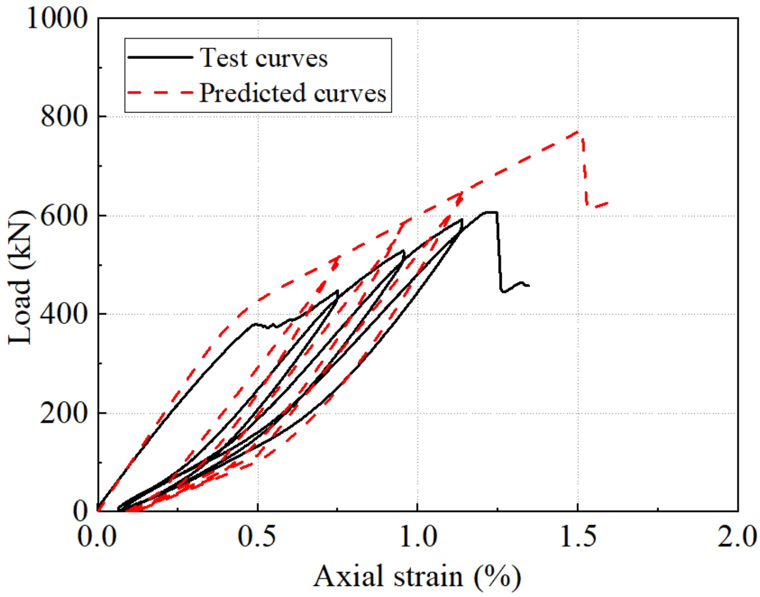

(f) HR-H3L3-C2

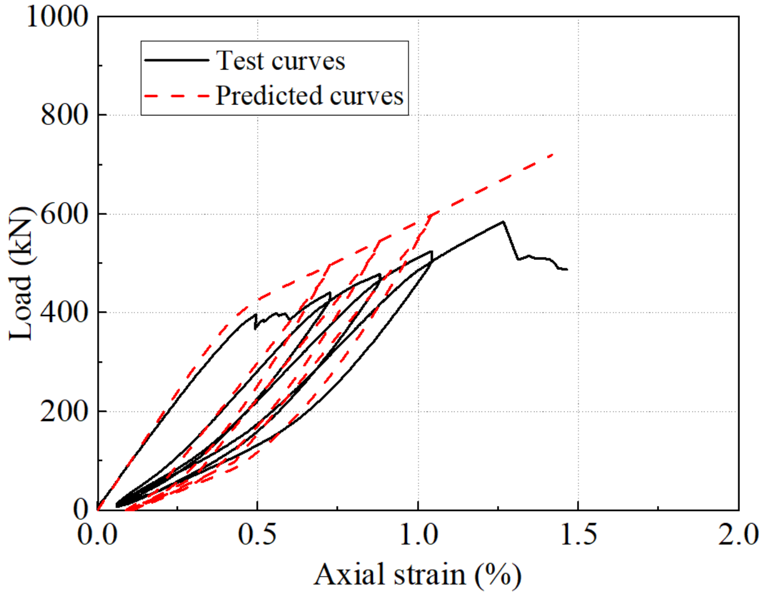

(g) HR-H5L3-C1

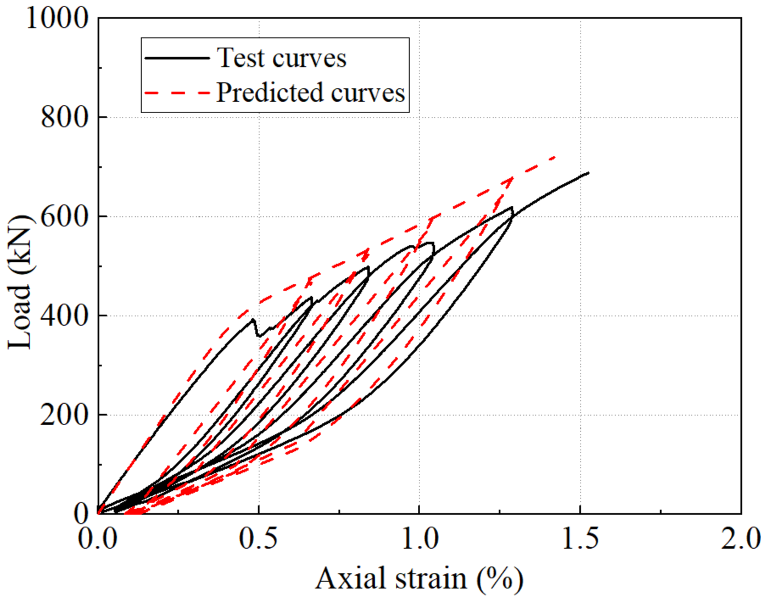

(h) HR-H5L3-C2

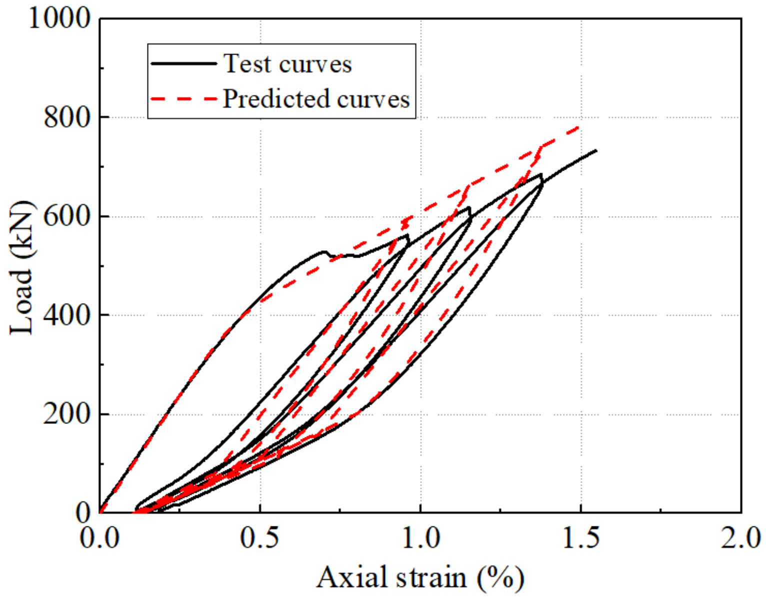

(i) HR-H0L5-C1

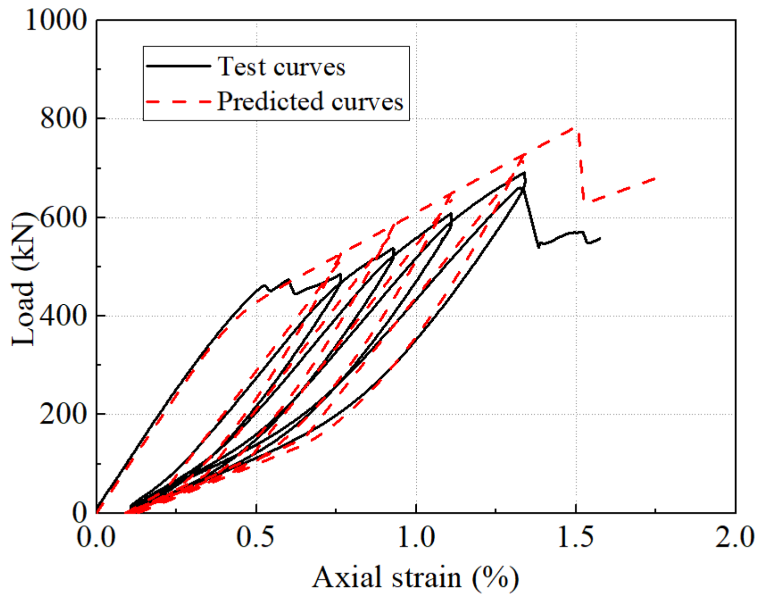

(j) HR-H0L5-C2

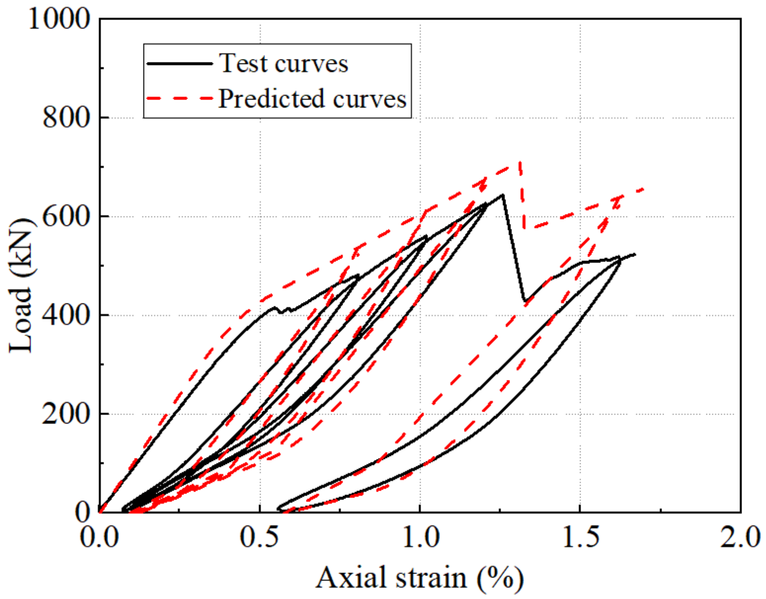

(k) HR-H5L5-C1

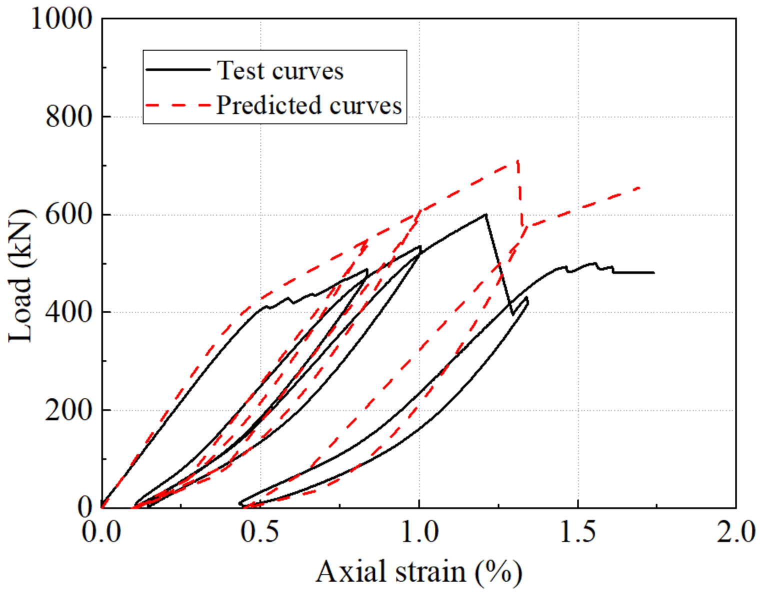

(l) HR-H5L5-C2

Figure 6.18 Comparisons of envelope unloading/reloading curves between test results and predictions for hybrid rebar specimens

CHAPTER 7
PULLOUT TESTS OF WAVY-SHAPED HYBRID REBARS

7.1 INTRODUCTION

As discussed in the preceding chapters, the bond behaviour of hybrid rebars in concrete, which is of critical importance to the performance of concrete members reinforced with hybrid rebars, has never been investigated. Particularly, a new type of wavy-shaped hybrid rebars for enhanced bond performance has been proposed in this Ph.D. research project. In Chapters 5 and 6, the mechanical behaviour of such wavy-shaped hybrid rebars under monotonic and cyclic axial compression has been investigated through experimental studies. This chapter presents the results of a systematic experimental study via pull-out tests on the bond behaviour of hybrid rebars in concrete. In addition, to clarify the relative deformations among different components of hybrid rebars, FRP rebars were directly pulled out from FRP-confined UHPC in hybrid rebars. The test variables in these pull-out tests included the FRP confinement level, the bond length, and the type of FRP rebars with different surface features. A recommended development length of wavy-shaped hybrid rebars was proposed based on the test results.

7.2 EXPERIMENTAL PROGRAMME

7.2.1 Specimen Details

The specimens were categorised into two groups. Group I was aimed at the investigation of the bond behaviour between the central FRP rebar and UHPC in a hybrid rebar. As illustrated in Figure 7.1, a central GFRP rebar was embedded in an FRP-confined UHPC specimen; one end of the GFRP rebar was pultruded from the UHPC for facilitating the measurement of the free end displacements while the other end was anchored in a steel tube filled with epoxy. The GFRP rebar was pulled-out from the FRP-confined UHPC by applying a tensile force at the anchorage end. The dimensions of the steel tube at the anchorage end were designed in accordance with ASTM D7205/D7205M-21. Due to the relatively large diameter of the GFRP rebar, steel tubes with a yield stress of 355 MPa were utilised to prevent premature failure of the anchorage region. Based on trial tests, steel tubes with an inner diameter of 38 mm, an outer diameter of 48 mm and a length of 460 mm were used.

To further investigate the bond behaviour between a hybrid rebar and its surrounding concrete, pull-out tests of hybrid rebar specimens embedded in concrete were also conducted (i.e., Group II). In such specimens, the following three interfaces existed: the GFRP rebar - UHPC interface, UHPC - FRP tube interface, and FRP tube - concrete interface. Figure 7.2 illustrates the schematic diagram of the test specimens and the test set-up in Group II. As shown in Figure 7.2(a), hybrid rebars were embedded in concrete blocks of cylinders with a diameter of 300 mm. Both carbon FRP (CFRP)-confined concrete blocks and unconfined concrete blocks were considered to investigate the bond behaviour between the hybrid rebars and the surrounding concrete under confined and unconfined conditions.

Table 7.1 lists the total 30 specimens prepared for the pull-out tests, with 18 specimens in Group I and 12 specimens in Group II. The specimens were labelled as follows: the first letter “H” and a number “0”, “3” and “5” denoting a wave height of 0 mm, 3 mm, and 5 mm for a wavy-shaped tube, respectively; the followed letter “L” and a number “3” or “5” representing 3 or 5 layers of fibres in the GFRP tube; subsequently, “6D”, “10D”, “20D”, and “30D” indicating the bond length of the FRP rebar in Group I or the bond length of the hybrid rebars in Group II (6, 10, 20, 30 times the nominal diameter of the FRP rebars, i.e., 25 mm). For Group I specimens, the label was then followed by a letter “S” denoting sand-coated and helically wrapped rebars or “R” denoting helically ribbed FRP rebars, respectively (see Figure 7.3). For Group II specimens, only sand-coated and helically wrapped FRP rebars were included. For those Group II specimens, the label was then followed by “C0”, “C1”, “C2” and “C3” representing the number of layers of fibres (i.e., 0, 1, 2 and 3) of the outer CFRP jacket. For some specimens, the label ended with number “1” or “2” to differentiate two nominally identical specimens.

7.2.2 Material Properties

Two types of FRP rebars available in the market were used in this experimental programme, including those manufactured by Dextra Building Products (Guangdong) Co., Ltd. (Dextra) and those by Haining Anjie Composite Material Co., Ltd. (Anjie). The two types of FRP rebars possessed different surface treatments. The FRP rebars produced by Dextra featured a rough sand-coated surface with helically wrapped yarns, whereas those manufactured by Anjie exhibited a ribbed surface pattern of helical grooves (Figure 7.2). The former rebars are referred to as “sand-coated and helically wrapped rebars”, while the latter are referred to as “ribbed rebars” hereafter. The nominal diameter of all FRP rebars was 25 mm. Tensile tests on five FRP rebar specimens were conducted for each type of rebar in accordance with ASTM D7205/D7205M-21 (2021). The elastic moduli, the tensile strengths, as well as the ultimate tensile strains of the FRP rebars obtained from the tensile tests are listed in Table 7.2. Since these two types of FRP rebars were produced by different manufacturers, the differences in production processes are believed to have resulted in significant variations in their tensile strength.

For Group II specimens with hybrid rebars embedded in concrete blocks, two grades of normal-strength concrete (NSC) (i.e., C30 and C50 for target cylindrical compressive strength of 30 and 50 MPa, respectively) were employed to construct the concrete blocks. The same UHPC as described in the preceding chapters was used, which was produced using cement, silica fume, quartz powder, fine aggregates, superplasticizer, and water (Teng et al., 2018). Table 7.3 presents the weight mix proportions of the NSC and UHPC. Five 50 mm × 50 mm cubes were cast and tested to determine the compressive properties of plain UHPC. The average compressive strength of UHPC was found to be 170.2 MPa. The NSC specimens in Group II were casted in three batches due to the limited capacity of the concrete mixer. Three 150 mm × 300 mm cylinders were cast together with each batch of NSC and compressed to determine the compressive strengths of NSC. The results are listed in Table 7.3. The concrete cylinder compressive strengths of the three batches of concrete were 47.3 MPa, 27.0 MPa, and 30.8 MPa, respectively.

7.2.3 Specimen Preparation

Steel tubes were utilised to fabricate the anchorage ends of the FRP rebars in specimens of both the pull-out tests and the tensile tests. A plastic cap with a central hole was inserted at the end of the steel tube, and then the FRP rebar was fixed in the hole of the plastic cap. Epoxy was poured into the gap between the FRP rebar and the steel tube, and then another plastic cap was installed at the opposite end of the steel tube for fixing the FRP rebar concentrically to the steel tube. For tensile tests on bare FRP rebar specimens, both ends of the FRP rebar were anchored with steel tubes filled with epoxy.

The specimens in Group I were fabricated in the following steps: (1) the wavy-shaped GFRP tubes were fabricated following the manufacturing procedure presented in Chapter 3; (2) the wavy-shaped GFRP tube and the FRP rebar were fixed concentrically with foam tape at one end (the foam tape was wrapped around the surface of the FRP rebar at the end until the FRP rebar could be plugged into the GFRP tube); (3) UHPC was poured into the gap between the FRP rebar and the GFRP tube; (4) a plastic cap with a central hole was installed at the other end of the FRP tube to ensure the alignment of the central FRP rebar; (5) the hybrid rebar specimen was cured in a thermostatic water tank with a temperature of 22 ± 2 ℃ for 28 days. After curing, the plastic cap and foam tape were removed, the ends of the FRP rebars were anchored with steel tubes filled with epoxy, and the specimens were ready for testing. Before loading, a CFRP strip with a width of 20 mm was used to strengthen the ends of the FRP tube to avoid premature failure at the ends of the specimens.

The hybrid rebars in the specimens of Group II were fabricated with the same procedure as that for the specimens in Group I. After 28 days of curing in water, hybrid rebars were taken out from the water tank and dried in the air. For fabricating a bonded joint specimen (i.e., a hybrid rebar embedded in a concrete block), the hybrid rebar and a circular wooden tube were first fixed onto a baseplate. Concrete was then cast into the wooden tube. After concrete was hardened, the wooden tube and the baseplate were removed from the specimen. Then, specimens were cured in air at a room temperature of 22 ± 2 ℃ for another 28 days. For some specimens, CFRP sheets were wrapped around the concrete block to avoid splitting failure of the concrete block during hybrid rebar pulling out. Before testing, the surface of the concrete block at the loaded end was capped with high-strength gypsum to ensure a full contact between the concrete block and the testing frame.

7.2.4 Test Set-Up

Figures 7.1 and 7.2 present the schematical diagrams of the test specimens and the test set-up of the pull-out tests for Group I and Group II specimens, respectively. The concrete block used in Group II had a diameter of 300 mm. An unbonded length of 50 mm was left at both ends of the concrete block for specimens with a bond length of 6*d* and a 0- or 3-layer CFRP jacket, i.e., specimens H5L3-6D-S-C0-1,2, H0L3-6D-S-C3, and H5L3-6D-S-C3. For specimens with a bond length of 10*d* (i.e., specimens H5L3-10DS-C1-1, 2, H5L3-10D-S-C0, and H0L3-10D-S-C0), only one unbonded zone with a length of 50 mm was left at the loaded end of the concrete block due to the space limit of the test machine. The unbonded regions were created by inserting plastic sleeves around the hybrid rebar before concrete casting; the plastic sleeves prevented the concrete from adhering to the hybrid rebar in the unbonded regions. For comparison, the arrangement of the unbonded zone (i.e., only one unbonded zone at the loaded end) for specimens H5L3-6D-C1-1, 2 and H5L3-6D-C2-1, 2 was nominally identical with those of specimens H5L3-10D-C1-1, 2. For these four specimens, one unbonded zone with a length of 100 mm was left at the loaded end. For Group I, four LVDTs with a gauge length of 50 mm were mounted to the specimen to record the relative displacements between the FRP rebar and the UHPC [see Figure 7.1 (b)]. A hollow hydraulic jack with a load capacity of 931 kN was adopted to provide a pulling force to the FRP rebar. During the test, the loads were measured by a load cell placed between the anchorage steel tube of the FRP rebar and the hydraulic jack, while the loaded-end slips and free-end slips were monitored by two LVDTs respectively.

For Group II, a universal tensile testing machine with a load capacity of 4500 kN was adopted for applying tensile forces. Only two LVDTs were used to measure the loaded end slips due to the space limitation of the test machine [see Figure 7.3 (b)]. For both Group I and Group II specimens, the test was manually controlled with a displacement rate of 1 mm/min.

7.3 EXPERIMENTAL RESULTS AND DISCUSSIONS

7.3.1 Failure Modes

Figures 7.4 and 7.5 show the typical failure modes of the specimens in Group I and Group II, respectively. Group I specimens failed either by the pulling-out of the FRP rebar or the rupture of the FRP rebar, as denoted by "PO" or "F" respectively in Table 7.4. To reduce the risk of damage to LVDTs, the LVDTs mounted at the loaded-end of specimens H3L3-20D-S-1/2 and H3L3-30D-1/2 were removed prior to failure of those specimens. This precaution was taken because these particular specimens were anticipated to endure significantly higher peak tensile forces compared with the others. It can be observed that only one specimen (i.e., specimen H3L3-10D-S-1) experienced "PO" of FRP rebar before the rupture of the FRP rebar. This suggests that for sand-coated and helically wrapped FRP rebars, an anchorage length of approximately 20 times the diameter may be sufficient for a reliable anchorage. For the ribbed FRP rebars, all the specimens failed by the rupture of the FRP rebar, indicating that a bond length of 10 times the rebar diameter may be sufficiently long to provide a reliable anchorage to this type of FRP rebars.

For Group II specimens, two types of failure modes could be observed: (1) the splitting failure of the concrete block: (2) the pulling-out failure of the hybrid rebar, as respectively denoted by "S" and "PO" in Table 7.4. As shown in Figure 7.5(a), the concrete block was split into several pieces when there was no CFRP jacket around the outer surface of the concrete block. As summarised in Table 7.4, concrete splitting was prohibited successfully by employing CFRP jacketing for the test specimens, regardless of the number of jacket layers. For the specimens without concrete splitting, bond slip failure may occur at different interfaces, including that between FRP tube and concrete, that between FRP tube and UHPC, as well as that between FRP rebar and UHPC [Figure 7.5(b-c)].

To observe the internal state of the test specimens, the specimens were cut open after the completion of the pull-out tests. For specimens with a uniform hybrid rebar embedded in concrete (e.g., H0L3-6D-S-C3), evident slips were observed both at the interface between FRP tube and UHPC and the interface between UHPC and FRP rebar. For specimens with a wavy-shaped hybrid rebar embedded in concrete (e.g., H5L3-6D-S-C3), obvious slips were observed only at the interface between the FRP rebar and UHPC, with nearly no slips between the wavy tube and the UHPC or the outer concrete.

7.3.2 Bond Stress-Slip Relationship

7.3.2.1 General

The curves of average bond stress versus loaded end slip or free end slip of the hybrid rebars, obtained from pull-out tests of Group I specimens are presented in Figure 7.6. Figure 7.7 presents the curves of average bond stress versus loaded end slip for the hybrid rebars in Group II. The average bond stress of an FRP rebar is calculated by the following equation:

$$\tau = \frac{F}{\pi d l} \tag{7.1}$$

where F is the tensile load; l is the embedment length (i.e., bond length); and d is the diameter of the FRP rebar ($d = 25\ mm$). The bond length, peak load, peak bond stress (i.e., bond strength) τ_m, loaded end slip at peak bond stress S_{ml} and free end slip at peak bond stress S_{mf} of all test specimens are summarized in Table 7.4. The embedment length l used here is the bond length of the FRP rebar (Group I) or the hybrid rebar (Group II) within the concrete. Note that for Group II specimens, the diameter of the central FRP rebar was used to calculate the average bond stresses. Although the focus of Group II was on hybrid rebars embedded in concrete, theoretically, the diameter of the hybrid rebar should be used to calculate bond stress. However, the experimental results of Group II specimens needed to be compared with those of Group I specimens to investigate the bonding mechanisms of the hybrid rebar. If the diameter of the hybrid rebar were used, the resulting bond stress values would be exceedingly small, making a direct comparison between the two groups impractical. Simultaneously, there is a paucity of research in the literature concerning large-diameter rebars, which makes it challenging to compare the results of this study with existing literature and standards. Therefore, the diameter of the central FRP rebar was utilised in the calculations to facilitate a straightforward comparison between the two groups.

7.3.2.2 Group I specimens

Figure 7.6 depicts the bond stress-slip curves of specimens in Group I. The curves of free end slips and loaded end slips are presented respectively. The slips were obtained from the average readings of the two LVDTs at the free end or the loaded end. Figure 7.7 shows the influence of GFRP tube thickness and bond length on bond stress-slip curves of Group I specimens. From Figure 7.7(a), it can be found that hybrid rebars with thicker GFRP tubes possessed higher bond strength. The smallest bond strength of wavy-shaped hybrid rebar specimens with a bond length of 10*d* was 16.4 MPa, which is higher than the minimum characteristic bond strength advised by ASTM D7957-17 (i.e., 7.6 MPa) and ACI 440.6-08 (i.e., 9.6 MPa) for FRP rebars.

Figures 7.7(b) and (c) show the effect of bond length on the bond stress-slip curves of sand-coated and helically wrapped FRP rebar specimens and ribbed FRP rebar specimens of Group I, respectively. For sand-coated and helically wrapped FRP rebars with a bond length of 10D, the average bond stress-slip curves at the free end could be divided into four branches [Figure 7.7(b)]: a first linear ascending stage with micro-slippage, a second branch with greatly enhanced slips, a descending branch with the bond stress decreasing with the increase in the slip, and a residual branch. It can be found that free end slips of specimens with a bond length of 20*d* and 30*d* were negligibly small until the rupture of FRP rebars, indicating that for sand-coated and helically wrapped FRP rebars, a bond length of 20*d* or smaller is required for a full anchorage [Figure 7.7(b)]. Therefore, 20*d* can be regarded as the embedment length of the sand-coated and helically wrapped-FRP rebars. For ribbed FRP rebars in Group I, Figure 7.7(c) shows that all the specimens failed by FRP rebar rupture during the ascending stage. For specimens with longer bond lengths, the bond strengths were lower correspondingly. The test results indicated that a bond length of 10*d* was sufficiently long for a full anchorage for such ribbed FRP rebars.

7.3.2.3 Group II specimens

Figure 7.8(a-d) shows the bond stress-slip curves of Group II specimens. The effect of wave height on the bond stress-slip curves of Group II specimens are presented in Figure 7.8(e-f). In Figure 7.8 (a), the bond stress-slip curves for specimen H5L3-6D-S-C0-1 and specimen H5L3-6D-S-C0-2 terminated prematurely at the ascending branch compared to other specimens. As summarised in Table 7.4, the two specimens ultimately failed due to the splitting of the outer concrete block.

In contrast, Figure 7.8 (b) illustrates the complete bond stress-slip curves of specimen H5L3-6D-S-C1-1 and specimen H5L3-6D-S-C1-2. The two curves are closely aligned with each other and exhibit a similar shape to the pull-out failure curve observed in Group I. Similarly, the specimens shown in Figure 7.8 (c) also display complete curves and were classified under the pull-out failure mode. However, the bond strength of specimen H5L3-6D-S-C2-1 is significantly lower than that of its duplicate. The significantly lower bond strength of this specimen may be attributed to defects at the FRP rebar-UHPC bonding interface in this specimen. Observation after the experiment revealed that significant voids were present within the UHPC in this specimen due to inadequate vibration during the casting process. Figure 7.8 (d) shows thar the specimen H5L3-10D-S-C1-1 possess a higher bond stress than that of its duplicate at a given slip but failed earlier with concrete splitting. This may be due to eccentric tension occurring during the experiment, resulting in a relatively high bond stress for this specimen.

As shown in Figure 7.8(e), the bond stresses of specimen H5L3-6D-S-C3 with a wave height of 5 mm are higher than those of specimen H0L3-6D-S-C3 with a wave height of 0 mm. With the same bond length and CFRP jacket confinement, the peak bond stress (τ_m) of specimen H5L3-6D-S-C3 was 148% larger than that of specimen H0L3-6D-S-C3. In contrast to uniform FRP tubes, wavy-shaped FRP tubes offer the mechanical interlocking with concrete, thus significantly enhancing the bond strength and mitigating slippage at the FRP tube-concrete interface. Although the two specimens ultimately exhibited FRP rebar pull-out [Figure 7.5(b-c)], specimen H0L3-6D-S-C3 had a particularly weak UHPC-FRP interface which prevented the full development of the bond strength of the internal FRP rebar, resulting in significant lower peak bond stress and increased slip of the specimen.

As shown in Figure 7.8(f), the bond stress-slip curves of specimen H0L3-10D-S-C0 and specimen H5L3-10D-S-C0 with splitting failure in concrete due to the absence of a CFRP jacket are highly different from the curves of specimens H5L3-10D-S-C1-1,2 with the same bond length in Figure 7.8(d). Due to the premature failure caused by the splitting of the concrete block, the former two specimens possessed much lower bond strengths compared to specimens H5L3-10D-S-C1-1,2. Compared to specimen H0L3-10D-S-C0, specimen H5L3-10D-S-C0 possessed much larger (35% larger) peak bond stress with smaller slips due to the use of a wavy-shaped FRP tube. The loaded end slip at peak bond stress (S_{ml}) of the wavy-shaped specimen was 2.48 mm, while that of specimen H0L3-10D-S-C0 was 11.03 mm. The aforementioned comparisons demonstrated that wavy-shaped hybrid rebars could exhibit much better performance than uniform hybrid rebars under conditions of both splitting failure and pull-out failure.

The effect of CFRP jacket thickness and bond length on the bond stress-slip curves of Group II specimens are presented in Figure 7.9. It should be noted that the results of specimen H5L3-6D-S-C2-1 were not included in this comparison since its bond strength was significantly lower than that of its duplicate specimen [Figure 7.8(c)].Previous comparisons had shown that when wavy-shaped tubes were used, mechanical interlocking occurred between the hybrid rebar and the concrete, with slippage mainly occurred at the FRP rebar-UHPC interface. Therefore, in the subsequent analysis, the actual bond lengths of FRP rebars, which started from the point of UHPC fracture and ended at the free end of the entire hybrid rebar, were used to calculate the bond stresses. In other words, the unbonded zone between the hybrid rebar and the surrounding concrete at the loaded end were excluded, while the unbonded zones at the free end were included. For instance, for specimens H5L3-6D-S-C0-1/2, the actual bond length was 200 mm, and for specimens H5L3-6D-S-C1-1/2 and H5L3-6D-S-C2-1/2, the actual bond length was 150 mm.

As shown in Figure 7.9(a), with the confinement provided by the external CFRP jacket, the splitting failure of the concrete block was prohibited, leading to complete bond stress-slip curves for the specimens. Premature failure could be observed for specimen H5L3-6D-C0-1 and specimen H5L3-6D-C0-2 without FRP confinement. This premature failure is attributed to the splitting of the concrete block. When the specimens were confined with CFRP jackets, the crack development within the concrete blocks was effectively controlled, thereby ensuring the complement of the full-range pull-out process. Figure 7.9(a) demonstrates that the specimens with varying CFRP jacket thicknesses exhibited similar bond stress-slip curves. Previous studies found that the use of a confining material, such as FRP sheets or stirrups, could significantly improve the bond strength of FRP rebars NC structural members (Gao et al., 2019; Wang et al., 2020). However, since the failure modes of the present specimens with outer CFRP confinement were characterised by the pull-out failure of the internal FRP rebar, the influence of the outer CFRP confinement on the bond behaviour of the internal FRP rebar was insignificant. The confining effect of CFRP jackets may have been diminished during the transfer process from the external concrete to the internal UHPC as it passed through the GFRP tube. As a result, it may be inferred that while the presence of FRP jackets influenced the failure mode of the test specimens, the level of confinement did not affect the bond behaviour at the studied confinement levels.

Figure 7.9(b) shows the bond stress-slip curves of four specimens with two different bond lengths (i.e., 6*d,* 10*d*). Specimen H5L3-10D-S-C1-1 possessed a higher bond stress than the other specimens at a given slip but failed earlier with concrete splitting than the other specimens when the bond stress reached nearly 15 MPa. The early failure indicates that one layer of CFRP jacket may not be strong enough for preventing concrete splitting for the considered FRP rebars, which is consistent with the conclusions reached by previous studies for FRP rebars (e.g., Li et al. (2022). The bond strength of specimen H5L3-10D-S-C1-2 is slightly smaller than those of specimen H5L3-6D-S-C1-1 and specimen H5L3-6D-S-C1-2. This is consistent with the conclusions in the literature that an FRP rebar with a shorter bond length would generally develop a higher bond strength (Tighiouart et al., 1998).

7.3.3 Comparison and Discussions

The effect of concrete block on the bond stress-slip curves of hybrid rebar specimens is shown in Figure 7.10 which compares the bond stress-slip curves of specimens with a bond length of 10*d* and a 3-ply GFRP tube (i.e., L3-10D specimens) from the two groups. In the figure, the first four specimens were in Group I and the remaining four specimens were in Group II with a concrete block. Specimen H0L3-10D-S-C0 had a uniform hybrid rebar and thus the bond stress-slip curve of this specimen is much lower than the other curves due to the significant slippage at the inner and outer interfaces of the straight FRP tube in the hybrid rebar. Specimens H3L3-10D-R-1/2 utilised a ribbed FRP rebar. Owing to the failure of the FRP rebar, the bond-slip curves terminated in the ascending phase. Specimen H5L3-10D-S-C0 involved the pulling of a wavy-shaped hybrid rebar from an unconfined concrete block. The lack of confinement in the concrete block led to its splitting failure, resulting in the curve terminating in the ascending phase as well. Specimens H3L3-10D-S-1/2 and H5L3-10D-S-C1-2 exhibited complete bond-slip curves and higher bond strength compared to other specimens.

Figure 7.11 compares the key parameters of the test specimens, including the peak bond stresses and the corresponding slips at the loaded end [Figure 7.11(a)], as well as the slips at the loaded end when the bond stress reached 10 MPa [Figure 7.13(b)]. It should be noted that specimens H0L3-10D-S-C0 and H5L3-10D-S-C0 are excluded from Figure 7.13(b) as their bond stresses did not reach 10 MPa. It should be noted that CSA S807-19 stipulates that the slip at the loaded end should be within 0.5 mm when the bond stress reaches 10 MPa for FRP rebars. Evidently, the slips at the loaded end at a bond stress of 10 MPa for the test specimens ranged between 2 and 3 mm, which does not comply with the standard requirements. This discrepancy arises because the standard mandates a bond length of five times the FRP rebar diameter, whereas the bond lengths in the present experiment were ten times the FRP rebar diameter, leading to greater slips. Besides, the slip in the present experiment refers to the total slip between the entire hybrid rebar and the outer concrete, as well as the slips at the interfaces within the hybrid rebar.

It can be observed that the slips at the loaded end at a bond stress of 10 MPa among different specimens with a wavy shape are close to each other. For instance, the slips for specimens H3L3-10D-S-1/2 are 2.21 mm and 2.3 mm, whereas for specimens H5L3-10D-C1-1/2, the slips are 2.45 mm and 2.55 mm, respectively. This indicates that the majority of the slips at the loaded end for wavy-shaped hybrid rebars embedded in a concrete block may be primarily due to the slippage of the FRP rebar with respect to UHPC.

However, the peak bond stresses and the corresponding slips for specimens without an outer concrete block are greater than those with an outer concrete block. For instance, the peak bond stresses for specimens H3L3-10D-S-1/2 are 16.4 MPa and 18.5 MPa, respectively, whereas H5L3-10D-S-C1-1/2 with higher wave heights exhibit peak bond stresses of only 14.8 MPa and 11.3 MPa. This does not imply that the presence of an outer concrete block reduces the peak bond stress of the FRP rebar. A possible reason for this observation could be the differences in the design of the experimental apparatus, leading to slight variations in the stress state of the FRP rebar in the specimens of the two groups. The specimens in Group I, as detailed in Sections 7.2.3 and 7.2.4, were strengthened with CFRP strips at the loaded end of the FRP tube to avoid premature failure at the end of the specimen. As a result, the load-bearing capacity of the confined UHPC at the strengthened location was improved, thereby preventing premature failure of the specimen. However, the expansion of the confined UHPC under compression may exert an additional confining effect on the internal FRP rebar, thereby slightly increasing the peak bond stress of the FRP rebar.

To minimise the effect of confinement on determining the development length (i.e., the anchorage length that ensures the rupture of FRP rebar during pull-out tests) of the FRP rebars, the experimental results from Group II specimens should be used. Figure 7.12 illustrates the relationship between the ratios of the peak loads to the FRP rebar rupture loads against the embedment lengths for the specimens of H5L3-S-C1. A trendline was derived for the relationship based on the experimental results. It can be observed that the development length (or anchorage length) for the wavy-shaped hybrid rebars with sand-coated and helically wrapped GFRP rebars should be around 18.8*d*.

7.4 CONCLUSIONS

In this chapter, the bond behaviour of FRP rebars embedded in UHPC in hybrid rebars and the bond behaviour of hybrid rebars in concrete have been examined through two groups of pull-out tests. The effects of different factors, such as the wave height, the GFRP tube thickness, the CFRP jacket thickness, and the bond length on the bond behaviours were evaluated. Based on the interpretation and discussion of the experimental results, the following conclusions can be drawn:

(1) For Group I specimens with sand-coated and helically wrapped GFRP rebars (where FRP rebars within hybrid rebars were subjected to pulling out forces), pull-out failure of FRP rebars occurred when the bond length was 10*d*, whereas FRP rebars ruptured when the bond length was 20*d*. For Group I specimens with ribbed GFRP rebars, within the bond length range covered in the present study (i.e., 10*d* to 30*d*), all the FRP rebars experienced rupture failure.

(2) For Group II specimens (i.e., hybrid rebars embedded in concrete) without FRP confinement, concrete splitting failure occurred to the concrete blocks. When sufficient confinement was provided, the pull-out failure of the FRP rebar from UHPC could be

achieved. More specifically, for uniform hybrid rebars in Group II, the pull-out test revealed significant slippage between the FRP rebar and the UHPC, as well as between the UHPC and the GFRP tube. However, for concrete specimens reinforced with wavy-shaped hybrid rebars in Group II, slippage was only observed between the FRP rebar and the UHPC.

(3) The pull-out test results of Group I specimens showed that the anchorage length of the 25 mm sand-coated and helically wrapped GFRP rebars was in a range of 10*d* to 20*d* for ensuring FRP rebar rupture and that of the ribbed GFRP rebars was less than 10*d*. The pull-out test results of Group II specimens indicated more precise values for the anchorage length of the 25 mm sand-coated and helically wrapped GFRP rebars, which should be 18.8*d*.

(4) The experimental findings indicated that wavy-shaped hybrid rebars exhibited superior bond performance, characterised by higher bond strengths and smaller slips, in comparison to uniform hybrid rebars. This improvement was attributed to the mechanical interlocking introduced by the use of wavy-shaped GFRP tubes.

(5) The different thicknesses of the outer CFRP jacket in Group II specimens led to little variations in bond strength; however, an increase in the thickness of the GFRP tube in Group I specimens led to higher bond strengths.

7.5 REFERENCES

ACI 440.6-08 (R2017). *Specification for Carbon and Glass Fiber-Reinforced Polymer Bar Materials for Concrete Reindorcement*, American Concrete Institute, Farmington Hills, Michigan, USA.

ASTM D7957/D7957M-17 (2017b). *Standard specification for solid round glass fiber* *reinforced polymer bars for concrete reinforcement*, American Society for Testing and Materials (ASTM), West Conshohocken, PA.

ASTM D7205/D7205M (2021). *Standard test method for tensile properties of fiber reinforced polymer matrix composite bars*, American Society for Testing and Materials (ASTM), West Conshohocken, PA.

CSA S806-12 (R2017). *Design and construction of building components with fiber reinforced polymers*, Canadian Standards Association, Rexdale, ON, Canada.

Gao, K., Li, Z., Zhang, J., Tu, J. and Li, X. (2019). "Experimental research on bond behavior between GFRP bars and stirrups-confined concrete", *Applied Sciences*, 9(7), 1340.

Li, P., Jin, L., Zhang, R. and Du, X. (2022). "Static bond performance between BFRP bars and concrete with stirrup confinement: A refined modelling", *Engineering Structures*, 262, 114379.

Teng, J.G., Zhang, B., Zhang, S.S. and Fu, B. (2018). "Steel-free hybrid reinforcing bars for concrete structures", *Advances in Structural Engineering*, 21(16), 2617-2622.

Tighiouart, B., Benmokrane, B. and Gao, D. (1998). "Investigation of bond in concrete member with fibre reinforced polymer (FRP) bars", *Construction and Building Materials*, 12(8), 453-462.

Wang, Y., Wang, M., Zhang, X. and Xu, Q. (2020). "Effect of BFRP lateral confinement on bond behavior between GFRP ribbed bars and concrete", *Composites Science and Engineering*, 4:5-12, in Chinese.

Table 7.1 Test matrix

Group	Specimen	Bond length (mm)	Thickness of GFRP tube	Wave height	Cylindrical compressive strength of concrete block (MPa)	Confinement ratio of outer CFRP ρ_k
Group I	H3L3-10D-S-1, 2	250	3-ply	3	/	/
	H3L3-20D-S-1, 2	500	3-ply	3		
	H3L3-30D-S-1,2	750	3-ply	3		
	H3L5-10D-S-1, 2	250	5-ply	3		
	H0L3-10D-S-1,2	250	3-ply	0		
	H0L3-30D-S-1, 2	750	3-ply	0		
	H3L3-10D-R-1, 2	250	3-ply	3		
	H3L3-20D-R-1,2	500	3-ply	3		
	H3L3-30D-R-1, 2	750	3-ply	3		
Group II	H5L3-6D-S-C0-1, 2	150	3-ply	5	47.3 (C50)	0
	H5L3-6D-S-C1-1, 2	150		5		0.02
	H5L3-6D-S-C2-1, 2	150		5		0.04
	H5L3-10D-S-C1-1, 2	250		5		0.02
	H0L3-6D-S-C3	150		0	27.0 (C30)	0.059
	H5L3-6D-S-C3	150		5		0.059
	H0L3-10D-S-C0	250		0	30.8 (C30)	0
	H5L3-10D-S-C0	250		5		0

Table 7.2 Mechanic properties of GFRP rebars

Type of FRP rebar	Ultimate tensile load (kN)	Tensile strength (MPa)	Elastic modulus (GPa)	Ultimate tensile strain (%)
Sand-coated and wrapped	500.3	931.1	56.3	1.61
Ribbed	266.6	546.4	49.9	1.05

Table 7.3 Mixture proportions of concrete (by weight)

Concrete	Cement	Silica fume	Quartz powder	Sand	10 mm aggregate	Water	Superpla sticizer
C30	1.00	/	/	2.26	2.99	0.53	0.01
C50	1.00	/	/	1.72	2.81	0.45	0.033
UHPC	1.00	0.25	0.25	1.10	/	0.216	0.026

Table 7.4 Key results

Group	Specimen	Bond length (mm)	Peak load (kN)	Peak bond stress τ_m (MPa)	Loaded end slip at peak bond stress S_{ml} (mm)	Free end slip at peak bond stress S_{mf} (mm)	Failure mode
Group I	H3L3-10D-S-1	250	328.3	16.4	10.00	5.30	PO
	H3L3-10D-S-2	250	376.7	18.5	9.10	3.60	F
	H3L3-20D-S-1	500	379.3	9.3	/	0.00	F
	H3L3-20D-S-2	500	457.5	11.2	/	0.05	F
	H3L3-30D-S-1	750	386.9	6.3	/	0.00	F
	H3L3-30D-S-2	750	354.6	5.8	/	0.00	F
	H3L5-10D-S-1	250	406.6	20.2	/	3.54	F
	H3L5-10D-S-2	250	413.8	20.5	9.79	5.15	F
	H3L3-10D-R-1	250	299.6	14.1	4.05	0.13	F
	H3L3-10D-R-2	250	297.8	14.0	4.50	0.13	F
	H3L3-20D-R-1	500	235.6	5.9	6.16	0.13	F
	H3L3-20D-R-2	500	139.3	3.6	7.36	0.00	F
	H3L3-30D-R-1	750	300.2	4.9	10.74	0.00	F
	H3L3-30D-R-2	750	295.4	4.9	11.34	0.05	F

Table 7.4 *(Continued)*

Group	Specimen	Bond length (mm)	Peak load (kN)	Peak bond stress τ_m (MPa)	Loaded end slip at peak bond stress S_{ml} (mm)	Free end slip at peak bond stress S_{mf} (mm)	Failure mode
Group II	H5L3-6D-S-C0-1	150	135.0	11.5	2.61	/	S
	H5L3-6D-S-C0-2	150	178.9	15.2	8.29	/	S
	H5L3-6D-S-C1-1	150	146.5	12.4	7.38	/	PO
	H5L3-6D-S-C1-2	150	145.6	12.4	7.41	/	PO
	H5L3-6D-S-C2-1	150	101.2	8.6	6.76	/	PO
	H5L3-6D-S-C2-2	150	139.6	11.8	7.86	/	PO
	H5L3-10D-S-C1-1	250	291.4	14.8	6.37	/	S
	H5L3-10D-S-C1-2	250	222.6	11.3	6.35	/	PO
	H0L3-6D-S-C3	150	85.8	6.8	13.95	/	PO
	H5L3-6D-S-C3	150	212.5	16.9	8.26	/	PO
	H0L3-10D-S-C0	250	112.5	6.0	11.03	/	S
	H5L3-10D-S-C0	250	152.5	8.1	2.48	/	S

Note: “PO” stands for pull-out failure; “F” stands for rupture of FRP rebar; and “S” stands for splitting failure of concrete block; Due to the early failure of UHPC without sufficient confinement near the loading frame, the results of specimens H0L3-10D-S1, H0L3-10D-S-2, H0L3-30D-S-1, and H0L3-30D-S-2 are not included in this table.

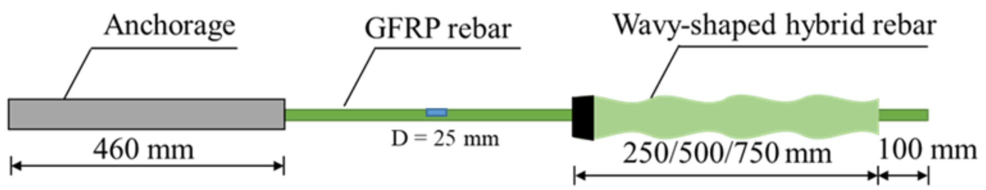

(a) Schematic diagram of the specimen

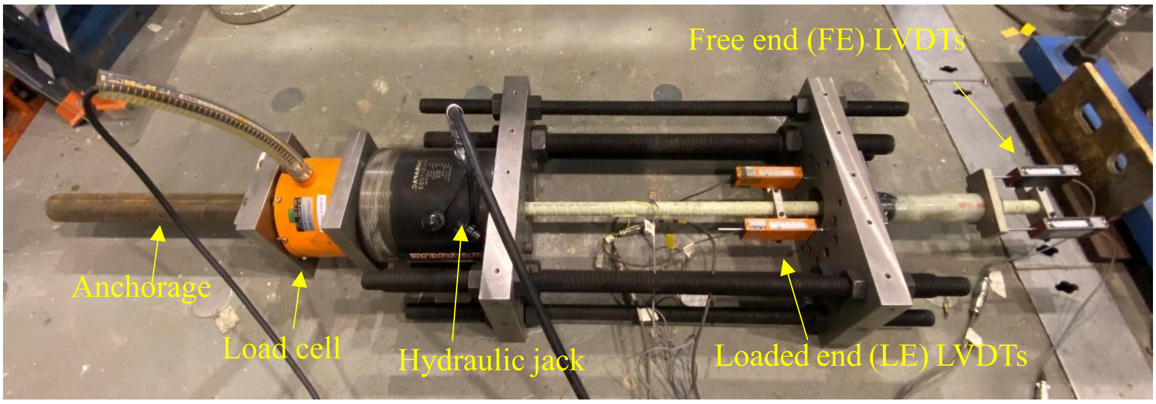

(b) Test set-up

Figure 7.1 Pull-out test (Group I)

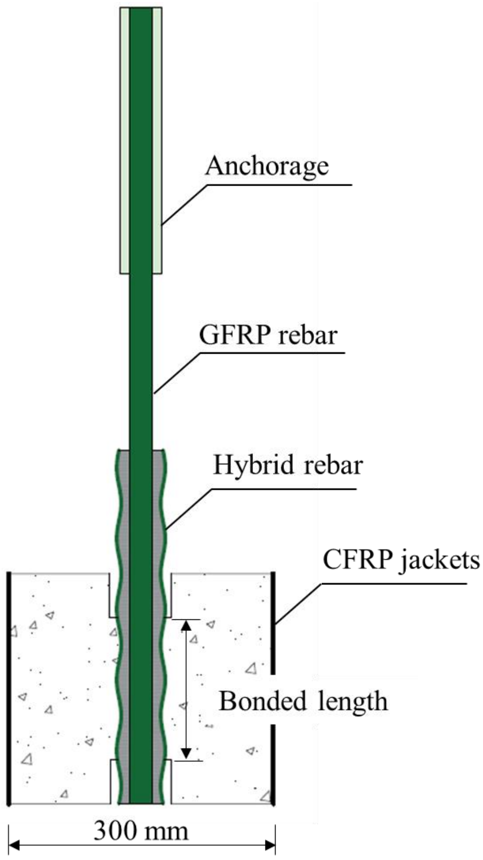

(a) Schematic diagram of the specimen

(b) Test set-up

Figure 7.2 Pull-out test (Group II)

(a) Sand-coated and helically wrapped FRP rebars

(b) Helically ribbed FRP rebars

Figure 7.3 Two types of GFRP rebars with different surface features

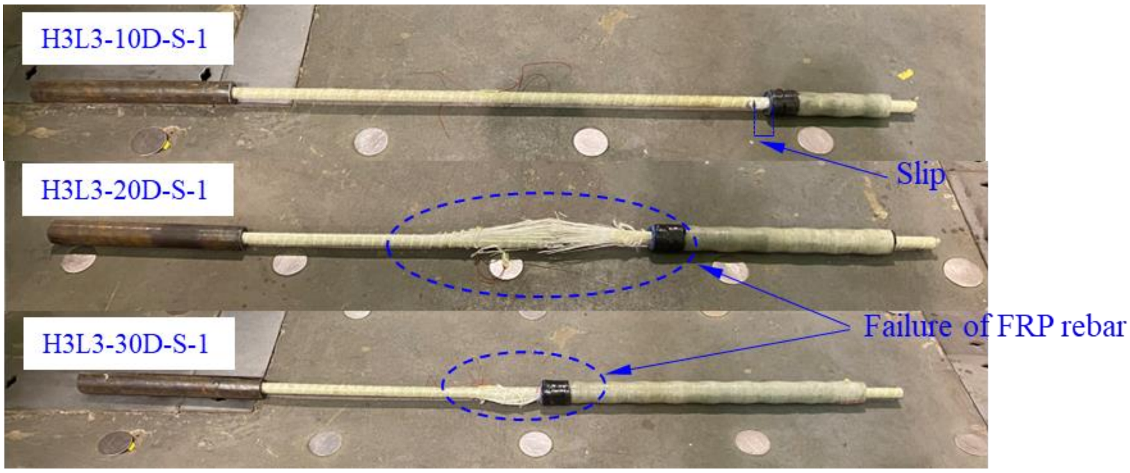

(a) Sand-coated and helically wrapped FRP rebars

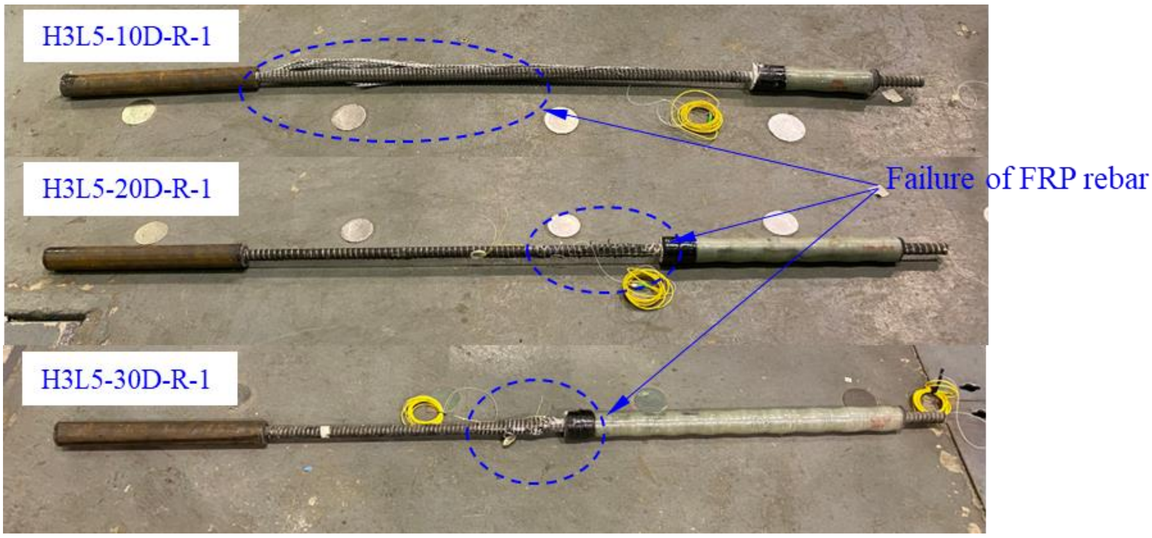

(b) Helically ribbed FRP rebars

Figure 7.4 Typical failure modes of specimens in Group I

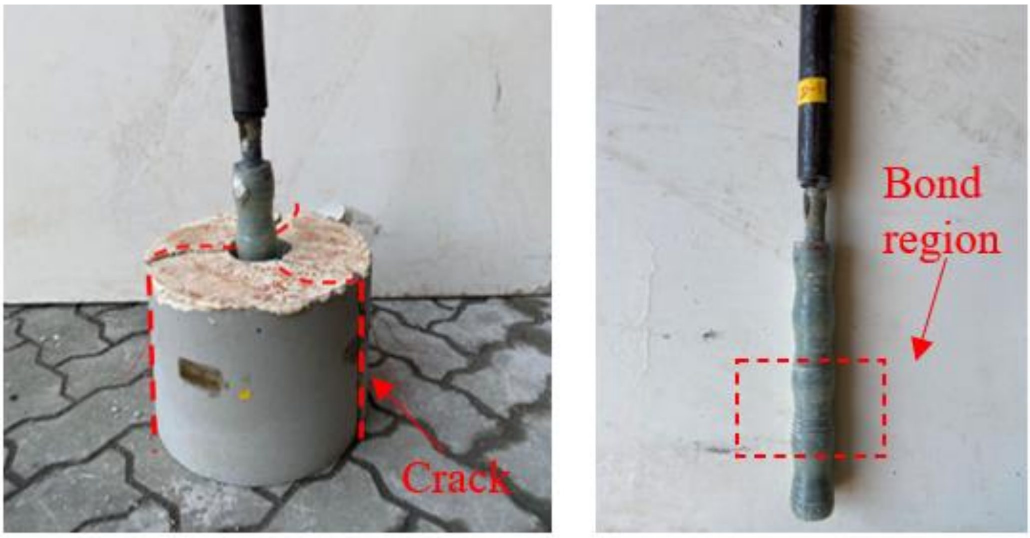

(a) Concrete splitting failure: specimen H5L3-6D-S-C0-1

(b) Pull-out failure of uniform hybrid rebar: H0L3-6D-S-C3

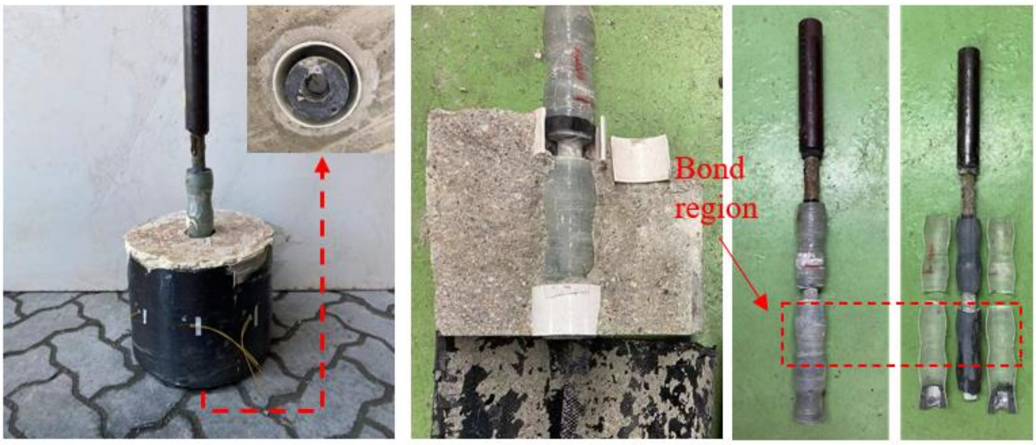

(c) Pull-out failure of wavy-shaped hybrid rebar: H5L3-6D-S-C3

Figure 7.5 Typical failure modes of specimens in Group II

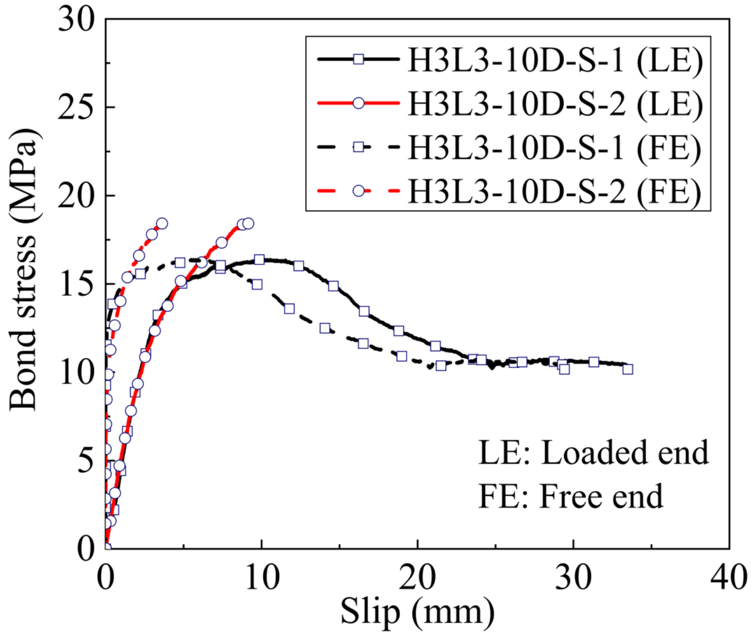

(a) H3L3-10D-S

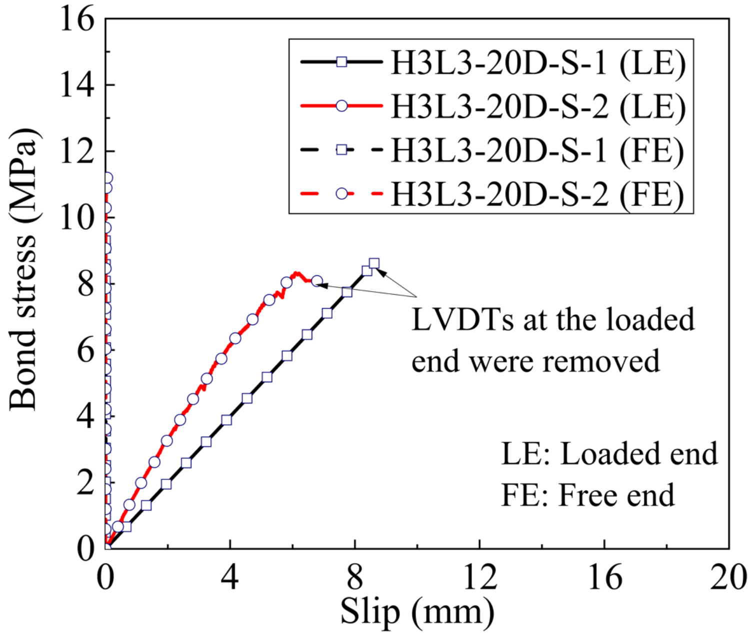

(b) H3L3-20D-S

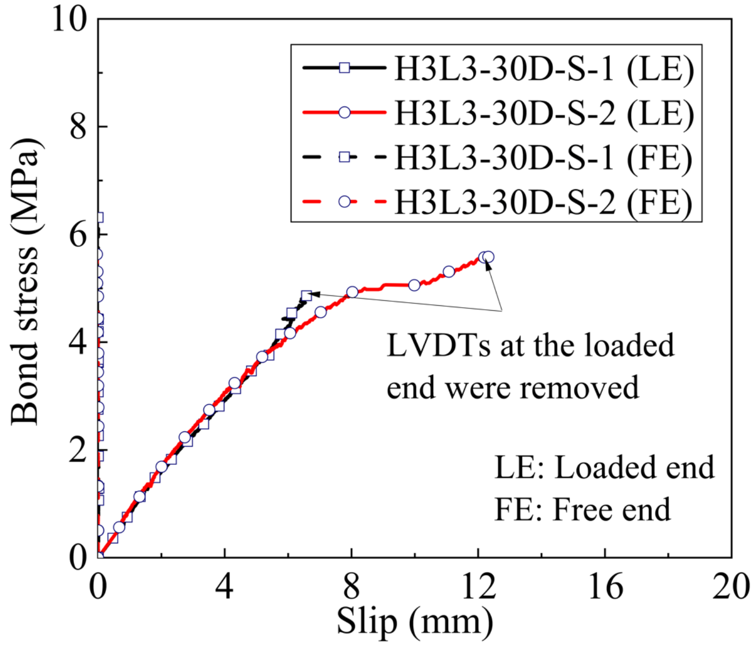

(c) H3L3-30D-S

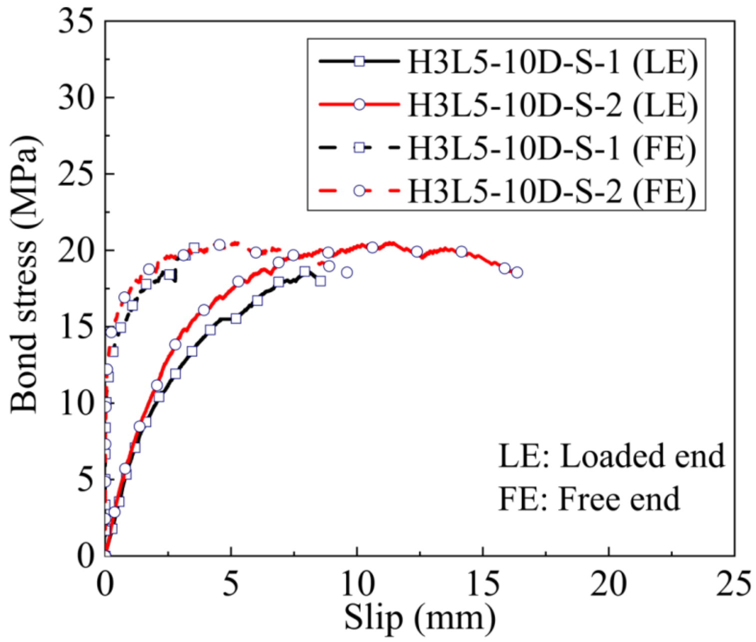

(d) H3L5-10D-S

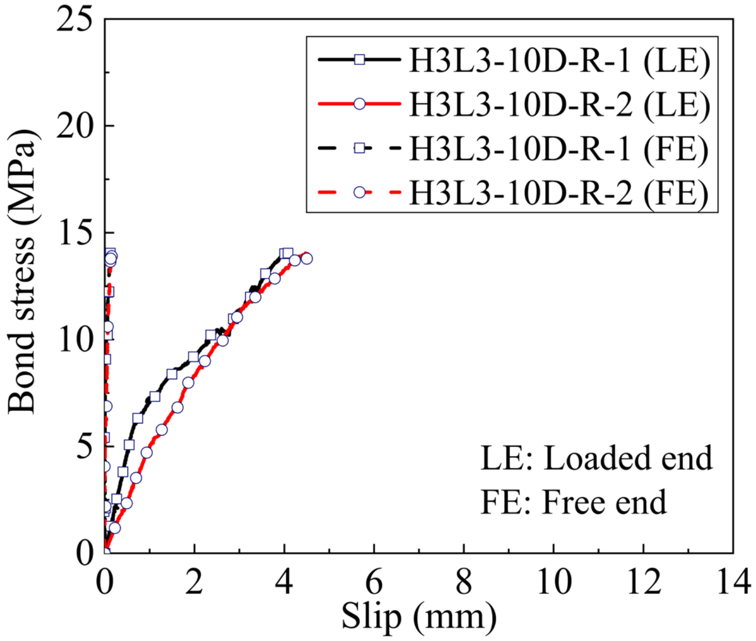

(e) H3L3-10D-R

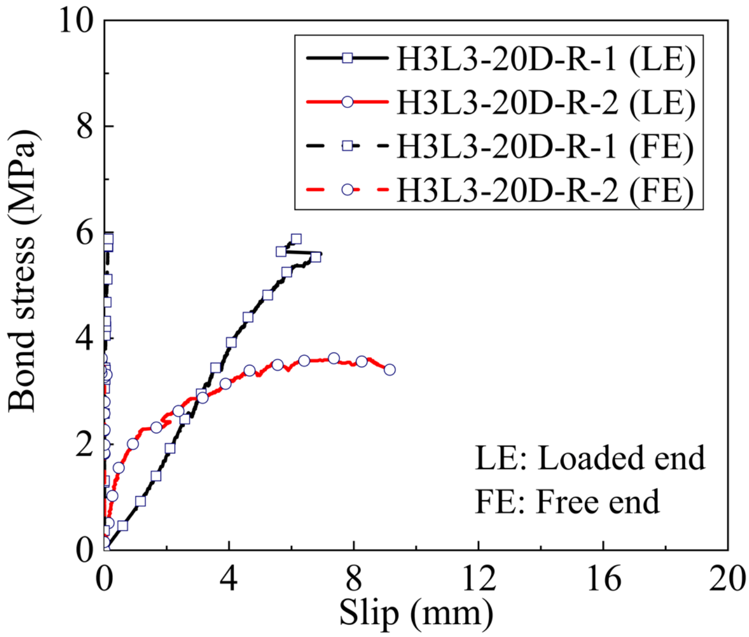

(f) H3L3-20D-R

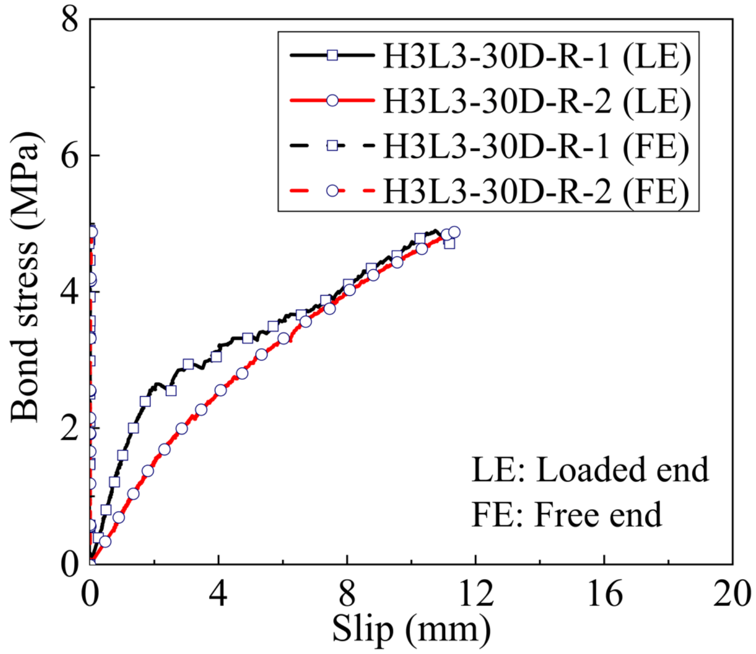

(g) H3L3-30D-R

Figure 7.6 Bond stress-slip curves of Group I specimens

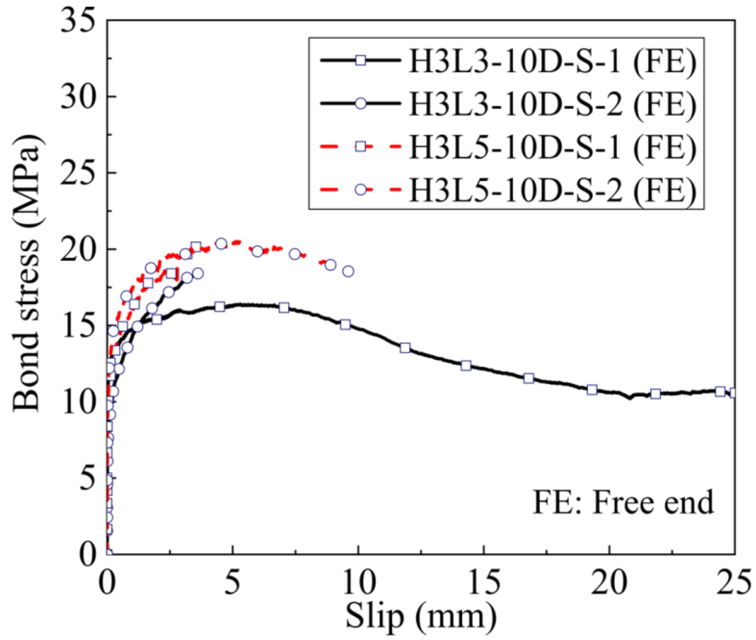

(a) Effect of GFRP tube thickness

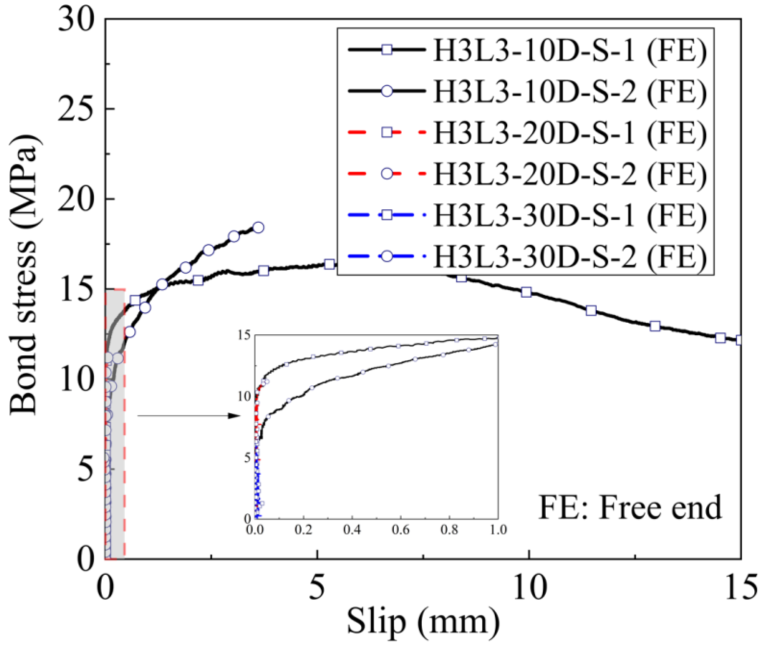

(b) Effect of bond length (sand-coated and helically wrapped FRP rebars)

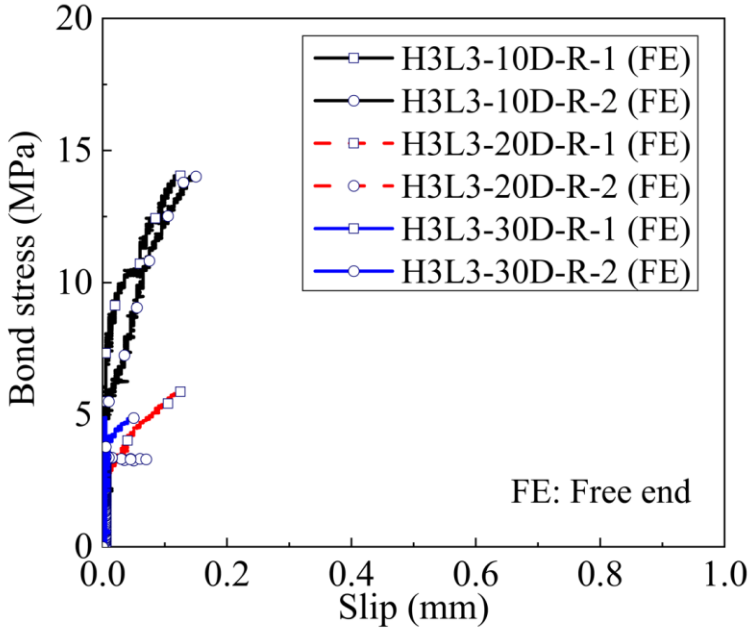

(c) Effect of bond length (ribbed FRP rebars)

Figure 7.7 Effect of GFRP tube thickness and bond length on bond stress-slip curves of Group I specimens

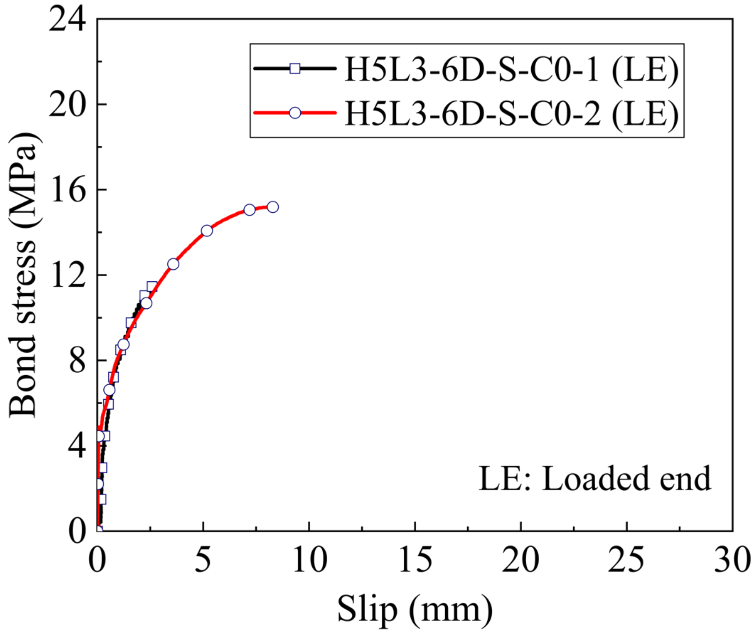

(a) H5L3-6D-S-C0

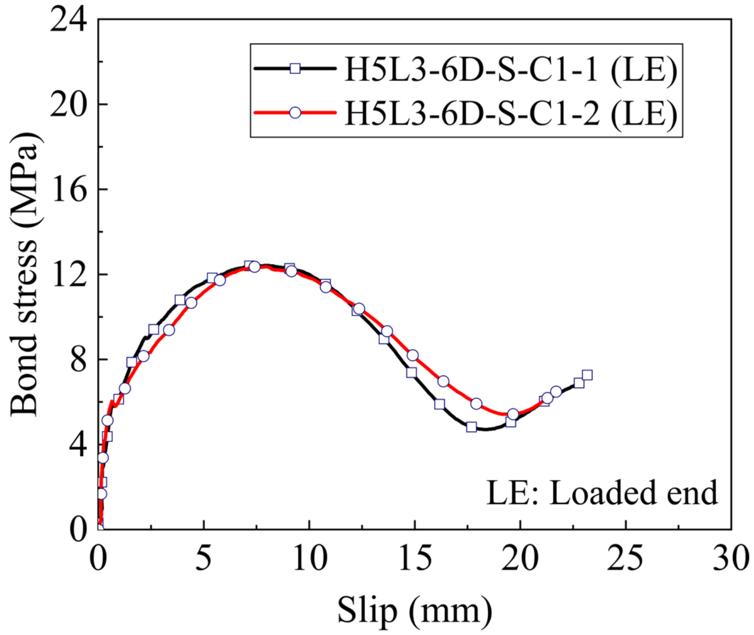

(b) H5L3-6D-S-C1

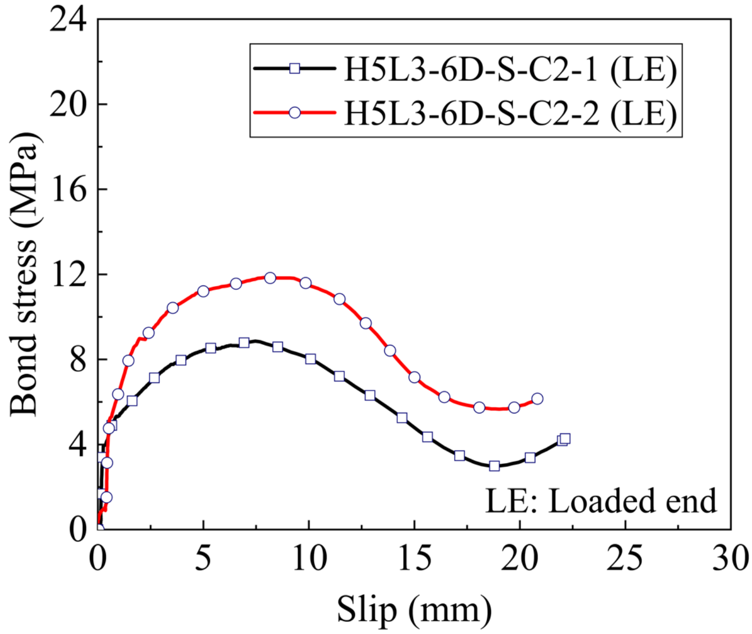

(c) H5L3-6D-S-C2

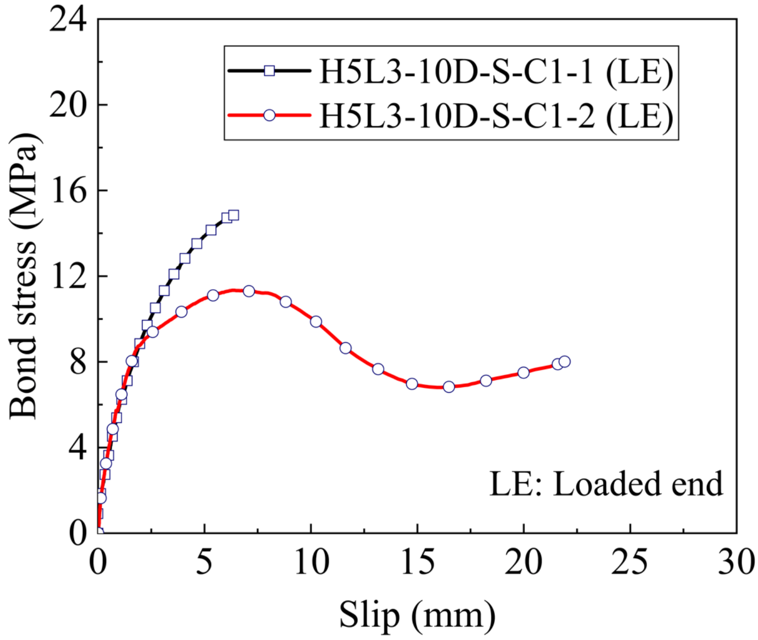

(d) H5L3-10D-S-C1

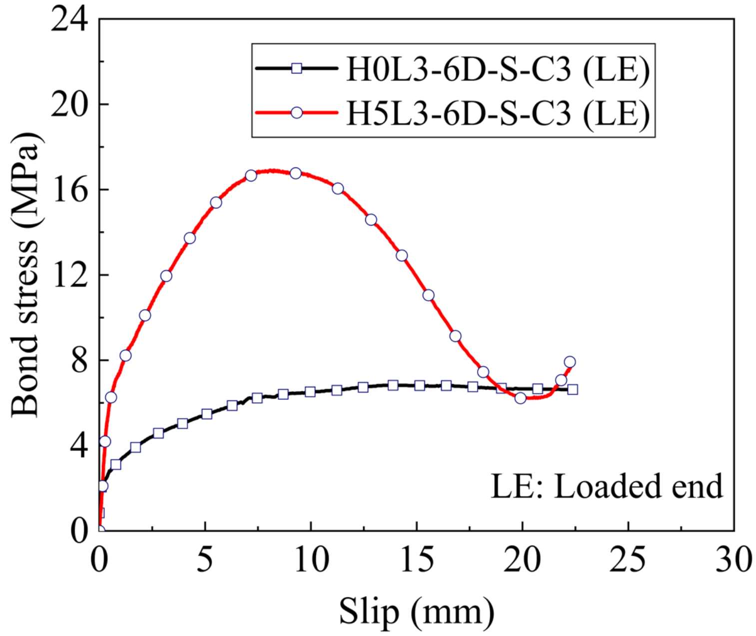

(e) H0L3/H5L3-6D-S-C3

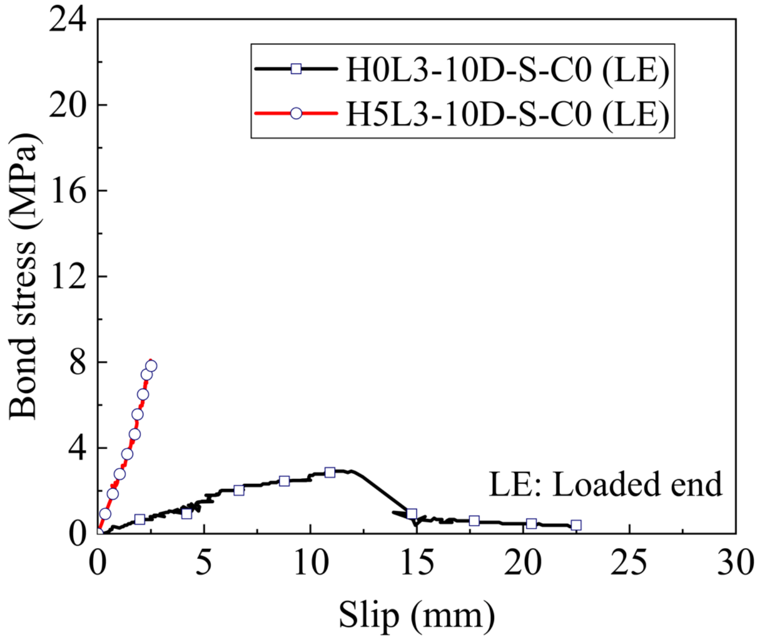

(f) H0L3/H5L3-10D-S-C0

Figure 7.8 Bond stress-slip curves of Group II specimens

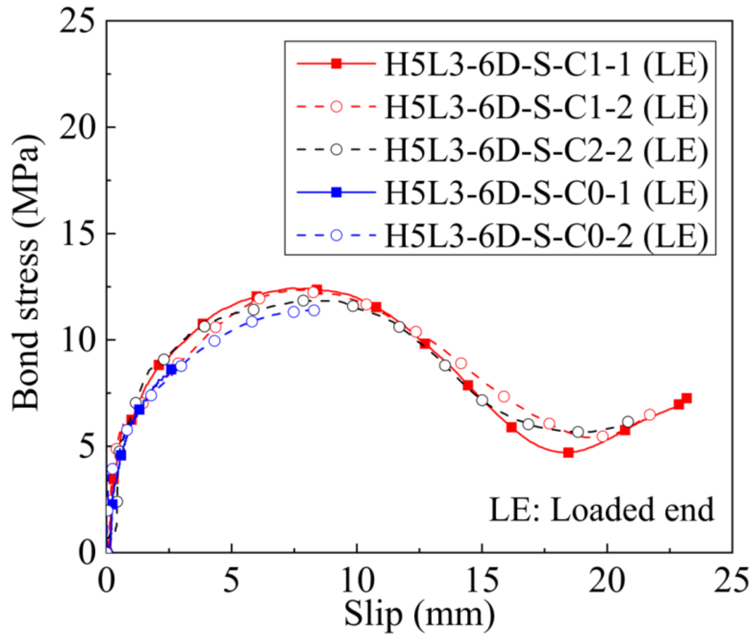

(a) Effect of CFRP thickness

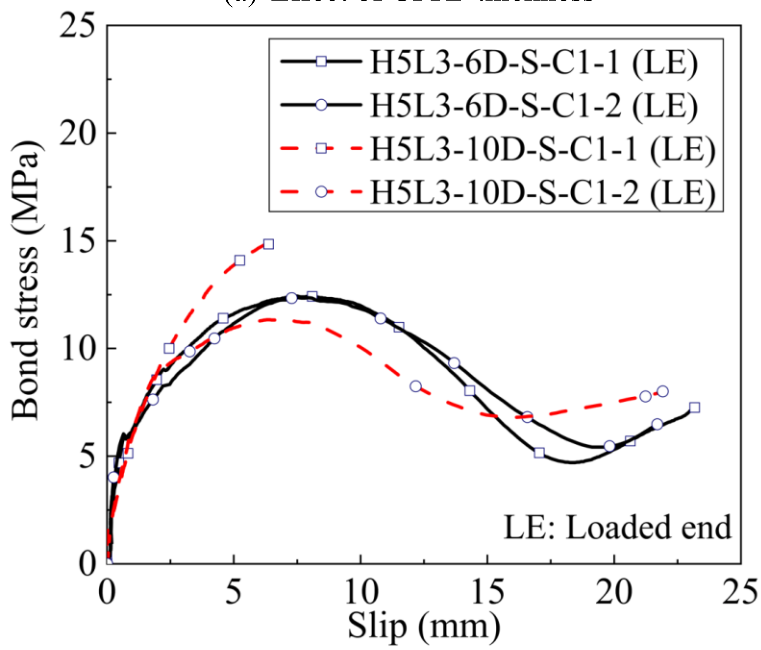

(b) Effect of bond length

Figure 7.9 Effect of CFRP thickness and bond length on bond stress-slip curves of Group II specimens

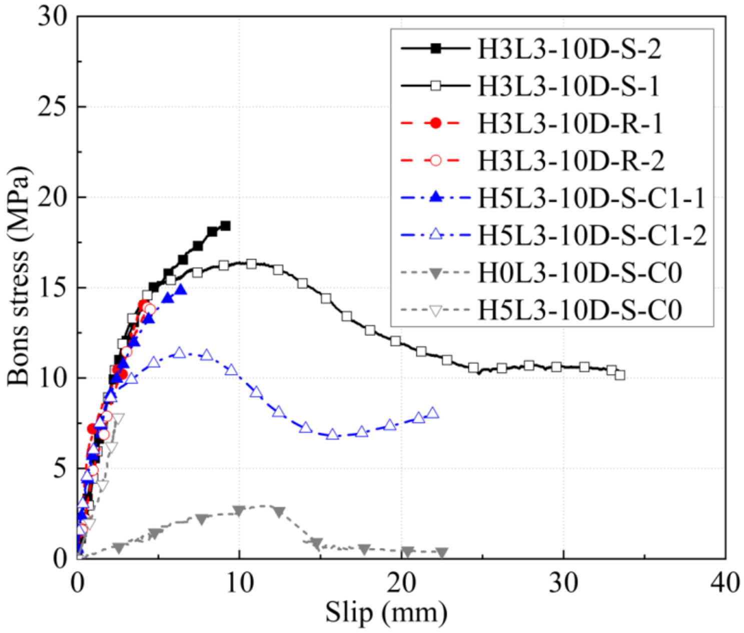

Figure 7.10 Effect of concrete block on bond stress-slip curves of hybrid rebar specimens with a bond length of 10*d* and a 3-ply GFRP tube (L3-10D Group)

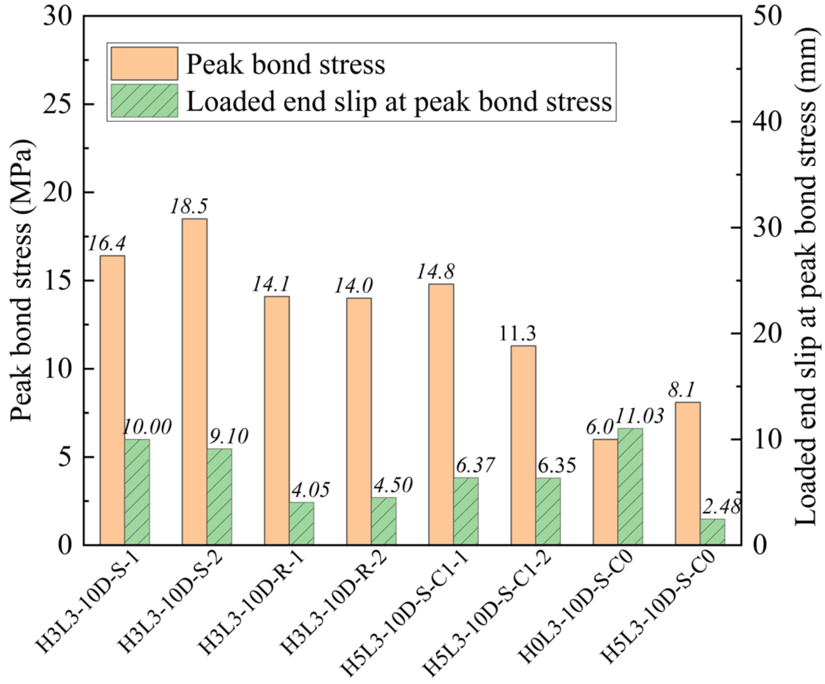

(a) Peak bond stress and corresponding loaded end slip

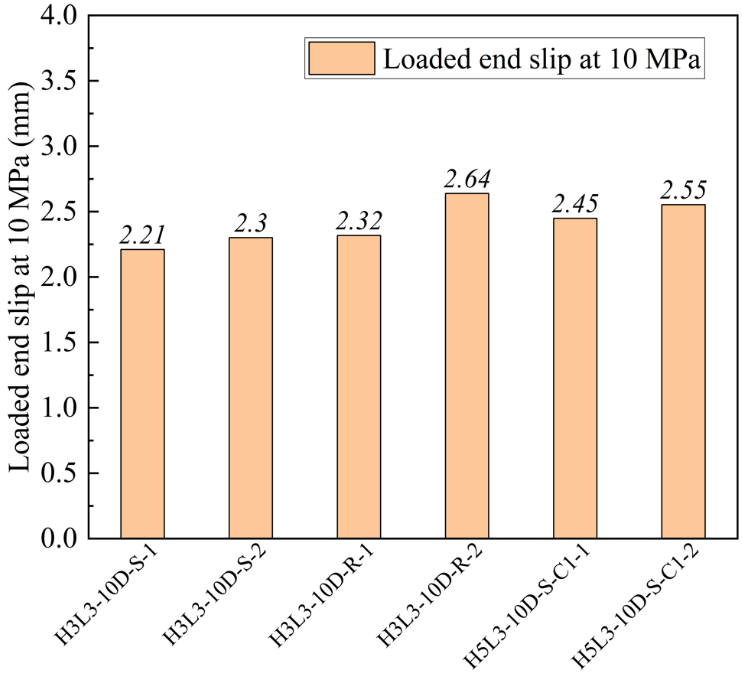

(b) Loaded end slip at 10 MPa

Figure 7.11 Comparisons of key parameters for specimens with a bond length of 10*d* and 3-ply GFRP tube (L3-10D Group)

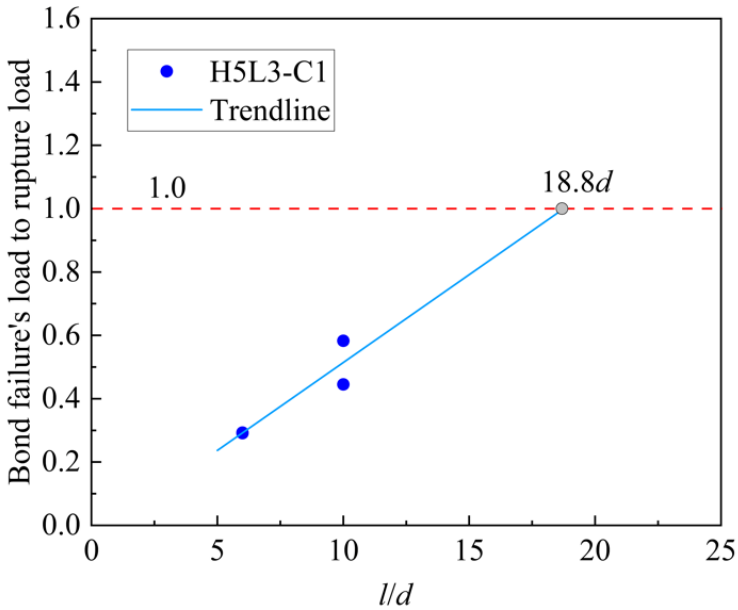

Figure 7.12 Relationship between ratios of peak loads to FRP rebar rupture loads against the embedment lengths for specimens H5L3-S-C1

CHAPTER 8
CONCLUSIONS

8.1 INTRODUCTION

A novel type of filament-wound FRP tubes with a wavy shape has been proposed and used successfully to fabricate wavy-shaped hybrid rebars in this Ph.D. research project. Wavy-shaped hybrid rebars are a new form of hybrid rebars which consist of an outer wavy-shaped FRP confining tube and a central FRP rebar, with the space between them filled with high-strength cementitious material such as ultra-high performance concrete (UHPC). The adoption of an outer wavy-shaped FRP tube was expected to enhance the bond performance of the hybrid rebar by introducing mechanical interlocking between the hybrid rebar and the surrounding concrete.

This Ph.D. thesis has presented the results of a systematic research programme aimed at understanding the behaviour of wavy-shaped hybrid rebars, including (1) manufacturing and properties of wavy-shaped GFRP tubes; (2) compressive behaviour of FRP-confined UHPC and ultra-high performance fibre reinforced concrete (UHPFRC); (3) compressive behaviour of wavy-shaped hybrid rebars under monotonic and cyclic axial compression; and (4) pullout tests of wavy-shaped hybrid rebars.

8.2 MANUFACTURING AND PROPERTIES OF WAVY-SHAPED GFRP TUBES

In Chapter 3, a manufacturing method of wavy-shaped GFRP tubes with the filament winding technology was introduced. A systematic experimental investigation [i.e., including burn-off (BO) tests, microscopic observations (i.e., digital image processing, DIP), split disk tests and internal air pressure tests] on the properties of fabricated wavy-shaped GFRP tubes was conducted and the results were presented in Chapter 3. The BO tests and the DIP method were successfully conducted to determine the fibre volume fractions at different locations of the fabricated GFRP tubes. The results between the BO tests and the DIP method differed only up to 4.21%. The conventional uniform tubes exhibited higher fibre volume fractions compared to the wavy-shaped tubes with the same number of fibre layers. The middle region between the peak and trough locations possessed the smallest fibre volume fraction for the wavy tubes with wave heights of 5 mm and 3 mm. The internal air pressure tests demonstrated that the proposed testing device could yield elastic modulus results comparable to those from split disk tests for conventional uniform GFRP tubes. However, the results obtained for wavy-shaped tubes may not be sufficiently accurate due to the friction between the gasbag and the GFRP tube. The total amount of fibres of wavy-shaped tubes was similar to that of uniform tubes with the same number of fibre layers. In summary, the test results demonstrated the successful fabrication of wavy-shaped GFRP tubes in this Ph.D. research programme.

8.3 COMPRESSIVE BEHAVIOUR OF FRP-CONFINED UHPC/UHPFRC

A systematic experimental study of FRP-confined UHPC/UHPFRC with an unconfined compressive strength of over 150 MPa was conducted and the test results were presented in Chapter 4. The test results revealed that the compressive behaviour of FRP-confined UHPC/UHPFRC was highly different from that of FRP-confined NSC. For the FRP-confined UHPC/UHPFRC specimens with a relatively low level of FRP confinement, the axial stress-strain curves displayed an ascending first branch followed by a descending branch. In contrast, for the specimens with a relatively large FRP confinement level, the axial stress-strain curves exhibited an ascending first branch, followed by an axial stress drop and then an ascending third branch.

A minimum value of $\rho_k \approx 0.036$ or 0.015 was determined to achieve a compressive strength exceeding the unconfined concrete strength for FRP-confined UHPC or FRP-confined UHPFRC. This threshold value of ρ_k was significantly higher than the value of 0.01 reported by Teng et al. (2009) for FRP-confined NSC, suggesting that a greater amount of FRP material is necessary to effectively confine UHPC/UHPFRC due to its brittle nature. Dang et al.'s (2022) stress-strain model provides reasonably accurate predictions for the axial stresses and strains at ultimate condition of FRP-confined UHPC/UHPFRC collected in the test database. However, the sudden axial stress drop after the ascending first branch for the specimens with a relatively large FRP confinement level could not be captured by the model. The equation in Liao et al. (2022) is capable of predicting the stress/strain enhancement ratios at the first characteristic point reasonably well. New equations for predicting the compressive strengths and the ultimate axial strains of FRP-confined UHPC and UHPFRC were proposed, which were demonstrated to perform better than the existing models in predicting the test results of the collected database.

8.4 COMPRESSIVE BEHAVIOUR OF WAVY-SHAPED HYBRID REBARS UNDER MONOTONIC AND CYCLIC AXIAL COMPRESSION

A total of 56 specimens were tested under axial compression to investigate the behaviour of wavy-shaped hybrid rebars in Chapters 5 and 6, including 32 specimens tested under monotonic axial compression and 24 specimens under cyclic axial compression. Two failure modes of hybrid rebars were observed: failure due to GFRP tube rupture which occurred before the failure of the internal GFRP rebar and failure of the internal GFRP rebar prior to the rupture of the GFRP tube, leading to a significant load drop. The presence of a wavy shape in the GFRP tube did not significantly affect the failure modes of the hybrid rebars.

The wavy-shaped GFRP tubes fabricated in this research project could provide sufficient confinement to the internal UHPC and FRP rebar. The test results in Chapter 5 indicated that if sufficient confinement was applied (i.e., $\rho_k > 0.036$), the hybrid rebars demonstrated high efficacy in improving the compressive performance of FRP rebars ranging from 13 mm to 25 mm in diameter. Compared to FRP rebars, significant enhancements in ductility were observed for the hybrid rebars. Therefore, the wavy-shape GFRP tubes produced using the method described in Chapter 3 were demonstrated to provide adequate confinement to the internal UHPC and FRP rebar. The axial stress-strain behaviours of wavy-shaped hybrid rebars with wave heights ranging from 1 mm to 5 mm were similar, suggesting that within this range, the wave height had a limited impact on the confinement mechanism in hybrid rebars. The theoretical method based on Jiang and Teng's (2007) model for FRP-confined concrete could provide a reasonable prediction of the axial load-strain curves for the wavy-shaped hybrid rebars, particularly when there is no significant load drop following the first peak axial load (Jiang and Teng, 2007).

For cyclic axial compression, the envelope curves of the cyclically loaded wavy-shaped hybrid rebars could also be divided into three or four stages, similar to the stress-strain curves of monotonically loaded wavy-shaped hybrid rebars. The envelope load-strain curves of wavy-shaped FRP tube-confined UHPC specimens and wavy-shaped hybrid rebars under cyclic axial compression were close to the load-strain curves of their corresponding specimens under monotonic axial compression. The equation of parameter η (i.e., Eq. 6.1) in Yu et al.'s (2015) model could provide accurate predictions for the shape of unloading paths of wavy-shaped FRP tube-confined UHPC specimens. In Chapter 6, new equations for plastic strains and stress deteriorations were proposed for both wavy-shaped FRP tube-confined UHPC specimens and wavy-shaped hybrid rebars, and these equations could provide reasonably accurate predictions for the current test results. The proposed theoretical model was reasonably accurate in predicting the compressive behaviour of wavy-shaped FRP tube-confined UHPC specimens and wavy-shaped hybrid rebars under cyclic axial compression.

8.5 PULLOUT TESTS OF WAVY-SHAPED HYBRID REBARS

To investigate the bond behaviour of hybrid rebars in concrete, pull-out tests were conducted, and the results are presented in this Ph.D. research project. In Chapter 7, the bond behaviour of FRP rebars in UHPC in hybrid rebars and the bond behaviour of hybrid rebars embedded in concrete were examined through two groups of pull-out tests. For Group I specimens with sand-coated and helically wrapped GFRP rebars, where the FRP rebars within hybrid rebars were subjected to pull-out forces, pull-out failure of FRP rebars occurred at a bond length of 10*d* (i.e., 10 times the nominal diameter of the FRP rebars), while rupture of the FRP rebars was observed with a bond length of 20*d*. However, for Group I specimens with ribbed GFRP rebars, all FRP rebars ruptured within the bond length range of 10*d* to 30*d* covered in the present study.

For Group II specimens (i.e., hybrid rebars embedded in concrete) without FRP confinement, concrete splitting failure occurred to the concrete blocks. However, when sufficient confinement was provided, the pull-out failure of the FRP rebar from the UHPC could be achieved. Specifically, for uniform hybrid rebars in Group II, the pull-out tests revealed significant slippage between the FRP rebar and the UHPC, as well as between the UHPC and the GFRP tube. However, for concrete specimens reinforced with wavy-shaped hybrid rebars, slippage was observed only between the FRP rebar and the UHPC.

The pull-out test results of Group I specimens indicated that the anchorage length of the 25-mm sand-coated and helically wrapped GFRP rebars ranged from 10*d* to 20*d*, while for ribbed GFRP rebars, it was less than 10*d*. The pull-out test results of Group II specimens indicated more precise values for the anchorage length of the 25 mm sand-coated and helically wrapped GFRP rebars, which should be 18.8*d*.

The experimental findings demonstrated that wavy-shaped hybrid rebars exhibited superior bond performance (i.e., higher bond strengths and smaller slips) compared to the corresponding uniform hybrid rebars. This enhancement was credited to the mechanical interlocking provided by wavy-shaped GFRP tubes. Based on the experimental results described in Chapter 7, the different thicknesses of the outer CFRP jacket in Group II specimens led to little variations in bond strength; however, an increase in the thickness of the GFRP tube in Group I specimens led to higher bond strengths. Although increasing confinement proved beneficial for enhancing the bond strength, the effect of the outermost CFRP jacket was less significant as the failure in the specimens was primarily attributed to the pulling-out of the FRP rebar.

8.6 FUTURE RESEARCH

This Ph.D. thesis has presented the results of a comprehensive research programme on the development, mechanical behaviour and bond performance of wavy-shaped hybrid rebars. While the objectives of this Ph.D. research project have been successfully accomplished, some issues remain and require further study, as detailed below:

(1) Further study is needed to understand the structural performance of columns reinforced with such wavy-shaped hybrid rebars under different loading conditions, including monotonic axial compression, cyclic axial compression, eccentric compression, and cyclic/seismic loadings;

(2) Future research should include a more in-depth investigation into the effects of wave height and wavelength on the bond behaviour of hybrid rebar;

(3) The buckling of wavy-shaped hybrid rebars in concrete needs to be well understood so that the contribution of hybrid rebars to the load resistance of the concrete members could be identified;

(4) Detailed studies on the resistance of wavy-shaped hybrid rebars to bending and shear stresses, particularly for those of large diameters, should also be conducted;

(5) Comprehensive investigations into the cyclic bond behaviour between wavy-shaped hybrid rebars and concrete should also be undertaken;

(6) The long-term performance of wavy-shaped hybrid rebars in severe environments (e.g., marine environment) should be investigated to demonstrate their durability; and

(7) The connection between two wavy-shaped hybrid rebars should be studied before they can be widely used in practice.

8.7 REFERENCES

Dang, Z., Li, Z.Y. and Feng, P. (2022). "Axial compressive behavior of UHPC confined by FRP", *Composite Structures*, 300, 116110.

Jiang, T. and Teng, J.G. (2007). "Analysis-oriented stress–strain models for FRP–confined concrete", *Engineering Structures*, 29(11), 2968-2986.

Liao, J.J., Zeng, J.J., Gong, Q.M., Quach, W.M., Gao, W.Y. and Zhang, L.H. (2022). "Design-oriented stress-strain model for FRP-confined ultra-high performance concrete (UHPC)", *Construction and Building Materials*, 318, 126200.

Teng, J.G., Jiang, T., Lam, L. and Luo, Y.Z. (2009). "Refinement of a design-oriented stress–strain model for FRP-confined concrete", *Journal of Composites for Construction*, ASCE, 13(4), 269-278.

Yu, T., Zhang, B. and Teng, J.G. (2015). "Unified cyclic stress–strain model for normal and high strength concrete confined with FRP", *Engineering Structures*, 102, 189-201.